Alma Mater Studiorum – Università di Bologna

DOTTORATO DI RICERCA IN

MECCANICA E SCIENZE AVANZATE
DELL'INGEGNERIA

Ciclo XXXIII

Settore Concorsuale: 09/A3

Settore Scientifico Disciplinare: ING-IND/14

NANOFIBROUS-STRUCTURED POLYMERS AND THEIR ENGINEERING APPLICATIONS

Presentata da: **Davide Cocchi**

Coordinatore Dottorato:

Prof. Marco Carricato

Supervisore:

Prof. Andrea Zucchelli

Esame finale anno 2021

a Chiara
e ai nostri figli presenti e futuri

ABSTRACT

Monolithic materials cannot always satisfy the demands of today's advanced requirements. Only by combining several materials at different length-scales, as nature does, the requested performances can be met. *Polymer nanocomposites* are intended to overcome the common drawbacks of pristine polymers, with a multidisciplinary collaboration of material science with chemistry, engineering, and nanotechnology. These materials are an active combination of polymers and nanomaterials, where at least one phase lies in the nanometer range. By mimicking nature's materials is possible to develop new nanocomposites for structural applications demanding combinations of strength and toughness.

In this perspective, nanofibers obtained by electrospinning have been increasingly adopted in the last decade to improve the fracture toughness of Fiber Reinforced Plastic (FRP) laminates. Although nanofibers have already found applications in various fields, their widespread introduction in the industrial context is still a long way to go.

This thesis aims to develop methodologies and models able to predict the behaviour of nanofibrous-reinforced polymers, paving the way for their practical engineering applications. It consists of two main parts. The first one investigates the mechanisms that act at the nanoscale, systematically evaluating the mechanical properties of both the nanofibrous reinforcement phase (Chapter 1) and hosting polymeric matrix (Chapter 2).

The second part deals with the implementation of different types of nanofibers for novel pioneering applications, trying to combine the well-known fracture toughness enhancement in composite laminates with improving other mechanical properties or including novel functionalities. Chapter 3 reports the development of novel adhesive carriers made of nylon 6,6 nanofibrous mats to increase the fracture toughness of epoxy-bonded joints. In Chapter 4, recently developed rubbery nanofibers are used to enhance the damping properties of unidirectional carbon fiber laminates. Lastly, in Chapter 5, a novel self-sensing composite laminate capable of detecting impacts on its surface using PVDF-TrFE piezoelectric nanofibers is presented.

CONTENTS

Nano-structured materials

The prefix "nano" derives from the Greek word νάνος and the Latin one "*nanus*" both meaning a dwarf, i.e. a very small person. It is adopted by the International System (SI) of units as an official prefix to indicate 10^{-9} part of a unit, and, generally, to refer to really small objects. In this perspective, according to the National Science Foundation, *nanotechnology* means the capability of controlling, assembling, manipulating, and characterizing matter at atomic and molecular length-scale [1]. Materials that are realized and processed in this way, and that exhibit at least one dimension below 100 nm, are conventionally known as *nanomaterials* [2]. Traditionally, 100 nm is considered the upper threshold, but, as a matter of fact, both in the literature and in industrial fields, the term nanomaterial refers to a large variety of objects and structures having a dimension below 1 μm [2,3]. This is partially because some mechanical, physical, and chemical properties and characterization tools actually start to "feel" the size reduction effects already at the microscopic scale [3]. The source of inspiration for the implementation and development of nanotechnologies most likely originated from the famous talk held on December 29, 1959, by the physicist and Nobel Prize R.P. Feynman, with his lecture entitled "*There's plenty of room at the bottom - An invitation to enter a new field of physics*" at the annual congress of the American Physical Society at the California Institute of Technology [4]. Nowadays, sixty years later, the development of nanotechnology has increased exponentially in different fields and more and more effort is being spent in this direction.

One of the fundamental aspects of nanotechnology is the creation of new materials, known as nanomaterials, engineered at nanoscale to have entirely different properties than their "bulk" counterpart [5]. The branch of nanotechnology involved in the research, development, and production of novel nano-structured architectures, functional nanomaterials, and smart nanocomponents with specific properties is called *nanomaterials science*. The nanomaterials can be classified according to dimension, chemical composition, materials properties, material applications and manufacturing technology [6]. Regarding the dimensional classification, reported in Figure 1.1, it is based on the number of dimensions that are outside the nanoscale range (> 1 μm). Accordingly, zero-dimensional (0-D) nanomaterials have all the dimensions within the nanoscale, i.e. three direction of nano-symmetry, like nanoparticles. One-dimensional nanomaterials (1-D) have one dimension outside the nanoscale and two directions of nano-symmetry. This class present filamentary structures where the length is significantly greater than the cross-sectional dimensions, like nanofibers, nanotubes, nanorods, nanowhiskers, and nanowires. Lastly, in two-dimensional nanomaterials (2-D), two dimensions are outside the nanoscale. This class includes plate-like structures such as nanoclays, graphene sheets, nanoplatelets, nanolayers, and nanocoatings.
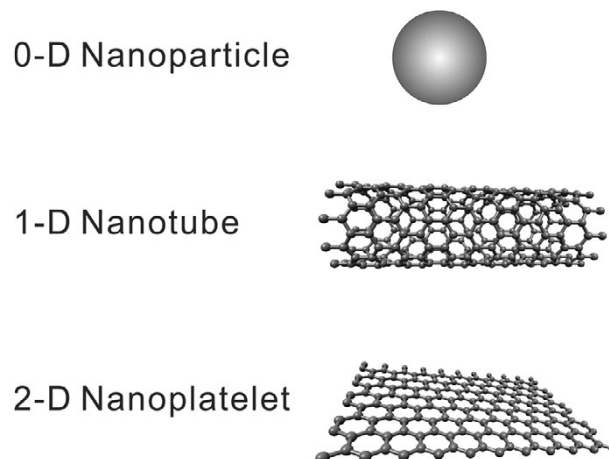
Figure 1.1 – Examples of dimensional classification of nanomaterials. Reproduced from F.K. Ko and Y. Wan [6] with kind permission of Cambridge University Press.

Nanocomposite is a multiphase solid material where at least one of the phases has at least one dimension lying in the nanometer range [7]. Generally, nanocomposites are the solid combination of a bulk matrix and nanoscale phase(s) which differ in properties due to dissimilarities in structure and chemistry [8]. The idea behind nanocomposite is to use building blocks with dimensions in the nanometre range to design and create new materials with a higher order of structural hierarchy, increasing their physical and mechanical properties. In particular, they are adopted in several fields to improve mechanical performance [9], electrical conductivity [10], thermal stability [11], chemical

properties [12], hinder flame and reduce smoke generations [13], reduce the permeability of gases, water, and solvents [14,15] as well as for optical [16], tissue engineering [17], sensing [18], energy storage [11], and fuel cells [19] applications.

Nanocomposites show enhanced characteristics respect to the conventional composite materials thanks to the extremely high surface to volume ratio of the reinforcing phase(s) and/or its exceptionally high aspect ratio. In this perspective, it is worth noting that the interface area between the matrix and the reinforcement phase is typically an order of magnitude greater than for conventional composite materials [20], increasing exponentially the active surface sites [21]. Moreover, the nano-size of the reinforcement phase ensures low surface defects and less imperfection inside the material [5]. Such a large specific surface allows a macroscopic effect to be observed even for a small amount of nano-reinforcement [20].

The typical characteristics of nanocomposites can be found in many natural composite materials as well as. After billions of years of evolution, natural materials, such as bamboo, bone, and nacre, show unique mechanical properties due to their intrinsic hierarchical multiscale architecture and plentiful interfacial interactions [22]. The comprehension of these advantageous features of living organisms are a particularly fertile source of inspiration in the development of bioinspired innovative material architectures [23].

In the creation of plants and organisms, nature uses a variety of innovative principles. It can be shown that biological construction methods are always produced with the least possible energy, have low mass and are durable [24]. Nature has evolved complex bottom-up methods for fabricating nanostructured materials with specific functionalities and enhanced properties [25]. For example, in human body, the skeletal muscle shows a hierarchical architecture of aligned structures like other connective tissues, such as tendons and ligaments [26]. In this natural composite material, the fundamental building-blocks acting at the nanoscale are the sarcomeres, which are composed of different filamentous proteins, called myofilaments, as reported in Figure 1.2. Similarly, tendons and bones are made up of collagen protein (Figure 1.3a). Each collagen molecule consists of three self-assembled polypeptide chains, supercoiled around a central axis to form a triple helix, which further self-assembles in both lateral and longitudinal directions into fibrillar nanofibers [27,28].
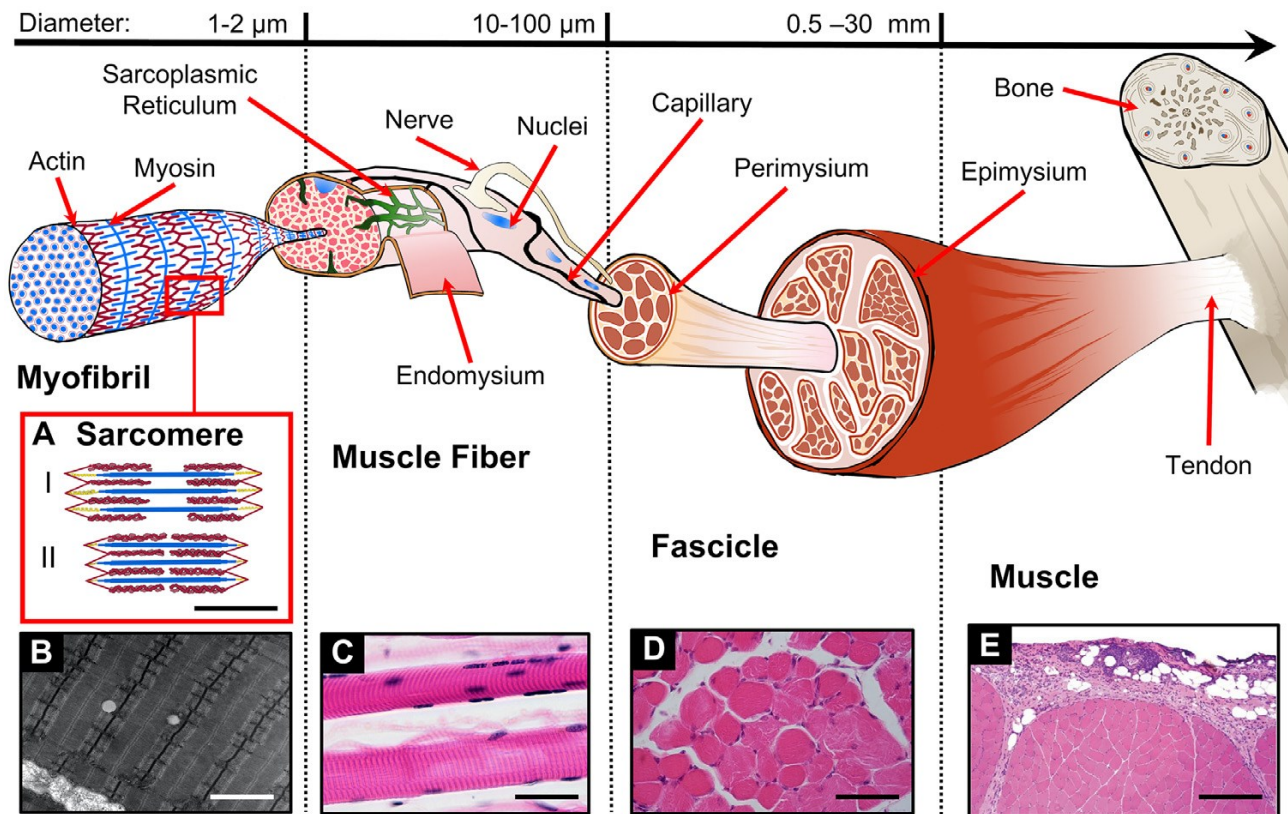
Figure 1.2 – Hierarchical structure of skeletal muscle. A) Sarcomere morphology and sliding mechanism (scalebar 0.5 nm): Actin (red), Myosin (blue) and Titin (yellow) filaments are shown in the relaxed state (I) and during the contraction (II). B) Transmission Electron Microscopy (TEM) image of myofibrils (scalebar = 1 nm. C) Phase Contrast Microscope (PCM) image of skeletal muscle fibers. Dark violet elliptical elements are the myocytes nuclei (scalebar = 50 μm). D) Histological image of a fascicle cross-section. Circular structures are the muscle fibers, while the darker violet dots are the myocytes nuclei (scalebar = 100 μm). E) Histological image of a portion of muscle cross-section (scalebar = 0.5 mm). Reproduced from C. Gotti et al. [26] under the terms and conditions of the Creative Commons Attribution-NonCommercial-No Derivatives License (CC BY NC ND).

Other natural composite examples are bamboo and palm. Thanks to their optimized hierarchical structure, they show high mechanical properties per unit weight [29]. As can be seen in Figure 1.3b, bamboo is a fiber-reinforced cellular material in which the fibers are aligned parallel to the stem, forming an orthotropic composite. Furthermore, it can be noted that the structure is not homogeneous, but the load-bearing microfibrils are on the outer periphery of the fibril, where the stress is higher [30]. So, the structure of bamboo, as well as other biocomposites, is optimized to use the smallest quantity of the most highly efficient cell-wall material to perform its function.
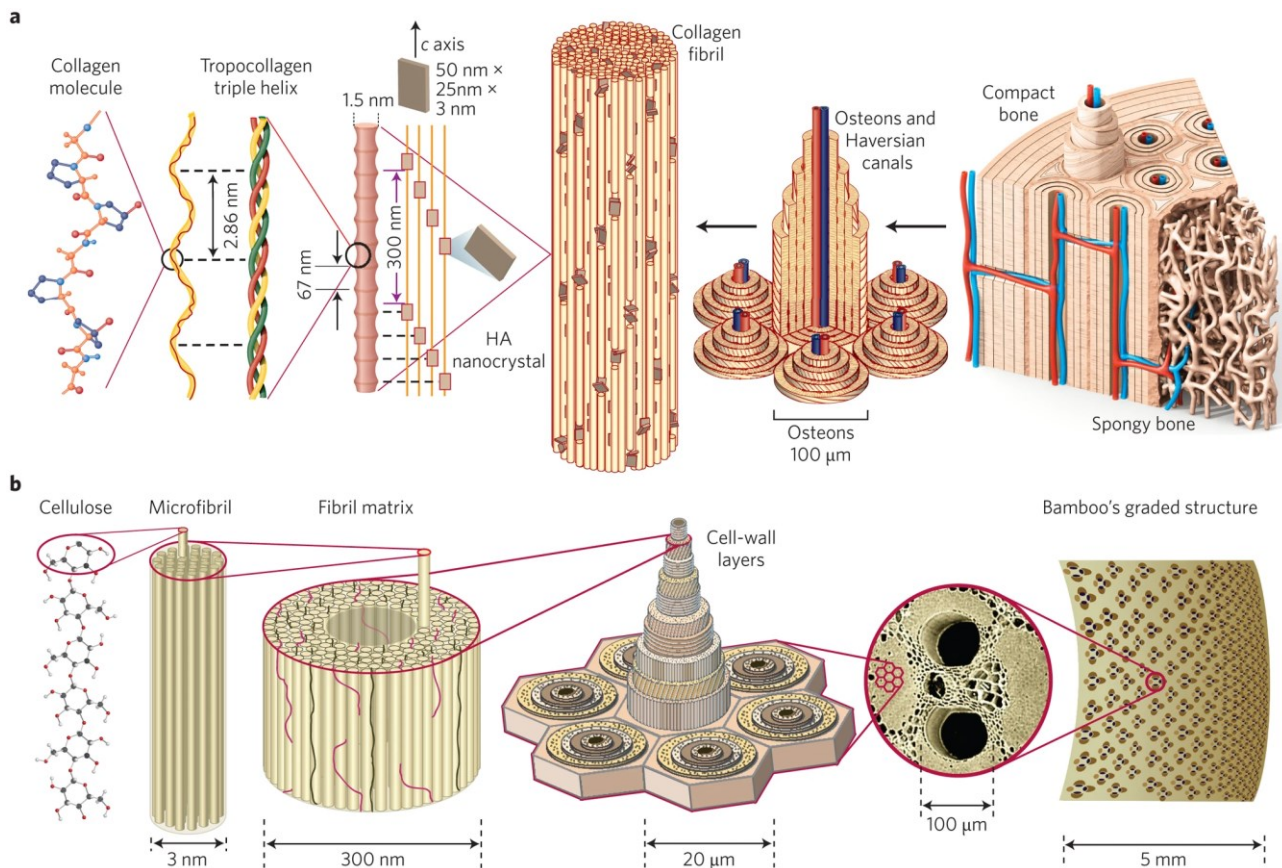
Figure 1.3 – Hierarchical structure of bone and bamboo. a) In bone, macroscale arrangements involve both compact/cortical bone at the surface and spongy/trabecular bone (foam-like material with ~100 µm-thick struts) in the interior. Compact bone is composed of osteons and Haversian canals, which surround blood vessels. Osteons have a lamellar structure, with individual lamella consisting of fibers arranged in geometrical patterns. The fibers comprise several mineralized collagen fibrils, composed of collagen protein molecules (tropocollagen) formed from three chains of amino acids and nanocrystals of hydroxyapatite (HA), and linked by an organic phase to form fibril arrays. b) Bamboo is composed of cellulose fibers imbedded in a lignin–hemicellulose matrix shaped into hollow prismatic cells of varying wall thickness. In bamboo and palm, which have a more complex structure than wood, a radial density gradient of parallel fibers in a matrix of honeycomb-like cells increases each material flexural rigidity. Bamboo increases its flexural rigidity even further by combining a radial density gradient with a hollow-tube cross-sectional shape. Reproduced from U.G.K. Wegst et al. [29] with kind permission of Springer Nature.

These are just a few examples, but natural nanostructured composites are actually all around us, especially those fiber-reinforced with one-dimensional nanomaterial of different nature [28]. Therefore, by mimicking nature's biological composite materials, it is possible to define hierarchical design strategies for constructing high-performance lightweight nanocomposites, overcoming the drawbacks of bulk materials.

Nanofibers

Although promising, most nanotechnology research is limited to dozens to a few hundred particles or molecules [5,6,31,32]. To realize massive assembly techniques, large-scale devices and marketable products need to be developed [6]. In fact, one of the main issues of nanotechnology is the effective and efficient fabrication of nanomaterials to be adopted in macroscale structures.

Among different nano-scaled materials, nanofibers have been widely applied in industry due to the ease in production processes compared to other nanomaterials [21]. As already observed, 1-D fibrous structures at the nanometer scale are the fundamentals building blocks of living hierarchical systems. The combination of high specific surface area, flexibility and superior directional strength makes fibers a preferred solution for many applications [6].

As previously described, conventionally, artificial nanofibers are fibers with a diameter below 100 nm. However, generally, all the fibers with a diameter below 1 μm are considered as nanofibers. The term "nanofibers" identifies a solid-state nanomaterial characterised by a mechanically flexible nanostructure and by an aspect ratio greater than 1000:1 [2]. As reported in Figure 1.4, by reducing fiber diameters down to the nanoscale, an enormous increase in specific surface area to the level of 1000 m^2/g is possible [6]. The small dimension and the high surface area greatly affect the chemical and biological reactivity and the bonding with a surrounding matrix. Furthermore, as the diameter decreases, the resistance of the fiber increases due to the lower probability of an inherent flaw in the material, as happens for carbon fibers [33]. As the diameter becomes even smaller, as in the case of Carbon Nanotubes (CNTs), the perfect atomic range and the lack of defects can confer to it a strength up to 30 GPa [34].

Although the effect of fiber diameter on the performance has been long recognized, the scientific community has found interest in polymeric nanofibers only in the last two decades with the rediscovery by Doshi and Raneker of the electrospinning technology [35].

Thus, bioinspired artificial fibers and corresponding membranes, featuring precise variations in material characteristics and morphologies, are highly promising nanomaterials [28]. Nowadays, nanofibers are widely adopted by researchers and industries for energy storage cells, catalyst, sensors, wound dressing, batteries, fuel cells, solar cells, protective clothing filters, scaffolds [28]. Among these applications, in the last decades nanofibers are being increasingly adopted to reinforce composite laminates [36,37].
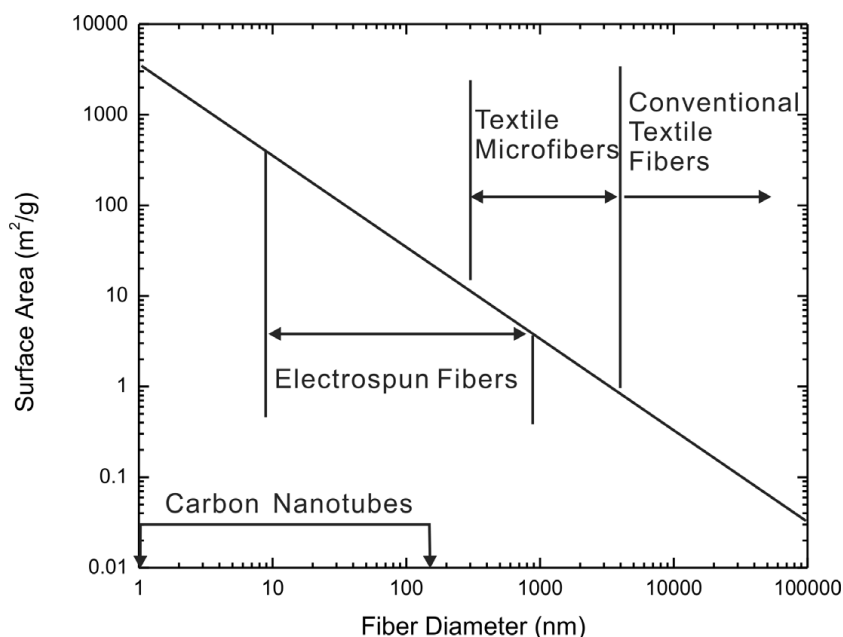
Figure 1.4 – Relation of surface area to fiber diameter. Reproduced from E. Gallo et al. [38] with kind permission of Springer Nature.

Electrospinning

Considering the potentialities offered by nanofibers, there is an increasing interest in nanofibers manufacturing technology [39]. There are various processes available to generate nanofibers, including template synthesis [40], vapour grown [41], phase separation [42], self-assembly [43], and electrospinning [44]. Amongst these technologies, electrospinning has attracted the most recent interest. Indeed, electrospinning with its top-down approach is the simplest, most straightforward, and cheapest process of producing ultra-fine polymeric fibers in a very short period of time with minimum investment [5].

Electrospinning was patented by Cooley [45] and Morton [46] in 1902. Electrospinning process involves the application of a high electric field between the tip of a capillary, in which the polymeric solution is pumped, and a ground collector. Most of the synthetic and naturally occurring polymers can be electrospun after dissolving in appropriate one or more solvents [5]. When the intensity of the applied electric field increases, the liquid drop at the tip of the needle becomes charged and it is stretched by the electrostatic forces opposed to the surface tension (Figure 1.5a). As a critical voltage is reached, the electrostatic forces overcome the surface tension of the drop and the liquid is ejected from the needle generating a conical shape known as Taylor cone. If the entanglement of the polymer chains is sufficiently high, the solution stretches without breaking and forms a jet, otherwise, small drops are ejected, and electrospray occurs.
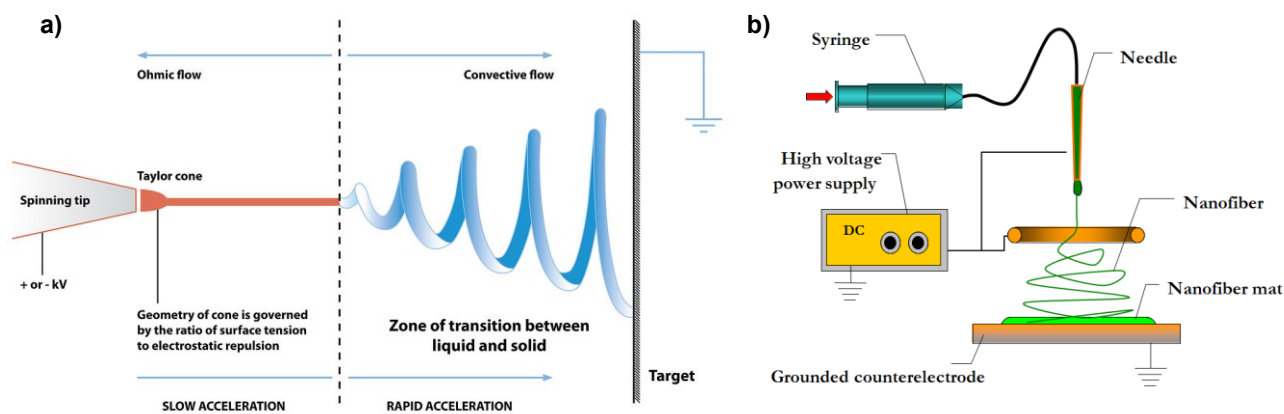
Figure 1.5 – a) Fiber formation during electrospinning process [47]. b) Basic lab-scale unit electrospinning setup. Adapted from Brugo et al. [48].

During the flight between the needle and the ground collector, the solvent evaporates, and the electric charges migrate to the surface of the forming fiber. The jet is then elongated in a whipped conical shape due to the bending instabilities induced by the electrostatic repulsion of the charges on the surface of the fiber. Finally, the jet is accumulated on the collector forming a nanofibrous mat. The elongation and the consequent fiber thinning leads to the formation of nanometric fibers.

In Figure 1.5b a lab-scale electrospinning setup is shown. It consists of four principal components: i) the high DC voltage generator, ii) a syringe with a metallic needle, iii) the pumping system, and iv) the collector. Typically, to produce membranes of consistent size and thickness, multi-needle systems are used [49,50]. Recently, a needleless technology has been developed, which allows the production of nanofibers on a large-scale for industrial applications [51].

Electrospinning parameters

The proper control of the electrospinning parameters allows to electrospun nanofibers with the desired morphology and diameter. As follows the different parameters, regarding both solution and process, and their effect are briefly described [52,53].

Solution parameters

Molecular weight affects the entanglement of the polymer chains. For a fixed concentration, lowering the molecular weight of the polymer leads to the formation of beads, while increasing makes smooth fibers, and further increasing micro-ribbon will be obtained [54] (Figure 1.6).

Concentration of the polymeric solution is a key parameter in the fiber formation, both for the aspect of nanofibers (diameter and morphology) and for their properties. It is possible to classify the concentration in four levels from low to high [53]:

- with a very low polymer concentration, electrospray process occurs instead of electrospinning one;
- increasing the concentration, a mix of fiber and beads is obtained;
- when the concentration is proper smooth fibers can be obtained;
- with a very high concentration, helix-shaped microfibers or ribbons are obtained.

Viscosity is the critical key in determining fiber morphology and diameter. If it is too high, the ejection from the needle becomes more difficult. If it is too low, fibers with beads will be obtained. It is worth noting that molecular weight, polymer concentration, and viscosity are closely related and dependent on each other.
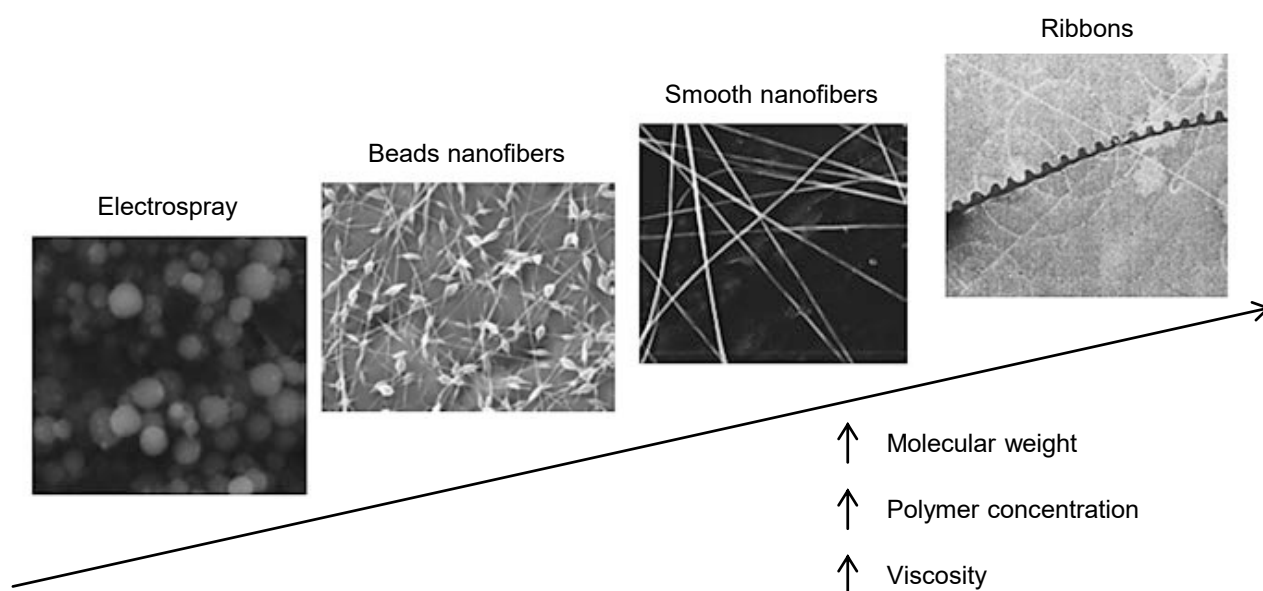
Figure 1.6 – SEM images showing the effect of the molecular weight, polymer concentration and viscosity on nanofiber morphology. Adapted from Z. Li and C. Wang [55] with kind permission of Springer Nature.

Surface tension plays an important role in the definition of the nanofibers final morphology. Fixing the polymer concentration, a reduction on the surface tension of the solution can transform beaded fibers into smooth fibers. A method to decrease surface tension is to use a solvent or a solvent mixture with a lower surface tension or by using a surfactant.

Boiling point affects how fast the spun polymeric solution evaporates during the flight. If it is too low, wet fibers will deposit on the collector, with the risk of melting each other and creating a film instead of a nanofibrous mat. If it is too high, the capillary needle may become clogged.

Dielectric constant involves the electric charge carrying capability of the polymer jet subjected to the electric field. The higher it is and stronger the polymer jet is attracted to the collector, resulting in thinner nanofibers [52].

Process parameters

Voltage is the driver parameter of the electrospinning process. Electrospinning occurs only when the applied voltage overcomes the threshold voltage, charging the polymer solution ejected from the Taylor cone. Its effect on the nanofiber morphology is controversial.

Distance between collector and spinneret is important to allow the evaporation of the solvents contained in the polymeric solution. If the distance is too short, the solvent will not have enough time to evaporate during flight and a melted nanofibrous mat will be obtained. If it is too long, bead fibers may be obtained [52].

Flow rate is the rate with which the solution ejects from the needle thanks to the pumping system. By increasing it, the productiveness of the process grows. However, if it is too high, thick fibers will be obtained due to the amount of solvent that cannot evaporate completely, and so low fiber stretching occurs. In the worst case, the needle can sputter little dots of polymeric solution on the nanofibrous membrane. On the other hand, lower flow rate allows for a better degree of polarization of the polymer solution. However, if the rate is too small it may cause a non-constant jet ejection.

Temperature and humidity are keys factors in obtaining a stable process and high-quality nanofibers. Low humidity and high temperature facilitate the solvent evaporation and reduce the solution viscosity, respectively, but they may dry too fast the solvent before it gets spun, clogging the capillary. Too high humidity can lead to thicker fibers because of the inhibited solvent evaporation.

All the aforementioned parameters, although governed by physical equations, are intimately interconnected, so strict control of the process is difficult to achieve. Often, the electrospinning process setup of a new polymer involves a heuristic approach, based on the knowledge of the effect of each parameter, the available data reported in the literature, and the user's expertise.

Polymer nanocomposites

Over the past decade, nanomaterials and polymer nanocomposites have gained tremendous impetus in various fields, as reflected by the exponential increase in the number of publications since their start [20] (Figure 1.7). *Polymer nanocomposites* are an active combination of polymer(s) and nanomaterial(s) (other additives may be also present) where at least one phase lies in the nanometric range. This special class of advanced materials, intended to overcome the common drawbacks of pristine polymers, requires a genius multidisciplinary collaboration of material science with chemistry, engineering, and nanotechnology to explore novel material architectures. Monolithic materials cannot always satisfy the demands of today advanced requirements. Only by combining several materials at different length-scales, as nature does, the requested performances can be met.
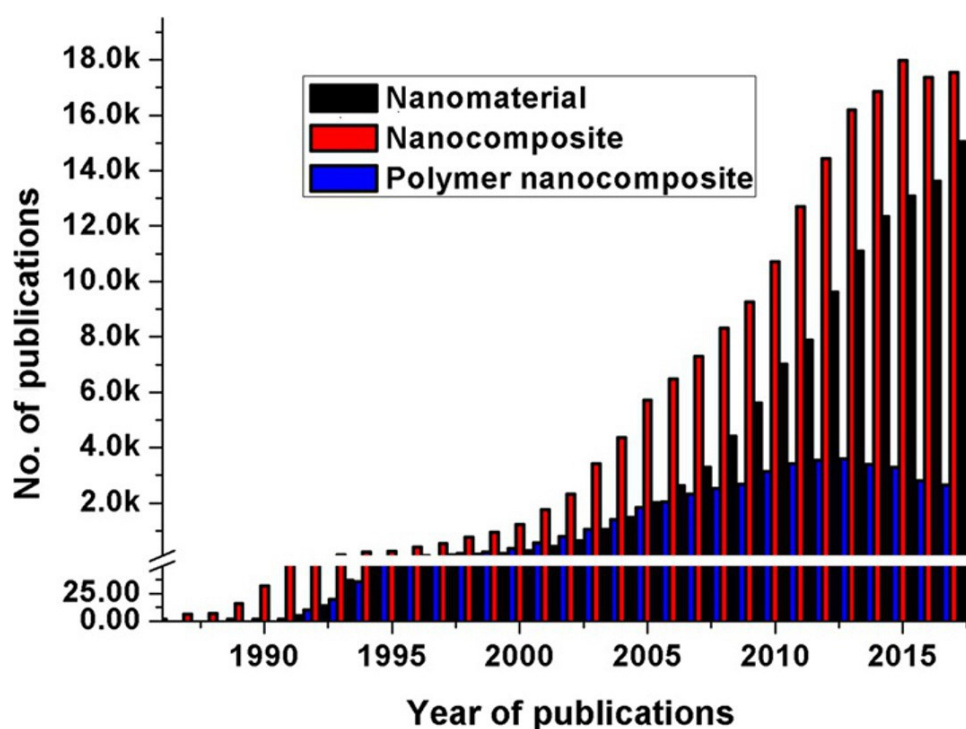
Figure 1.7 – Number of publications per year on the topics of nanomaterials, nanocomposites, and polymer nanocomposites (as obtained from Scifinder Scholar, on January 6, 2018). Reproduced from N. Karak [20] with kind permission of Elsevier.

Among polymeric matrices, epoxy resins are the most widely adopted in structural applications, like aerospace, wind turbine, and automotive, thanks to their high-performance. Epoxies are thermosetting polymers mainly used as matrices of fiber reinforced plastic (FRP) composite materials and as adhesives. Compared to other thermosets, epoxies exhibit excellent engineering properties, like high modulus and strength, low creep, and good thermal and dimensional stability. However, due to their highly cross-linked structure, epoxies have inherently low toughness and reduced resistance

to impacts, making them brittle and low resistant to crack initiation and growth [56]. By observing the Ashby diagram in Figure 1.8, it is possible to appreciate the high specific strength of epoxies with respect to other polymers, but, on the other hand, looking at the other Ashby diagram in Figure 1.9, their very low fracture toughness.

Unfortunately, this drawback of epoxy resin requires caution in their use in structural applications. In FRPs, for example, the high cross-linking density of the epoxy matrix leads to a highly brittle interface between plies. Due to their ply-by-ply nature, indeed, composite laminates are susceptible to delamination along interlaminar planes, whose propagation brings the structure to a rapid catastrophic failure. This intrinsic problem obliges designers to adopt high safety factors in the design of composite laminate structures, thus limiting the full exploitation of the extremely high specific strength of FRPs.
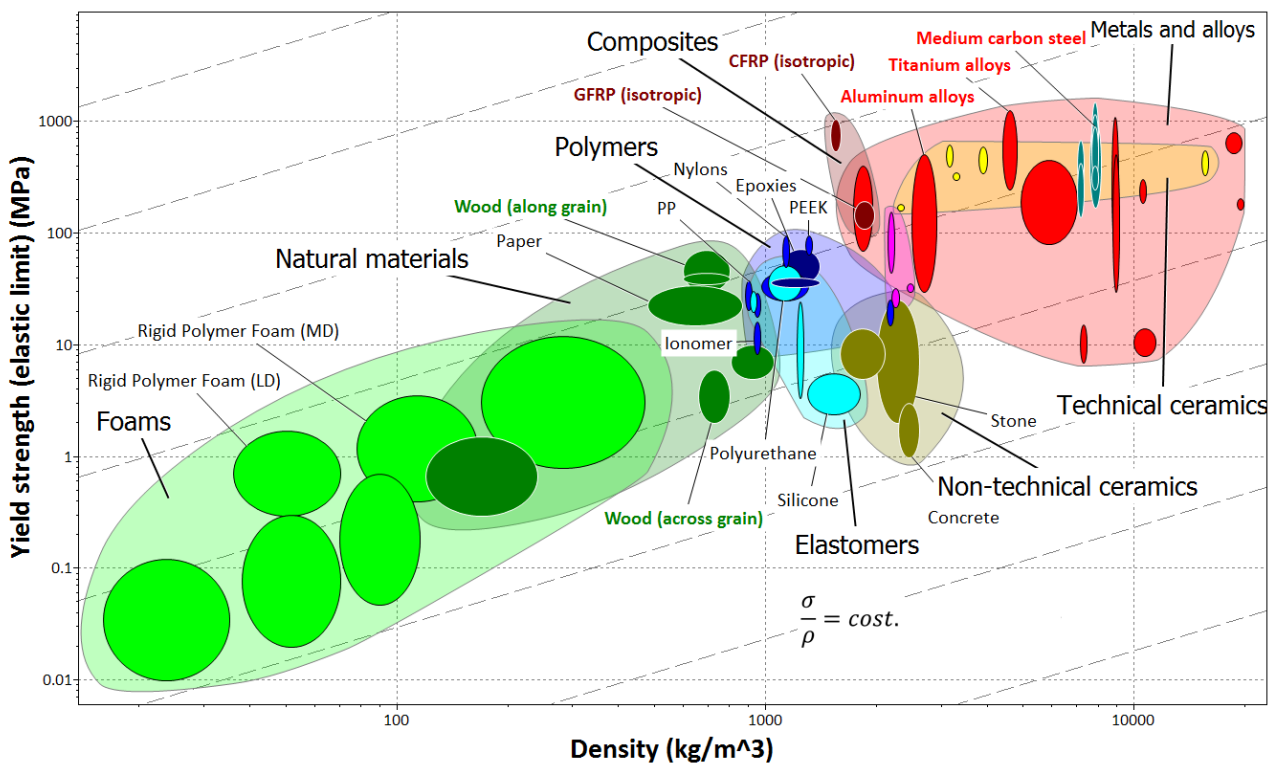
Figure 1.8 – Ashby diagram yield strength versus density.

Therefore, the attainment of both strength and toughness is fundamental for most structural materials, but these properties are generally mutually exclusive, and so compromises are necessary [25,29]. Bone and nacre are typical examples of damage-tolerant natural materials that efficiently combine strength and toughness [57–61]. For example, as previously mentioned, the human cortical bone is a natural composite made of a fibrous polymer (collagen) and hard mineral nanoparticles (carbonated hydroxyapatite) that resists fracture thanks to complementary *intrinsic* and *extrinsic* mechanisms throughout its multiscale hierarchical structure [59,62] (Figure 1.10). Similarly, nacre,

one of nature's toughest materials, consists of a brick-and-mortar like structure spanning through all the dimensional scale, in which hard aragonite tablets are glued together with soft organic materials to form tiles [63]. Its lamellar architecture interleaved by soft organic layers causes crack deflection and resists slip thanks to the brick-like assembly interlocking of the molecules, providing enhanced toughness and impact resistance [64]. In these biocomposite materials, *intrinsic* toughening mechanisms (that promote in situ inherent resistance on fracture propagation ahead the crack tip) and *extrinsic* shielding mechanisms (that act behind the crack tip to inhibit this) operate synergically and simultaneously at different length-scale thanks to an optimized hierarchical architecture at each structural level [29,65]. As previously suggested, by mimicking nature's biological materials it is possible to develop new nanocomposites for structural applications demanding combinations of both strength and toughness [25].
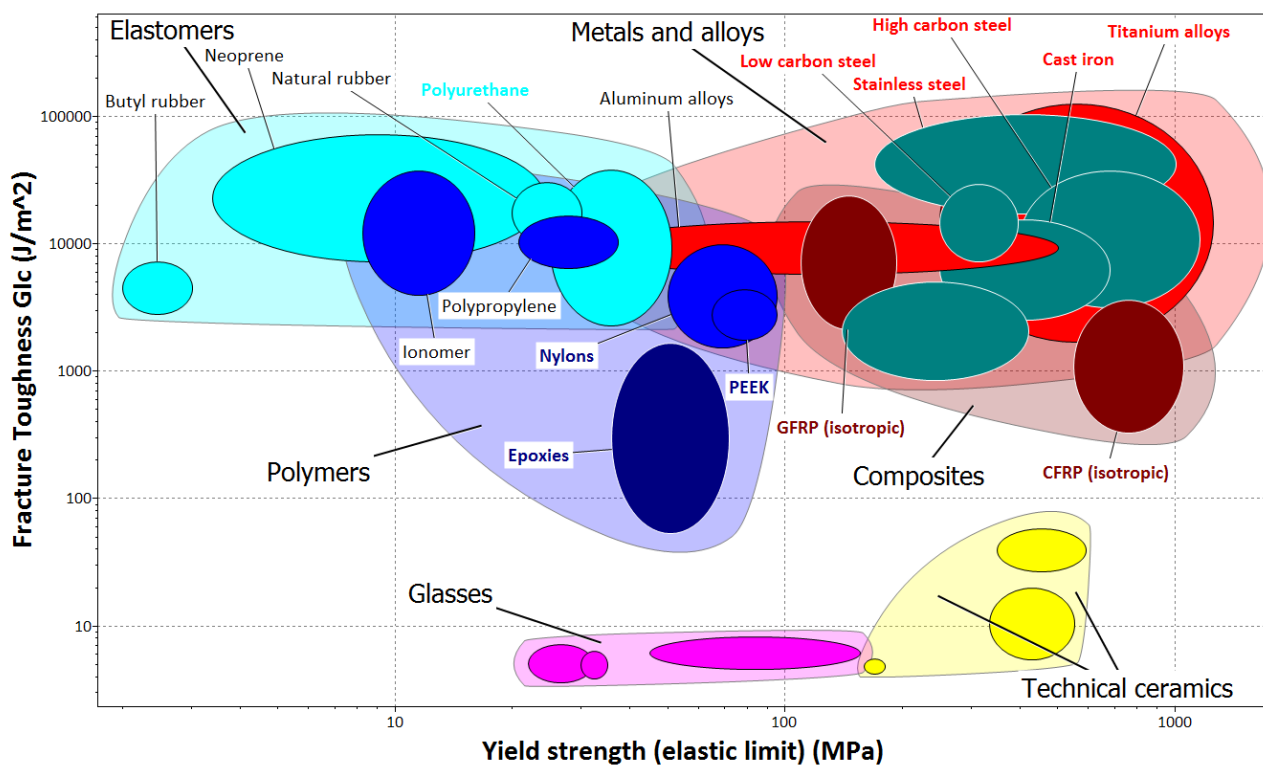
Figure 1.9 – Ashby diagram fracture toughness (G_{Ic}) versus yield strength.

In this perspective, the improvement of polymers mechanical properties, and in particular toughness, by adding second-phase fillers like dispersed rubber [66–68], inorganic particles [69,70] or thermoplastic polymers [71] is a well-known solution adopted in the last few decades by researchers and industries worldwide. Through micro- and nano-modification, it is possible to expand the material hierarchical structure and so enhance the polymeric matrix properties with limited filler contents [72]. The reason for the outstanding properties of nano-modified polymers lies in the significant amount of energy dissipated by the several damaging mechanisms taking place at the

nanoscale. Specifically, (i) poor adhesion between fillers and matrix creates voids in the material, imposing a tortuous crack propagation [73,74], (ii) reaction between filler and matrix might cause substantial changes in the properties of the interfacial region [75–78], and (iii) the filler can slow crack propagation by pinning, pull-out, bridging, fiber locking and deflecting mechanisms, according to its size and tenacity [79–82].
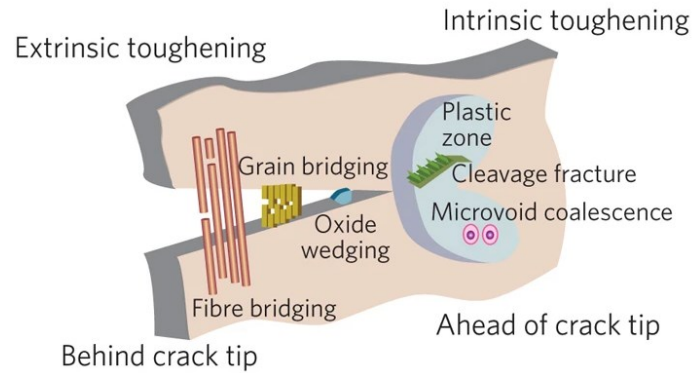
Figure 1.10 – In healthy human cortical bone, intrinsic toughening mechanisms that promote plasticity occur ahead of the crack tip and act primarily at the nanoscale, whereas extrinsic toughening mechanisms, specifically those that shield local stresses or strains from promoting fracture, act at larger length scales and mostly behind the crack tip. Adapted from U.G.K. Wegst et al. [29] with kind permission of Springer Nature.

The use of nano-reinforcement for composite material has attracted tremendously the scientific community in the last two decades. By adding a nano-reinforcement to a composite laminate, the hierarchical structure is increased from two to three hierarchical levels: i) the laminae defined at the sub-millimetre scale, ii) the fiber at the micron length-scale and iii) the nano-reinforcement at the nanoscale. In this context, the geometrical shape, surface chemistry, aspect ratio, and size of the embedded nanomaterials are critical parameters in tuning such interactions and, hence, the properties of the resultant systems. For example, nanoparticles, because of their ultrafine size, have the tendency to aggregate, especially if not stabilized during their formation and implementation [20].

Similarly, the graphene based nano-structures, like single-walled carbon nanotubes (SWCNTs) – often simply called CNTs – and multi-walled carbon nanotubes (MWCNTs), are widely adopted to increase the mechanical performance of composite laminates. These particularly small nano-structures, ranging from 1 to 100 nm, present incredibly high mechanical performance due to their perfect atomic arrangement free of flaws. In their review work on CNTs reinforced composite laminates, Kim *et al.* [83] reported a wide variation on the increase of the interlaminar fracture toughness, ranging from 25 % to 150 % for Mode I and from 27 % to 200 % for Mode II. In this case as well as, the cause of this widespread was attributed to the difficulties in the homogeneous dispersion of CNTs into the epoxy matrix [84]. A major issue for the use of CNT and MWCN, rather than the process, it is their still not

clear impact on the human health [85]. In United States and Europe, the safety and health institutions detailed the potential hazards and recommended a limited exposure to this type of nano-reinforcement.

Among nano-structuring methods, in recent years nanofibers obtained by electrospinning have been increasingly used in FRP laminates to increase mode I and mode II fracture toughness [86–88].

From a more general point of view, nanofibers complete the missing ring of the hierarchical scale in composite materials, which starts from the laminate dimension and ends with the epoxide functional groups (Figure 1.11). In fact, their one-dimensional characteristic allows to have two directions of nano-symmetry, and one, namely the length, which is close to the dimensional scale of the microfibers.
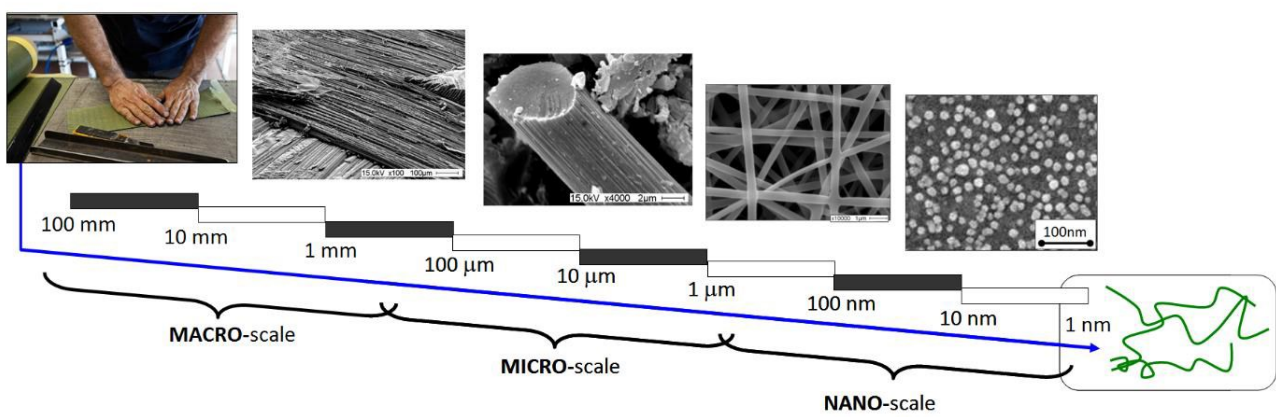
Figure 1.11 – Hierarchical structure composite laminates completed by nanofibers.

Compared to conventional interlaminar toughening techniques, nanofibrous mat interleaving presents different advantages:

- The high porosity of the nanofibrous mat allow the resin to easily flow through the nanofibers and impregnate it. Moreover, being porous its weight is relatively low and a negligible amount of weight is added.

- The thickness of the nanofibrous mat is small enough that the resin already contained in the prepreg is enough to impregnate it. Hence, no needs of additional matrix resin is required.

- The fine polymeric nanofibers are flexible and are expected to fit the shape of the primary reinforcement architecture at the ply interfaces, eliminating the resin pockets and thus creating a solid bonding between two the adjacent plies.

- The polymeric nanofibrous mat usually does not dissolve in the epoxy matrix and is confined in the interlayer, hence does not affect the matrix-microfiber adhesion and the stiffness of the matrix within the fiber tow of the single plies (which is crucial to keep the microfibers in position and avoid micro buckling).

In their review work, Palazzetti and Zucchelli [37] present a detailed state-of-the-art on the effect of nanofibrous interleaves into composite laminates with focus on the mechanical performances and behaviours of nano-modified materials. They found an increase in fracture toughness up to 340 % in Mode I and up to 400 % in Mode II. By comparing Mode I and Mode II overall results, they found that nanofibers are more effective in the latter case. But what is more interesting to note is that in the vast majority of the analysed works an increase in fracture toughness is achieved, meaning that an increase in delamination resistance can be obtained for very brittle as well as very tough laminates.
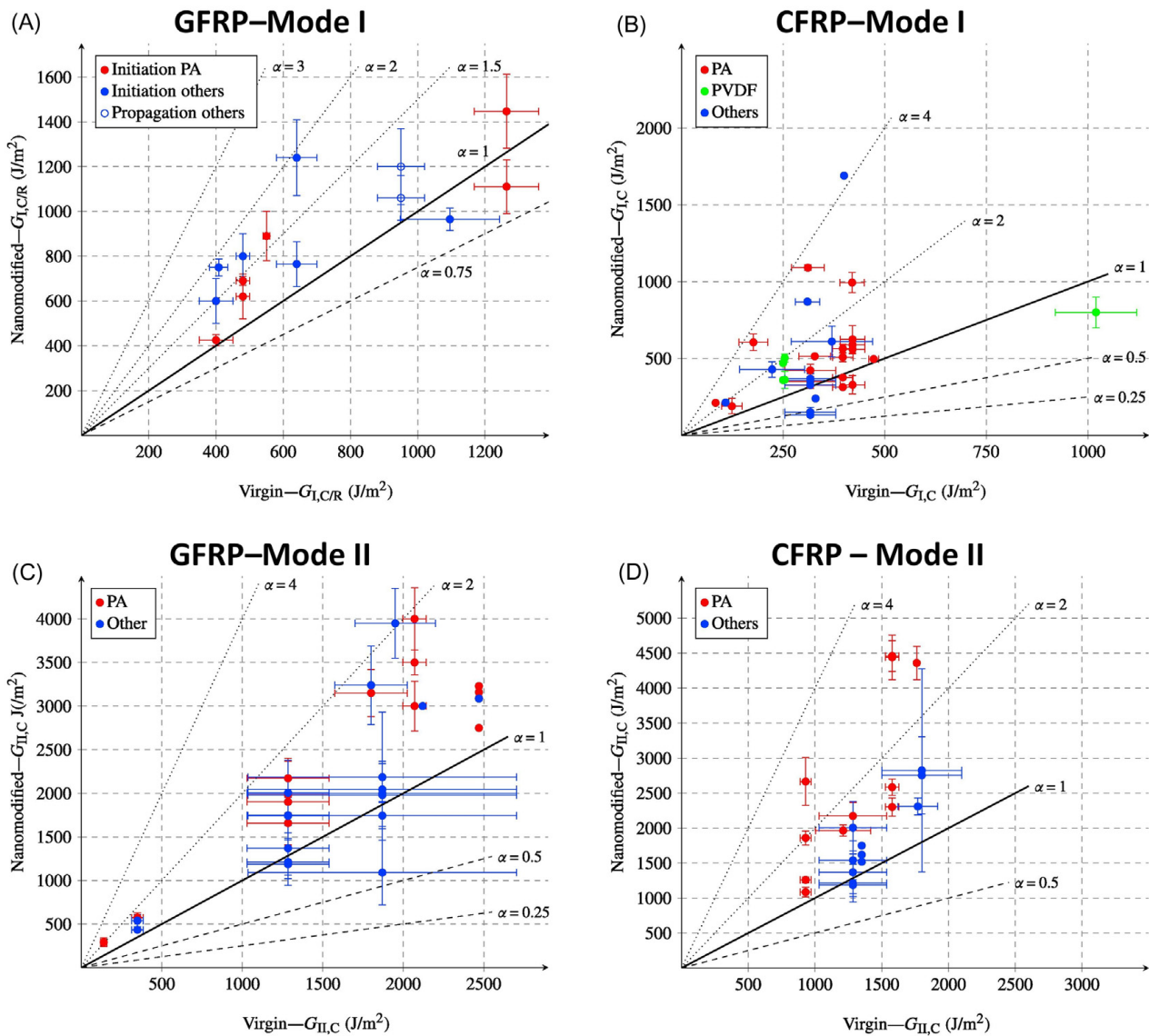
Figure 1.12 – Overview of literature data for the effects of nanofiber interleaves on the Mode I (GI;C) and Mode II (GII;C) delamination resistance: (A) GFRP GI;C, (B) CFRP GI;C, (C) GFRP GII;C, and (D) CFRP GII;C. The ratio of the nanomodified to virgin delamination resistance α is plotted for several cases to allow quick assessment of the improvements reported in different studies. CFRP, Carbon fiber-reinforced polymers; GFRP, glass fiber reinforced polymer. Reproduced from [89] with kind permission of Elsevier.

For example, the datapoints in Figure 1.12 show that increases of the delamination resistance can be obtained over a range of base laminates with an interlaminar toughness of $100 \div 1000$ J/m^2 for G_{Ic} and $500 \div 2500$ J/m^2 for G_{IIc}. These ranges indeed cover most of the structural composite materials used in industrial applications, proving the viability of the nanofiber interleaving technique [89]. Moreover, an increase in fatigue life [90] and impact behaviour was proven [91,92].

It seems that toughening is achieved both by nanofiber bridging effects and the inherent toughness and plastic deformation of the nanofibers both by the crack path deflection and forking towards adjacent non-reinforced interlayers. Comparing it to traditional rubber- or thermoplastic particle-toughened epoxies, it is clear that the nanofibers aspect ratio favours bridging effects, in addition to crack deflection, resulting in higher toughening efficiency [89,91]. In particular it was observed that nanofiber bridging only occurs at the interlaminar crossings in interleaved laminates due to an interaction between the delamination path and the nano-toughened interlayer (Figure 1.13). This means that the base delamination energy is retained and increased by the interlaminar crossings where nanofiber bridging occurs by the crack through the nano-toughened epoxy matrix [89].
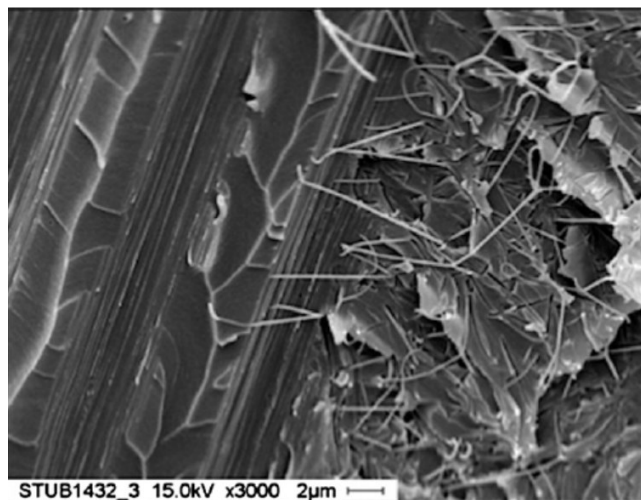
Figure 1.13 – SEM investigation of nano-modified interfaces after impact. It is possible to observe the nanofiber bridging effect along the crack interface. Adapted from Palazzetti et al. [91] with kind permission of Elsevier.

Therefore, it was demonstrated that nanofibrous interlayer can bring significant benefits to composite laminates from structural and load-bearing points of view. Nanofibers impact in terms of increase of weight and sizes is negligible, but the mechanical properties of the interleaved nano-composite laminate are significantly enhanced compared to that one of the pristine laminates.

Despite nanofibers have already found application in various fields, their wide introduction in laminates for reinforcing purposes has still a long way to go [37]. To exploit at best the potential of

these nanomaterials, it is necessary to have tight control and awareness of the mechanisms that take place at the different dimensional scales. The aim of this thesis is to develop methodologies and models to predict the behaviour of these materials in order to pave the way for their practical engineering applications in the industrial context.

The thesis is divided into two main parts. The first one is more about research topics on nanofibrous-reinforced materials, while the second one deals with the implementation of nanofibers for novel pioneering applications.

The aim of the first part is to investigate the mechanisms that act at the nanoscale trying to implement models and methodologies aimed to systematically evaluate the effect of both phases of the polymer nanocomposite. A detailed investigation of both the nanofibrous reinforcement phase and the hosting matrix of the nanocomposite is carried out. In Chapter 1, a methodology to evaluate the mechanical properties of nanofibrous membranes and a detailed investigation of the nanomat tensile behaviour are presented.

In Chapter 2, instead, a numerical and experimental multiscale analysis of the effect of geometric cavities generated by the presence of the nanofibers themselves on the macroscale mechanical properties of the hosting matrix is presented.

In the second part, new applications of nanofibers for engineering applications will be analysed. As shown, nanofiber mats are widely adopted to increase the fracture toughness of composite laminates. However, up to now, by the Author's knowledge, nobody has developed methodologies to combine the well-known fracture toughness enhancement with the improvement of other mechanical properties or to include novel functionalities. In this context, the crack toughening induced by electrospun nanomats can be potentially used in adhesive bonding to produce adhesive carriers, or in composite laminates to enhance the damping properties, or to realize self-sensing laminates. To this end, nanofibers of different materials are analysed in each Chapter, depending on the functions they are intended to perform.

In Chapter 3, the use of thermoplastic nanofibers made of nylon 6,6 to increase the fracture toughness of epoxy adhesive bonding and to act as an adhesive carrier is presented.

In Chapter 4, recently developed rubbery nanofibers made by NBR / PCL (nitrile butadiene rubber / poly(ϵ-caprolactone)) blend are used to enhance the damping properties of unidirectional carbon fiber composite laminates.

In Chapter 5 a novel self-sensing composite laminate capable of detecting impacts on its surface using piezoelectric poly(vinylidenefluoride-trifluoroethylene) (PVDF-TrFE) nanofibers is presented.

In each Chapter a more exhaustive analysis of the state-of-the-art on each topic is reported.

References

[1]   M.C. Roco, The long view of nanotechnology development: The National Nanotechnology Initiative at 10 years, J. Nanoparticle Res. 13 (2011) 427–445. https://doi.org/10.1007/s11051-010-0192-z.

[2]   D. Pisignano, Polymer Nanofibers: Building Blocks for Nanotechnology, 2013. https://books.google.com/books?id=QkqR3n6Zvp8C&pgis=1.

[3]   F. Trotta, A. Mele, Nanomaterials: Classification and Properties, in: Nanosponges, 2019: pp. 1–26. https://doi.org/10.1002/9783527341009.ch1.

[4]   R.P. Feynman, There's plenty of room at the bottom: An invitation to enter a new field of physics, in: Handb. Nanosci. Eng. Technol., 2002: pp. 1-1-1–9.

[5]   R. Asmatulu, W.S. Khan, Introduction to electrospun nanofibers, in: Synth. Appl. Electrospun Nanofibers, 2019: pp. 1–15. https://doi.org/10.1016/b978-0-12-813914-1.00001-8.

[6]   F.K. Ko, Y. Wan, Introduction to nanofiber materials, 2014. https://doi.org/10.1017/CBO9781139021333.

[7]   D. Vollath, Nanomaterials and Nanocomposites Synthesis, Properties, Characterization Techniques and Applications, 2013.

[8]   M. Sen, Nanocomposite Materials [Online First], in: Nanotechnol. Environ., IntechOpen, 2020. https://doi.org/10.5772/intechopen.93047.

[9]   R. Sengupta, S. Chakraborty, S. Bandyopadhyay, S. Dasgupta, R. Mukhopadhyay, K. Auddy, A.S. Deuri, A short review on rubber/clay nanocomposites with emphasis on mechanical properties, Polym. Eng. Sci. 47 (2007) 1956–1974. https://doi.org/10.1002/pen.20921.

[10]   Y. Geng, M.Y. Liu, J. Li, X.M. Shi, J.K. Kim, Effects of surfactant treatment on mechanical and electrical properties of CNT/epoxy nanocomposites, Compos. Part A Appl. Sci. Manuf. 39 (2008) 1876–1883. https://doi.org/10.1016/j.compositesa.2008.09.009.

[11]   L.W. Fan, X. Fang, X. Wang, Y. Zeng, Y.Q. Xiao, Z.T. Yu, X. Xu, Y.C. Hu, K.F. Cen, Effects of various carbon nanofillers on the thermal conductivity and energy storage properties of paraffin-based nanocomposite phase change materials, Appl. Energy. 110 (2013) 163–172. https://doi.org/10.1016/j.apenergy.2013.04.043.

[12]   W. Wang, G. Xu, X.T. Cui, G. Sheng, X. Luo, Enhanced catalytic and dopamine sensing properties of electrochemically reduced conducting polymer nanocomposite doped with pure graphene oxide, Biosens. Bioelectron. 58 (2014) 153–156. https://doi.org/10.1016/j.bios.2014.02.055.

[13]   S. Merighi, L. Mazzocchetti, T. Benelli, E. Maccaferri, A. Zucchelli, A. D'Amore, L. Giorgini, A New Wood Surface Flame-Retardant Based on Poly-m-Aramid Electrospun Nanofibers, Polym. Eng. Sci. 59 (2019) 2541–2549. https://doi.org/10.1002/pen.25235.

[14]   J. Yin, B. Deng, Polymer-matrix nanocomposite membranes for water treatment, J. Memb. Sci. 479 (2015) 256–275. https://doi.org/10.1016/j.memsci.2014.11.019.

[15]   H. Cong, M. Radosz, B.F. Towler, Y. Shen, Polymer-inorganic nanocomposite membranes for gas separation, Sep. Purif. Technol. 55 (2007) 281–291. https://doi.org/10.1016/j.seppur.2006.12.017.

[16]   M. Khairy, M.E. Gouda, Electrical and optical properties of nickel ferrite/polyaniline nanocomposite, J. Adv. Res. 6 (2015) 555–562. https://doi.org/10.1016/j.jare.2014.01.009.

[17]   T. Dvir, B.P. Timko, D.S. Kohane, R. Langer, Nanotechnological strategies for engineering complex tissues, Nat. Nanotechnol. 6 (2011) 13–22. https://doi.org/10.1038/nnano.2010.246.

[18]   N. Hu, Y. Karube, C. Yan, Z. Masuda, H. Fukunaga, Tunneling effect in a polymer/carbon nanotube nanocomposite strain sensor, Acta Mater. 56 (2008) 2929–2936. https://doi.org/10.1016/j.actamat.2008.02.030.

[19]   B.P. Tripathi, V.K. Shahi, Organic-inorganic nanocomposite polymer electrolyte membranes for fuel cell applications, Prog. Polym. Sci. 36 (2011) 945–979. https://doi.org/10.1016/j.progpolymsci.2010.12.005.

[20]   N. Karak, Fundamentals of Nanomaterials and Polymer Nanocomposites, in: Nanomater. Polym. Nanocomposites Raw Mater. to Appl., 2018: pp. 1–45. https://doi.org/10.1016/B978-0-12-814615-6.00001-1.

[21]   Y.-S. Lee, J. Sun, Preparation of Functionalized Nanofibers and Their Applications, in: Nanofibers, 2010. https://doi.org/10.5772/8150.

[22]   S. Gong, H. Ni, L. Jiang, Q. Cheng, Learning from nature: constructing high performance graphene-based nanocomposites, Mater. Today. 20 (2017) 210–219. https://doi.org/10.1016/j.mattod.2016.11.002.

[23]   J. Peng, Q. Cheng, High-Performance Nanocomposites Inspired by Nature, Adv. Mater. 29 (2017). https://doi.org/10.1002/adma.201702959.

[24]   B. Klein, B. Klein, Gestaltungsprinzipien im Leichtbau, in: Leichtbau-Konstruktion, 2013: pp. 65–73. https://doi.org/10.1007/978-3-658-02272-3_7.

[25]   M.E. Launey, R.O. Ritchie, On the fracture toughness of advanced materials, Adv. Mater. 21 (2009) 2103–2110. https://doi.org/10.1002/adma.200803322.

[26]   C. Gotti, A. Sensini, A. Zucchelli, R. Carloni, M.L. Focarete, Hierarchical fibrous structures for muscle-inspired soft-actuators: A review, Appl. Mater. Today. 20 (2020) 100772. https://doi.org/10.1016/j.apmt.2020.100772.

[27]   A. Gautieri, S. Vesentini, A. Redaelli, M.J. Buehler, Hierarchical structure and nanomechanics of collagen microfibrils from the atomistic scale up, Nano Lett. 11 (2011) 757–766. https://doi.org/10.1021/nl103943u.

[28]   S. Agarwal, S. Jiang, A. Greiner, Nanofibrous structures, in: Electrospinning Nanofabrication Appl., 2018: pp. 93–122. https://doi.org/10.1016/B978-0-323-51270-1.00004-2.

[29]   U.G.K. Wegst, H. Bai, E. Saiz, A.P. Tomsia, R.O. Ritchie, Bioinspired structural materials, Nat. Mater. 14 (2015) 23–36. https://doi.org/10.1038/nmat4089.

[30]   U.G.K. Wegst, Bending efficiency through property gradients in bamboo, palm, and wood-based composites, J. Mech. Behav. Biomed. Mater. 4 (2011) 744–755. https://doi.org/10.1016/j.jmbbm.2011.02.013.

[31]   M.S. Huda, L.T. Drzal, A.K. Mohanty, M. Misra, Effect of fiber surface-treatments on the properties of laminated biocomposites from poly(lactic acid) (PLA) and kenaf fibers, Compos. Sci. Technol. 68 (2008) 424–432. https://doi.org/10.1016/j.compscitech.2007.06.022.

[32]   Y. Wang, Nanomanufacturing Technologies: Advances and Opportunities, Proc. 18th Int. Conf. Manag. Technol. (2008). https://pdfs.semanticscholar.org/839f/e9edf8273c5527c43898040004d7ebad9f81.pdf.

[33]   E. de Lamotte, A.J. Perry, Diameter and strain-rate dependence of the ultimate tensile strength and Young's modulus of carbon fibres, Fibre Sci. Technol. 3 (1970) 157–166. https://doi.org/10.1016/0015-0568(70)90021-7.

[34]   A. Takakura, K. Beppu, T. Nishihara, A. Fukui, T. Kozeki, T. Namazu, Y. Miyauchi, K. Itami, Strength of carbon nanotubes depends on their chemical structures, Nat. Commun. 10 (2019). https://doi.org/10.1038/s41467-019-10959-7.

[35]   J. Doshi, D.H. Reneker, Electrospinning process and applications of electrospun fibers, J. Electrostat. 35 (1995) 151–160. https://doi.org/10.1016/0304-3886(95)00041-8.

[36]   A. Zucchelli, M.L. Focarete, C. Gualandi, S. Ramakrishna, Electrospun nanofibers for enhancing structural performance of composite materials, Polym. Adv. Technol. 22 (2011) 339–349. https://doi.org/10.1002/pat.1837.

[37]   R. Palazzetti, A. Zucchelli, Electrospun nanofibers as reinforcement for composite laminates materials – A review, Compos. Struct. 182 (2017) 711–727. https://doi.org/10.1016/j.compstruct.2017.09.021.

[38]   E. Gallo, A. Anwar, B. Nabet, Contact-Induced Properties of Semiconducting Nanowires and Their Local Gating, 2004.

[39]   S. Ramakrishna, K. Fujihara, W.E. Teo, T.C. Lim, Z. Ma, An introduction to electrospinning and nanofibers, 2005. https://doi.org/10.1142/5894.

[40]   H.R. Allcock, F.W. Lampe, J.E. Mark, Contemporary polymer chemistry (3rd edition), 2004. http://doi.wiley.com/10.1002/pi.1494.

[41]   Y.Y. Fan, H.M. Cheng, Y.L. Wei, G. Su, Z.H. Shen, Influence of preparation parameters on the mass production of vapor-grown carbon nanofibers, Carbon N. Y. 38 (2000) 789–795. https://doi.org/10.1016/S0008-6223(99)00178-5.

[42] T. Hongu, G.O. Philips, New fibers, 1997. https://doi.org/10.1533/9781855737570.

[43] J.D. Hartgerink, E. Beniash, S.I. Stupp, Self-assembly and mineralization of peptide-amphiphile nanofibers, Science (80-.). 294 (2001) 1684–1688. https://doi.org/10.1126/science.1063187.

[44] D.H. Reneker, I. Chun, Nanometre diameter fibres of polymer, produced by electrospinning, Nanotechnology. 7 (1996) 216–223. https://doi.org/10.1088/0957-4484/7/3/009.

[45] J.F. Cooley, Apparatus for electrically dispersing fluids, US Pat. 692631. (1902).

[46] W.J. Morton, Method of dispersing fluids, US Pat. 705691. (1902).

[47] J. Gatford, A diagram of the electrospinning process showing the onset of instability, 2008.

[48] T.M. Brugo, F. Musiari, A. Pirondi, A. Zucchelli, D. Cocchi, D. Menozzi, Development and fracture toughness characterization of a nylon nanomat epoxy adhesive reinforcement, Proc. Inst. Mech. Eng. Part L J. Mater. Des. Appl. 233 (2019) 465–474. https://doi.org/10.1177/1464420718807733.

[49] E. Maccaferri, L. Mazzocchetti, T. Benelli, T.M. Brugo, A. Zucchelli, L. Giorgini, Rubbery nanofibers by co-electrospinning of almost immiscible NBR and PCL blends, Mater. Des. (2020). https://doi.org/10.1016/j.matdes.2019.108210.

[50] D. Cocchi, F. Musiari, T.M. Brugo, A. Pirondi, A. Zucchelli, F. Campanini, E. Leoni, L. Mazzocchetti, Characterization of aluminum alloy-epoxy bonded joints with nanofibers obtained by electrospinning, J. Adhes. 96 (2020) 384–401. https://doi.org/10.1080/00218464.2019.1666716.

[51] G. Yan, H. Niu, T. Lin, Needle-less electrospinning, in: Electrospinning Nanofabrication Appl., 2018: pp. 219–247. https://doi.org/10.1016/B978-0-323-51270-1.00007-8.

[52] C. Zhang, X. Yuan, L. Wu, Y. Han, J. Sheng, Study on morphology of electrospun poly(vinyl alcohol) mats, Eur. Polym. J. 41 (2005) 423–432. https://doi.org/10.1016/j.eurpolymj.2004.10.027.

[53] Z. Li, C. Wang, One dimensional Nanostructures Electrospinning Technique and Unique Nanofibers, One-Dimensional Nanostructures. (2013) 1–70. http://link.springer.com/10.1007/978-3-642-36427-3.

[54] A. Koski, K. Yim, S. Shivkumar, Effect of molecular weight on fibrous PVA produced by electrospinning, Mater. Lett. 58 (2004) 493–497. https://doi.org/10.1016/S0167-577X(03)00532-9.

[55] Z. Li, C. Wang, Effects of Working Parameters on Electrospinning, in: 2013: pp. 15–28. https://doi.org/10.1007/978-3-642-36427-3_2.

[56] J. Chen, A.J. Kinloch, S. Sprenger, A.C. Taylor, The mechanical properties and toughening mechanisms of an epoxy polymer modified with polysiloxane-based core-shell particles, Polymer (Guildf). 54 (2013) 4276–4289. https://doi.org/10.1016/j.polymer.2013.06.009.

[57] M.A. Meyers, P.Y. Chen, A.Y.M. Lin, Y. Seki, Biological materials: Structure and mechanical properties, Prog. Mater. Sci. 53 (2008) 1–206. https://doi.org/10.1016/j.pmatsci.2007.05.002.

[58] R. Wang, H.S. Gupta, Deformation and fracture mechanisms of bone and nacre, Annu. Rev. Mater. Res. 41 (2011) 41–73. https://doi.org/10.1146/annurev-matsci-062910-095806.

[59] M.E. Launey, M.J. Buehler, R.O. Ritchie, On the mechanistic origins of toughness in bone, 2010. https://doi.org/10.1146/annurev-matsci-070909-104427.

[60] B. Ji, H. Gao, Mechanical principles of biological nanocomposites, Annu. Rev. Mater. Res. 40 (2010) 77–100. https://doi.org/10.1146/annurev-matsci-070909-104424.

[61] A.R. Studart, Towards high-performance bioinspired composites, Adv. Mater. 24 (2012) 5024–5044. https://doi.org/10.1002/adma.201201471.

[62] P. Fratzl, R. Weinkamer, Nature's hierarchical materials, Prog. Mater. Sci. 52 (2007) 1263–1334. https://doi.org/10.1016/j.pmatsci.2007.06.001.

[63] J. Sun, B. Bhushan, Hierarchical structure and mechanical properties of nacre: A review, RSC Adv. 2 (2012) 7617–7632. https://doi.org/10.1039/c2ra20218b.

[64] M.A. Meyers, A.Y.M. Lin, P.Y. Chen, J. Muyco, Mechanical strength of abalone nacre: Role of the soft organic layer, J. Mech. Behav. Biomed. Mater. 1 (2008) 76–85. https://doi.org/10.1016/j.jmbbm.2007.03.001.

[65] B. Liu, L. Huang, L. Geng, F. Yin, Multiscale Hierarchical Structure and Laminated Strengthening and Toughening Mechanisms, Lamination - Theory Appl. (2018). https://doi.org/10.5772/intechopen.69976.

[66] A.J. Kinloch, S.J. Shaw, D.A. Tod, D.L. Hunston, Deformation and fracture behaviour of a rubber-toughened epoxy: 1. Microstructure and fracture studies, Polymer (Guildf). 24 (1983) 1341–1354. https://doi.org/10.1016/0032-3861(83)90070-8.

[67] R.A. Pearson, A.F. Yee, Toughening mechanisms in elastomer-modified epoxies - Part 2 Microscopy studies, J. Mater. Sci. 21 (1986) 2475–2488. https://doi.org/10.1007/BF01114294.

[68] A.J. Kinloch, Toughening epoxy adhesives to meet today's challenges, MRS Bull. 28 (2003) 445–448. https://doi.org/10.1557/mrs2003.126.

[69] B.B. Johnsen, A.J. Kinloch, R.D. Mohammed, A.C. Taylor, S. Sprenger, Toughening mechanisms of nanoparticle-modified epoxy polymers, Polymer (Guildf). 48 (2007) 530–541. https://doi.org/10.1016/j.polymer.2006.11.038.

[70] D.J. Bray, P. Dittanet, F.J. Guild, A.J. Kinloch, K. Masania, R.A. Pearson, A.C. Taylor, The modelling of the toughening of epoxy polymers via silica nanoparticles: The effects of volume fraction and particle size, Polymer (Guildf). 54 (2013) 7022–7032. https://doi.org/10.1016/j.polymer.2013.10.034.

[71] A.J. Kinloch, M.L. Yuen, S.D. Jenkins, Thermoplastic-toughened epoxy polymers, J. Mater. Sci. 29 (1994) 3781–3790. https://doi.org/10.1007/BF00357349.

[72] M. Quaresimin, K. Schulte, M. Zappalorto, S. Chandrasekaran, Toughening mechanisms in polymer nanocomposites: From experiments to modelling, Compos. Sci. Technol. 123 (2016) 187–204. https://doi.org/10.1016/j.compscitech.2015.11.027.

[73] T.H. Hsieh, A.J. Kinloch, K. Masania, A.C. Taylor, S. Sprenger, The mechanisms and mechanics of the toughening of epoxy polymers modified with silica nanoparticles, Polymer (Guildf). 51 (2010) 6284–6294. https://doi.org/10.1016/j.polymer.2010.10.048.

[74] M. Quaresimin, M. Salviato, M. Zappalorto, A multi-scale and multi-mechanism approach for the fracture toughness assessment of polymer nanocomposites, Compos. Sci. Technol. 91 (2014) 16–21. https://doi.org/10.1016/j.compscitech.2013.11.015.

[75] M. Salviato, M. Zappalorto, M. Quaresimin, Plastic shear bands and fracture toughness improvements of nanoparticle filled polymers: A multiscale analytical model, Compos. Part A Appl. Sci. Manuf. 48 (2013) 144–152. https://doi.org/10.1016/j.compositesa.2013.01.006.

[76] X. Wang, J. Jin, M. Song, An investigation of the mechanism of graphene toughening epoxy, Carbon N. Y. 65 (2013) 324–333. https://doi.org/10.1016/j.carbon.2013.08.032.

[77] S. Chandrasekaran, N. Sato, F. Tölle, R. Mülhaupt, B. Fiedler, K. Schulte, Fracture toughness and failure mechanism of graphene based epoxy composites, Compos. Sci. Technol. 97 (2014) 90–99. https://doi.org/10.1016/j.compscitech.2014.03.014.

[78] A. Allaoui, S. Bai, H.M. Cheng, J.B. Bai, Mechanical and electrical properties of a MWNT/epoxy composite, Compos. Sci. Technol. 62 (2002) 1993–1998. https://doi.org/10.1016/S0266-3538(02)00129-X.

[79] F.F. Lange, The interaction of a crack front with a second-phase dispersion, Philos. Mag. 22 (1970) 983–992. https://doi.org/10.1080/14786437008221068.

[80] M.T. Aljarrah, N.R. Abdelal, Improvement of the mode I interlaminar fracture toughness of carbon fiber composite reinforced with electrospun nylon nanofiber, Compos. Part B Eng. 165 (2019) 379–385. https://doi.org/10.1016/j.compositesb.2019.01.065.

[81] M.H.G. Wichmann, K. Schulte, H.D. Wagner, On nanocomposite toughness, Compos. Sci. Technol. 68 (2008) 329–331. https://doi.org/10.1016/j.compscitech.2007.06.027.

[82] T. Liu, W.C. Tjiu, Y. Tong, C. He, S.S. Goh, T.S. Chung, Morphology and fracture behavior of intercalated epoxy/clay nanocomposites, J. Appl. Polym. Sci. 94 (2004) 1236–1244. https://doi.org/10.1002/app.21033.

[83] S.U. Khan, J.K. Kim, Impact and delamination failure of multiscale carbon nanotube-fiber reinforced polymer composites: A review, Int. J. Aeronaut. Sp. Sci. 12 (2011) 115–133. https://doi.org/10.5139/IJASS.2011.12.2.115.

[84] K.K. Singh, P. Rawat, Mechanical behavior of glass/epoxy composite laminate with varying amount of MWCNTs under different loadings, Mater. Res. Express. (2018). https://doi.org/10.1088/2053-1591/aabf99.

[85] I. Guseva Canu, T.F. Bateson, V. Bouvard, M. Debia, C. Dion, K. Savolainen, I.J. Yu, Human exposure to carbon-based fibrous nanomaterials: A review, Int. J. Hyg. Environ. Health. 219 (2016) 166–175. https://doi.org/10.1016/j.ijheh.2015.12.005.

[86] H. Saghafi, T. Brugo, G. Minak, A. Zucchelli, The effect of PVDF nanofibers on mode-I fracture toughness of composite materials, Compos. Part B Eng. 72 (2015) 213–216. https://doi.org/10.1016/j.compositesb.2014.12.015.

[87] T. Brugo, R. Palazzetti, The effect of thickness of Nylon 6,6 nanofibrous mat on Modes I–II fracture mechanics of UD and woven composite laminates, Compos. Struct. 154 (2016) 172–178. https://doi.org/10.1016/j.compstruct.2016.07.034.

[88] R. Mohammadi, M.A. Najafabadi, H. Saghafi, D. Zarouchas, Fracture and fatigue behavior of carbon/epoxy laminates modified by nanofibers, Compos. Part A Appl. Sci. Manuf. 137 (2020). https://doi.org/10.1016/j.compositesa.2020.106015.

[89] L. Daelemans, W. Van Paepegem, K. De Clerck, Effect of interleaved polymer nanofibers on the properties of glass and carbon fiber composites, INC, 2020. https://doi.org/10.1016/b978-0-12-819904-6.00011-6.

[90] T.M. Brugo, G. Minak, A. Zucchelli, H. Saghafi, M. Fotouhi, An Investigation on the Fatigue based Delamination of Woven Carbon-epoxy Composite Laminates Reinforced with Polyamide Nanofibers, in: Procedia Eng., 2015: pp. 65–72. https://doi.org/10.1016/j.proeng.2015.06.208.

[91] R. Palazzetti, A. Zucchelli, I. Trendafilova, The self-reinforcing effect of Nylon 6,6 nano-fibres on CFRP laminates subjected to low velocity impact, Compos. Struct. 106 (2013) 661–671. https://doi.org/10.1016/j.compstruct.2013.07.021.

[92] L. Daelemans, S. Van Der Heijden, I. De Baere, H. Rahier, W. Van Paepegem, K. De Clerck, Damage-Resistant Composites Using Electrospun Nanofibers: A Multiscale Analysis of the Toughening Mechanisms, ACS Appl. Mater. Interfaces. (2016). https://doi.org/10.1021/acsami.6b02247.

PART I
RESEARCH ON NANOFIBROUS-STRUCTURED MATERIALS

In this first part, a research on nano-structured materials paving the way for their practical engineering applications is presented. A detailed investigation of both the nanofibrous reinforcement phase and the hosting matrix of the nanocomposite is carried out. In Chapter 1, a methodology to evaluate the mechanical properties of nanofibrous membranes and a detailed investigation of the nanomat tensile behaviour are presented. In Chapter 2, instead, a numerical and experimental multiscale analysis of the effect of geometric cavities generated by the presence of the nanofibers themselves on the macroscale mechanical properties of the hosting matrix is presented.

<div align="right">Chapter 1</div>

How nanofibers carry the load: towards a systematic approach for tensile testing of nanofibrous membranes

Emanuele Maccaferri[1], Davide Cocchi[2,3], Laura Mazzocchetti[1,3], Tiziana Benelli[1,3], Tommaso Maria Brugo[2,3], Loris Giorgini[1,3], Andrea Zucchelli[2,3]

[1]Dipartimento di Chimica Industriale "Toso Montanari", Alma Mater Studiorum - Università di Bologna viale del Risorgimento 4, 40136 Bologna, Italy

[2]Dipartimento di Ingegneria Industriale, Alma Mater Studiorum - Università di Bologna viale del Risorgimento 2, 40136 Bologna, Italy

[3]Interdepartmental Center for Industrial Research in the field of Advanced Applications in Mechanical Engineering and Materials Technology (CIRI MAM) - Università di Bologna viale del Risorgimento, 2, 40136 Bologna, Italy

The candidate is one of the investigators of this study. He contributes to the conception and design of the study, data acquisition and analysis, manuscript drafting, revision and approval. The work has been recently submitted to Materials & Design journal.

1.1   Abstract

Nanofibrous nonwovens show high versatility and outstanding properties, with reduced weight. The porous morphology and the high material flexibility and deformability make complex their mechanical testing, severely affecting results reliability. Still today, a specific technical standard that establishes a method to carry out tensile testing of nonwoven nanofibrous mats is not available, nor studies concerning tensile test data reliability. In this work, the Authors present an accurate, systematic, and critical study concerning tensile testing of nonwovens, using electrospun Nylon 66 random nanofibrous mats as case study. Nanofibers diameter and specimen geometry were investigated to thoroughly describe the nanomat tensile behaviour, also considering the polymer thermal properties, and the nanofibers crossings number as a function of the nanofibers diameter.

Below a threshold value, which lies between 150÷250 nm, the overall mat mechanical behaviour changes from ductile to brittle, showing enhanced elastic modulus for a high number of nanofibers crossings. While specimen geometry does not affect tensile results. Stress-strain data were analysed using a phenomenological data fitting model to better interpret the tensile behaviour. The experimental results demonstrate the high reliability of the proposed mass-based load normalization, providing a simple, effective, and universally suitable method for obtaining high reproducible tensile stress-strain curves.

Keywords: nanofiber, tensile test, mechanical properties, grammage, thickness, electrospinning
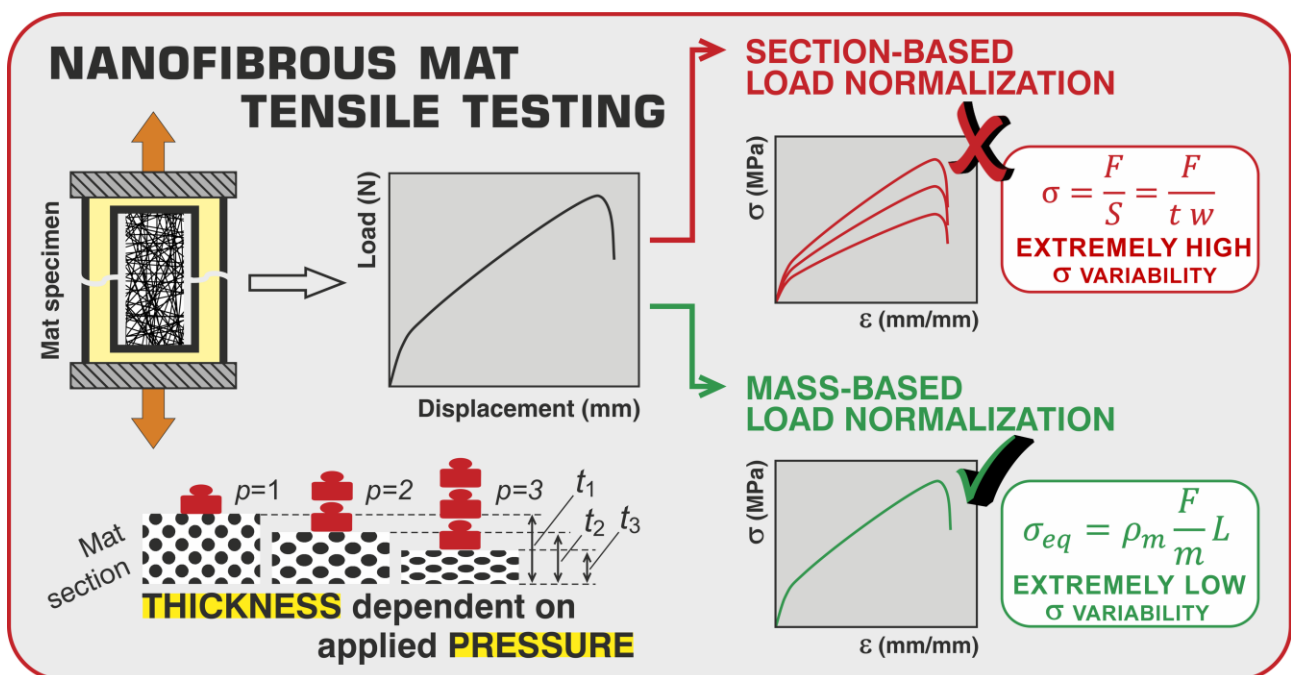
1.2 Introduction

Nonwoven fabrics are structures where fibers are not arranged in a specific pattern (e.g. warp and weft) while still maintaining the aspect and most of the properties of a woven textile. These materials have a lot in common with textiles, paper and some polymeric products. Nonetheless, they also display some peculiarities: in place of weaving of textiles, the fibers in the form of staple or continuous filaments are kept together by frictional forces through entanglements or adhesive forces between fibers, with or without the use of binders [1], as a consequence of chemical, mechanical, heat or solvent treatment. The fibers can be natural or man-made and characterized by any diameter [1], but usually are in the micrometer range. It is not a simple task to define "nonwovens", so that in the years various definitions were proposed (and amended) by different organizations for taking into

account the multifaceted aspects which characterize this class of materials [2]. BS EN ISO 9092:2019 defines nonwoven as "engineered fibrous assembly, primarily planar, which has been given a designed level of structural integrity by physical and/or chemical means, excluding weaving, knitting or papermaking". Structural integrity, as specified by the standard, means a "measurable level of added tensile strength", namely the nonwoven should possess some mechanical strength derived from the fiber assembly structure, highlighting the importance of (tensile) mechanical properties.

Nowadays, nonwovens find use in a wide variety of applications, often with high added value, like medical devices, filters, technical clothes, home and industrial furniture, thermal and acoustic insulation, and engineered materials [3]. Several properties are dependent on the diameter size, such as porosity and pore dimension [4], which in turn impact, for example, on filtering capacity [4]. Mechanical properties, in particular, are significantly enhanced moving from micrometer to nanometer scale [5]. In the last two decades, indeed, nonwoven fabrics made of nanofibers gained increasing attention, thanks to their high surface to volume ratio and outstanding properties. Besides the application as highly efficient filters [6], nanofibrous nonwoven mats are successfully used in tissue engineering [7,8], sensor [9–11], catalysis [12], adhesive bonded joints [13] and composite materials with enhanced mechanical performances [14,15] and/or peculiar properties [16].

In most applications the assessment of mat mechanical properties is fundamental for evaluating effective applicability, and tensile testing is commonly performed. However, the highly porous morphology, together with the overall material flexibility and deformability, strongly limit the results reliability and the obtained data cannot be used to design the material for specific applications. Nanofibrous mats are usually very thin and delicate, making them difficult to be handled. For this reason, usually, the mats are handled with their original support substrate until their final usage. Therefore, the specimen preparation for tensile testing requires particular attention for avoiding mat damage, pre-tensioning, or fibers slipping from the grips during testing. The use of a paper frame to be cut before testing is a valid solution [17], helping to handle and positioning the specimen, and to better measure the gauge length. However, even when all cautions are taken to run the test, evaluation of the cross-section area, required to normalize recorded load data to calculate the stress (σ), is still troublesome in particular in terms of thickness determination. Indeed, while thickness measurement of non-porous "bulk" materials is simple, it may be tricky for porous and soft ones. Being nanofibrous mats characterized by high porosity, with values close to 90 % [18], the measured thickness is surely affected by the measurement itself. Since nonwovens are very thin and the cross-section area is directly proportional to the thickness, the normalized load values (i.e. stress, σ) may be particularly affected by this drawback.

Within this frame, testing of materials is ruled by technical standards published by national and international standards organizations, such as ASTM International, ISO, BSI, UNI, with the aim of obtaining comparable results. However, there are only a few standards for the testing of nonwovens, such as ISO 9073 and BS EN 29073, with a lack of specific indications for nanofibrous nonwovens, making them practically not applicable to nanometric fibrous systems. As an example, BS EN 29073-3:1992 (ISO 9073-3:1989), related to the "determination of tensile strength and elongation" of nonwovens, prescribes to prepare a rectangular specimen 50 mm width and, possibly, 200 mm length (gauge length), for "avoiding risks due to local heterogeneity of nonwovens or to undue cutting of long-fibre nonwovens". As a matter of fact, due to the previously discussed difficult handling of nanofibrous mats, the preparation of specimens with these characteristics is practically precluded in most cases. Furthermore, the reason why such a specimen size is prescribed clearly suggests that the considered fibers are not nanometric. It is worth noting that in the cited standard the breaking strength is to be expressed in newtons (N), so actually, it represents the breaking load rather than a "real" strength (σ at break). Again, this is to underline that neither here nor in other standards regarding nonwovens (excluding geotextiles nonwovens [19] and paper [20,21], which are not considered nonwovens by definition [1]) a method is reported to evaluate the elastic modulus (in MPa) and the strength (load per unit area of cross-section, in MPa) of this type of engineered materials. These tensile properties require σ calculation and, in turn, the evaluation of the mat thickness. The lack of an indication on how to determine tensile properties stems probably from the difficulty in measuring thickness, and in defining uniquely *the* thickness. Even if there is a standard for the determination of "conventional" nonwovens thickness [22], it appears not applicable to nanofibrous nonwovens, since this standard refers to "thicker" nonwovens respect to nanofibrous ones (mm vs µm scale). Besides, the discussed test apparatus is quite complex and not available to common laboratories for routinely procedures. However, the thickness dependency from the applied pressure during measurement surely affects the measured thickness also in "conventional" nonwovens, since BS EN ISO 9073-2 specifies the measuring pressure to be adopted. Also the standard for paper thickness determination [23] seems to be not helpful, since the paper is made by cellulose fibers consolidated via pressure during calendering. Consequently, the thickness measurement is less dependent on the measuring pressure, and therefore, the related problem is not as important as in nanofibrous nonwovens. The well-known standard for tensile testing of bulk plastics (ASTM D638) is not useful too.

The mat thickness dependency on the way it is assessed makes it a real comparison of mechanical performances of nanofibrous nonwovens a difficult task, especially when comparing mats tested by different laboratories. The knowledge of the thickness measurement conditions (mainly the applied

pressure) should help, but usually, this information is missing [24–36]. The underestimation of this aspect, affecting almost all the studies about tensile testing of nanofibers, prevents in fact any reliable comparison.

Presently, a technical standard that establishes a method and the technical criteria to carry out tensile testing of nonwoven nanofibrous mats is not available. To the best of the Authors' knowledge, not even studies concerning data reliability of tensile testing of nanofibrous nonwovens exist. However, given the tremendous boost in the use of nanofibrous nonwovens, searching for a reliable and simple way to tensile test this type of materials is of primary importance.

In this work, the Authors present an accurate, systematic and critical study concerning tensile testing of nonwoven mats, using electrospun Nylon 66 nanofibrous mats as a case study. The "classical" approach to normalization of load by means of specimen cross-section area is compared to a mass-based normalization proposed by the Authors, as well as a normalization based on the mat grammage (areal density). A viable way to convert tensile data of previously tested mats is presented too. Nanofibrous mat characteristics, such as fibers diameter, grammage, and specimen geometry (width and gauge length) are deeply investigated to thoroughly describe the tensile behaviour of nonwovens. Mats mechanical performances were discussed considering polymer properties (degree of crystallinity and glass transition temperature), and the number of potential nanofibers crossings as a function of the nanofiber diameter. Experimental stress-strain data are then analysed using a phenomenological data fitting model to better understand the tensile behaviour.

1.3 Materials and methods

1.3.1 Materials

Nylon 66 (Zytel E53 NC010 kindly provided by DuPont) was dried in a stove at 110 °C for minimum 6 hours before use. Trifluoroacetic acid (TFA), formic acid, and chloroform, all reagent grade, were purchased from Sigma-Aldrich and used without further purifications.

1.3.2 Nylon 66 solutions and nanofibrous mats production

Nylon 66 solutions having a concentration of 9, 13 and 18 %wt were prepared in a TFA/formic acid/chloroform 10:60:30 %vol. (11:55:34 wt%) solvent system. Solutions were made dissolving Nylon 66 pellets under magnetic stirring and mild heating (maximum 50 °C) until complete polymer dissolution.

Nanofibrous mats were produced via electrospinning process, with a Spinbow® electrospinning machine unit equipped with four 5 mL syringes (needles 55 mm length and 0.84 mm internal diameter). Fibers were collected on a rotating drum of 150 mm diameter (tangential speed: 0.39 m/s) covered with poly(ethylene)-coated paper. Mats have final dimensions of approximately 350 × 450 mm and they were labelled Ny*XXX* according to the rough average diameter of the obtained fibers. In Table 1.1 electrospinning process and environmental parameters for mats production are reported.

Table 1.1 – Electrospinning process parameters and nanofibers diameters of produced nanofibrous mats.

Nanofibrous mat	Nylon concentration	Flow rate	Electric potential	Distance	Electric field[a]	Temperature	Relative humidity	Nanofibers diameter[b]
	%wt	mL/h	kV	cm	kV/cm	°C	%	nm
Ny150	9	0.30	21.0	7.0	3.0	20-22	25-28	154 ± 38
Ny250	13	0.80	25.0	6.0	4.2	24-26	28-31	256 ± 42
Ny400	18	0.80	25.0	7.0	3.6	20-22	26-28	405 ± 84

[a] calculated as electric potential to distance ratio

[b] average values derived from at least 100 diameter measurements on SEM micrographs, manually done on single nanofibers by means of the Photoshop measurement tool

For tensile testing, two nanofibrous mats for each membrane type (Ny150, Ny250 and Ny400) were electrospun for a deposition time one twice the other (dt and 2dt), for a total of 6 nanomats. Nanofibrous mats for the grammage-thickness relationship assessment were electrospun, picking a membrane strip from the drum (approximately 350 × 60 mm) every 45 minutes up to 270', obtaining 6 strips with incremental deposition time (detailed procedure on Supplementary Information SI1).

1.3.3 Characterization of nanofibrous mats and grammage/thickness evaluation

Nanofibrous mats were analysed by Scanning Electron Microscopy (SEM, Phenom ProX) to determine nanofibers morphology, after gold sputtering. SEM images of the three nanofibrous mat types under analysis are shown in Figure 1.1. Nanofibers diameter, determined measuring at least 50 fibers by an image analysis software, is given as the average diameter ± standard deviation in Table 1.1.
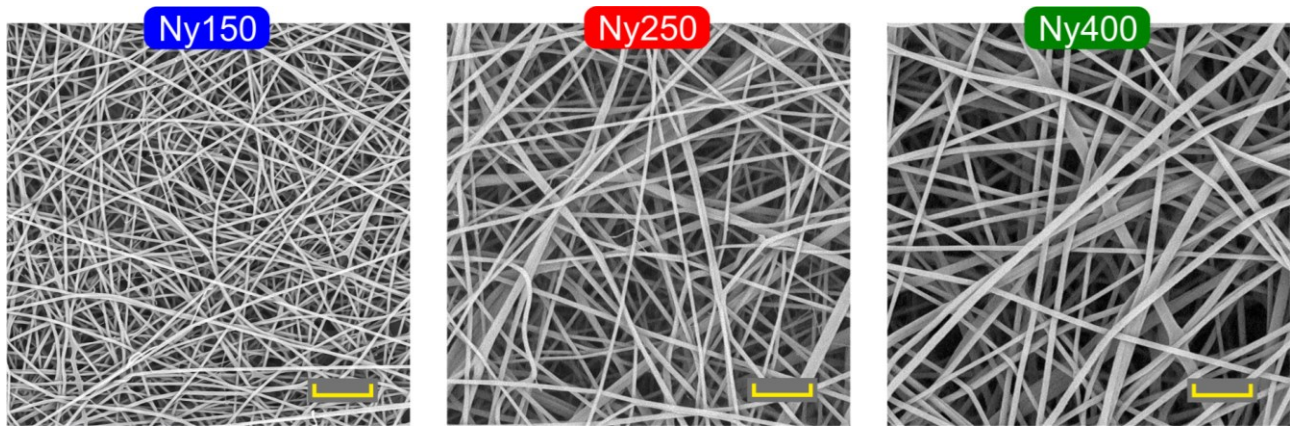
Figure 1.1 – SEM images of the three nanomat types. Scale bar: 4 μm.

Differential Scanning Calorimetry (DSC) analyses were carried out on a TA Instruments Q2000 DSC Modulated apparatus equipped with RCS cooling system. A sample of 7 mg was heated from 20 °C to 120 °C, cooled to –60 °C, then heated again to 320 °C in nitrogen atmosphere (heating/cooling rate 20 °C/min).

Tensile tests were carried out using a Remet TC10 universal testing machine equipped with a 10 N load cell, with a crosshead separation speed of 10 mm/min. Tensile specimens were prepared anchoring the membrane to a paper frame for better handling and avoiding any nanofibers slippage in the machine fixtures, cutting the frame before the test started, as reported before [17,37]. Specimens dimensions are reported in Table 1.2. For each membrane type (Ny150, Ny250 and Ny400) two mats were electrospun, one with a deposition time twice as long as the other (called dt and 2dt). Each tensile specimen is identified by the name of the membrane type (Ny*XXX*) followed by the specimen configuration. Elastic modulus was determined via linear regression of stress-strain data in the strain range 0÷1 % for all tested specimens (the selection of this specific range was based on the minimization of the linear fitting error).

Table 1.2 – Details of tensile tests specimens.

Tensile specimen configuration	Specimen width (w)	Specimen gage length (L)
	mm	mm
Ny*XXX*_10/30_dt	10	30
Ny*XXX*_10/30_2dt	10	30
Ny*XXX*_10/45_dt	10	45
Ny*XXX*_10/45_2dt	10	45
Ny*XXX*_20/30_dt	20	30
Ny*XXX*_20/30_2dt	20	30
Ny*XXX*_20/45_dt	20	45
Ny*XXX*_20/45_2dt	20	45

Ny*XXX*: membrane type (Ny150, Ny250, Ny400)

Membranes thickness was evaluated using 6 different instruments: (i) a scanning electron microscope, (ii) an analog centesimal indicator, (iii) a digital millesimal indicator, (iv) an analog millesimal indicator with two different pressure configurations, (v) a micrometer and (vi) a digital caliper. SEM measurements were carried out on liquid nitrogen fractured mat sections. Details of the resolution and applied pressure by each measurement tool are reported in Table 1.3.

Regarding grammage-thickness relationship, from each membrane strip 5 patches were extracted (nominally 60 × 25 mm) from different positions along the strip (Figure 1.15, in Supplementary Information SI1). The mat thickness was measured using the analog indicator 2 in the low-pressure configuration (iv, Table 1.3), as it allows to compare the measured values with an acceptable resolution. The mat mass was determined using a AS 60/220.R2 Radwag scale with a resolution of 0.01 mg. Detailed description and representation of the adopted procedure are reported in Supplementary Information SI1. The patch area was evaluated via MATLAB software by image processing of scanned images (see Supplementary Information SI2).

Table 1.3 – Technical specifications of measurement tools used for evaluating membranes thickness.

	i	ii	iii	iv	v	vi
Instrument	SEM	Analog indicator 1	Digital indicator	Analog indicator 2	Analog micrometer	Digital caliper
Type of measurment	Electron Microscopy	Mechanical	Mechanical	Mechanical	Mechanical	Mechanical
Producer	Phenom ProX PhenomWorld Netherlands	Borletti Italy	Alpa MegaRod Italy	Borletti Italy	Holex Germany	Alpa Italy
Resolution	≤ 8 nm	10 µm	1 µm	1 µm	10 µm	10 µm
Pressure	n.d.	83 g/cm^2	94 g/cm^2	Low config. 360 g/cm^2 High config. 1062 g/cm^2	Depending on operator	Depending on operator
Color identification				Low configuration / High configuration		

1.4   Results

1.4.1 Membrane thickness evaluation and "classical approach" to tensile test

The accurate evaluation of the thickness is a key factor to characterize several materials properties. This measurement is quite simple when dealing with bulk materials, but it may be very tricky in case of porous and soft materials, since the measurement procedure itself affects the measured thickness value. Nonwovens, to which electrospun nanofibers clearly belong, are surely affected by this drawback. To demonstrate it, two Ny250 membranes, named Ny250_dt and Ny250_2dt, were electrospun for a deposition time one twice the other (dt and *2*dt), to assess the thickness of each membrane, evaluated in a limited area, where the nanofiber deposition is expected to be homogeneous. The histograms in Figure 1.2A show the thickness measured on the two different Ny250 membranes using the measurement tools reported in Table 1.3.

The measured thickness is strongly affected by the tool used for its evaluation, resulting in very different values, with a maximum observed discrepancy of about 300 % within the same area. It can be surely affirmed that overall Ny250_dt mat is thinner than Ny250_2dt (provided that the comparison is done using the same instrument), but it is not possible to define *the* mat thickness uniquely, as the measurement tool influences the recorded value as a function of the applied pressure.

The use of different thickness values may, in turn, affect enormously tensile test results. The recorded load-displacement data, which do not consider dimensions and geometry of the specimen, require normalization to obtain comparable stress-strain curves. The classical approach used for stress evaluation (σ, in MPa) requires the specimen thickness (t, in mm) for evaluating the cross-section area (S, in mm^2) normal to the applied load direction, as shown by the following equation:

$$\sigma = \frac{F}{S} = \frac{F}{wt}$$

Eq. 1.1

where F is the force (in N) and w the specimen width (in mm). Clearly, any variation in t significantly affects σ, being the section S directly proportional to it.

Tensile tests were performed on two specimens with a dimension of 20 × 45 mm sampled from the analysed region of Ny250_dt and Ny250_2dt. For each specimen, stress values were calculated according to Equation 1.1 using the thicknesses reported in Figure 1.2A, obtaining the multiple stress-strain curves represented in Figure 1.2B. The curves display significantly different profiles, while they should be in principle overlapped or, at least, highly resembling one each other. As a consequence, both elastic modulus (E) and maximum stress (σ_{max}) assume completely different

values, ranging from 35÷100 MPa and 4÷14 MPa, respectively (Figure 1.2C-D). It is, therefore, demonstrated that the thickness measurement methodology deeply affects the results. Moreover, it is worth mentioning that even using the same tool, different stress-strain curves are obtained for the two considered specimens, though in theory the result should be the same. Indeed, the lower the thickness of the nanofibrous mat to be measured, the greater the relative error, since the dimension of the mat is evaluated as the difference between the overall thickness of the mat and the supporting paper minus the one of the paper alone.
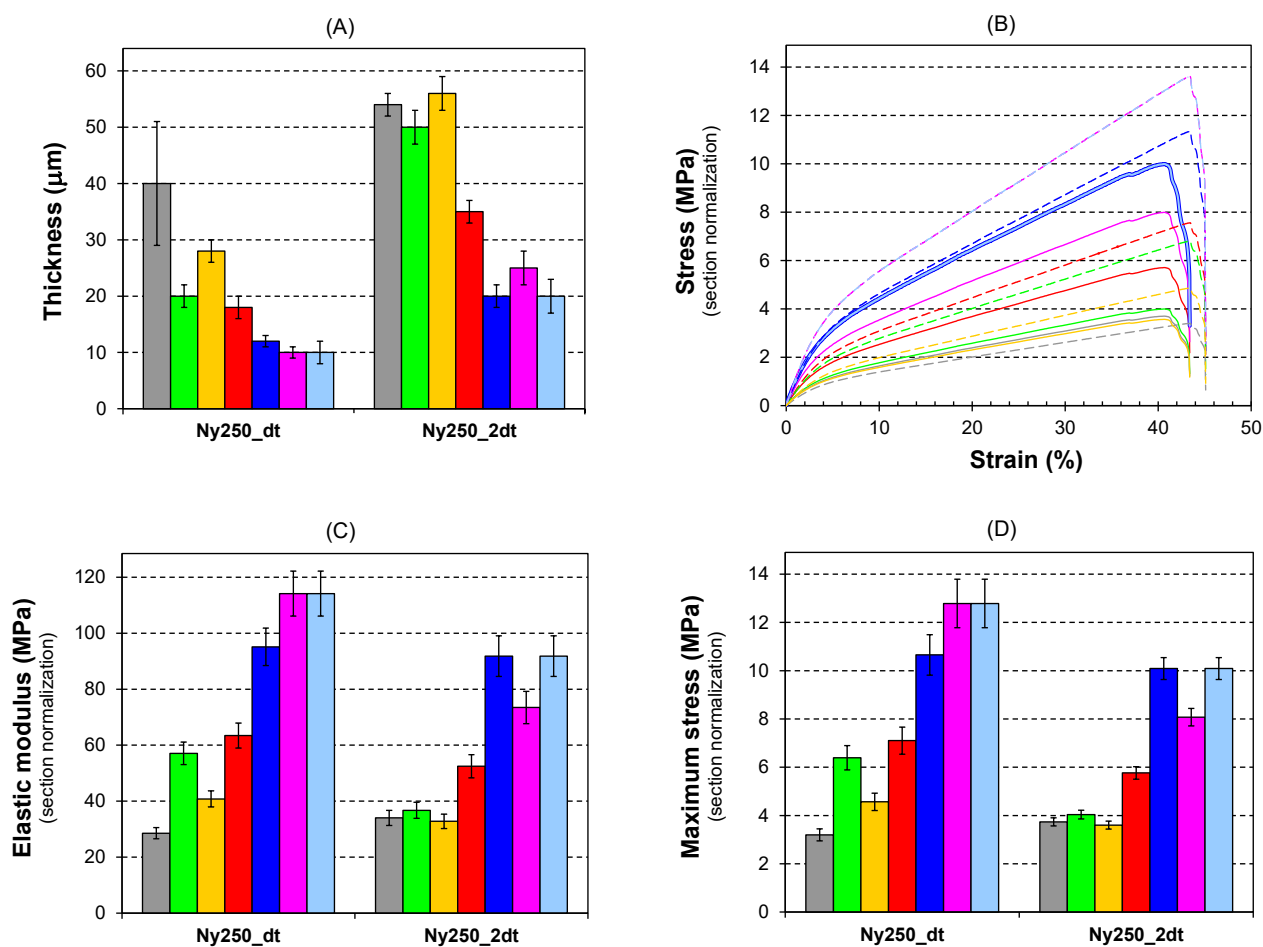
Figure 1.2 – (A) Thickness measurements on the two distinct Ny250 nanofibrous mats, using different measurement tools. (B) Comparison of stress-strain curves of the tensile tests performed on Ny250_dt (dashed lines) and Ny250_2dt (solid lines) obtained from the application of the "classical approach" as per Equation 1.1, using the different thicknesses reported in (A). (C) Elastic modulus and (D) maximum stress derived from the analysis of stress-strain curves in (B). The colours are coherent with the ones adopted for the identification of the measurement instruments (see Table 1.3).

Such scattered results are obviously unacceptable, pointing at the impossibility of making any reliable comparison of nanofibrous mats tensile properties made by different research groups. Curves can be reliably compared only within the same type of nanofibrous mats measured with the same

instrument and in the same conditions. Nonetheless, even under these assumptions stress-strain curves may not be comparable when dealing with "extremely low" thickness, as the measurement error compares to the actual measurement value. E and σ_{max} should, instead, be unaffected by the particular specimen geometry, being these values characteristics of the material. Finally, beside all the above considerations on the correct thickness evaluation, an additional issue arises when trying to follow Equation 1.1, since the nanofibrous mat is wrongly considered as a bulk material: the voids among nanofibers are assumed to be filled by the polymeric material, leading to a significant underestimation of σ and of all related properties.

1.4.2 Tensile test data normalized with respect to nanofibrous mat grammage

A general, simple, and reliable method to normalize the load-displacement data for obtaining more comparable stress-strain curves is highly needed. The use of nanofibrous mat grammage (G, in g/m^2, defined as per Equation 1.4), which involves the mat mass measurement and its surface area (A, in m^2), may be a viable solution. Hereafter mathematical steps are reported to express the stress (σ, in MPa) as a function of grammage (Equation 1.7).

$$\sigma = \frac{F}{S} \qquad\qquad \text{Eq. 1.2}$$

$$\sigma_{eq} = \frac{F}{S_{eq}} \qquad\qquad \text{Eq. 1.3}$$

$$G = \frac{m}{A} = \frac{m}{L\,w} \qquad\qquad \text{Eq. 1.4}$$

$$\rho_m = \frac{m}{V_{eq}} = \frac{m}{L\,w\,t_{eq}} \qquad\qquad \text{Eq. 1.5}$$

$$t_{eq} = \frac{m}{\rho_m L\,w} = \frac{G}{\rho_m} \qquad\qquad \text{Eq. 1.6}$$

$$\sigma_{eq} = \frac{F}{S_{eq}} = \frac{F}{w\,t_{eq}} = \rho_m \frac{F}{G\,w} \qquad\qquad \text{Eq. 1.7}$$

where σ_{eq} (in MPa) is the stress "equivalent" to a specimen with the same dimensions (length, L and width, w, both in m) and mass (m, in g), but condensed in a bulk film characterized by equivalent thickness t_{eq} (in μm), volume V_{eq} (in m^3), and cross-section area S_{eq} (in m^2); ρ_m is the density (in

mg/mm^3) of the material used to manufacture the nanofibers (1.14 mg/mm^3 for Nylon 66). Applying Equation 1.7 to the previously discussed Ny250_dt and Ny250_2dt mats, the resulting stress-strain curves are now closer each other (Figure 1.3).

Figure 1.3 – (A) Stress-strain curves of the two specimens sampled from Ny250_dt (in red) and Ny250_2dt (in black) mats, obtained following load data normalization based on membrane grammage (Equation 1.7); (B) Enlargement of the stress-strain curve in the low deformation range (0÷3 %).

This stress normalization method, however, suffers from some drawbacks too. Indeed, the application of Equation 1.7 presumes that the mat grammage is constant across the entire membrane area from which the tensile specimens are sampled out. This assumption, though, may not be true because of the nanofibers additive deposition typical of the electrospinning process, which could lead to local inhomogeneities in fibers distribution. Besides, the grammage evaluation needs a certain amount of material and several measure repetitions to obtain reliable values.

1.4.3 Tensile test data normalized with respect to specimen mass

Using the specimen mass for the load-displacement data normalization, instead of the overall mat grammage, allows for a better match of the recorded load values with the tested specimen, resulting in reliable and absolutely comparable stress-strain curves, as shown in Figure 1.4. Hereafter equations are reported to explain the relationship between stress and specimen mass (Equation 1.10):

$$\sigma_{eq} = \rho_m \frac{F}{G\,w} \qquad\qquad \text{Eq. 1.8}$$

$$G = \frac{m}{A} = \frac{m}{L\,w} \qquad\qquad \text{Eq. 1.9}$$

$$\sigma_{eq} = \rho_m \frac{F}{G\,w} = \rho_m \frac{F}{w} \frac{L\,w}{m} = \rho_m \frac{F}{m} L \qquad\qquad \text{Eq. 1.10}$$

In this case, the behaviour of the two tested specimens looks utterly comparable: the stress-strain curves are almost superimposed, with a little deviation only at high strain values, in the final nonlinear segment of the curve, where nanomat failure occurs. The differences in the maximum stress are due to the specimens failure mode, usually unpredictable due to peculiar imperfections.
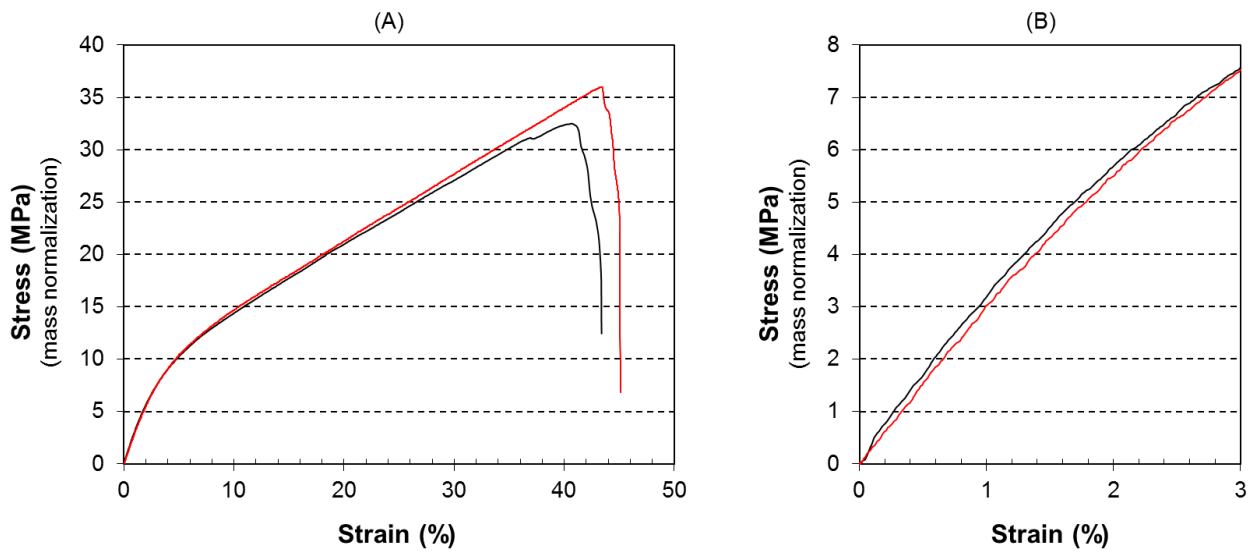
Figure 1.4 – (A) Stress-strain curves of the two specimens sampled from Ny250_dt (in red) and Ny250_2dt (in black) mats, obtained according to load normalization based on specimen mass (Equation 1.10). (B) Enlargement of the stress-strain curve in the low deformation range (0÷3 %).

By applying this normalization method, it is therefore possible to obtain perfectly reliable and repeatable results, similarly to what happens for bulk materials. A direct comparison between the load normalization based on mat grammage and on specimen mass (according to Equation 1.7 and Equation 1.10, respectively) is reported in Figure 1.5. The graph shows that the use of nanomat grammage for load normalization is less reliable and less convenient than the specimen mass normalization, though it allows to re-normalize tested specimens whose mass is unknown. Whether the specimen mat grammage nor the nanomat from which the specimens were obtained are unavailable, it is possible to assess the grammage via the linear grammage-thickness relationship, as later demonstrated. Although the grammage normalization of the load is less reliable respect to the mass one, it nevertheless appears better than the "classic" normalization approach based on the specimen cross-section area.
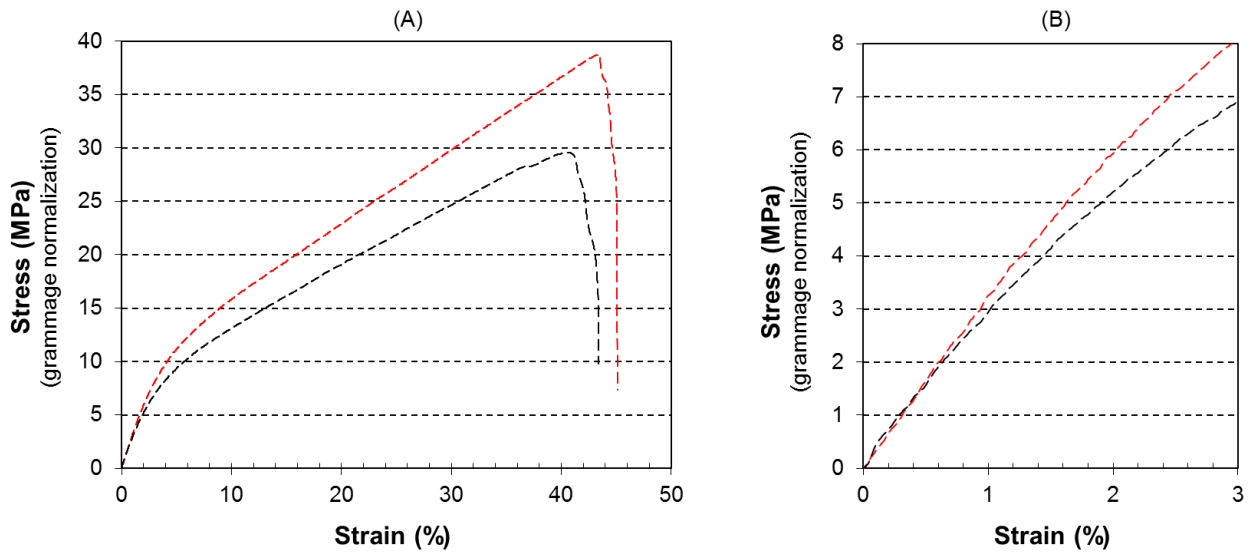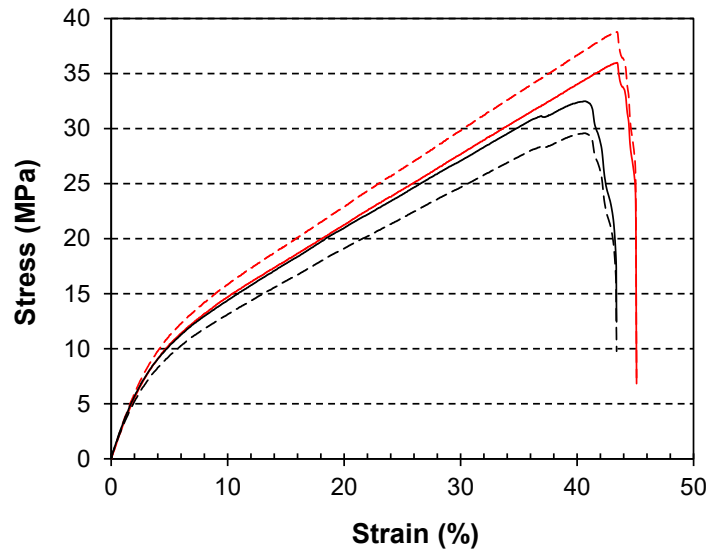
Figure 1.5 – Comparison of stress-strain curves of the two specimens sampled from Ny250_dt (in red) and Ny250_2dt (in black) mats, obtained according to load normalization based both on mat grammage (Equation 1.7, dashed lines) and on specimen mass (Equation 1.10, solid lines).

Figure 1.6 shows the comparison between the different approaches to load-displacement curve normalization, reporting for each one its pros and cons.

Methods for load normalization of tensile test data

based on **MAT SECTION**	based on **MAT GRAMMAGE**	based on **SPECIMEN MASS**
Mat thickness measurement (w to be known)	**Mat area and mat mass measurements** (ρ_m and w to be known)	**Specimen mass measurement** (ρ_m and L_0 to be known)
thickness measurement is **NOT RELIABLE** **NOT SPECIFIC** for each specimen	which are **SIMPLE and RELIABLE** measurements **Measurements NOT SPECIFIC** for each specimen	which are **SIMPLE and RELIABLE** measurements **Measurement SPECIFIC** for each specimen
EXTREME σ **VARIABILITY** $\sigma = \dfrac{F}{S} = \dfrac{F}{t\,w}$	**LOW** σ **VARIABILITY** $\sigma_{eq} = \rho_m \dfrac{F}{G\,w}$	**EXTREMELY LOW** σ **VARIABILITY** $\sigma_{eq} = \rho_m \dfrac{F}{m}\,L_0$

Figure 1.6 – Comparison between the different approaches to load normalization.

1.4.4 Nanomats tensile tests analysis

In this Section the mass normalization approach has been applied to the analysis of tensile tests carried out on the different tensile specimen configurations (Table 1.2). Figure 1.7 shows the representative stress-strain curves of the three different membrane types (Ny150, Ny250 and Ny400), while the curves for all the specimen configurations are shown in Supplementary Information SI3. At

first glance, the mechanical behaviour of Ny150 mat is completely different from the other two, which are, instead, very similar. The analysis of these curves will be discussed in detail in the next Sections.
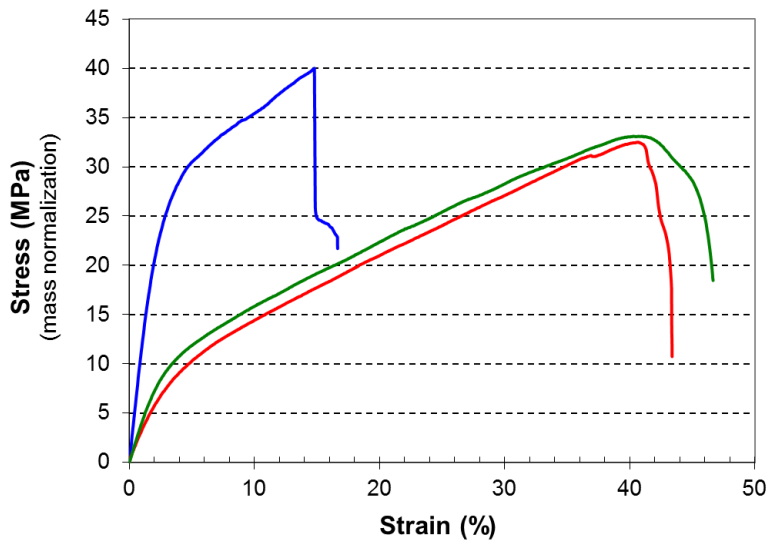
Figure 1.7 – Representative stress-strain curves of the three different membrane types (Ny150 blue, Ny250 red, and Ny400 green). The displayed specimens were selected from the 20/45_2dt configuration.

1.4.4.1 Effect of specimen geometry

Load-displacement curves are characteristic of each specimen, as they are size-dependent. To remove the dependence on geometry, it is necessary to consider the stress-strain curves, which allow characterizing the intrinsic mechanical properties of the material. To evaluate a possible dimensional effect on the mechanical characteristics, for each membrane type several specimens with different dimensions (width, length and grammage, Table 1.2) were tested. Figure 1.8 shows the elastic modulus and the maximum stress for the specimens obtained from the membrane Ny250_dt and Ny250_2dt, normalized both on mass (A and C, respectively) and on section (B and D, respectively).

Data from Figure 1.8 show that the size of the specimens does not significantly affect both the elastic modulus and the maximum stress. The dramatic differences in numerical values between the two normalization methods are due to the inaccuracies of the section normalization method. Indeed, the thickness measurement, besides not being reliable, also considers the voids inside the nanomat as actively contributing to its response to the tensile stimulus, accounting for a fictious far larger cross-section area than the actual one bearing the load. On the contrary, the mass-based load normalization discards the voids contribution, considering the mat specimen a bulk material characterized by the same length, width and mass, with the exception of the thickness (t_{eq}), and still maintaining the nanofibrous morphology. Similar results were also observed for the Ny150 and Ny400 mat types (histograms are reported in the Supplementary Information SI4). The results derived from grammage-

based load normalization are not presented here because the aim is to compare the effectiveness of the proposed mass-based normalization method with the commonly adopted approach based on section normalization.
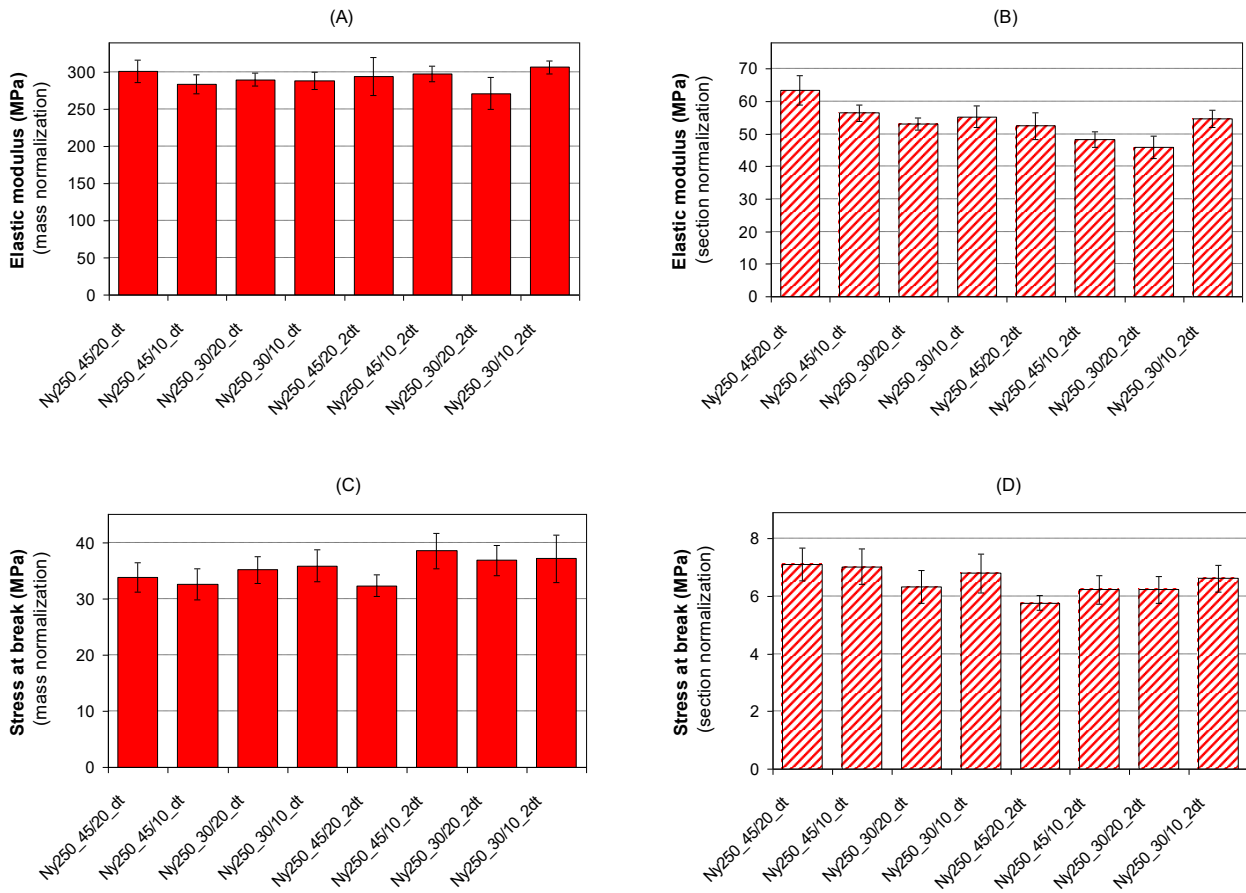
Figure 1.8 – Elastic modulus and maximum stress for the specimens obtained from the membrane Ny250_dt and Ny250_2dt, normalized both on mass (A and C respectively, solid filling) and on cross-section area (B and D respectively, dashed filling).

1.4.4.2 Effect of nanofiber diameter

To evaluate the effect of the nanofiber diameter on the mechanical properties of the nanomat, three different types of membranes were electrospun, each characterized by different nanofibers diameter: 150 nm, 250 nm and 400 nm (Ny150, Ny250 and Ny400, respectively).

The histograms show for each specimen configuration the elastic modulus (Figure 1.9A), maximum stress (Figure 1.9B) and strain at maximum stress (Figure 1.9C). Elastic modulus and maximum stress derive from the mass-based load normalization.
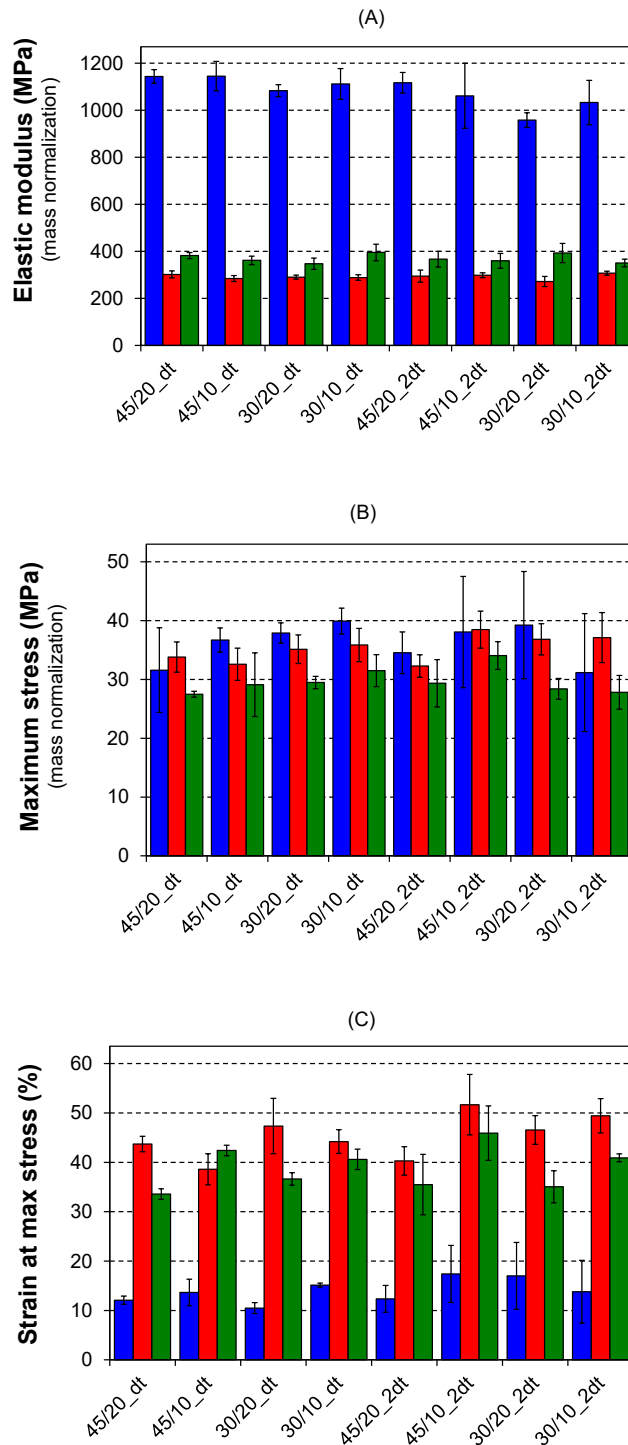
Figure 1.9 – (A) Elastic modulus, (B) maximum stress and (C) strain at maximum stress for each specimen configuration reported in Table 1.2. In blue Ny150 specimens, in red Ny250 specimens and in green Ny400 specimens.

The tensile properties of each mat type, averaged regardless of the specimen geometry, are collected in Table 1.4. The Ny150 membrane type, characterized by a significantly higher elastic modulus than the other two mat types (about three times), is more rigid and consequently displays a more brittle behaviour, with a strain at maximum stress ($\varepsilon_{\sigma max}$) about 1/3 and a halved toughness (*U*)

respect to Ny250 and Ny400. E, σ_{max}, and $\varepsilon_{\sigma max}$ values of the Ny250 and Ny400 membranes are almost comparable, as well as the toughness. It is worth to mention that Ny250 and Ny400 mats show a ductile behaviour, while Ny150 exhibits a more brittle one, as can be also observed from stress-strain curves of Figure 1.7.

Table 1.4 – Average tensile properties for each membrane type.

Membrane type	E (MPa)		σ_{max} (MPa)		$\varepsilon_{\sigma max}$ (%)		U (J/cm^3)	
	Mean ± SD	CV (%)	Mean ± SD	CV (%)	Mean ± SD	CV (%)	Mean ± SD	CV (%)
Ny150	1071 ± 90	8	36 ± 7	19	13 ± 5	38	4.0 ± 1.5	38
Ny250	296 ± 28	9	35 ± 3	9	46 ± 6	13	9.4 ± 1.3	14
Ny400	355 ± 37	10	30 ± 4	13	39 ± 6	15	7.8 ± 1.8	23

Two main reasons may be given for explaining the different mechanical behaviour among the mat types: (i) a difference in the polymeric material, such as a variation of the Nylon 66 degree of crystallinity, and (ii) an effect related to the nanofibrous mat morphology, like the number of nanofibers intersections.

The Nylon ability to crystallize may be affected by the processing conditions, which could lead to different average size of the crystallites and/or affect the degree of crystallinity [17]. Electrospun Nylon 66 nanofibers may change their degree of crystallinity, as well as the "quality" of the crystallites, depending on the electrospinning solution solvent system [5,38], the presence of nano-reinforcements like graphene which may act as nucleant [17], and the nanofiber size [5]. According to Baji *et al.* [5], the fiber diameter strongly affects mechanical properties, resulting significantly enhanced below a threshold diameter, which in their case was near ≈500 nm for Nylon 66 nanofibers electrospun from a formic acid / dichloromethane solvent system. The nanofibers under study in the present work, especially Ny150 and Ny250, are clearly below this value. Tensile tests, however, show a significant increment of elastic modulus and strength only for nanofibers with the smallest diameter (150 nm), while thicker fibers mats behave alike. In this context, it is worth mentioning that in the cited work [5] Nylon 66 nanofibers were aligned, while in the present case the tested nanofibers are randomly oriented, so the two cases cannot be straightforwardly compared. The nanofibrous mats were thus investigated via DSC analysis to evaluate the effect of the nanofiber morphology on the Nylon 66 thermal properties, which may contribute to the observed different mechanical behaviour of the nanomats (Figure 1.10).
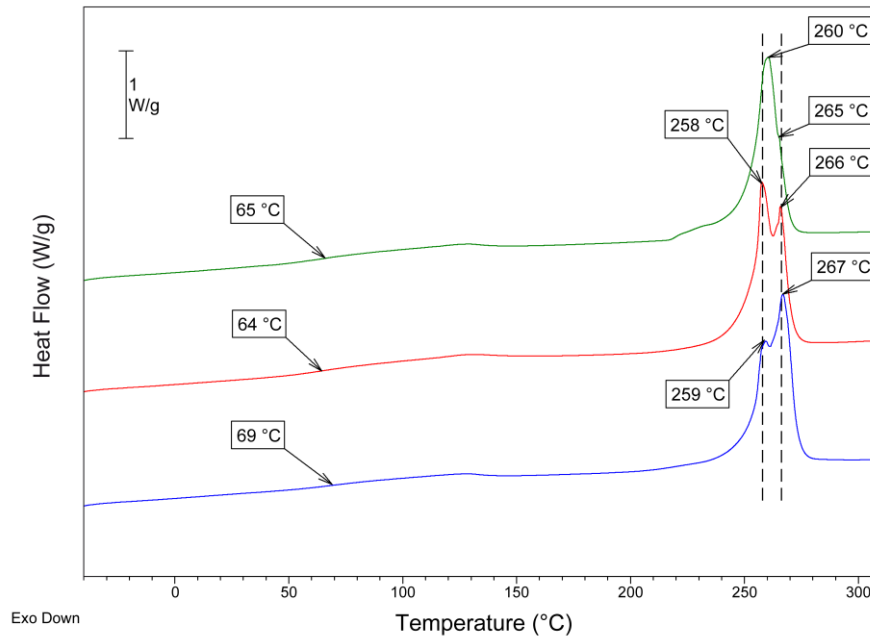
Figure 1.10 – DSC analysis of the three membrane types (Ny150 blue, Ny250 red, Ny400 green).

As expected for a semicrystalline polymer, the thermograms show a stepwise variation of the thermal capacity ascribable to the polymer glass transition and an endothermic signal accounting for the melting of the polymer crystalline fraction. All the mats have a similar degree of crystallinity ($\chi_c \approx 45$ %), even if some differences on peaks shape and positioning were observed. Also the glass transition temperatures (T_gs) show slight differences, which are, however, not enough to justify the utterly different mechanical behaviour. Indeed, the observed T_gs are almost comparable, with only a slightly higher value for the Ny150 (69 °C vs. 64 °C and 65 °C of Ny250 and Ny400, respectively), accounting for a possible slightly higher orientation of the Nylon 66 amorphous phase of Ny150 mat. Detailed explanation of DSC analysis regarding degree of crystallinity evaluation and melting peaks interpretation is reported in Supplementary Information SI5.

Since the mats thermal behaviour are well comparable, it was investigated whether there is an influence of the nanofibrous morphology on the mechanical properties, particularly the number of intersections between nanofibers (crossings). These can be, for example, localized weldings between nanofibers, electrostatic connections, slipping-resistance points. The knowledge of number and type of intersections, in fact, would be extremely important to interpret the mechanical behaviour of a random nanomat at the macro-scale. While it is very difficult to establish the type of intersections, their numeric estimation is certainly more viable. Different software for image analysis can be adopted for their quantification. However, from SEM micrograph it is impossible to correctly assess the number of intersections through the entire thickness. To this end, an alternative and easy-to-apply

method has been adopted. Several approaches have been proposed to estimate the number of crossings per unit area of stochastic fibrous networks [39–41]. Assuming the nanofibers as infinite length lines, it is possible to model the random mat as a network of lines crossing in points distributed according to a point Poisson process in the plane [40]. As reported in [41], the expected number of crossings per unit area (n_c^{fibers}) depends only on the total fibers length per unit area (τ, in m^{-1}):

$$n_c^{fibers} = \frac{\tau^2}{\pi}$$

Eq. 1.11

Assuming a nanofibrous sample consisting of a single continuous cylindrical filament, with an average diameter d, it is possible to estimate its equivalent length (l_{eq}) starting from its volume ($V_{filament}$) by the following steps:

$$V_{filament} = \frac{\pi d^2}{4} l_{eq}$$

Eq. 1.12

$$\frac{m}{\rho_m} = \frac{\pi d^2}{4} l_{eq}$$

Eq. 1.13

$$l_{eq} = \frac{4m}{\rho_m \pi} \frac{1}{d^2}$$

Eq. 1.14

where τ is defined as the l_{eq} per unit area (m/m^2). It should be noted that Equation 1.11 is true only in the case of two-dimensional networks, as it is assumed that each crossing generates contact between nanofibers. The nanofibers of real networks, instead, may or may not contact each other, depending on the influence of nearby nanofibers. However, considering only 1 g of nanofibers randomly distributed on a 1 m^2, it is reasonably possible to assume that Equation 1.11 holds true. By replacing Equation 1.14 in Equation 1.11, it is possible to estimate n_c^{fibers}, knowing only the mass of the mat (m), the density of the electrospun material (ρ_m), and the average diameter of the nanofibers (d), obtaining:

$$n_c^{fibers} = \frac{16m^2}{\rho_m^2 \pi^3} \frac{1}{d^4}$$

Eq. 1.15

Figure 1.11 shows, for each nanomat type, the equivalent filament length (l_{eq}) and the number of crossings per unit area (n_c^{fibers}) considering a unitary grammage.

Nanofibrous mat	d	l_{eq}		n_c^{fibers} [a]	
	nm	m	% var.	m⁻²	% var.
Ny150	154	4.7E+07	–	7.1E+14	–
Ny250	256	1.7E+07	-64%	9.3E+13	-87%
Ny400	405	6.8E+06	-86%	1.5E+13	-98%

[a] evaluated on an area of 1 m² for a 1 g of nanofibers (unitary grammage)
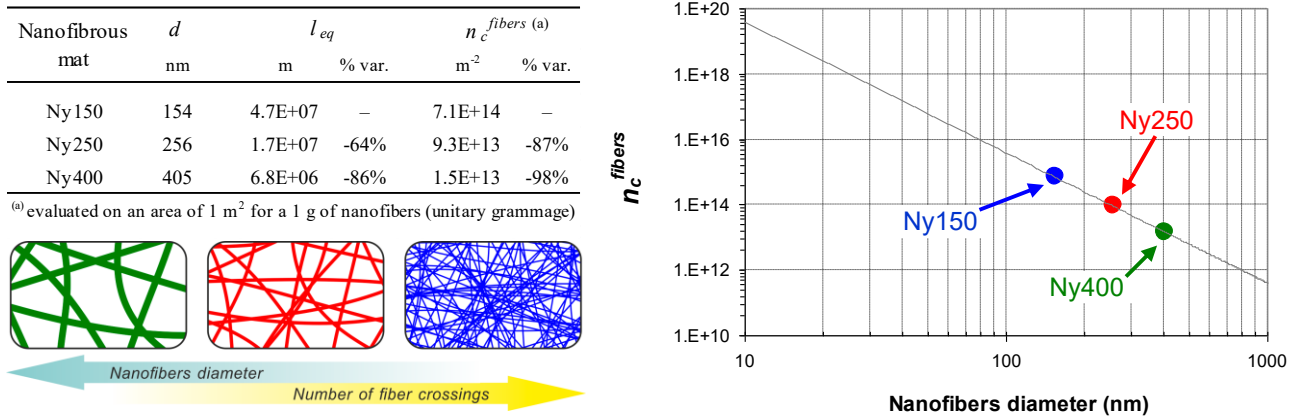
Figure 1.11 – Equivalent filament length (l_{eq}), number of nanofibers crossings per unit area (n_c^{fibers}) and its plot versus nanofibers diameter (d).

It is interesting to note that l_{eq} is inversely proportional to the square of its diameter (Equation 1.14), so nanofibers with smaller diameters determine a higher potential number of intersections. By plotting the number of crossings as a function of the nanofiber diameter in a log-log scale, a linear trend can be observed. Knowing the average value of the nanofiber diameter, it is possible to estimate the n_c^{fibers} for different nanomats, provided the same material is used. It can be observed that the calculated crossing number for the Ny250 and the Ny400 mats are 87 % and 98 % lower than the Ny150 one, respectively.

Given the high difference in the number of n_c^{fibers} that characterize each nanomat, it can therefore be assumed that the changes in mechanical behaviour are mainly ascribable to this aspect. A similar result was also observed in a numerical study on the mechanical characterization of 2D fibrous networks [42]. As shown in Table 1.4, elastic modulus, strain at maximum stress and toughness values of Ny150 mat are substantially different from those of Ny250 and Ny400 membranes, which instead do not diverge significantly in between each other. Therefore, it can be supposed that there is a threshold value of the nanofibers diameter, in the range 150÷250 nm, that leads to a substantial change in the macro-scale mechanical behaviour, and it can be hypothesized that the number of nanofibers crossings is also connected to this aspect. For a high number of crossings (in the case under investigation more than 10^{14} for unitary grammage), indeed, the mechanical properties are higher and the behaviour more brittle. It is to remark that the crossings estimation, as well as the application of the data fitting model explained in the next subsection, are applicable only for random fibrous networks and not for aligned fibrous mats.

1.4.4.3 Application of the phenomenological data fitting model

Tensile stress-strain curves of mats with randomly oriented fibers have a peculiar shape, which displays a nonlinear trend followed by a linear one, as largely found in the literature [17,25,28,33–37,43–46]. The tested mats show this behaviour too: the stiffness decreases from an initial value down to an asymptotic constant trend for high strains. In particular, the mechanical behaviour is characterized by three main stages: an initial nonlinear trend (Stage I), followed by a linear one (Stage II), and finally an additional nonlinear behaviour where the stress reaches a maximum value before mat failure (Stage III). To better understand the phenomena, the Authors developed, and already successfully applied [17,37], a data fitting model. The calculated stress (σ) can be expressed as the superimposition of two stress contributions: a linear one (σ_1) and a nonlinear one (σ_2), formulated as in the following equation:

$$\sigma(\varepsilon) = \sigma_1(\varepsilon) - \sigma_2(\varepsilon) = (a\varepsilon + b) - (be^{-c\varepsilon}) = a\varepsilon + b(1 - e^{-c\varepsilon}) \qquad \text{Eq. 1.16}$$

where a, b and c are parameters experimentally determined to obtain the data fitting. In the present work, the solver tool implemented in Microsoft Excel was used for minimizing the sum of square error (method of least squares).

In Figure 1.12A the comparison between the experimental stress-strain curve and the data fitting curve is shown for Ny250 mat (Ny250_20/45_2dt), as well as the average data fitting parameters resulting from the application of Equation 1.16 to all the tested specimens (in the Supplementary Information SI6 other examples of data fitting are presented).

While the common analysis of stress-strain curves involves, mainly, the determination of Young's modulus and the properties at break, the use of the present data fitting model allows to thoroughly analyse the mechanical behaviour of the nonwoven mat.

The elastic modulus is commonly expressed as the slope of the tangent to the stress-strain curve at a low strain. This approach was applied for the elastic modulus calculation in Sections 1.4.4.1 and 1.4.4.2, and in Supplementary Information SI4, by means of the linear regression of the stress-strain data at the early strain stage (0÷1 %). However, the mat is characterized by a nonlinear trend and a subsequent linear one, as clearly displayed in Figure 1.12A. The linear trend, which appears at "higher" strains, should also be considered for a thoroughly evaluation of the mat tensile properties.

By deriving the stress, as expressed in Equation 1.16, respect to the strain, the following relation represents the slope of the tangent to the stress-strain curve:

$$\frac{d\sigma}{d\varepsilon} = E(\varepsilon) = a + bce^{-c\varepsilon}$$

Eq. 1.17

where $E(\varepsilon)$ describes the local material stiffness as a function of the strain. This relation is useful for evaluating the mat stiffness at very low (for $\varepsilon \to 0$) and at very high (for $\varepsilon \to \infty$) strains, allowing to define an initial mat stiffness (or initial Young's modulus, E_0, Equation 1.18), and an asymptotic constant stiffness (or the Young's modulus of the linear trend of stress-strain curve, E_{lin}, Equation 1.19):

$$E_0 = \underset{\varepsilon \to 0}{Lim} E(\varepsilon) = a + bc$$

Eq. 1.18

$$E_{lin} = \underset{\varepsilon \to \infty}{Lim} E(\varepsilon) = a$$

Eq. 1.19
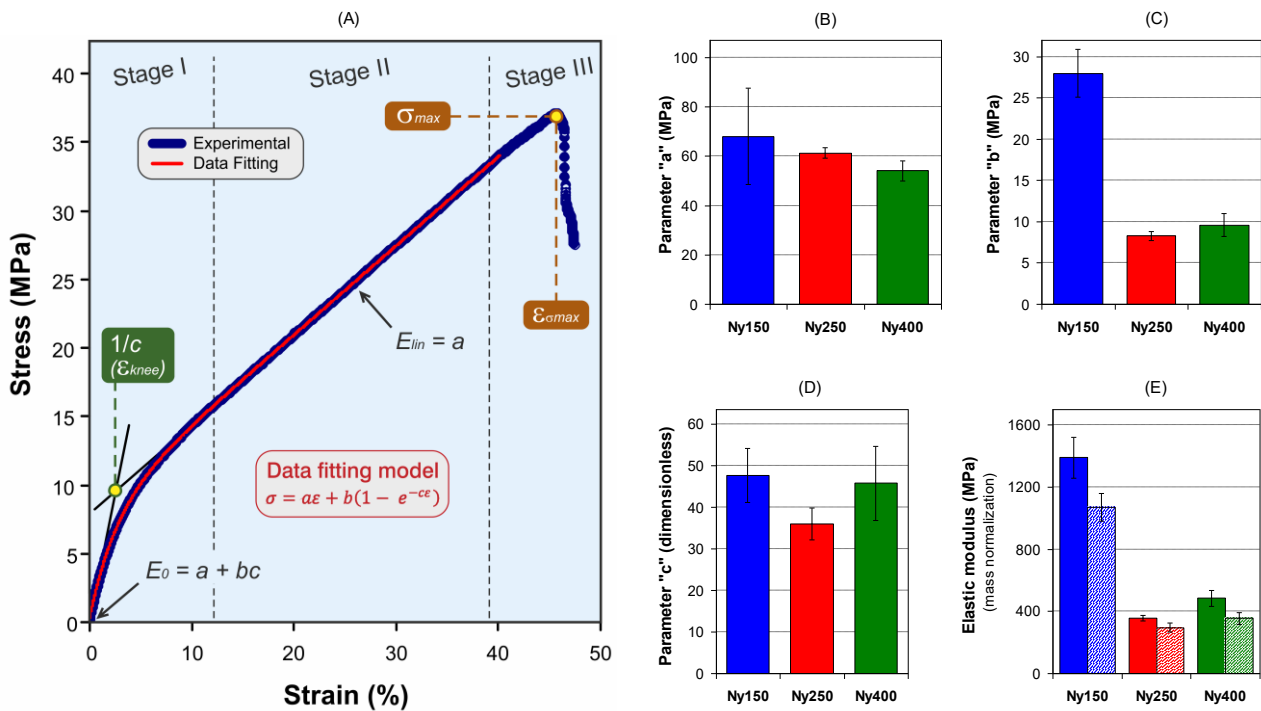
Figure 1.12 – (A) Application of the data fitting model to Ny250_20/45_2dt stress-strain curve. (B-D) average data fitting parameter for Ny150 (blue), Ny250 (red) and Ny400 (green) mats. (E) Comparison between E_0 calculated as per Equation 1.18 (solid colours) and the elastic modulus calculated as the slope of the tangent to the stress-strain curve (dashed).

Therefore, the mat is characterized by two elastic moduli, E_0 and E_{lin}, accounting for two distinct material behaviours. E_0 is shown in Figure 1.12E, as well as the elastic modulus calculated as the slope of the tangent to the stress-strain curve (same data in Table 1.4) for the sake of comparison. E_{lin} values, corresponding to a parameter, are shown in histograms of Figure 1.12B.

The elastic moduli calculated with the two approaches show a similar trend, but are different in absolute values: on average, E_0 is from one fourth (Ny250) to one third (Ny150 and Ny400) higher than the "classically" determined elastic modulus. This discrepancy can be explained considering the nonlinear trend displayed by the stress-strain curve in Stage I. At a first look, the curve seems to have an initial "linear" trend and, consequently, a proportional limit within the Hooke's law ($\sigma = E \cdot \varepsilon$) is valid. Deep focus on the curve shows that no Hookean region is detectable, not even for low strains as the range considered for the slope determination (0÷1 %). Indeed, the mat local stiffness lowers progressively, as clearly evidenced by the trend of $E(\varepsilon)$. E_0, being the extrapolation of the mat elastic modulus at null strain (for $\varepsilon \rightarrow 0$), has a higher value respect to any other elastic modulus value calculated by means of the slope tangent method. Consequently, E_0 should be considered a "theoretical" elastic modulus. Nonetheless it may be useful to obtain a value which is operator-independent, contrarily to the slope tangent method which suffer from the specific strain range considered.

According to Equation 1.18 and Equation 1.19, E_0 and E_{lin} are only functions of the parameters a, b, c, therefore their deeper analysis may help to interpret the mat mechanical behaviour. The comparison of the experimental parameters (Figure 1.12B-D), averaged from the data obtained from all the tested specimen geometries, highlights a significant difference in the b parameter of Ny150 (28 ± 3 MPa) respect to Ny250 and Ny400, that are statistically comparable (8.3 ± 0.5 and 9.6 ± 1.4, respectively). The other two parameters, a and c, seem to be unrelated to the geometrical/morphological factors of the nanofibrous mat.

The a parameter, as declared by Equation 1.19, represents the mat elastic modulus in the linear trend at high strain (Stage II). The obtained values are comparable for all the mat types (54÷68 MPa). In that region the membrane already underwent large deformations: as a result, the fibers, still random at a nanoscale level, are growing oriented in the direction of the applied load. In these conditions, the resulting stiffness should be mostly related to the intrinsic mechanical properties of the material, regardless of its morphology. The a mean value, irrespective of the standard deviation, becomes slightly lower as the diameter increases: this may be attributed to the different mechanical properties derived by the differences of the polymer crystallites "quality", as highlighted by DSC analysis (Section 1.4.4.2 and Supplementary Information SI5). The high standard deviation of the a parameter in Ny150 (coefficient of variation of 29 %, respect to 3 % and 8 % for Ny250 and Ny400, respectively) stems from the troubles in applying the data fitting model to mats with brittle behaviour, which do not display a sufficient linear trend extension (Stage II).

The b parameter is involved in both σ_1 and σ_2 (Equation 1.16), but its contribution is different depending on the strain region considered. At very low strains (for $\varepsilon \rightarrow 0$), both σ_1 and σ_2 converge to

b value. While, at high strains, σ_1 and σ_2 are partially affected by this parameter. Consequently, the *b* impact on the resulting $\sigma(\varepsilon)$ is significant in Stage I (non-linear region), where *b* acts as a multiplier of the exponential $e^{-c\varepsilon}$. σ_2 describes how rapidly the stress-strain curve deviates from the linear trend at low strains.

The *c* parameter refers to the region where the stress-strain curve change slope from the E_0 value to the E_{lin} one. More specifically, $1/c$ represents the onset extrapolation of the slope change (ε_{knee}), as can be derived from Equation 1.18 and Equation 1.19 reported in [37]. Ny150 and Ny400 have a similar average *c* (48 and 46, respectively) which corresponds to $\varepsilon_{knee} = 0{,}0021$, while Ny250 has $c = 36$ and consequently a higher ε_{knee} (0,0028). All the *c* values are statistically comparable, nonetheless. This parameter affects only σ_2 and, similarly to *b*, contributes to $\sigma(\varepsilon)$ via the exponential term.

Since a significant difference is found only for *b* parameter (for Ny150 mat is three times higher), it is possible to assume that this parameter is related to the morphology of the nanofibrous mat, and in particular to the number of intersections. It is interesting to note that the same trend has been found for the experimental elastic modulus (Figure 1.9A and Table 1.4).

1.4.5 Grammage-thickness relationship for grammage re-normalization of load-displacement curves

Finally, with the aim to characterize nanofibrous mats not only mechanically but also morphologically, a study was carried out to assess whether there is a relationship between the thickness and the grammage of a nanomat. This relationship is easily predictable for bulk materials, but it is not for nonwoven fabrics, and particularly for electrospun nanomats, which contain a high fraction of voids. Moreover, this analysis is useful for the grammage re-normalization of load-displacement curves previously normalized on the cross-section area, for which only the thickness of the mat is known. To this end, for each membrane type, thickness, weight, and area (and therefore grammage) of the nanofibrous patches were assessed (detailed description in Sections 1.3.2 and 1.3.3 and in Supplementary Information SI1 and SI2). At this stage, only one instrument was used for thickness assessment to obtain comparable measurements. The instrument used is the analog indicator 2 in the low-pressure configuration (iv, Table 1.3), as it allows to compare the measured values with an acceptable resolution. In the following equations the steps to obtain the relationship between the grammage *G* and the thickness *t* of the nanomat are reported. By knowing the density ρ_m of the electrospun material, it is possible to express the mass *m* of the mat as a function of the fiber volume

$V_f (m = \rho_m V_f)$. Furthermore, the percentage fiber volume $V_{f\%}$ can be expressed as the ratio between the fiber volume V_f and the total volume V of the mat:

$$V_{f\%} = \frac{V_f}{V} = \frac{V_f}{L\,w\,t} \qquad \text{Eq. 1.20}$$

where L, w and t are the length, the width, and the thickness of the nanomat. According to Equation 1.4, concerning the grammage G of the nanofibrous mat, and replacing the previous equations, it can be proven that:

$$G = \frac{m}{L\,w} = \frac{\rho_m V_f}{L\,w} = \frac{\rho_m V_{f\%}\,L\,w\,t}{L\,w} = \rho_m V_{f\%}\,t \qquad \text{Eq. 1.21}$$

Equation 1.21 clearly displays the linear relationship between grammage and thickness. This dependence can also be experimentally proved, by plotting the values of grammage assessed for each patch as a function of the nanomat thickness (Figure 1.13).
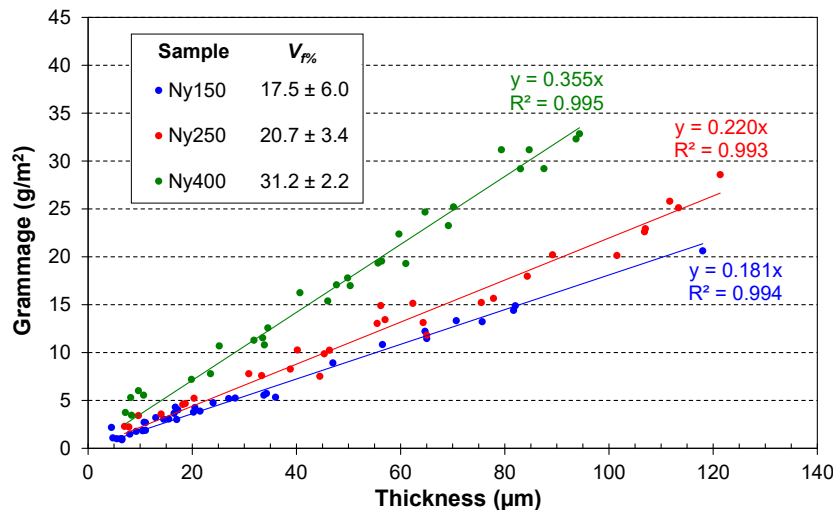
Figure 1.13 – Grammage-thickness plot. The coloured dots represent the experimental measurements, while the regression lines represent the calibration lines for each type of membrane (Ny150, Ny200, and Ny400).

In the graph are shown the experimental data in terms of the percentage fiber volume $V_{f\%}$ (evaluated via Equation 1.21) and are also reported the angular coefficient α of the linear regression lines for each type of membrane. Interestingly, as the nanofibers diameter increases (from Ny150 to Ny400) the slope of the linear regression line, and thus the angular coefficient α, increases ($G = \alpha t$). Consequently, it is worth pointing out that to obtain the same grammage with smaller nanofibers diameter (smaller α), it is necessary to electrospin thicker membranes.

This means also that smaller diameter nanofibers generate a higher percentage of porosity during the electrospinning deposition process. Indeed, rearranging Equation 1.21, higher diameters (higher α) correspond to higher $V_{f\%}$:

$$V_{f\%} = \frac{G}{\rho_m\,t} = \frac{\alpha\,t}{\rho_m\,t} = \frac{\alpha}{\rho_m} \qquad\qquad \text{Eq. 1.22}$$

Observing the experimental data (reported in the inset of Figure 1.13), a linear relationship between the diameter of the nanofibers and the percentage of fiber volume $V_{f\%}$ was found. The grammage-thickness plot allows to re-normalize previous tensile tests in which the load had been normalized as a function of the cross-section area. In fact, having the calibration lines (in the present study reported for different Nylon 66 mats), it is possible to determine the grammage of any type of nanofibrous mat knowing its thickness. Therefore, given the grammage, it is possible to apply Equation 1.7 to obtain more reliable stress-strain curves based on grammage normalization of load. To apply this method, it is mandatory to adopt the same thickness measuring tool used for the previous cross-section area normalizations. In the Supplementary Information SI7 is reported the step-by-step procedure block diagram to recover previous tensile tests with load normalized respect to the specimen section.

1.5   Conclusions

The high porosity, flexibility, and deformability of nanofibrous nonwovens make troublesome their tensile testing, severely affecting results reliability. In this work an accurate, systematic, and critical study concerning tensile testing of nonwoven mats, using electrospun Nylon 66 nanofibrous membranes as a case study has been presented. Three randomly-oriented nanofibrous mats with different diameter (Ny150, Ny250, and Ny400) were produced and then morphologically, mechanically and thermally characterized. In this frame, the "classical" approach to load normalization by means of specimen cross-section area was compared to a mass-based normalization proposed by the Authors, as well as a normalization based on the mat grammage, overcoming the trouble of the nanomat thickness measurement. The mass-based normalization method allows to obtain reliable and repeatable results, similarly to what happens for bulk materials. Although the grammage-based normalization is less reliable respect to the mass-based one, the use of mat grammage proved to provide better results than the "classic" normalization approach based on the specimen cross-section area. Moreover, the grammage-based method allows to re-normalize already tested specimens whose load-displacement curves were previously normalized on the cross-section area, thus benefitting of improved reliability and comparability of old data. Indeed, a linear

dependence between these two parameters was found, whose angular coefficient depends on the nanofiber morphology.

Nanofibrous mat characteristics, such as nanofibers diameter, grammage, and specimen geometry (width and gauge length) were deeply investigated and the mats mechanical performance were interpreted also considering the polymer properties (degree of crystallinity and glass transition temperature), as well as the number of potential nanofibers crossings as a function of the nanofiber diameter. The tensile properties are found mainly dependent on the nanofibers diameter, which in turn strongly impacts the number of nanofibers crossings. Below a threshold value, which lies between 150÷250 nm, the overall mat mechanical behaviour changes from ductile to brittle. At the same time, the elastic modulus has a significant boost, while the mat strength is not affected. In particular, for the Ny150 membrane a Young's modulus of 1071 MPa was found, about three times respect to the other mats under investigation (296 MPa for Ny250 and 355 MPa for Ny400, respectively). Moreover, the experimental stress-strain data were analysed using a phenomenological data fitting model to better interpret the tensile mechanical properties. The experimental results demonstrate the higher reliability of the proposed mass-based load normalization, providing a simple, effective and universally applicable method for obtaining tensile stress-strain curves characterized by high reproducibility.

1.6   Supplementary Information

1.6.1 SI1 – Specimens for grammage-thickness relationship

For the grammage-thickness relationship assessment, a nanomat for each membrane type (Ny150, Ny250 and Ny400) was electrospun for a total time of 270 min. For each membrane type, 6 poly(ethylene)-coated paper strips (with a dimension of 350 × 60 mm approximately) were fixed with the tape onto the collecting drum, as reported in Figure 1.14. During the electrospinning process, a membrane strip was picked from the drum every 45 minutes, so obtaining 6 strips with incremental deposition time for each membrane type.
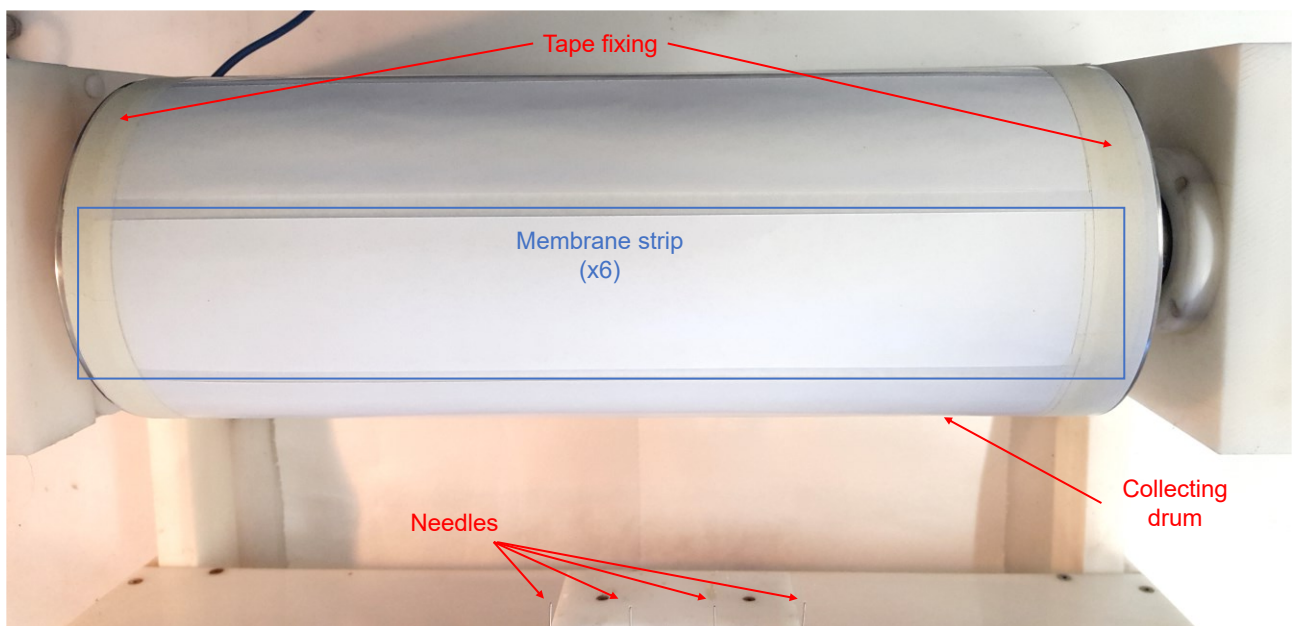
Figure 1.14 – Electrospinning set-up for the grammage-thickness relationship.

At the end of the electrospinning process, from each membrane strip 5 patches with a nominal size of 60 × 25 mm were extracted. As reported in Figure 1.15, the sampling positions of the patches were: left (L), centre-left (CL), centre (C), centre-right (CR), right (R). In this way, 30 patches were obtained for each type of membrane, resulting in an overall amount of 90 patches.

For each patch, thickness, weight, and area of the nanofibrous mat were assessed. To evaluate the mat thickness, the overall thickness of the nanofibrous mat together with the supporting paper was measured in 6 different equidistant zones (red dots in Figure 1.16). Then the thickness of the sole support paper was measured in the same zones to determine the membrane thickness by difference.
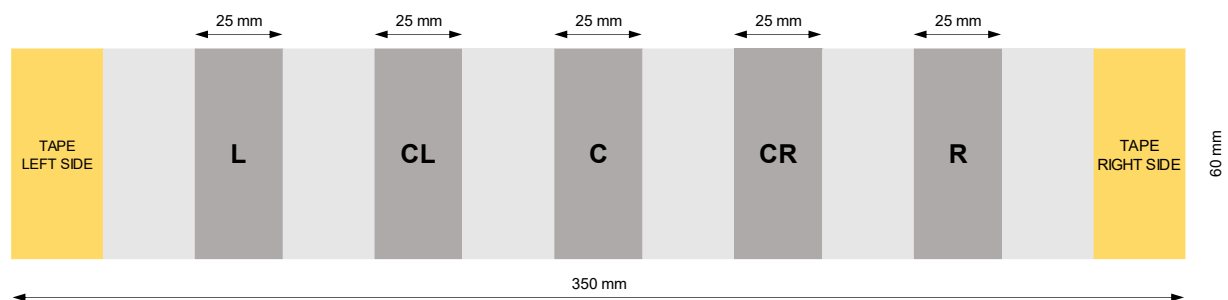
Figure 1.15 – Patches sampling positions for each membrane strip.
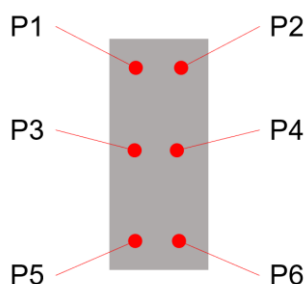
Figure 1.16 – Sampling positions for mat thickness evaluation.

The 6 thickness values for each patch were averaged and used, together with the mass and area values, to build the grammage-thickness graph (Figure 1.13). That required a total of 1080 thickness measurements. At this stage, only one instrument was used for thickness measurement to obtain comparable measurements. The analog indicator 2 in the low-pressure configuration (iv, Table 1.3) was used, as it allows to compare the measured values with an acceptable resolution.

The mat mass from each patch was determined by weight (nanofibrous mat with paper support minus supporting paper) using a AS 60/220.R2 Radwag scale with a resolution of 0.01 mg. Authors suggest adopting a scale with an appropriate resolution, at least equal to 5 % of the specimen mass. Finally, each patch area was evaluated via MATLAB software by image processing of scanned images (detailed procedure on Supplementary Information SI2).

1.6.2 SI2 – Evaluation of the patch area

To obtain the grammage-thickness relationship for the different types of membranes (Ny150, Ny250 and Ny400), it was necessary to evaluate for each patch not only the mass and thickness but also the grammage. The calculation of the grammage requires the knowledge of both the mass and the surface area of each patch. To carefully assess the area, after measuring both the mass and the thickness of each nanofibrous patch by subtracting the thickness of the supporting paper from the overall thickness (nanomat + supporting paper), the supporting papers were retained and analysed. The area evaluation was carried out on the supporting paper as it is easy to handle, unlike the

nanofibrous mat. Every single patch of supporting paper was properly classified by an alphanumerical code so that it can be uniquely referred to as its nanofibrous sample. The number identifies the membrane stripe (from 1 to 6, increasing with electrospinning deposition time), whilst the letters identify the relative position of each patch inside the considered stripe: left (L), centre-left (CL), centre (C), centre-right (CR), right (R).

The patches were scanned through a Kyocera TASKalfa 3551ci KX photocopier at a resolution of 600 dpi, to have a high precision on the edges and therefore an accurate evaluation of the area. A ruler was placed on the scanning plane together with the patches to verify that there was no scaling during the copy (Figure 1.17A). Subsequently, the scans were imported into Adobe Photoshop and, for each of them, the correlation between pixels and millimeters was assessed. The images were then segmented in B/W at a 50 % threshold and the ruler area removed, leaving only the patches (Figure 1.17B).
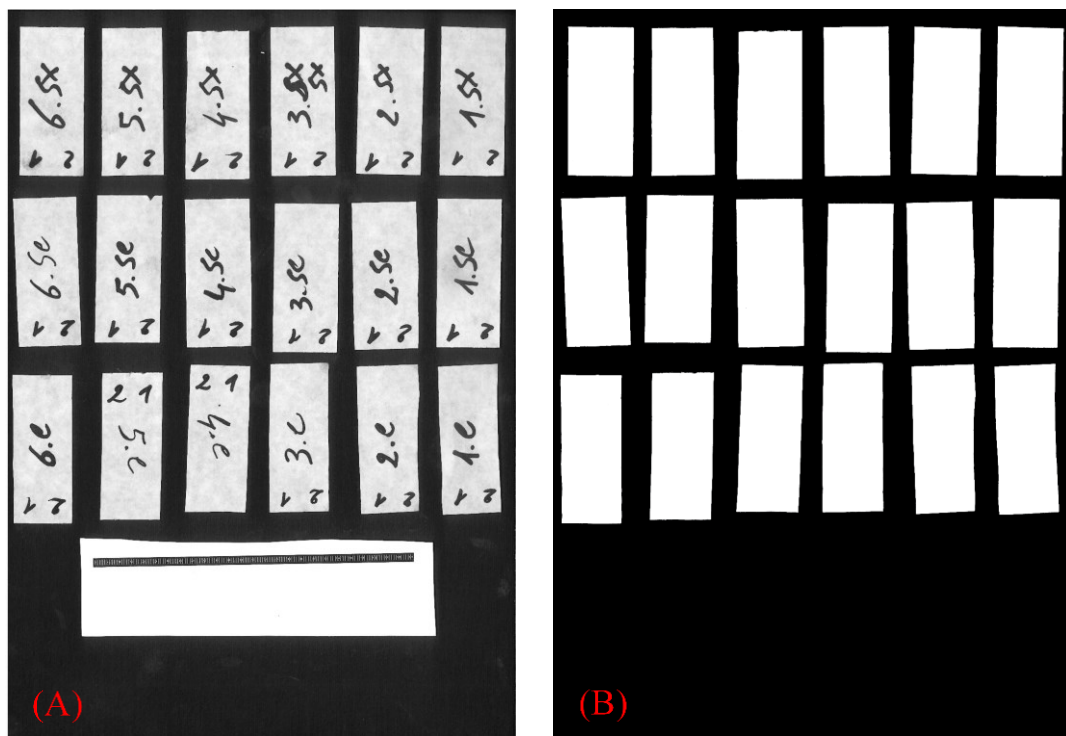
Figure 1.17 – (A) Representative scan of Ny250 membrane and (B) the same image segmented in B/W at a 50 % threshold.

The images thus obtained were imported into MATLAB software and analysed with the Image Segmenter tool. This tool allows, by creating a binary mask, to segment and convert the images into logical class. The images were then analysed with the Image Region Analyzer tool, which allows obtaining the area in pixels of each patch. Finally, knowing the pixel - millimeters conversion coefficient previously established, it is possible to transform in mm^2 the area values expressed in pixels, and so calculate the patch grammage as the mass on area ratio.

1.6.3 SI3 – Tensile stress-strain curves
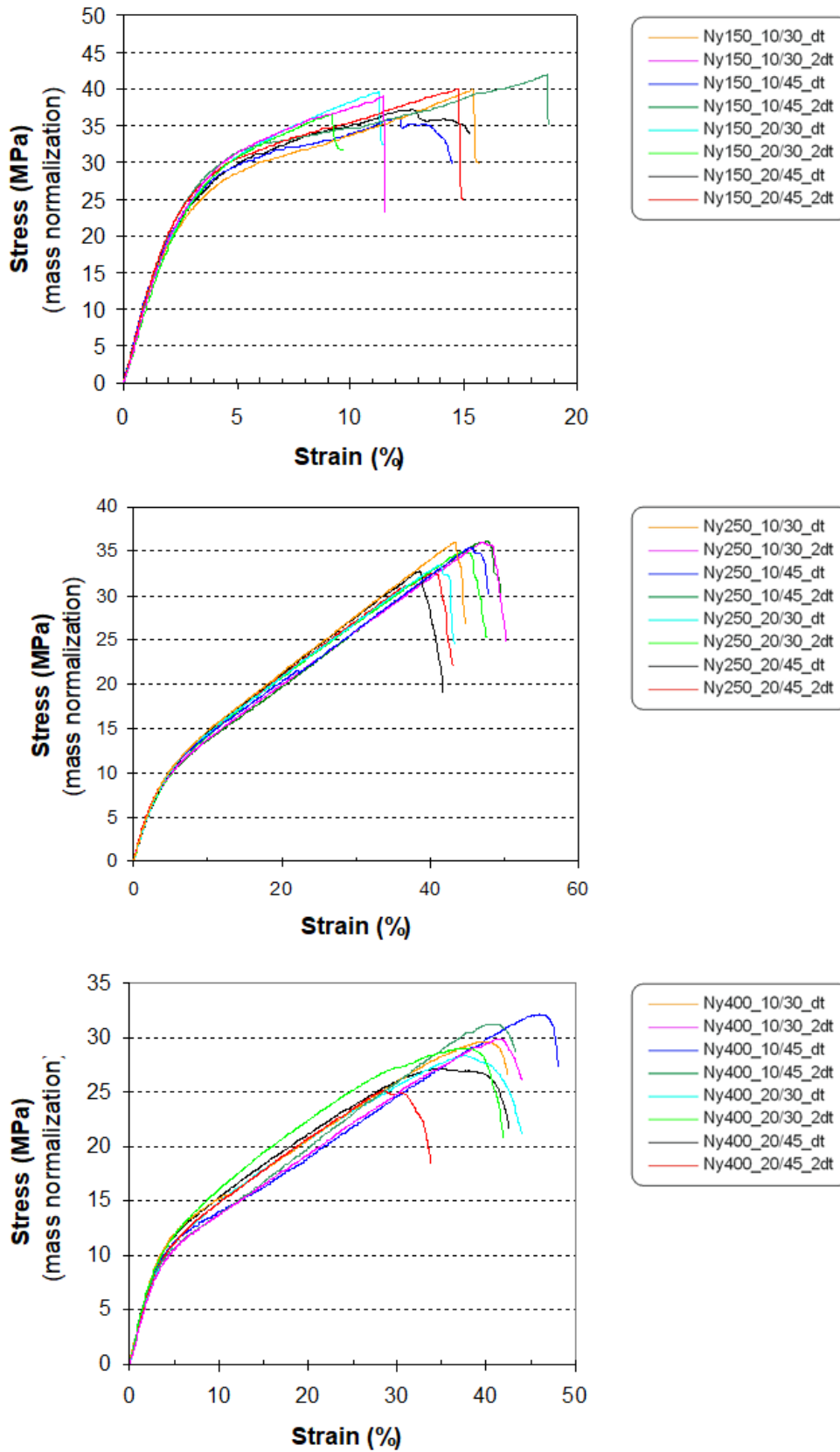
Figure 1.18 – Representative stress-strain curves of the different specimen configurations for each membrane type.

1.6.4 SI4 – Effect of the specimen geometry on the tensile properties
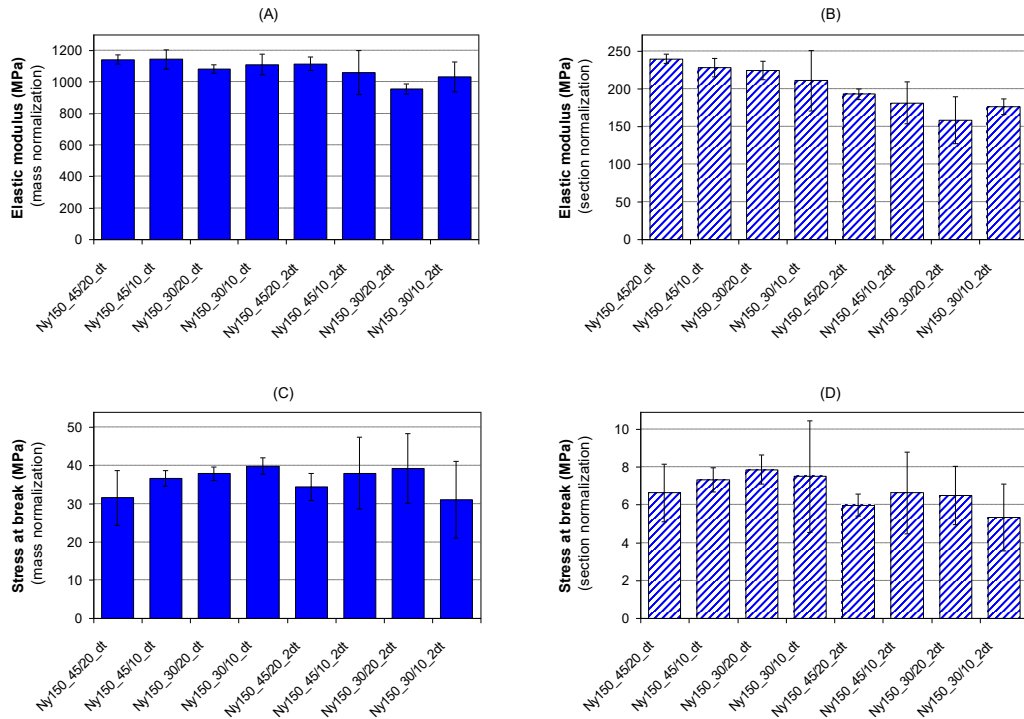
Figure 1.19 – Elastic modulus and maximum stress for the specimens obtained from the membrane Ny150_dt and Ny150_2dt, normalized both on mass (A and C respectively, solid filling) and on cross-section area (B and D respectively, dashed filling).
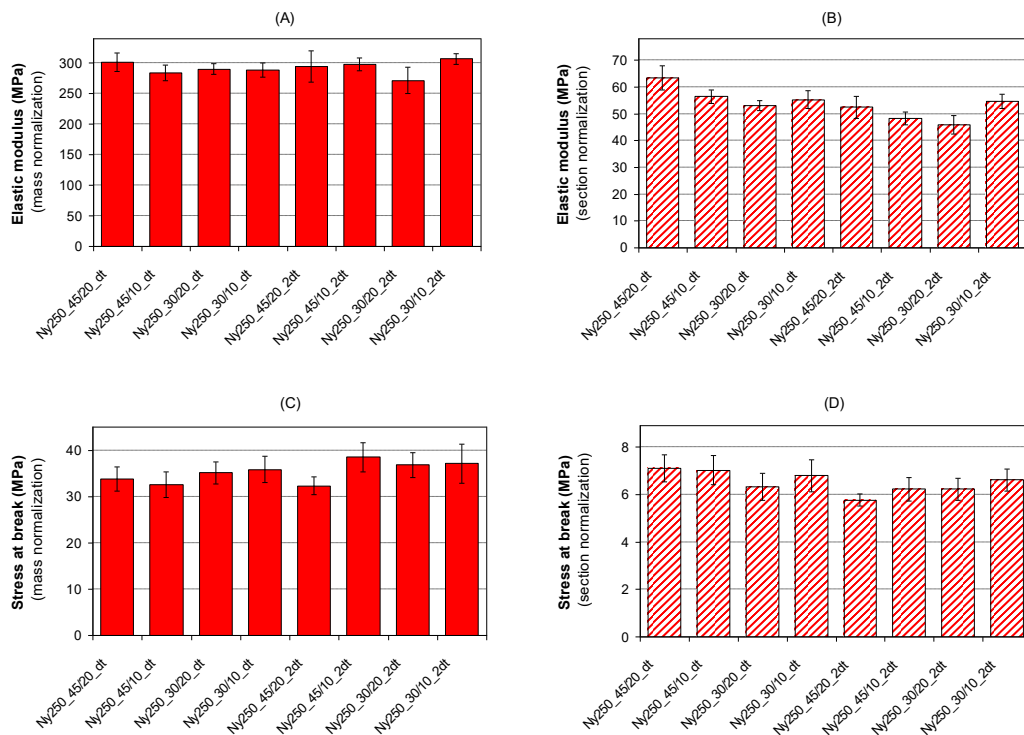
Figure 1.20 – Elastic modulus and maximum stress for the specimens obtained from the membrane Ny250_dt and Ny250_2dt, normalized both on mass (A and C respectively, solid filling) and on cross-section area (B and D respectively, dashed filling).
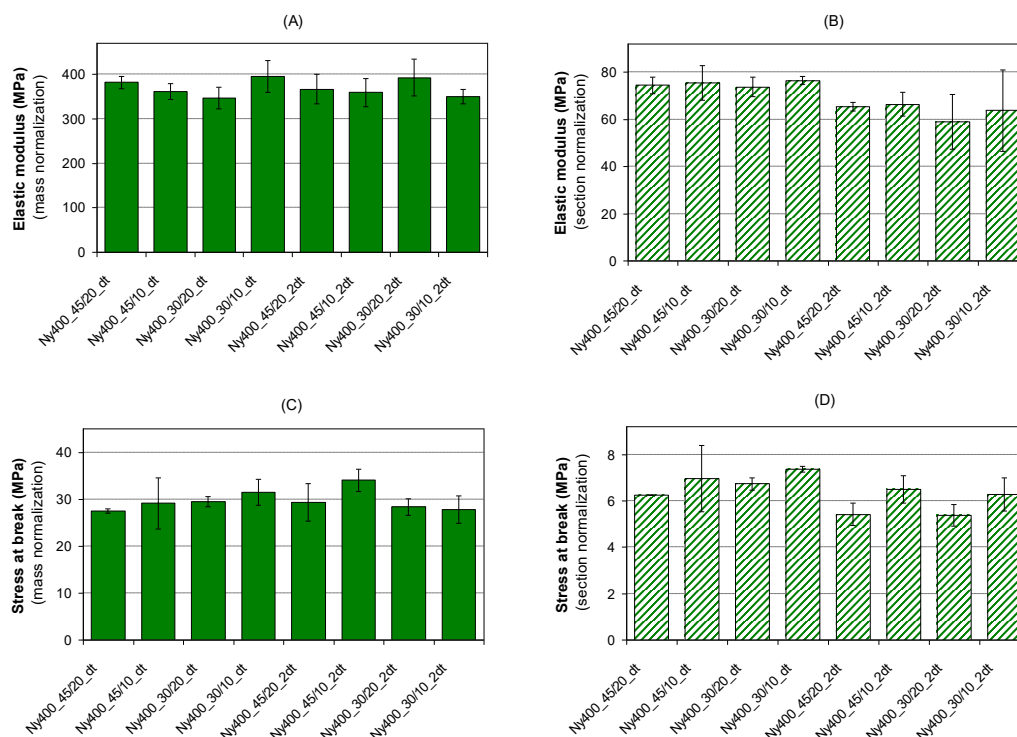
Figure 1.21 – Elastic modulus and maximum stress for the specimens obtained from the membrane Ny400_dt and Ny400_2dt, normalized both on mass (A and C respectively, solid filling) and on cross-section area (B and D respectively, dashed filling).

1.6.5 SI5 – DSC analysis

The nanofibrous mats were investigated via DSC analysis to evaluate the effect of the nanofiber morphology on the Nylon 66 thermal properties, which may contribute to the observed different mechanical behaviour of the nanomats (Figure 1.22, also reported in Figure 1.10 in the main text).

As expected for a semicrystalline polymer, the thermograms show a stepwise variation of the thermal capacity ascribable to the polymer glass transition and an endothermic signal accounting for the melting of the polymer crystalline fraction. The degree of crystallinity (χ_c) was calculated according to the well-known equation:

$$\chi_c = \frac{\Delta H_m}{\Delta H_{m,100\%}} 100$$

Eq. 1.22

where ΔH_m is the melting enthalpy of the sample and $\Delta H_{m,100\%}$ is the melting enthalpy of a hypothetical 100 % crystalline Nylon 66, assumed equal to 196 J/g [47].

No differences were found in the χ_c of Ny150, Ny250 and Ny400, which have values of 47 %, 45 % and 45 %, respectively. Analysing their melting peaks, it is worth noting differences in their shape. In particular, the presence of multiple peaks is observed in the mats characterized by fibers

with smaller diameters (Ny150 and Ny250), while the Ny400 does not display the peak splitting. The peak positioning (peak temperature) is related to the quality of the crystallites, which present a higher melting temperature for large and more perfect crystals, promoted by the drawing process during electrospinning [38].
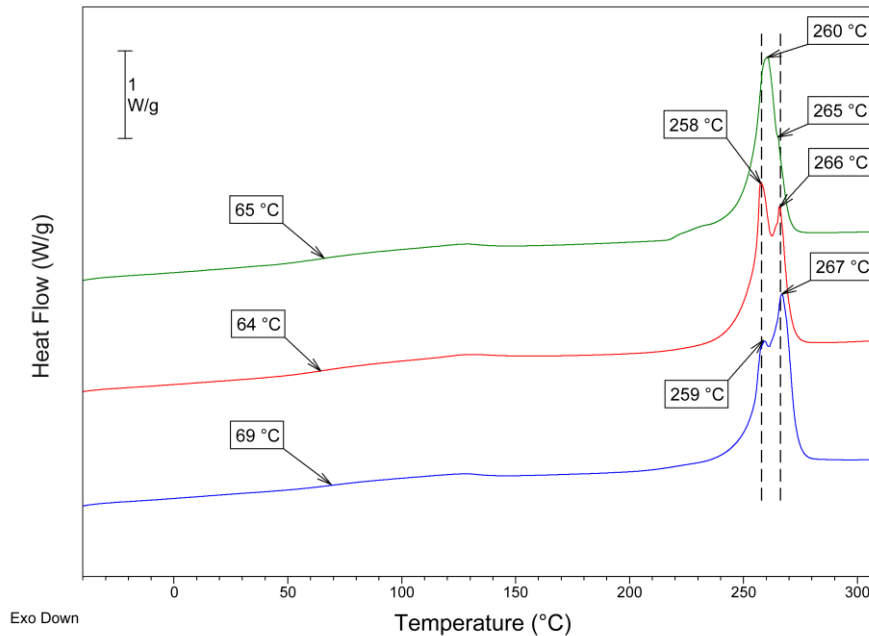
Figure 1.22 – DSC analysis of the three membrane types (Ny150 blue, Ny250 red, Ny400 green).

The Ny150 and Ny250 present a low-temperature melting peak at 258 °C and a high-temperature one at 266 °C, suggesting a bimodal distribution size of crystals. By contrast, the Ny400 presents an almost symmetrical peak centred at 260 °C, and positioned in the middle of the cited double peaks, with only a very little shoulder at 266 °C. It is worth noting a well pronounced endotherm event at low temperature (onset at 218 °C), which represents the melting of small and less perfect crystallites formed during the nucleation stage of crystallization process. This fraction of crystals, which are anyway counted in the χ_c evaluation, have a less important contribution to the mechanical properties of Nylon. However, since the observed mechanical properties of Ny250 and Ny400 are comparable, the different mechanical behaviour of Ny150 cannot be associated to the differences on their thermal properties. The analysis of the glass transition temperatures (T_gs) shows slight differences, which are not able to justify the high different mechanical behaviours. Indeed, the observed T_gs are almost comparable, with only a slightly higher value for the Ny150 (69 °C vs. 64 °C and 65 °C of Ny250 and Ny400, respectively), accounting for a possible slightly higher orientation of the Nylon 66 amorphous phase of Ny150 mat.

1.6.6 SI6 – Examples of data fitting model application
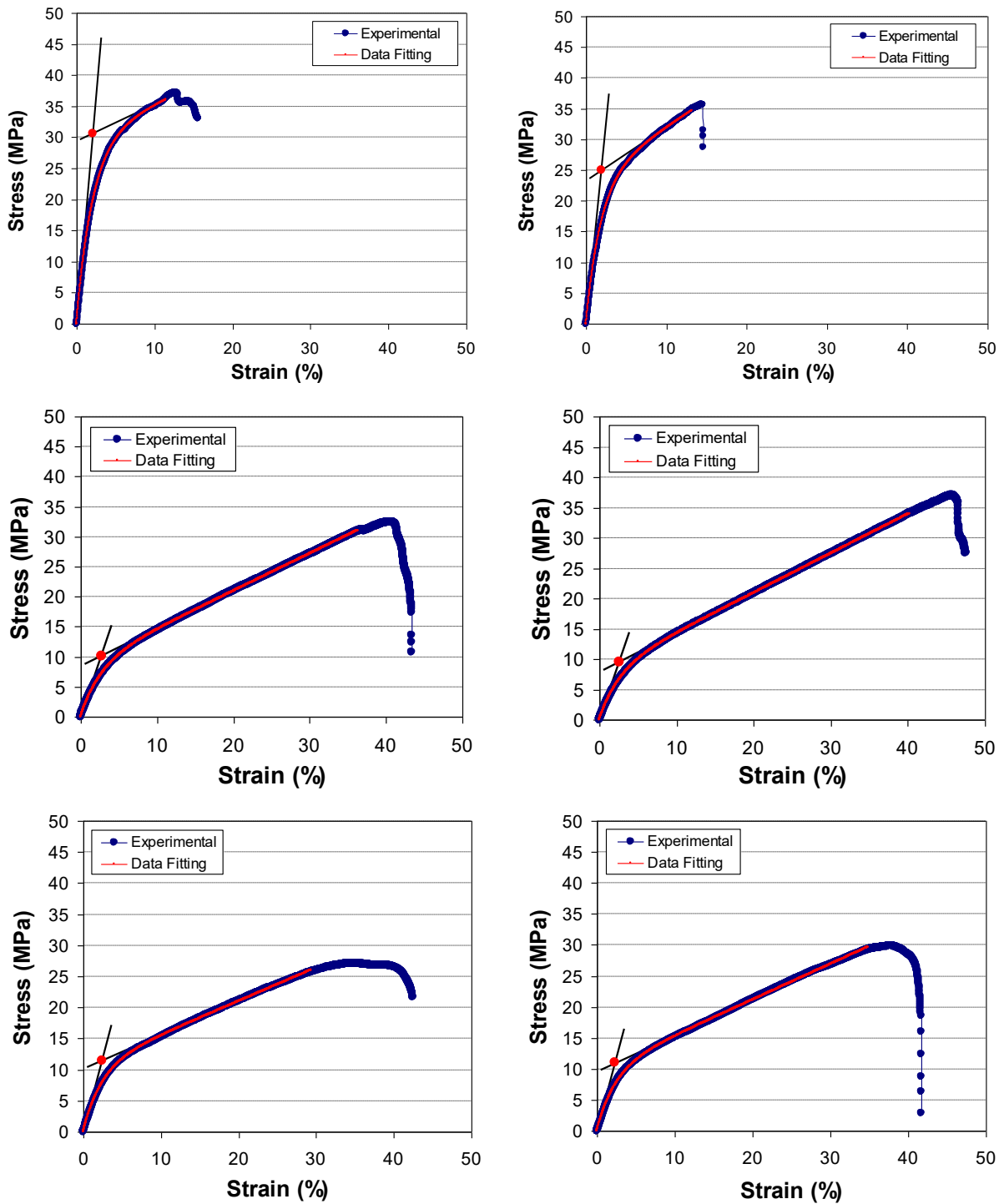
Figure 1.23 – Comparison between experimental stress-strain curve and data fitting model for some nanomats of Ny150 (1ˢᵗ row), Ny250 (2ⁿᵈ row) and Ny400 (3ʳᵈ row) for the configurations 20/45_dt (left column) and 20/45_2dt (right column).

1.6.7 SI7 – Re-normalization of load-displacement curves by grammage-thickness relationship

The grammage-thickness plot allows to re-normalize previous tensile tests in which the load had been normalized respect to the cross-section area. In fact, having the calibration lines (Figure 1.13), it is possible to determine the grammage of any type of nanofibrous mat knowing its thickness. Therefore, given the grammage, it is possible to apply Equation 1.7 to obtain more reliable stress-strain curves based on grammage normalization.

**HOW TO "RECOVER" PREVIOUS TENSILE TESTS
WITH LOAD NORMALIZED RESPECT TO THE SPECIMEN SECTION**
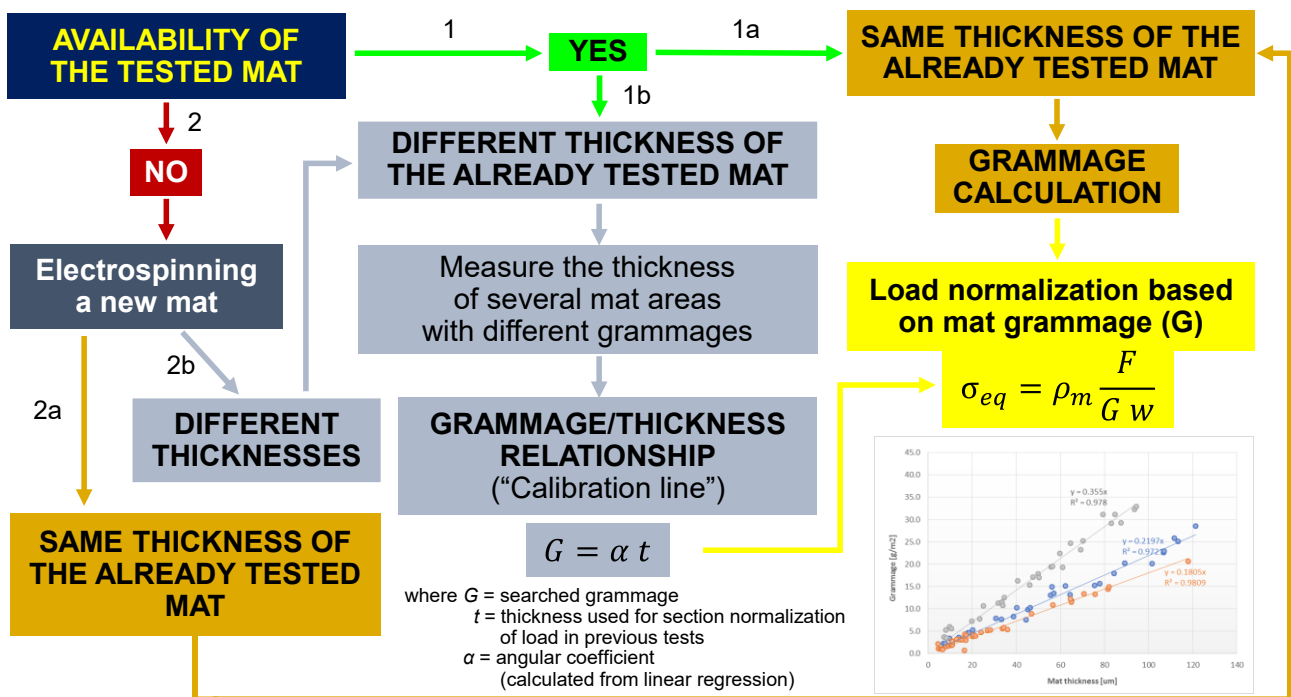
Figure 1.24 – Logical diagram to "recover" previous tensile tests with load normalized respect to the specimen cross-section area.

The diagram shows the possible scenarios, and the relative ways to re-normalize the load data with respect to the mat grammage. If a piece of the already tested mat is available (*path 1*), the re-normalization is readily applicable in case the mat has the same thickness (*case 1a*), or possible after the construction of the "calibration line" (*case 1b*). On the contrary, if the tested mat is no longer available, it is necessary to electrospin a new mat (*path 2*), using the previously adopted solution and process parameters, and proceed following *case 2a* or *case 2b* depending on the situation.

1.6   Nomenclature

t	measured mat thickness	$V_{f\%}$	percentage fibers volume
S	mat cross section area	ρ_m	material density
d	average nanofibers diameter	U	material toughness
w	tensile specimen width	χ_c	degree of crystallinity
L	tensile specimen length	T_g	glass transition temperature
F	tensile force	ΔH_m	melting enthalpy of the sample
σ	tensile stress	n_c^{fibers}	number of crossings per unit area
σ_{eq}	tensile equivalent stress	τ	total fiber length per unit area
σ_{max}	maximum stress	l_{eq}	filament equivalent length
$\varepsilon_{\sigma max}$	strain at maximum stress	$V_{filament}$	filament volume
A	specimen surface area	a,b,c	data-fitting model parameters
m	specimen mass	σ_1	linear stress contribution
G	mat grammage	σ_2	non-linear stress contribution
V	mat enclosure volume	E_0	model initial Young's modulus
t_{eq}	thickness of an equivalent bulk film	E_{lin}	model asymptotic Young's modulus
V_{eq}	volume of an equivalent bulk film	ε_{knee}	strain at the onset extrapolation of the model slope change
S_{eq}	cross section area of an equiv. bulk film		
V_f	fibers volume	α	angular coefficient calibration line

1.7   References

[1]   BS EN ISO 9092:2019 - Nonwovens – Vocabulary, (2019).

[2]   T. Hussain, M. Ashraf, A. Rasheed, S. Ahmad, Z. Ali, Textile Engineering, De Gruyter, Berlin, Boston, 2016. https://doi.org/10.1515/9783110413267.

[3]   S.J. Russell, Handbook of Nonwovens, Elsevier, 2006. https://doi.org/10.1533/9781845691998.

[4]   D. Semnani, Geometrical characterization of electrospun nanofibers, in: Electrospun Nanofibers, Elsevier, 2017: pp. 151–180. https://doi.org/10.1016/B978-0-08-100907-9.00007-6.

[5]   A. Baji, Y.W. Mai, S.C. Wong, Effect of fiber diameter on the deformation behavior of self-assembled carbon nanotube reinforced electrospun Polyamide 6,6 fibers, Materials Science and Engineering A. 528 (2011) 6565–6572. https://doi.org/10.1016/j.msea.2011.05.012.

[6]   X. Qin, S. Subianto, Electrospun nanofibers for filtration applications, in: Electrospun Nanofibers, 2017: pp. 449–466. https://doi.org/10.1016/B978-0-08-100907-9.00017-9.

[7]   A. Sensini, C. Gualandi, A. Zucchelli, L.A. Boyle, A.P. Kao, G.C. Reilly, G. Tozzi, L. Cristofolini, M.L. Focarete, Tendon Fascicle-Inspired Nanofibrous Scaffold of Polylactic acid/Collagen with Enhanced 3D-Structure and Biomechanical Properties, Scientific Reports. 8 (2018) 17167. https://doi.org/10.1038/s41598-018-35536-8.

[8]   Q.P. Pham, U. Sharma, A.G. Mikos, Electrospinning of polymeric nanofibers for tissue engineering applications: A review, Tissue Engineering. 12 (2006) 1197–1211. https://doi.org/10.1089/ten.2006.12.1197.

[9]   D. Fabiani, F. Grolli, M. Speranza, S.V. Suraci, T.M. Brugo, A. Zucchelli, E. Maccaferri, Piezoelectric Nanofibers for Integration in Multifunctional Materials, in: Annual Report - Conference on Electrical Insulation and Dielectric Phenomena, CEIDP, IEEE, 2018: pp. 14–17. https://doi.org/10.1109/CEIDP.2018.8544896.

[10]   D. Fabiani, F. Grolli, G. Selleri, M. Speranza, T.M. Brugo, E. Maccaferri, D. Cocchi, A. Zucchelli, Nanofibrous piezoelectric structures for composite materials to be used in electrical and electronic components, in: Proceedings of the Nordic Insulation Symposium, 2019: pp. 1–5. https://doi.org/10.5324/nordis.v0i26.3263.

[11]   T.M. Brugo, E. Maccaferri, D. Cocchi, L. Mazzocchetti, L. Giorgini, D. Fabiani, A. Zucchelli, Self-sensing hybrid composite laminate by piezoelectric nanofibers interleaving, Composites Part B: Engineering. 212 (2021). https://doi.org/https://doi.org/10.1016/j.compositesb.2021.108673.

[12]   D. Bonincontro, F. Fraschetti, C. Squarzoni, L. Mazzocchetti, E. Maccaferri, L. Giorgini, A. Zucchelli, C. Gualandi, M.L. Focarete, S. Albonetti, Pd/Au based catalyst immobilization in polymeric nanofibrous membranes via electrospinning for the selective oxidation of 5-hydroxymethylfurfural, Processes. 8 (2020) 45. https://doi.org/10.3390/pr8010045.

[13] D. Cocchi, F. Musiari, T.M. Brugo, A. Pirondi, A. Zucchelli, F. Campanini, E. Leoni, L. Mazzocchetti, Characterization of aluminum alloy-epoxy bonded joints with nanofibers obtained by electrospinning, Journal of Adhesion. 96 (2020) 384–401. https://doi.org/10.1080/00218464.2019.1666716.

[14] R. Palazzetti, A. Zucchelli, Electrospun nanofibers as reinforcement for composite laminates materials – A review, Composite Structures. 182 (2017) 711–727. https://doi.org/10.1016/j.compstruct.2017.09.021.

[15] E. Maccaferri, L. Mazzocchetti, T. Benelli, T.M. Brugo, A. Zucchelli, L. Giorgini, Rubbery nanofibrous interleaves enhance fracture toughness and damping of CFRP laminates, Materials & Design. (2020). https://doi.org/10.1016/j.molliq.2020.112490.

[16] L. Mazzocchetti, T. Benelli, E. Maccaferri, S. Merighi, J. Belcari, A. Zucchelli, L. Giorgini, Poly-m-aramid electrospun nanofibrous mats as high-performance flame retardants for carbon fiber reinforced composites, Composites Part B: Engineering. 145 (2018) 252–260. https://doi.org/10.1016/j.compositesb.2018.03.036.

[17] E. Maccaferri, L. Mazzocchetti, T. Benelli, A. Zucchelli, L. Giorgini, Morphology, thermal, mechanical properties and ageing of nylon 6,6/graphene nanofibers as Nano2 materials, Composites Part B: Engineering. (2019). https://doi.org/10.1016/j.compositesb.2018.11.096.

[18] J.H. Wendorff, S. Agarwal, A. Greiner, Electrospinning: Materials, Processing, and Applications, 2012.

[19] BS EN ISO 10319:1996 - Geotextiles — Wide-width tensile test, (1996).

[20] BS EN ISO 1924-2:2008 - Paper and board — Determination of tensile properties, Draft International Standard ISO/DIS 1924-2. (2008).

[21] BS ISO 1924-3:2005 - Paper and board — Determination of tensile properties, 3 (2005).

[22] BS EN ISO 9073-2:1997 - Textiles — Test methods for nonwovens — Part 2: Determination of thickness, Management. 3 (1997).

[23] BS EN ISO 534:2011 - Paper and board — Determination of thickness, density and specific volume, (2011).

[24] X. Yu, C. Li, H. Tian, L. Yuan, A. Xiang, J. Li, C. Wang, A.V. Rajulu, Hydrophobic cross-linked zein-based nanofibers with efficient air filtration and improved moisture stability, Chemical Engineering Journal. 396 (2020) 125373. https://doi.org/10.1016/j.cej.2020.125373.

[25] X. Yang, Y. Pu, Y. Zhang, X. Liu, J. Li, D. Yuan, X. Ning, Multifunctional composite membrane based on BaTiO3@PU/PSA nanofibers for high-efficiency PM2.5 removal, Journal of Hazardous Materials. 391 (2020) 122254. https://doi.org/10.1016/j.jhazmat.2020.122254.

[26] U.Y. Karatepe, T. Ozdemir, Improving mechanical and antibacterial properties of PMMA via polyblend electrospinning with silk fibroin and polyethyleneimine towards dental applications, Bioactive Materials. 5 (2020) 510–515. https://doi.org/10.1016/j.bioactmat.2020.04.005.

[27] S.J. Kim, B.M. Hong, W.H. Park, The effects of chitin/chitosan nanowhiskers on the thermal, mechanical and dye adsorption properties of electrospun PVA nanofibrous membranes, Cellulose. 27 (2020) 5771–5783. https://doi.org/10.1007/s10570-020-03191-w.

[28] B. Li, F. Xiong, B. Yao, Q. Du, J. Cao, J. Qu, W. Feng, H. Yuan, Preparation and characterization of antibacterial dopamine-functionalized reduced graphene oxide/PLLA composite nanofibers, RSC Advances. (2020). https://doi.org/10.1039/d0ra03224g.

[29] F. Tuğcu-Demiröz, S. Saar, S. Tort, F. Acartürk, Electrospun metronidazole-loaded nanofibers for vaginal drug delivery, Drug Development and Industrial Pharmacy. 46 (2020) 1015–1025. https://doi.org/10.1080/03639045.2020.1767125.

[30] S. Tiwari, A. Gaur, C. Kumar, P. Maiti, Electrospun hybrid nanofibers of poly(vinylidene fluoride) and functionalized graphene oxide as a piezoelectric energy harvester, Sustainable Energy and Fuels. 4 (2020) 2469–2479. https://doi.org/10.1039/d0se00033g.

[31] M. Mushtaq, M. Wasim, M.A. Naeem, M.R. Khan, S. Yue, H. Saba, T. Hussain, M.Q. Siddiqui, A. Farooq, Q. Wei, Composite of PLA nanofiber and hexadecyl trimethyl-ammonium chloride-modified montmorillonite clay: Fabrication and morphology, Coatings. 10 (2020) 484. https://doi.org/10.3390/COATINGS10050484.

[32] A. Góra, L. Tian, S. Ramakrishna, S. Mukherjee, Design of novel perovskite-based polymeric poly(L-lactide-co-glycolide) nanofibers with anti-microbial properties for tissue engineering, Nanomaterials. 10 (2020) 1–19. https://doi.org/10.3390/nano10061127.

[33] H. Gallah, F. Mighri, A. Ajji, J. Bandyopadhyay, Flexible electrospun PET/TiO2 nanofibrous structures: Morphology, thermal and mechanical properties, Polymers for Advanced Technologies. (2020). https://doi.org/10.1002/pat.4890.

[34] D. Chuan, R. Fan, Y. Wang, Y. Ren, C. Wang, Y. Du, L. Zhou, J. Yu, Y. Gu, H. Chen, G. Guo, Stereocomplex poly(lactic acid)-based composite nanofiber membranes with highly dispersed hydroxyapatite for potential bone tissue engineering, Composites Science and Technology. 192 (2020) 108107. https://doi.org/10.1016/j.compscitech.2020.108107.

[35] S. An, H.S. Jo, G. Li, E. Samuel, S.S. Yoon, A.L. Yarin, Sustainable Nanotextured Wave Energy Harvester Based on Ferroelectric Fatigue-Free and Flexoelectricity-Enhanced Piezoelectric P(VDF-TrFE) Nanofibers with BaSrTiO3 Nanoparticles, Advanced Functional Materials. 30 (2020) 2001150. https://doi.org/10.1002/adfm.202001150.

[36] S. Hu, J. Wu, Z. Cui, J. Si, Q. Wang, X. Peng, Study on the mechanical and thermal properties of polylactic acid/hydroxyapatite@polydopamine composite nanofibers for tissue engineering, Journal of Applied Polymer Science. (2020). https://doi.org/10.1002/app.49077.

[37] E. Maccaferri, L. Mazzocchetti, T. Benelli, T.M. Brugo, A. Zucchelli, L. Giorgini, Rubbery nanofibers by co-electrospinning of almost immiscible NBR and PCL blends, Materials and Design. (2020). https://doi.org/10.1016/j.matdes.2019.108210.

[38] M. Gazzano, C. Gualandi, A. Zucchelli, T. Sui, A.M. Korsunsky, C. Reinhard, M.L. Focarete, Structure-morphology correlation in electrospun fibers of semicrystalline

polymers by simultaneous synchrotron SAXS-WAXD, Polymer. 63 (2015) 154–163. https://doi.org/10.1016/j.polymer.2015.03.002.

[39]   O. Kallmes, H. Corte, The Structure of Paper - The statistical geometry of an ideal two dimensional fiber network, Tappi Journal. 43 (1960) 737–752.

[40]   R.E. Miles, RANDOM POLYGONS DETERMINED BY RANDOM LINES IN A PLANE, II, Proceedings of the National Academy of Sciences. 52 (1964) 1157–1160. https://doi.org/10.1073/pnas.52.5.1157.

[41]   S.J. Eichhorn, W.W. Sampson, Relationships between specific surface area and pore size in electrospun polymer fibre networks, Journal of the Royal Society Interface. 7 (2010) 641–649. https://doi.org/10.1098/rsif.2009.0374.

[42]   P. Chavoshnejad, M.J. Razavi, Effect of the Interfiber Bonding on the Mechanical Behavior of Electrospun Fibrous Mats, Scientific Reports. 10 (2020) 1–10. https://doi.org/10.1038/s41598-020-64735-5.

[43]   X. Zhang, X. Yang, G.G. Chase, Filtration performance of electrospun acrylonitrile-butadiene elastic fiber mats in solid aerosol filtration, Separation and Purification Technology. 186 (2017) 96–105. https://doi.org/10.1016/j.seppur.2017.06.002.

[44]   T. Tanimoto, A new vibration damping CFRP material with interlayers of dispersed piezoelectric ceramic particles, Composites Science and Technology. 67 (2007) 213–221. https://doi.org/10.1016/j.compscitech.2006.08.022.

[45]   K. Molnar, L.M. Vas, T. Czigany, Determination of tensile strength of electrospun single nanofibers through modeling tensile behavior of the nanofibrous mat, in: Composites Part B: Engineering, Elsevier Ltd, 2012: pp. 15–21. https://doi.org/10.1016/j.compositesb.2011.04.024.

[46]   W. Li, Y. Zong, Q. Liu, Y. Sun, Z. Li, H. Wang, Z. Li, A highly stretchable and biodegradable superamphiphobic fluorinated polycaprolactone nanofibrous membrane for antifouling, Progress in Organic Coatings. 147 (2020) 105776. https://doi.org/10.1016/j.porgcoat.2020.105776.

[47]   M. Inoue, Studies on crystallization of high polymers by differential thermal analysis, Journal of Polymer Science Part A: General Papers. (1963). https://doi.org/10.1002/pol.1963.100010813.

From nano to macroscale modelling of a nano-vascularized epoxy resin

Davide Cocchi[1], Alessandro Pirondi[2], Marco Boi[3], Gabriela Graziani[3],

Nicola Baldini[3,4,5], Andrea Zucchelli[1]

[1]Dipartimento di Ingegneria Industriale, Alma Mater Studiorum - Università di Bologna

viale del Risorgimento 2, 40136 Bologna, Italy

[2]Dipartimento di Ingegneria e Architettura - Università di Parma

Parco Area delle Scienze 181/A, 43124 Parma, Italy

[3]IRCSS Istituto Ortopedico Rizzoli - Laboratory of NanoBiotechnology

via di Barbiano 1/10, 40136 Bologna, Italy

[4]Dipertimento di Scienze Biomediche e Neuromotorie, Alma Mater Studiorum - Università di Bologna

via Massarenti, 9 - Pad. 11, 40138 Bologna, Italy

[5]IRCCS Istituto Ortopedico Rizzoli - Biomedical Sciences and Technology

via di Barbiano 1/10, 40136 Bologna, Italy

The candidate is the main investigator of this multiscale analysis. He contributes to the conception and design of the study, data acquisition and analysis, and manuscript drafting. The work will be published shortly.

2.1 Abstract

Nano-vascularization is increasingly adopted in many research and industrial fields, in particular in biomedicine and orthopaedics, where it can be applied for the biofabrication of scaffolds for bone, cartilage, tendon, and ligament regeneration and for the design of 3D models for the study of bone disease and drug screening. In addition, it is largely used for the development of self-healing composite materials, able to hinder crack propagation in polymeric matrices through the use of vascular core-shell nanofibers containing low viscosity liquid healing agents. In this context, to take full advantage of nano-vascularized materials it is necessary to develop models capable of predicting and explaining their

mechanical behaviour at the macroscale, which in turn requires to understand the characteristic phenomena at each length-scale (nano-, micro-, macro-), through a multiscale modelling strategy.

In this study, a multiscale modelling approach has been proposed to evaluate and predict the effect of the nano-vascularization – obtained by sacrificial nanofibers – on the macroscale mechanical properties of an epoxy matrix. Nanochannels were produced using water-soluble Pullulan electrospun nanofibers. Tensile, three-point bending (3PB), and nanoindentation experimental tests were carried out to evaluate the mechanical properties of the neat epoxy resin and so to implement the extended Drucker-Prager (EDP) yield criterion to simulate the different tension-compression behaviour of the epoxy matrix. Three Representative Volume Elements (RVEs) of the nano-vascularized system were realized and tested to obtain the mesoscale mechanical properties, allowing the adoption of the EDP model again to define the characteristic parameters also for the nano-vascularized system. The latter was finally adopted to simulate tensile and 3PB numerical models, validating the RVE approach against experimental tests on nano-vascularized samples. The fracture surfaces of both 3PB and tensile specimens were analysed at the SEM and compared to RVEs simulations to understand the actual failure mechanisms.

Keywords: nano-vascularization; nanofibers; nano-composite; multiscale modelling; RVE; self-healing

2.2   Introduction

Epoxy resins are high-performance thermosetting polymers widely adopted in several industrial fields, mainly as matrices of Fiber Reinforced Plastic (FRP) composite materials and as adhesives. Compared to other thermosets, epoxies exhibit excellent engineering properties, like high modulus and strength, low creep, and good thermal and dimensional stability. However, due to their highly crosslinked structure, epoxies have inherently low toughness and reduced resistance to impacts, making them brittle and scarcely resistant to crack initiation and growth [1]. The attainment of both strength and toughness is fundamental for most structural materials, but these properties are generally mutually exclusive and so compromises are necessary [2,3]. Bone and nacre are typical examples of damage-tolerant natural materials that efficiently combine strength and toughness [4–8]. For example, the human bone is a natural composite that can be assimilated to a fiber-reinforced ceramic, as it is constituted by a porous mineral phase (biogenic hydroxyapatite nanocrystals), embedding collagen fibers. Thanks to its organic/inorganic composition and due to a highly organized multiscale hierarchical structure, bone does not show a fragile behaviour (characteristic of ceramics), but can

resist fracture, thanks to complementary intrinsic and extrinsic mechanisms, that include compositional and morphological cues (including haversian channels, that can stop cracks propagation) [6,9]. Just like bone, seashells, including nacre, show a composite organic/inorganic composition, and a hierarchical structure with a high degree of organization from the nano- to the micro- and macro- scale. In these composite materials, intrinsic toughening mechanisms (that promote in situ inherent resistance on fracture propagation ahead the crack tip) and extrinsic shielding mechanisms (that act behind the crack tip to inhibit propagation) operate synergically and simultaneously at different length-scales thanks to an optimized hierarchical architecture at each structural level [2,10]. Mimicking nature's biological materials, it is possible to define hierarchical design strategies for the development of new materials for structural applications demanding combinations of both strength and toughness [3,11].

In this perspective, the improvement of polymers mechanical properties, and in particular toughness, by adding second-phase fillers like dispersed rubber [12–14], inorganic particles [15,16] or thermoplastic polymers [17] is a well-known solution, and has been adopted in the last few decades by researchers and industries worldwide. Through micro- and nano-modification, it is possible to expand the material hierarchical structure and so enhance the polymeric matrix properties with limited filler contents [18]. The reason for the outstanding properties of nano-modified polymers lies in the significant amount of energy dissipated by the several damaging mechanisms taking place at the nanoscale. Specifically, (i) poor adhesion between fillers and matrix creates voids in the material, imposing a tortuous crack propagation [19,20], (ii) reaction between filler and matrix might cause substantial changes in the properties of the interfacial region [21–24], and (iii) the filler can slow crack propagation by pinning, pull-out, bridging, fiber locking and deflecting mechanisms, according to its size and tenacity [25–28].

Among nano-structuring methods, in recent years nanofibers obtained by electrospinning have been increasingly used in FRP laminates [29–32] and structural adhesives bonded joints [33–35] to increase mode I and mode II fracture toughness. In these cases, toughening is achieved both thanks to nanofiber bridging effects and to their inherent toughness and plastic deformation, resulting in crack path deflection and forking towards adjacent non-reinforced interlayers [36]. These nanoscale effects have an impact on every single length-scale, up to the macroscale. In this context, to take full advantage of nano-reinforced composites it is necessary to develop models capable of predicting and explaining the mechanical behaviour at the macroscale, by taking into consideration all the characteristic phenomena that occur at each length-scale, using a multiscale modelling strategy [20,37]. Nowadays, only few multiscale studies have been proposed in the literature to predict the macroscale properties of nanocomposites. In particular, these studies focused on the use of nanoparticles [19,38,39], Carbon

Nanofibers (CNFs) [40], and Carbon Nanotubes (CNTs) [41,42]. To the Authors' best knowledge, to date no studies have been presented about multiscale modelling of thermoplastic nanofibrous reinforced epoxies, that evaluate the effect of the nanofibers on the hosting polymeric matrix.

In this work, an attempt was made to simplify the problem, by evaluating how the mechanisms related to the presence of cavities generated by nanofibers can affect the mechanical properties at the macroscale through the different length-scales, and by separating these effects from those related to the presence of nanofibers themselves. To this purpose, both virgin (not nano-structured) and random nano-vascularized systems were manufactured by a structural epoxy resin, following the Authors' pioneering work on the production of nano-vascularized materials through sacrificial nanofibers [43]. A Representative Volume Element (RVE) model of the nano-vascularized matrix was developed, allowing the validation of the presented multiscale approach against experimental tests. Although it has been proved that nano-structuring increases fracture toughness, Torre-Muruzabal *et al.* [44], following the same production method proposed by the Authors [43], proved that the nano-vascularization of an epoxy resin leads to a reduction in both flexural modulus and strength. Although useful for a direct comparison, their study lacks a complete mechanical characterization and a multiscale modelling that enables to interpret and predict the mechanical properties through the different dimensional scales.

In the present study, to manufacture the random nano-vascularized specimens, water-soluble natural polysaccharide Pullulan was electrospun seamlessly to obtain a thick nanofibrous mat. A random nanofiber arrangement has been chosen, as it is that most commonly adopted for nano-reinforcing and when the delamination direction is not known a priori. The nanomat was then impregnated and integrated into the epoxy resin and vacuum cured in autoclave. Once cured and milled, both the virgin and nano-structured samples were immersed in deionized water to dissolve the Pullulan nanofibers, thus generating the nanochannels.

Experimental tensile and three-point bending (3PB) tests were carried out on both neat epoxy resin and nano-vascularized samples. A reduced tensile specimen was developed to evaluate the mechanical properties of the material as close as possible to those of the nanoscale, and a 2D Digital Image Correlation (DIC) system was adopted to evaluate the strain field. 3PB tests were performed to check for possible asymmetry of the stress-strain behaviour in compression. Moreover, nanoindentation tests on the virgin system were executed to obtain the most accurate information on the nanoscale mechanical properties to be implemented in the RVE.

The pressure-dependent extended Drucker-Prager (EDP) yield criterion was adopted to model the mechanical behaviour of the neat epoxy resin to be imported into the nano-vascularized RVE. The experimental curves obtained for the virgin system were used as targets to optimize the parameters of the EDP model by means of Finite Element Model (FEM) simulations. The nano-

vascularized RVE was realized by means of a Computer-Aided Design (CAD) software starting from the analysis of several random Pullulan nanomat images observed under a Scanning Electron Microscope (SEM). To guarantee a statistical value to the results, three RVEs were extrapolated. For each RVE, tensile and compressive FEM simulations were performed using periodic boundary conditions. The element death capability was employed to simulate the crack initiation and propagation in the most stressed areas. These simulations allowed to evaluate the mesoscale mechanical properties of the nano-vascularized material and to interpret the results considering the geometric features of each RVE. This approach enabled the use of the EDP model again to define the characteristic parameters also for the nano-vascularized system. The latter was finally adopted to simulate tensile and 3PB numerical models, validating the RVE approach against experiments on nano-vascularized samples. The fracture surfaces of both 3PB and tensile specimens were analysed at the SEM to also understand the actual failure mechanisms.

This multiscale study opens to the development of a new approach that allows predicting the macroscale mechanical properties of nanocomposite starting from the nanoscale. Future studies will focus on the development of multiscale models that integrate the effect of nanofibers and their extrinsic toughening mechanisms in epoxy nano-reinforced composites. Moreover, this method is particularly helpful for the improvement of tissue engineering applications [45,46], such as bone [47,48], cartilage [48], tendon and ligaments [49] substitutes, 3D models for disease study and drug screening and for the design of self-healing materials, which use a network of nano-vascular core-shell nanofibers containing low viscosity liquid healing agents to hinder the crack propagation [44,50].

2.3 Materials and methods

2.3.1 Materials

Pullulan (η= 15.0 ÷ 180.0 mPas, 10 % in H_2O at 30 °C) was purchased by TCI Europe. Two-component epoxy resin Elan-tech® EC152 / W152MR was supplied by ELANTAS (ELANTAS Europe s.r.l., Collecchio (PR), Italy).

2.3.2 Specimens production

2.3.2.1 Nanofibrous mat production

To manufacture the nano-vascularized samples, a Pullulan nanofibrous mat was produced by electrospinning process. Following a previous pioneering work by the Authors [43], Pullulan was

selected, because it is a water-soluble polysaccharide polymer that can be easily dissolved to obtain the nanochannels constituting the nano-vascularized matrix. Moreover, Pullulan nanofibers can maintain their morphology in a wide temperature range, up to 250 °C, allowing compatibility with the curing of epoxy matrix composites.

Pullulan solution for the electrospinning process was obtained dissolving the polymer into MilliQ water at a concentration of 28 %w/v. The electrospun non-woven mat was produced using a Spinbow® electrospinning machine unit (Spinbow s.r.l, Bologna, Italy), equipped with a single stainless-steel needle connected with the power supply electrode (Figure 2.1A). The fibers were collected on a 100 mm diameter round grounded plate. A random nanofibers distribution was chosen since it is notoriously the most adopted for nano-reinforcing and when the delamination direction is not known a priori. The nanofibrous mat was electrospun seamlessly until a total thickness of about 4 mm was obtained. The mat thickness was evaluated by means of a digital indicator (ALPA, Pontoglio (BS), Italy).

(A)   (B)
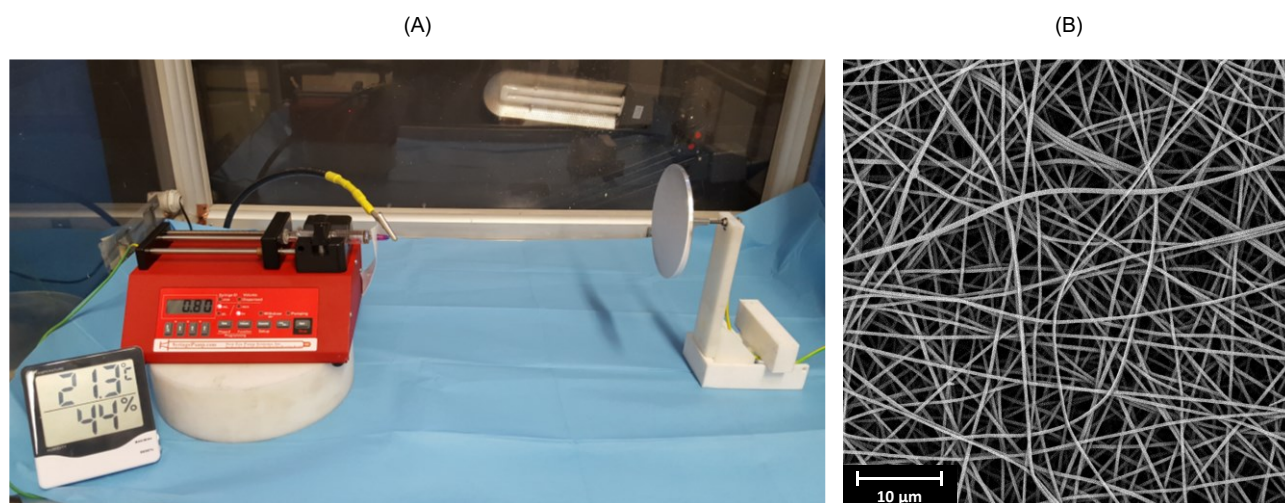
Figure 2.1 – (A) Electrospinning set-up and (B) SEM image of the Pullulan nanofibrous mat (at 5,000x magnification).

Table 2.1 – Electrospinning process parameters, nanofibers diameter and maximum mat thickness.

Pullulan concentration	Flow rate	Electric potential	Distance	Electric field[a]	Temperature	Relative humidity	Nanofibers diameter[b]	Max. mat thickness
%w/v	mL/h	kV	cm	kV/cm	°C	%	nm	μm
28	0.70	25.5	24.0	1.1	20-22	40-45	421 ± 52	~4200

[a] calculated as electric potential to distance ratio

[b] average values derived from at least 100 diameter measurements on SEM micrographs

In Table 2.1 the electrospinning process parameters and environmental conditions are reported. The non-woven nanomat was analysed by SEM (Phenom ProX) to determine nanofibers morphology,

after gold sputtering. SEM image is shown in Figure 2.1B. Nanofibers diameter (D_{nf}), given as the average diameter ± standard deviation, is reported in Table 2.1.

2.3.2.2 Impregnation and curing

The epoxy resin used for both virgin and nano-vascularized samples is a two-component system with relatively low viscosity (400÷600 mPas), to facilitate the nanomat impregnation and to minimize the entrapment of air bubbles. This problem, commonly known in the impregnation of nanofibrous mats [34,51], was here aggravated by the fact that this Pullulan mat was extremely thick. The epoxy resin was prepared by mixing the pre-polymer and the curing agent at RT at a ratio 100:30 by weight, according to manufacturer instructions. Then the mixture was degassed under vacuum and the Pullulan nanomat was impregnated with the uncured resin. At the end of the impregnation, the nanofibrous prepreg was put on a glass plane and placed into a vacuum bag. Finally, the composite was maintained under vacuum at 40 °C for 24 h, then the temperature was increased up to 60 °C at a heating rate of 10 °C/h, followed by an isotherm at 60 °C for 2 h, according to resin manufacturer. The same curing cycle was performed for the virgin samples. Once cured, both the nano-structured and virgin laminates were milled to obtain tensile, 3PB and nanoindentation specimens.

2.3.2.3 Vascularization

To remove the Pullulan electrospun nanofibers from the nano-structured laminate, the milled specimens were immersed in deionized water for 10 days under stirring. By adding Rhodamine B to the Pullulan electrospinning solution (0.1 %wt), it was possible to electrospun red-coloured nanofibers. By doing so, an evaluation of the dissolution level of nanofibers was possible by visually checking the colour of the aqueous solution in which they were immersed [43]. Finally, the vascularized specimens were oven-dried for 24 h at 40 °C to remove the excess water absorbed by the epoxy matrix. Virgin samples were subjected to the same treatments to take into account the water absorption effects on mechanical properties. During the drying process, the weight of each specimen was monitored over time until it reached a stable value. The SEM images of Figure 2.2 show the cross-sections of a virgin, a nano-reinforced (not vascularized), and a nano-vascularized specimens obtained by nitrogen brittle fracture. By weighing the specimens before and after vascularization (at the end of the drying process) it was possible to evaluate the percentage nanofibers volume for all the specimens, assessed in $V_{nf\%} = 9.6 \% \pm 3.3 \%$.
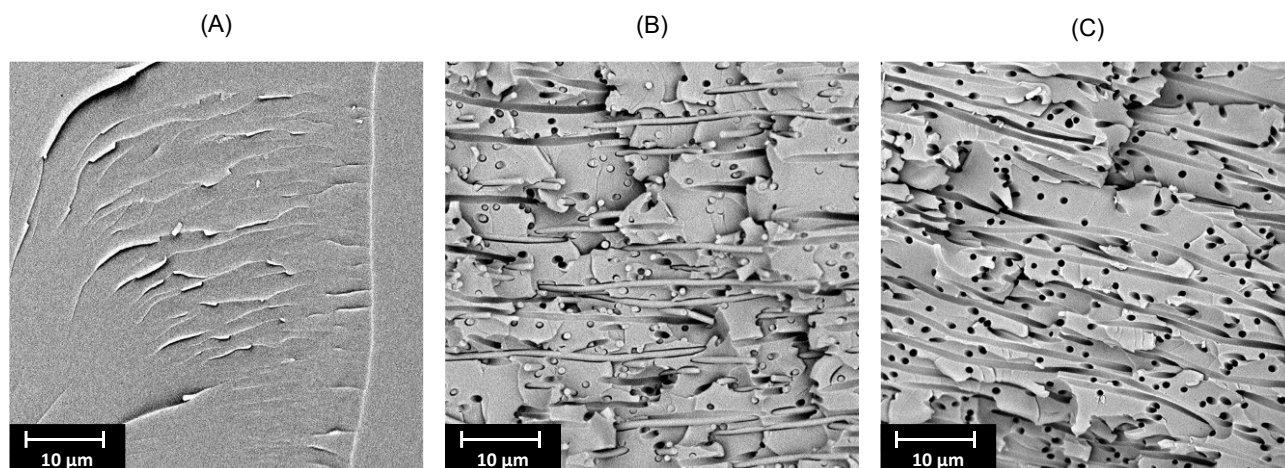
(A)   (B)   (C)

Figure 2.2 – SEM images of the cross-sections obtained by nitrogen brittle fracture of (A) virgin, (B) nano-reinforced, and (C) nano-vascularized specimens.

2.3.3 Experimental tests

2.3.3.1 Tensile and flexural tests

For both virgin and nano-vascularized systems, tensile and 3PB tests were performed to evaluate the mechanical properties at the macroscale. However, to successfully understand the relationships between the different dimensional scales, it is fundamental to evaluate the mechanical properties of the material as close as possible to those at the nanoscale. This is also necessary to import into the RVE, which is here developed, mechanical characteristics as accurate and reliable as possible. In fact, although the mechanical properties might depend only on the material and not on the specimen geometry, this is no longer true when the dimensional scale changes (known as *scale effect*) [52,53]. In particular, Zike *et al.* [54] found that the strain at the crack tip in Double Cantilever Beam (DCB) epoxy bulk specimens can reach values up to 20 %, which are much higher than those typically found at the macroscale. Besides, Odom *et al.* [52] proved that tensile stress failure is also correlated with the specimen size, as it increase as the specimen size decreases. Thus, since the tensile curves are used for the material model characterization, a custom reduced tensile specimen inspired to ASTM D638 (Type V specimen) was developed. The specimen dimensions, shown in Figure 2.3A, were optimized through FEM simulations to minimize the transverse stress components and to reduce the stress concentrations in the fillets [55]. The samples were produced making sure that the loading direction was in the nanofiber deposition plane. Moreover, customized steel tabs were developed for the specimen holding (Figure 2.3B), inspired by the ASTM E8/E8M loading principle. Moreover, additional tensile tests on few D638 standard virgin specimens were carried out to confirm the data of the bulk epoxy resin datasheet.
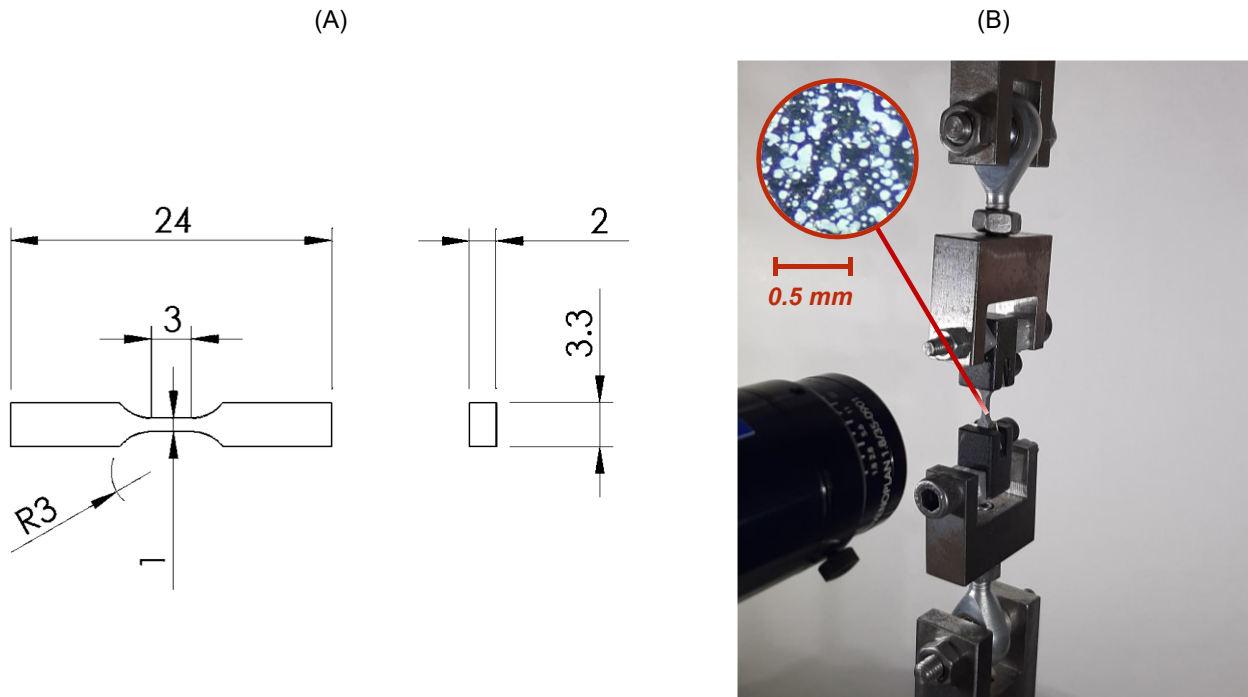
Figure 2.3 – (A) Custom tensile specimen dimensions (in mm) and (B) tensile test set-up with the 2D DIC system.

Tensile tests were performed at RT on an Instron universal testing machine series 5966, equipped with a 1 kN load cell, at a crosshead separation speed of 0.5 mm/min. The strain distribution was assessed during the tests using a 2D DIC system (Q-400, Dantec Dynamics), equipped with a 5 Megapixels camera and a high-quality metrology standard 17 mm lens (Apo-Xenoplan, Schneider-Kreuznach, Germany) with a 12 mm extension tube. A white spackle pattern on a black background was previously applied to both virgin and nano-vascularized samples by means of an airbrush (Figure 2.3B). Istra-4D software (Dantec Dynamics) was employed to capture the images, while GOM Correlate software (GOM, Braunschweig, Germany) was used to elaborate the images and to calculate the strain field. Facet size and grid spacing were set to 21 and 19 pixels, respectively.

3PB samples, instead, were simply scaled down respect to nominal dimensions given by ASTM D790. 3PB tests were performed to check for possible asymmetry of the stress-strain behaviour in compression. The dimensions of the flexural specimens were $40 \times 5 \times 2$ mm (length × width × depth) for both virgin and nano-vascularized systems. The samples were manufactured to ensure that the testing load was perpendicular to the nanofiber deposition plane. The 3PB tests were performed at RT at a crosshead speed of 1.5 mm/min, with a 14:1 support span-to-depth ratio.

Overall, 7 tensile specimens and 5 flexural specimens were tested for the virgin system (called V), i.e. for the neat epoxy resin. Instead, regarding the nano-vascularized system (called VP), 7 tensile specimens and 3 flexural specimens were tested. Stress-strain data of nano-vascularized specimens were corrected to consider the air bubbles entrapped by the impregnation process, by performing an image analysis of the fracture cross-section areas of the tested specimens. The Chauvenet's criterion

was applied to the data to assess the presence of any outliers. Moreover, 3 virgin tensile standard specimens, manufactured according to ASTM D638, were tested to check the neat epoxy datasheet information.

Tensile and flexural stress-strain curves of the virgin system were adopted, together with nanoindentation experimental results, to define and optimize the extended Drucker-Prager material model parameters, to be imported into the nano-vascularized RVE numerical model. Instead, tensile and 3PB stress-strain curves of nano-vascularized system were adopted to validate the RVE model against experimental data.

2.3.3.2 Nanoindentation tests

In addition to tensile and bending tests, nanoindentation tests were carried out to characterize the properties of the virgin epoxy system on a dimensional scale as close as possible to that of the RVE. The nanoindentation test is increasingly used for the characterization of polymeric materials [56], nanostructured composites [57–60], biocomposite scaffolds [61], and thin films for biomedical applications [62–64]. To characterize and model the epoxy also in compression, simple uniaxial compressive tests could have been carried out. However, compression specimens produced according to ASTM D695 would have been too large to be adopted for a mesoscale analysis. The dimensional scale involved by the nanoindentation test, instead, is a few tens of microns. In addition, the triaxial stress state generated by the nanoindentation [65] allowed to interpret and, therefore, to model the material characteristics in the most reliable way.

Nanoindentation tests were performed on virgin samples using the Nanoindentation Tester NHT^2 (CSM, Peseux, Switzerland) under load-controlled conditions. A spheroconical diamond tip with a radius of 100 μm and a cone angle of 90° was used. This type of tip was adopted as it allows reconstructing the stress-strain curve, with the advantage of increasing the strain for increasing load, moving from elastic to plastic regime, without excessively deforming the surface of the material at low load values [56,65–67].

A Continuous Multi Cycle (CMC) protocol was used to evaluate the nanoindentation elastic modulus (*E*) profile of the material as a function of the penetration depth. *E* was calculated using Oliver and Pharr (OP) method [68], through a linear fitting of the unloading curve, by assuming a purely elastic material response during unloading. To limit the contribution of the time-dependent component of the mechanical behaviour of epoxy resin, a rapid unloading rate and an extended creep time were used, which is recommended when applying the OP model to viscoelastic materials [69]. Specifically, a 300 mN maximum force was applied to the indenter. Load and unload were ramped

in 10 s, whereas in between the force was held constant for 600 s to limit viscous effects, as experimentally assessed. Moreover, loading-unloading tests without considering creep time (ramped in 10 s) were carried out to qualitatively compare the force-depth curves with those of FEM simulations, to validate the virgin material model for the RVE. This approach was adopted because creep was not implemented in the extended Drucker-Prager model here adopted, since it is not a fundamental effect for the purposes of this study. Three virgin samples were prepared and polished to obtain a reduced roughness and parallel surfaces for the nanoindentation test. A set of 10 CMC nanoindentation and 3 loading-unloading tests were performed on each sample.

2.3.4 Finite Element Analysis

2.3.4.1 *Numerical models for tensile, flexural and nanoindentation tests analysis*

To define the parameters of the epoxy resin EDP model to be introduced in the nano-vascularized RVE Finite Element Analysis (FEA), tensile, bending, and nanoindentation numerical simulations were carried out to find the fitting with the experimental data of the virgin samples.

For this purpose, 3D models with the same dimensions as the experimental specimens were developed for tensile and bending simulations. To simulate the nanoindentation, instead, a two-dimensional axisymmetric model was defined, to reduce computational time without loss of accuracy [64,70,71]. Simulations were performed using the commercial FEA software Ansys Workbench (Ansys, Inc., Canonsburg, PA, USA).

The tensile model, whose geometry is shown in Figure 2.4A, was meshed with higher-order 20-node hexahedral elements (SOLID186). A mapped mesh was applied, and a convergence criterion with different mesh grades was adopted. The element size, equal to 0.1 mm in the gauge length, was gradually increased until 0.5 mm in the holding regions (Figure 2.4D). The tensile model, consisting of 77,373 nodes, was simulated under displacement control.

The 3PB model consisted of the specimen, the two supporting pins, and the loading nose (Figure 2.4B). The pins and the nose were modelled as rigid bodies, and a frictionless contact was supposed between parts. In this case too, SOLID186 elements and a mapped mesh were adopted to model the beam. After a convergence analysis, an average element size of 0.2 mm was adopted (Figure 2.4E). The 3PB model consisted of 225,881 nodes and was simulated controlling the displacement of the loading nose.
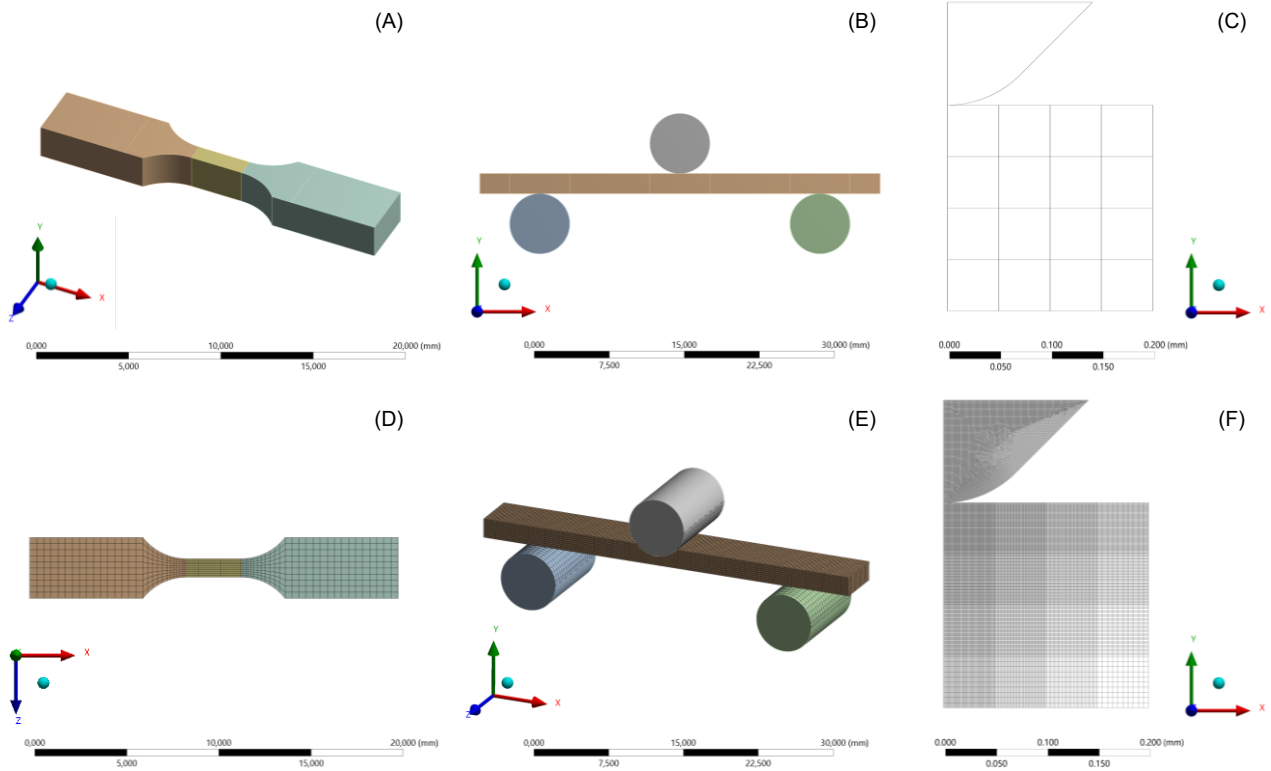
Figure 2.4 – Geometries for the (A) tensile, (B) 3PB, and (C) nanoindentation numerical simulations. Mesh detail of the (D) tensile, (E) 3PB, and (F) nanoindentation models.

For both tensile and 3PB numerical model, to simulate the material bearing strength reduction and the damage evolution a custom script was written to implement the element death capability trough the EKILL function. This function allows deactivating an element when it reaches a specified limit value, leaving it within the model but contributing to a near-zero stiffness [72]. Here, it was imposed that the element deactivates when the total equivalent strain (EPTO,EQV) exceeds the value of the true strain at break (ε_{break}), that was experimentally measured. The numerical tensile and 3PB stress-strain curves were used to find the fitting with the experimental ones to optimize the parameters of the extended Drucker-Prager model.

The 2D axisymmetric nanoindentation model was defined in the *Oxy* coordinate system, with the symmetry axis along the *y* direction (Figure 2.4C). The specimen was modelled as a 200 × 200 μm square, while the indenter was shaped as a moving half diamond spheroconical tip (as described above for the experimental tests), with a Young's modulus of 1140 GPa and a Poisson's ratio of 0.07. No displacement in *x* direction was allowed for the axis of symmetry, and the bottom side of the specimen was kept fixed along *y* direction. The indenter was allowed to translate only vertically, and the load was applied to the indenter in force control [64]. The contact between the indenter tip and the specimen was supposed frictionless [73]. Both the specimen and the indenter were meshed with 2D 8-node quadrilateral elements (PLANE183). A refined mesh, after a convergence evaluation, was

adopted in the contact region, with an element size of 0.5 × 0.5 µm². A gradually larger mesh was used for the farther regions, up to 5 × 5 µm² elements on the edges. The nanoindentation model consisted of 255,090 nodes (Figure 2.4F). During the nanoindentation simulation, both loading and unloading were investigated. The force-indenter depth numerical curves were used to find the fitting with the experimental ones and to optimize the parameters of the EDP model of the virgin system.

All the static analyses were solved by a direct method, under large strain conditions. All geometries and meshes are shown in Figure 2.4.

2.3.4.2 Material models

The experimental results on virgin samples were used to define the neat epoxy model parameters to be used for the numerical simulations, finding the fitting on the experimental curves. The epoxy resin behaviour under the different stress states was fitted with a plasticity law based on the pressure-dependent extended Drucker-Prager yield criterion (EDP). The classic Drucker-Prager model [74,75], often used to model the mechanical behaviour of epoxies [76–79], is a modification of the Von Mises yield criterion, using different tensile and compressive yield stresses and including an additional term dependent on the hydrostatic stress component. The extended criterion, used in this study, allows to change the yield surface with progressive yielding, allowing isotropic hardening [72,80,81]. The EDP yield function in the linear form is given by [72,82]:

$$F = t + \sigma_m \ tan \ \beta - d \qquad \qquad \text{Eq. 2.1}$$

where *t* is given by:

$$t = \frac{1}{2} q \left[1 + \frac{1}{K} - \left(1 - \frac{1}{K} \right) \left(\frac{r}{q} \right)^3 \right] \qquad \qquad \text{Eq. 2.2}$$

in which *q* is the deviatoric Cauchy stress tensor, defined as a function of the second deviatoric stress invariant ($q = \sqrt{3 \, J_2}$), *K* is the ratio between the yield stress in triaxial compression and triaxial tension, and *r* depends on the third deviatoric stress invariant ($r^3 = 27/2 \ J_3$). Moreover, σ_m is the hydrostatic stress component ($\sigma_m = 1/3 \ (\sigma_1 + \sigma_2 + \sigma_3)$), *d* is the material cohesion, and $tan \ \beta$ is the pressure sensitivity parameter, *β* being the friction angle (i.e. the cone angle in the meridional plane). Due to the lack of experimental triaxial data, the parameters *K* and *tanβ* were defined by matching the yield function of the EDP criterion with the Mohr-Coulomb (MC) one [77,82,83]. If the EDP yield surface circumscribes the MC one, the expressions for *K* and *tanβ* are:

$$K = \frac{3 - sin\,\varphi}{3 + sin\,\varphi} \qquad\qquad \text{Eq. 2.3}$$

$$tan\,\beta = \frac{3 - sin\,\varphi}{3 + sin\,\varphi} \qquad\qquad \text{Eq. 2.4}$$

where φ is the angle of internal friction in the MC model ($\varphi \neq \beta$). Moreover, the MC criterion allows to express the tensile and compressive uniaxial strengths as a function of the parameter φ, obtaining $\sigma_t = 2\,c\,cos\,\varphi\,/(1 + sin\,\varphi)$ in tension and $\sigma_c = 2\,c\,cos\,\varphi\,/(1 - sin\,\varphi)$ in compression, where c is the cohesion parameter in the MC model ($c \neq d$). Relating the uniaxial strengths in compression and in tension by means of the uniaxial stress ratio m defined at an arbitrary uniaxial plastic deformation p:

$$m = \left|\frac{\sigma_c}{\sigma_t}\right|_p \qquad\qquad \text{Eq. 2.5}$$

it is possible to express the angle of internal friction φ as $sin\varphi = (m - 1)/(m + 1)$. Replacing the last relationship within the Equation 2.3 and Equation 2.4, K and *tanβ* can be expressed as follows:

$$K = \frac{m + 2}{2m + 1} \qquad\qquad \text{Eq. 2.6}$$

$$tan\,\beta = \frac{3(m - 1)}{m + 2} \qquad\qquad \text{Eq. 2.7}$$

In this way it is possible to express these two parameters only as a function of the uniaxial tensile and compressive strengths. Since no compression tests were carried out, the uniaxial compression strength given in the epoxy supplier datasheet was used as a first attempt for the calculation of the EDP model parameters, which were then optimized by fitting the experimental tensile, bending, and nanoindentation curves.

The material cohesion d, which defines the onset of the plastic deformation, can be expressed as a function of the uniaxial tension yield stress as follows [82]:

$$d = \left(\frac{1}{K} + \frac{1}{3}tan\beta\right)\sigma_t \qquad\qquad \text{Eq. 2.8}$$

Besides the definition of the yield surface, yield is described by a plastic flow rule. For simplicity sake, the flow plastic potential function was assumed to be the same as the yield function and its parameters were set equal to the yield criterion. This means that the dilatation angle ψ of the plastic

flow rule (i.e. the increase in material volume due to yielding) is set equal to the friction angle β of the yield function, resulting in an associated flow rule [72,76,84]. This way, plastic straining occurs in a direction normal to the yield surface, that in turn causes a volumetric expansion of the material.

Finally, to completely define the elasto-plastic behaviour of the material, the hardening rule must be defined, which models the change of the yield criterion with evolving plastic strains. The multilinear isotropic hardening behaviour was taken from experimental uniaxial tensile tests, since the linear EDP model does not allow the dependence of the hardening rule on the stress-state [72,78,82]. To this end, the stress-strain tensile data were converted into true stress-true strain since the maximum strain values for the neat epoxy were particularly high. It was not necessary to use a fitting model (e.g., Ramberg-Osgood model), as the strain values are high enough to create a horizontal plateau up to failure strain. Finally, the so obtained average curve was extrapolated to higher failure strains, considering that the epoxy shows a higher strain to failure in the microscale tests, compared to the macroscale ones.

Thus, the elasto-plastic behaviour of the neat epoxy is characterized by the elastic modulus E and the Poisson's ratio ν of the virgin system (assuming an isotropic behaviour) and by the three parameters $tan\,\beta$, K, and d, as a function of the uniaxial stress ratio m. Thus, the optimized EDP model obtained for the virgin system was imported into the RVEs to characterize the nano-vascularized system.

Then, the EDP criterion was adopted again to fit the data obtained from the RVEs analyses, to also define a material model characteristic of the nano-vascularized system. The latter was used to perform tensile and 3PB FEM simulations, again assuming the behaviour isotropic. The simulation results were compared with the experimental stress-strain curves to validate the RVE approach here presented.

2.3.4.3 *Nano-vascularized RVE numerical model*

To study the effect of the nanochannels on the mechanical properties of the construct, a 3D Representative Volume Element (RVE) approach was adopted. An RVE is the smallest material volume element statistically representative of the overall microstructure, morphology, and macroscopic constitutive response of the bulk material [35,85–87]. The use of an RVE, with its multiscale approach, allows understanding the impact of microscale physics and mechanical phenomena at the macroscale. This approach can be adopted here because (i) the morphology is periodic inside the nano-vascularized samples and (ii) the nanofibers distribution within the epoxy matrix is random.

In literature, there are several methods to create virtual geometries of non-woven nanofibrous mats [88,89]. Among these, GeoDict software (Math2Market GmbH, Kaiserslautern, Germany) allows to model and simulate the microscale mechanical properties of 3D RVEs through morphological and physical parameters provided by the user or derived from μCT scans [90,91]. However, this software has some limitations in the modelling of both geometry and material, as for instance it does not allow the implementation of the asymmetric traction/compression behaviour provided by the EDP criterion. Instead, Domaschke *et al.* proposed a numerical framework for the development of nanofibrous 3D models through stochastic fiber distribution and subsequent explicit compaction numerical simulation [92]. Although statistically descriptive of the real morphology of the network, this method does not allow to control the compaction of nanofibers through the mat thickness, which may not provide a direct relationship with the real membrane morphology along with all the three directions. Given these limitations, it was therefore preferred to use a manual approach, which, although simplified, would allow obtaining a geometry as similar as possible to the real morphology of our membrane, starting from SEM images and knowing the $V_{nf\%}$ value of the nano-vascularized system.
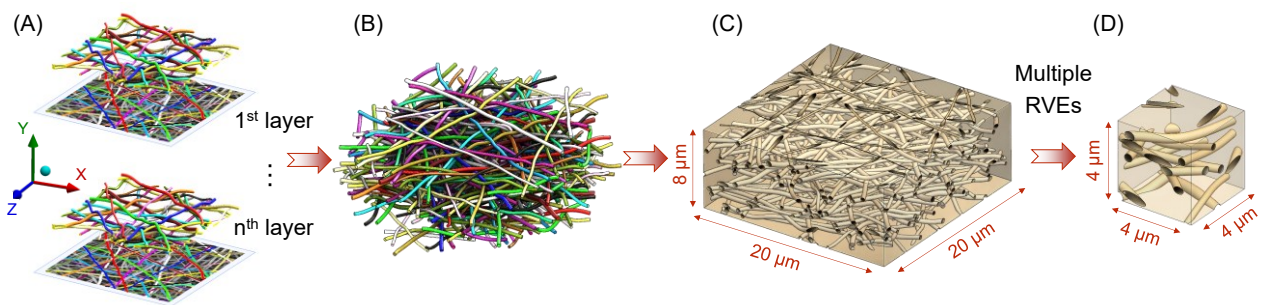

Figure 2.5 – RVEs construction process: (A) layers CAD virtualization starting from several SEM images, (B) layers assembly knowing the $V_{nf\%}$, (C) reference volume with hollow nanochannels obtained through Boolean subtraction operation, and (D) multiple RVEs extrapolation.

The RVE geometry was realized by means of a Computer Aided Design (CAD) software starting from the analysis of the random Pullulan nanomat SEM images. While the nanofibers distribution in the deposition plane is known (*xz* plane in Figure 2.5), only a few information can be derived from the SEM images about the distribution along the *y* axis, as the only information available are those concerning the position and morphology of the crossings between nanofibers in the first visible layers (Figure 2.5A). To obtain a structure that faithfully represents the model also along the *y* axis, the packing level of the nanofibers was adjusted to fit the experimental value of the percentage nanofibers volume ($V_{nf\%}$ = 9.6 %, see Section 2.3.2.3). Repeating the procedure starting from different SEM images and replicating the nanofibrous structure in the space in a random manner, it was possible to assembly the

layers obtaining a virtual thick nanomat (Figure 2.5B). Finally, through a Boolean subtraction operation, a reference volume of $20 \times 20 \times 8$ um^3 with hollow nanochannels was obtained (Figure 2.5C). To guarantee a statistical significance to the results, three cubic RVEs were extrapolated from the reference volume (Figure 2.5D).

The RVE dimensions must be as small as possible both to reduce the computational time and to better represent the geometrical features of the system [93]. Hence, here the dimensions were defined to ensure a ratio of about 10 between the RVE sides (4 µm) and the mean diameter of the electrospun nanofibers (D_{nf} = 421 nm, Table 2.1), providing a significantly representative geometry for the FEA. The three RVEs geometries are reported in Figure 2.6. For each RVE, the percentage nanofibers volume and the mean diameter of the nanofibers were evaluated (Table 2.2).
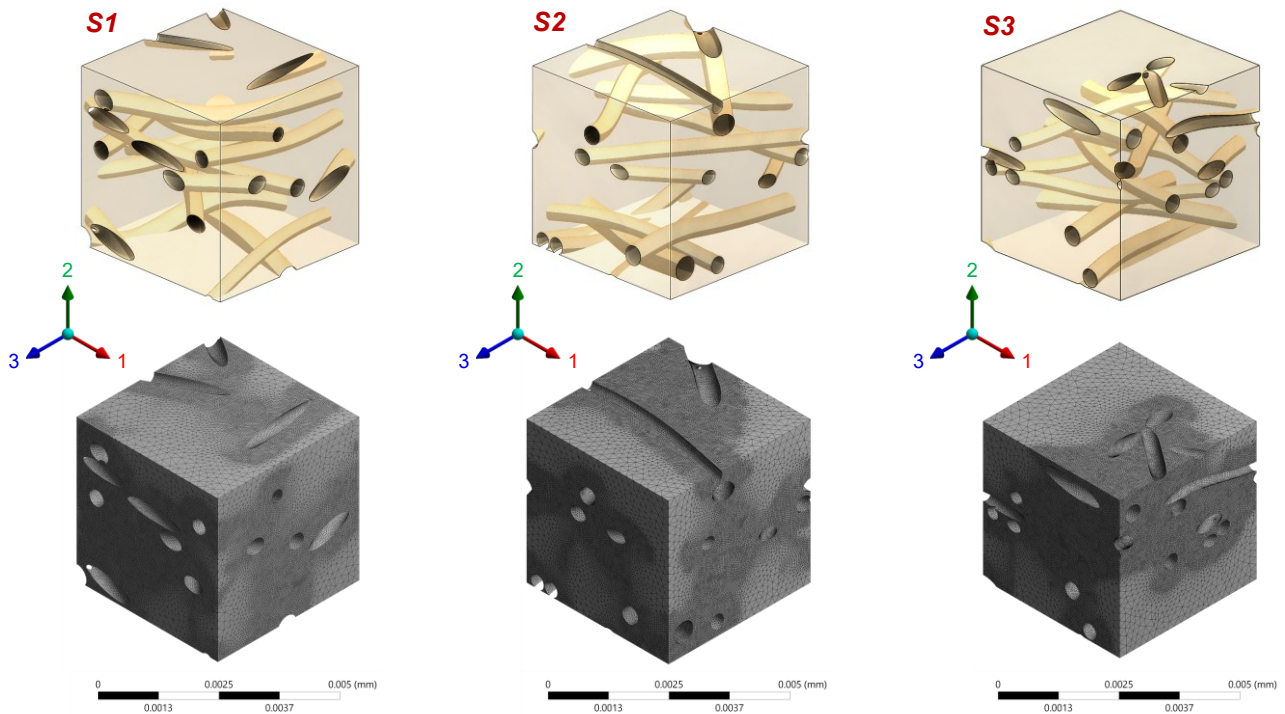
Figure 2.6 – Nano-vascularized RVE geometries and meshes.

The RVEs were meshed with higher-order 10-node tetrahedral elements (SOLID187), ensuring a progressive refinement around the cavities (Figure 2.6). An element size of 0.04 µm was adopted around the nanochannels, while a defeatured mesh with an element size of 0.2 µm was adopted for the farther regions. The mesh was optimized to guarantee at least a ratio of 10 between the element size and the mean diameter of the nanochannels, employing a convergence criterion. The main features of each RVE are reported in Table 2.2.

Table 2.2 – RVEs morphological features and model properties.

RVE	$V_{nf\%}$ %	D_{nf} nm	Nodes	Elements	Element type	DOF
S1	8.5%	382 ± 56	791,592	476,732	SOLID187	2,374,776
S2	8.6%	407 ± 41	744,326	448,007	SOLID187	2,232,978
S3	8.0%	374 ± 51	737,364	445,758	SOLID187	2,212,092

For each RVE, tensile and compressive FEM simulations were performed along all the three reference directions using the EDP material model defined for the virgin system. The RVEs simulations, solved by a direct method and under large strain conditions, were carried out under displacement control using periodic boundary conditions (PBCs). PBCs allow simulating the deformation of the surrounding material, ensuring that the external surfaces of the RVE remain periodic [35]. In this study, the RVE periodicity was represented by imposing boundary conditions that keep the outer surfaces of the RVE planar and parallel to each other during the deformation. This was done employing the Remote Point feature, which allows controlling the degrees of freedom (DOF) of the boundary nodes. The normal displacement of three RVE surfaces perpendicular to each other was constrained to define an orthogonal reference system.

For these simulations as well, the element death capability was employed to simulate the failure of the most stressed areas of the RVEs. The element deactivation condition is always referred to the total equivalent strain. For each simulation, the reaction force and the displacement along the three main directions were recorded as a function of time. These data enable to evaluate the elastic moduli and the Poisson's ratios for the mesoscale nano-vascularized system, as well as the tensile and the compressive yield stresses along each direction. These data were then averaged and used to apply the EDP model again, finding the characteristic parameters of the nano-vascularized system. The EDP model of the nano-vascularized system was finally adopted to simulate tensile and 3PB numerical models, validating the RVE approach against experiments.

2.4 Results and discussion

2.4.1 Experimental results

2.4.1.1 Tensile and flexural tests results

The stress-strain curves of tensile and 3-point bending tests for both virgin (V) and nano-vascularized (VP) systems are reported in Figure 2.7, while the overall comparison of the experimental results is reported in Table 2.3 and Table 2.4.

The main mechanical properties of the virgin system were in good accordance with the data provided by the resin supplier. The DIC analyses on tensile specimens revealed that the strain field varies regularly along the specimen length and it is almost uniform through the specimen width, ensuring the failure of the specimens occurs within the gauge section. It is interesting to note that the stress-strain curves of the virgin tensile specimens show a ductile behaviour (Figure 2.7A), contrary to the typical brittle behaviour of the neat epoxy resins. Tensile tests performed on D638 standard virgin specimens realized with the same resin, in fact, showed a brittle response, with ε_{break} values in good accordance with the datasheet (4.03 % ± 0.72 %). Evidently, the reduced size of the tensile specimens helped to show the plasticity of the neat epoxy. A similar stress-strain trend was found by Littell *et al.* [53], who reached high strain values with reduced size tensile epoxy specimens. This aspect is confirmed by the fact that the tensile strain at break (ε_{break}) and the maximum stress (σ_{max}) values are significantly higher at the mesoscale compared to the macroscale, since the probabilities to find numerous and large flaws are lower in smaller specimens [52,54]. This also influences the elastic modulus [94]. In fact, using smaller specimens, an increase in the elastic modulus was observed compared to standard specimens (3476 ± 82 MPa for the reduced virgin samples respect to 2938 ± 69 MPa for the D638 standard ones). The Poisson's ratio of virgin samples, equal to 0.418, is in good agreement with what was found in literature for other epoxy resins [53,78,95].

Comparing the tensile curves of the virgin system with the nano-vascularized one, it can be observed that the nano-vascularized system loses its ductile characteristic, showing an essentially brittle behaviour. The tensile failure strain is considerably reduced (-57 %) and so is the maximum stress, which drops by 24.6 % and 27.8 % at both tensile and bending, respectively. Concerning the elastic moduli, the nano-vascularized system showed a reduction of 18.1 % in tensile modulus and 21.4 % in flexural modulus, compared to the virgin one. Instead, no significant change was found in Poisson's ratio.
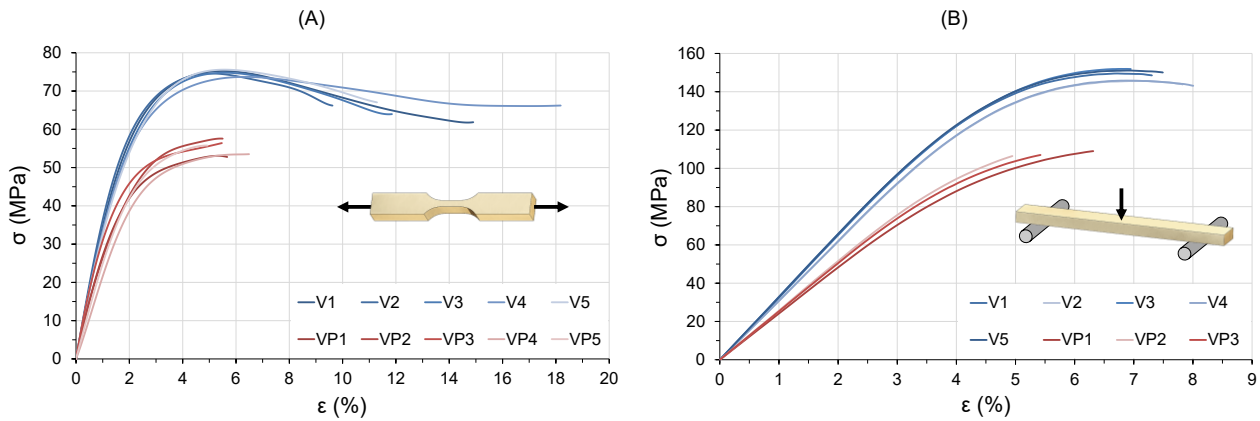
Figure 2.7 – Experimental stress-strain curves of (A) tensile and (B) 3-point bending tests for both virgin (V) and nano-vascularized (VP) systems.

Table 2.3 – Tensile properties of virgin and nano-vascularized systems.

System	E (Mpa)		σ_{max} (MPa)		$\varepsilon_{\sigma max}$ (%)		ε_{break} (%)		ν (-)	
	Mean ± SD	Var (%)	Mean ± SD	Var (%)	Mean ± SD	Var (%)	Mean ± SD	Var (%)	Mean ± SD	Var (%)
Virgin (V)	3476 ± 82	-	75 ± 1	-	5.62 ± 0.45	-	13.17 ± 3.39	-	0.418 ± 0.043	-
Nano-vascularized (VP)	2846 ± 431	-18.1%	56 ± 3	-24.6%	5.56 ± 0.55	-1.0%	5.66 ± 0.58	-57.0%	0.411 ± 0.062	-1.6%

Table 2.4 – Flexural properties of virgin and nano-vascularized systems.

System	E (Mpa)		σ_{max} (MPa)		$\varepsilon_{\sigma max}$ (%)		ε_{break} (%)	
	Mean ± SD	Var (%)	Mean ± SD	Var (%)	Mean ± SD	Var (%)	Mean ± SD	Var (%)
Virgin (V)	3186 ± 105	-	149 ± 3	-	6.90 ± 0.15	-	7.52 ± 0.42	-
Nano-vascularized (VP)	2504 ± 78	-21.4%	108 ± 1	-27.8%	5.56 ± 0.69	-19.4%	5.57 ± 0.68	-25.8%

Unlike tensile specimens, flexural ones do not exhibit noticeable plasticity. This is probably due to the larger size of the 3PB specimens compared to the tensile ones, not allowing a size effect to be observed. The percentual variation in flexural modulus and strength of the nano-vascularized system compared to the virgin one agreed with the values obtained by Torre-Muruzabal *et al.* in their experimental flexural characterization of a nano-vascularized epoxy resin [44].

2.4.1.2 Nanoindentation tests results

The nanoindentation tests were carried out only on virgin samples and allowed to evaluate the mechanical properties at the mesoscale, providing reliable values for the definition of the virgin system EDP model to be introduced in the RVE. Figure 2.8A shows the nanoindentation elastic modulus as a function of the indenter penetration depth for the three tested virgin specimens evaluated using the CMC protocol. The nanoindentation elastic modulus was derived from the reduced one (E_r) adopting the Poisson's ratio determined experimentally by tensile tests. It can be noticed that, after an initial stabilization phase, the elastic modulus remains basically constant for increasing penetration

depth ($E = 3166 \pm 119$ MPa). This phenomenon is also confirmed by other nanoindentation studies carried out on polymeric materials, showing that the elastic modulus evaluated by a spherical tip, unlike those found using pyramidal ones, is independent from the penetration depth [96–98].

In Figure 2.8B the indentation strain ($\varepsilon = a/2.4R$) is plotted against the indentation stress ($\sigma = P/\pi a^2$), where a is the indentation radius, R is the radius of the spherical indenter (100 μm) and P is the applied load. Even though the nanoindentation test is similar to the compressive one, the triaxial stress state generated during the test prevents a direct comparison of the mechanical properties determined by the two methods. However, this graph helped to interpret and optimize the parameters of the virgin system EDP model. In particular, it is interesting to note that while a more compliant behaviour is observed for specimen V2, the other two specimens exhibit a similar trend, with a clearly visible inflection point around 100 MPa. This behaviour discrepancy is probably due to the influence of the surface roughness of the specimen V2.
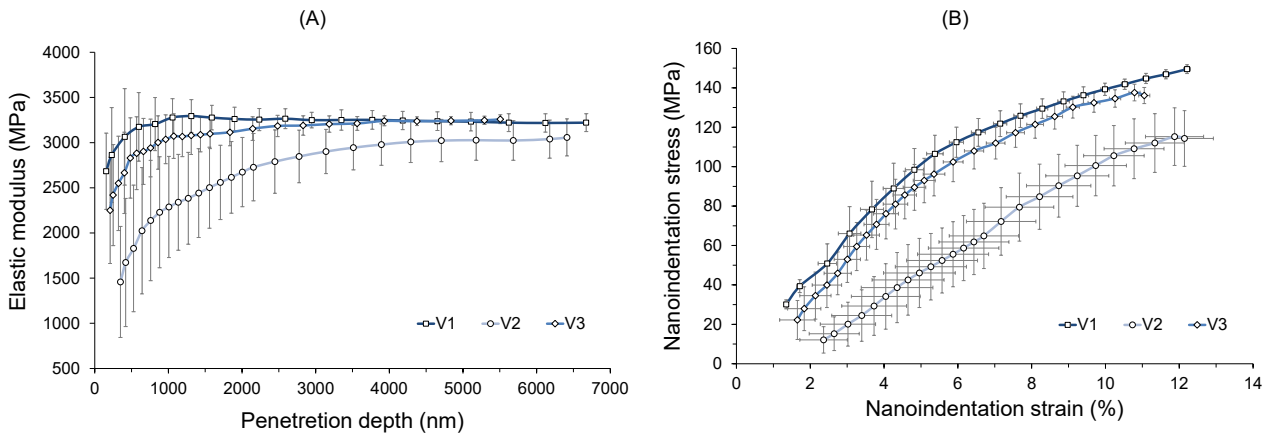

Figure 2.8 – (A) Nanoindentation elastic modulus as a function of the penetration depth and (B) stress-strain curves obtained from nanoindentation tests using CMC protocol.

2.4.2 Material model definition for virgin system

The experimental data obtained on virgin samples were used to define the neat epoxy EDP model parameters, finding the fitting on the experimental curves. To accurately model the mechanical behaviour on a dimensional scale as close as possible to that one of the RVE, the elastic modulus used to describe the virgin system is the average between the experimental values found with tensile and nanoindentation tests, resulting in 3321 MPa. Concerning the Poisson's ratio, the average value obtained from tensile tests (0.418) was taken as a reference. The behaviour was assumed isotropic.

Concerning the parameters of the EDP model, the experimental results on virgin samples were used to define the neat epoxy model parameters, finding the fitting on the experimental curves. The values obtained at the end of the optimization process are: $tan\,\beta = 0.21$ for the pressure sensitivity, $K = 0.93$

for the triaxial stress ratio, and $d = 86$ MPa for the cohesion, given by $m = 1.23$ for the uniaxial stress ratio. To implement the element death capability, the EKILL deactivation condition was referred to the total equivalent strain, considering the average true strain failure value found experimentally by tensile tests for the virgin system (12.37 %), since hardening was defined in tension.

Figure 2.9 shows the stress-strain curves obtained from the FEM analyses of tensile and 3PB numerical models with respect to the corresponding experimental results, using the EDP parameters above mentioned. Moreover, in Figure 2.10 a comparison is reported between the simulated curve and the average load–depth one obtained from the experimental nanoindentation tests (loading-unloading tests without creep time).
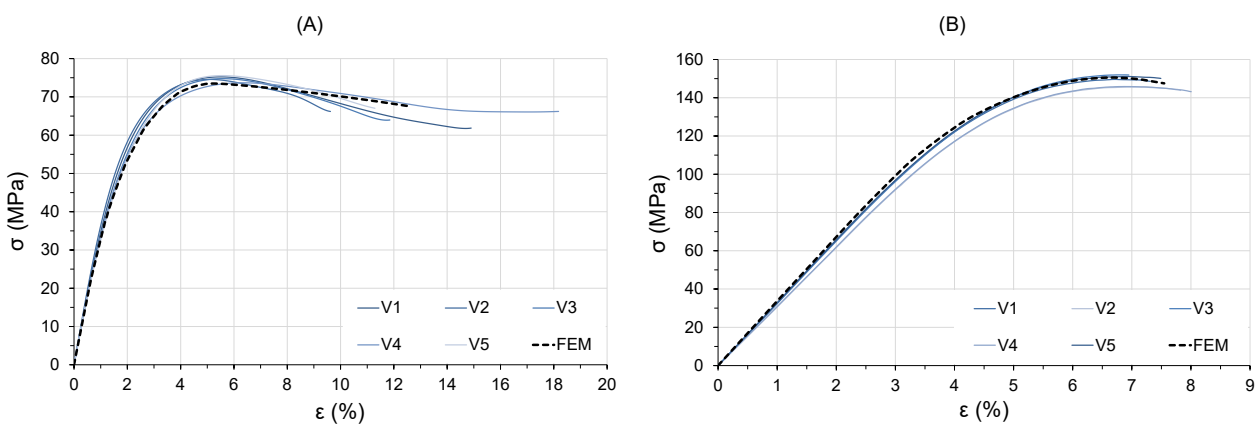

Figure 2.9 – Comparison between FEM and experimental stress-strain curves for (A) tensile and (B) 3PB tests for the virgin system.
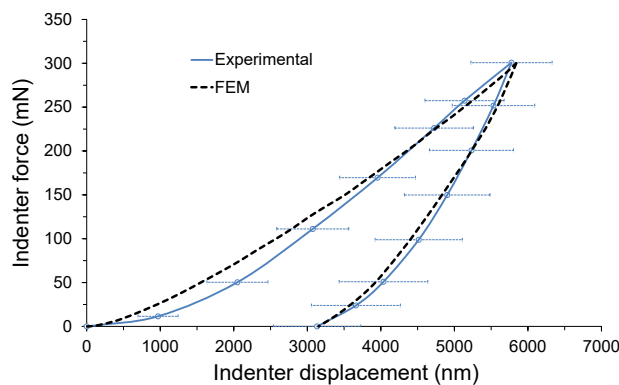
Figure 2.10 – Comparison between FEM and average experimental force-depth nanoindentation curves for the virgin system.

Regarding the tensile curves, it can be observed that the elasticity and the onset of plasticity are correctly described by the FEM simulation. The failure strain value is described quite reliably by the model, as is the maximum stress value. Concerning 3PB tests, the flexural elastic modulus is slightly overrated by the FEM simulation, while the onset of plasticity is accurately represented. Finally, the

fitting of the nanoindentation curves is good, especially during the unloading phase, in which the mechanical properties of the material are determined. However, in the loading phase, there is a discrepancy between the two curves, probably due to the missing implementation of the viscoelastic component in the EDP model [64], which, however, is not relevant for the present investigation.

Therefore, it can be stated that the EDP model for the virgin system reliably predicted the mechanical behaviour of the neat epoxy resin. The identified EDP parameters are in accordance with other studies on epoxies [76,77,84]. It is interesting to note that, although it is not possible to directly correlate compression and nanoindentation tests, the obtained *m* value gives a uniaxial compressive yield strength of about 93 MPa, comparable with the value identified by the knee of the stress-strain nanoindentation curves.

2.4.3 Material model definition for nano-vascularized system

The RVEs were simulated in tension and compression along the three reference directions using the EDP model defined for the virgin system. Figure 2.11 shows the equivalent stress, the equivalent plastic strain, and a detail of the element death evolution for the three RVEs tensioned along direction 1 for a global applied tensile strain of 1.5 %. Looking at the stress and strain distributions, it can be noticed that the damage initiates at the intersections between nanochannels and propagates to the surrounding areas, especially on the nanochannels linking directions [46].

Table 2.5 shows the overall mechanical properties of the nano-vascularized system at the mesoscale, obtained from the analysis of the RVEs simulations. The elastic modulus and the Poisson's ratio are the averages of the values obtained in tension and compression, which are almost identical to each other. It is interesting to note that the elastic modulus E_{22} (i.e. through the mat thickness) is lower than E_{11} and E_{33} elastic moduli. This means that perpendicularly to the nanofibers deposition plane, the crossings generated by the nanochannels significantly reduce the bearing strength of the matrix, causing a consequent reduction of the RVE stiffness. The same behaviour was observed also for the tensile and compressive yield strengths along direction 2, as well as a higher value of v_{13} (i.e. in the deposition plane) compared to v_{12} and v_{23}. The values obtained at the mesoscale using the RVEs are close to the experimental ones. In particular, E_{11} and E_{33}, which are defined in the nanofibers deposition plane, are similar to the experimental ones found for nano-vascularized tensile specimens, with a maximum difference of 3 %. Moreover, the variation between directions 1 and 3 are within 1 %. It is worth mentioning that also considering direction 2 the percentual variation of all mechanical properties is below 5 %. These results confirm that the chosen size of the RVE is acceptable.
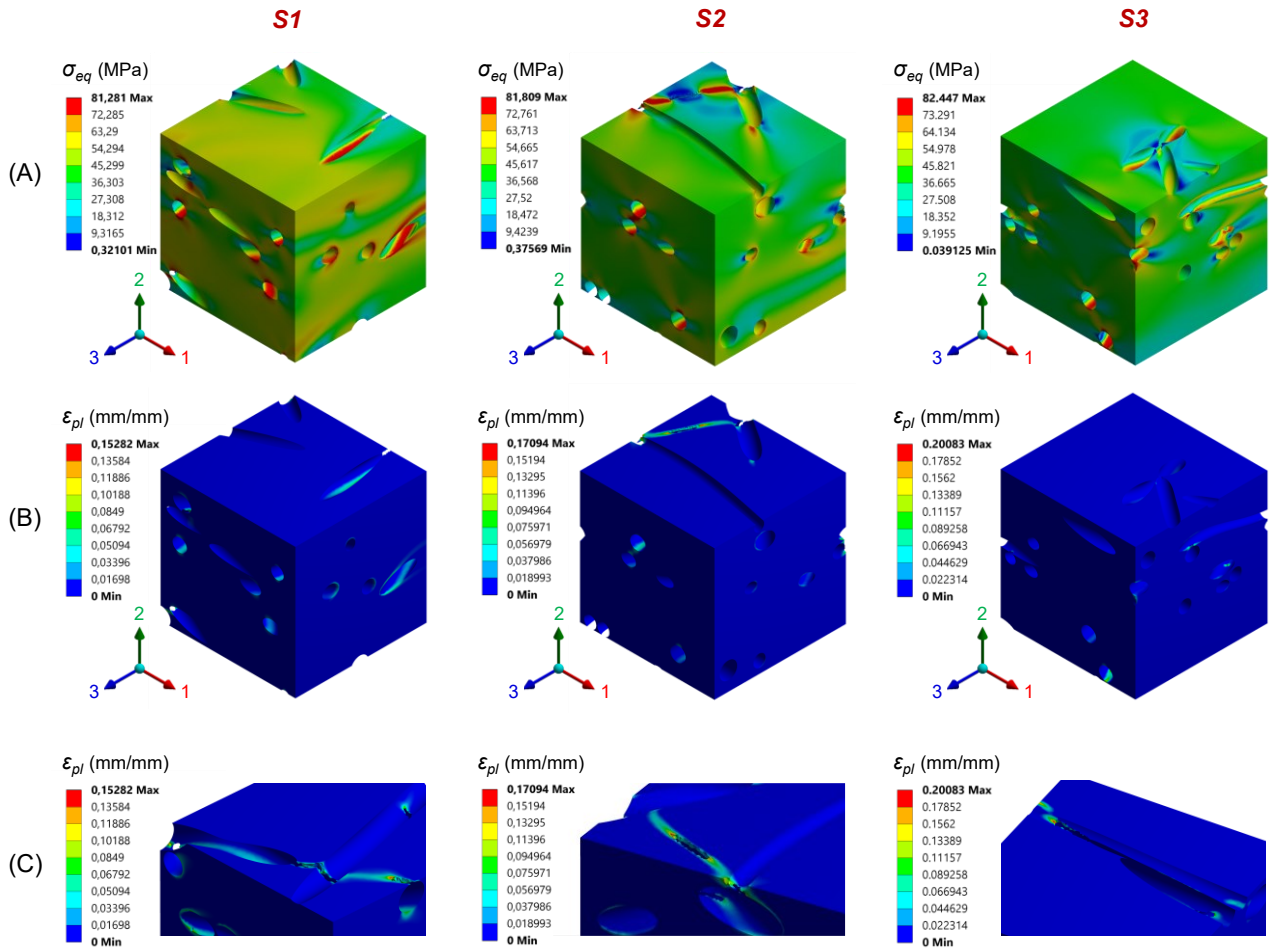
Figure 2.11 – (A) Equivalent stress, (B) equivalent plastic strain, and (C) a detail of the damage evolution for the S1, S2, and S3 RVEs tensioned along direction 1 for a global applied tensile strain of 1.5 %.

Table 2.5 – Mesoscale mechanical properties of the nano-vascularized system obtained from the analysis of the RVEs simulations.

RVE	Elastic modulus (MPa)			Poisson's ratio (-)			Tensile yield stress (MPa)			Compressive yield stress (MPa)		
	E_{11}	E_{22}	E_{33}	ν_{12}	ν_{13}	ν_{23}	σ_{t1}	σ_{t2}	σ_{t3}	σ_{c1}	σ_{c2}	σ_{c3}
S1	2897	2780	2917	0.405	0.418	0.409	60	58	59	72	68	71
S2	2901	2754	2895	0.408	0.417	0.411	59	57	61	71	69	70
S3	2908	2806	2925	0.403	0.421	0.407	61	58	60	71	69	72

Despite the slight anisotropic behaviour in the RVEs mechanical properties perpendicularly to the nanofibers deposition plane, the values obtained in the three reference directions were then averaged to model an isotropic material that was characteristic of the nano-vascularized system, allowing the definition of the elastic properties and the related EDP model. Having both tensile and compression data available, it was possible to directly calculate the uniaxial stress ratio ($m = \bar{\sigma}_c/\bar{\sigma}_t = 70.3/59.2 = 1.19$), thus obtaining all the other characteristic parameters of the EDP model for the nano-vascularized system.

Table 2.6 – Material model parameters for virgin and nano-vascularized systems.

Material model for FEA	ρ (g/cm^3)	E (MPa)	v (-)	Extended Drucker-Prager parameters				Ekill
				m (-)	$tan\beta$ (-)	K (-)	d (MPa)	ε_{break} (%)
Virgin (V)	1.128	3321	0.418	1.23	0.21	0.93	86	12.37
Nano-vascularized (VP)	1.128	2865	0.411	1.19	0.18	0.95	66	5.51

Table 2.6 shows the modelling parameters for FEA for both virgin and nano-vascularized materials. It is interesting to note that the average Poisson's ratio evaluated by RVEs numerical simulation for the nano-vascularized system is the same obtained experimentally. Similarly to what was performed on the virgin system, the average stress-strain tensile curve obtained from the RVEs analysis was extrapolated to higher strain values with a horizontal plateau, obtaining a multilinear monotonic increasing curve useful to implement the hardening behaviour in the nano-vascularized material model. Finally, the EKILL condition for the nano-vascularized material is applied when the equivalent total strain exceeds the true strain value of 5.51 % experimentally assessed through the tensile tests.

2.4.4 Nano-vascularized material model validation

Figure 2.12 shows the stress-strain curves obtained from the FEM analyses of tensile and 3PB numerical models with respect to the corresponding experimental results, using the material model parameters defined for the nano-vascularized system.
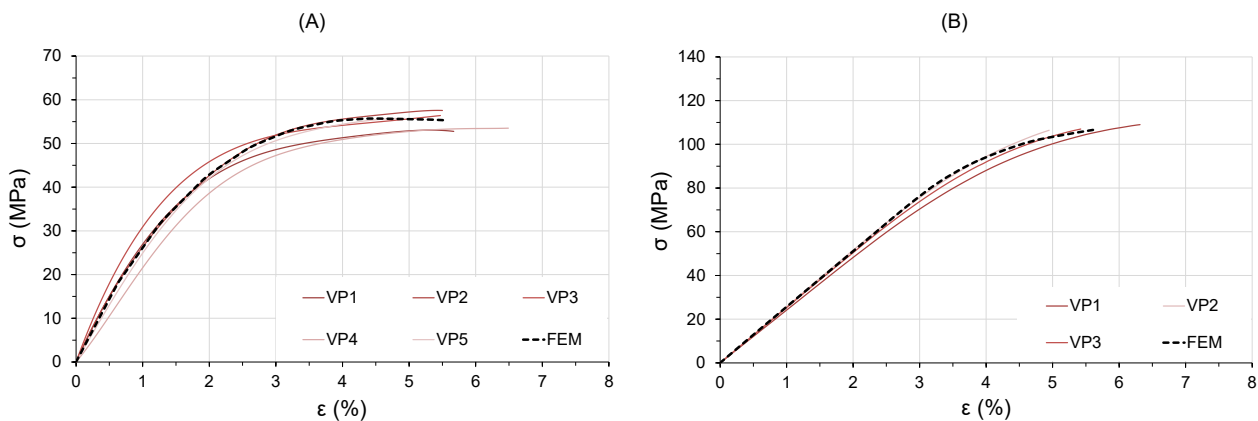

Figure 2.12 – Comparison between FEM and experimental stress-strain curves for (A) tensile and (B) 3PB tests for the nano-vascularized system.

As can be observed, the simulated curves are almost superimposed on the experimental ones. The elasticity and the onset of plasticity are correctly described by both simulations. The tensile elastic modulus obtained from the analysis of the simulated stress-strain curve is equal to 2880 MPa, while the modulus assessed experimentally is 2846 MPa. The FEM tensile curve shows a very slight

necking, not observed in the experimental ones, which leads to an underestimation of the stress for higher strains. Furthermore, the flexural elastic modulus evaluated from the numerical model presents an overestimation of 3 % compared to the experimental one (2576 MPa versus 2504 MPa, respectively). The failure strain values are correctly described by both models, as is the maximum stress values.

2.4.5 Fracture surfaces analysis

The fracture surfaces of both virgin and nano-vascularized systems loaded in tension are reported in Figure 2.13A and Figure 2.13B (tensile specimens V5 and VP2, respectively), while in Figure 2.13C the fracture surface of the VP1 flexural specimen is reported.
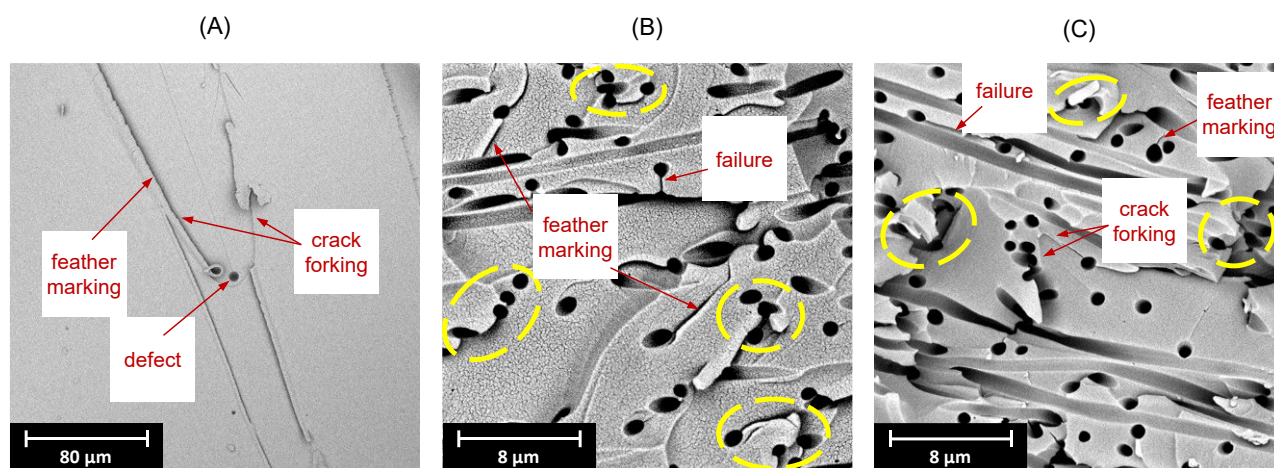

Figure 2.13 – Fracture surfaces of (A) virgin tensile specimen V5, (B) nano-vascularized tensile specimen VP2, and (C) nano-vascularized flexural specimen VP1. The red arrows reveal the morphological features of the fracture surface while the yellow dotted circles the multiple crack initiations at nanofibers intersections.

The fracture surfaces of the virgin samples appear smoothy and glassy, which is typical for a macroscopically brittle thermosetting polymer [99]. In Figure 2.13A, feather markings are clearly visible on the fracture surface of the neat epoxy, which are caused by the crack forking due to the excess energy associated with the relatively fast crack growth [1]. Commonly, as in this case, the crack initiates near to a defect like an air bubble or an inclusion. The forking repetition and the multiplanar morphology of the fracture surface are the principal mechanisms for absorbing the excess energy during the fracture of brittle materials [100]. The lower probability of finding numerous and large defects in small specimens, therefore, justifies the plastic behaviour and the high strain at break values found for the virgin system in tension [52].

Moving from virgin system to nano-vascularized one, it is observed that the fracture surfaces become irregular, indicating more complex absorption mechanisms. To appreciate the energy

absorption mechanisms acting in the nano-vascularized system it is necessary to go deeper, approaching the dimensional scale of the nanofibers. As can be seen both in tension and in bending (Figure 2.13B and Figure 2.13C), the damage of the epoxy matrix occurs mainly at the intersections between the nanochannels, and in particular where the intersections become denser (yellow dotted circles). Indeed, these regions act as defects, leading to a localized reduction of the bearing strength of the matrix, which progressively decrease from the nano to the macroscale, as the number of triggering cracks increases. Moreover, as also evidenced by the RVEs numerical simulations, feather markings as well as local failures are detected on the fracture surface along the nanochannels linking directions, where the stress state is higher [46]. The more brittle and compliant behaviour of the nano-vascularized system compared to the virgin one, therefore, is mainly due to the progressive reduction of the bearing strength of the matrix through the different dimensional scales. In fact, this mechanism prevents nano-vascularized material from withstanding high stress and strain macroscale values since a lot of microcracks are already involved. The obtained results confirm the inherent toughening mechanisms of nanofibrous-reinforced polymers [36], thanks to tortuous crack paths, characterized by multiple deviation and forking through the nano-structured layer.

2.5   Conclusions

In this study, a multiscale modelling approach has been proposed to evaluate and predict the effect of nano-vascularization – obtained by means of sacrificial nanofibers – on the macroscale mechanical properties of an epoxy matrix. Nanochannels were produced following the pioneering work of one of the Authors on the nano-vascularization of a polymeric matrix using water-soluble Pullulan electrospun nanofibers. A random nanofibers distribution was chosen since it is notoriously the most adopted for nano-reinforcing and when the delamination direction is not known a priori. Tensile, three-point bending, and nanoindentation experimental tests were carried out to evaluate the mechanical properties of the neat epoxy resin and so to implement the extended Drucker-Prager yield criterion to simulate the different tension-compression behaviour of the epoxy matrix.

The nano-vascularized RVEs were realized by means of a CAD software starting from the analysis of several random Pullulan nanomat images observed under a SEM and knowing the percentage nanofibers volume experimentally assessed. Three RVEs were tested in tension and compression under periodic boundary conditions using the EDP model defined for the virgin system. The element death capability was implemented to simulate the crack initiation and propagation inside the epoxy matrix. The RVEs simulations allowed to evaluate the mesoscale mechanical properties of the nano-vascularized material and to interpret the results considering the geometric features of each RVE. This

approach enabled the use of the EDP model again to define the characteristic parameters also for the nano-vascularized system. The latter was finally adopted to simulate tensile and 3PB numerical models, validating the RVE approach against experimental tests on nano-vascularized samples.

The obtained results proved that the multiscale approach here presented can accurately predict the macroscale behaviour of the nano-vascularized resin. The simulated stress-strain curves are almost superimposed on the experimental ones, with a maximum difference in mechanical properties within 3 %. It is interesting to note that the analysis of the RVEs revealed a slight anisotropy of the mechanical properties perpendicularly to the nanofiber deposition plane.

The fracture surfaces of both 3PB and tensile specimens were analysed at the SEM and compared to RVEs simulations to understand the actual failure mechanisms. The damage of the epoxy matrix occurs mainly at the intersections between the nanochannels, and in particular where the intersections become denser. Moreover, as also evidenced by the RVEs numerical simulations, feather markings as well as local failures are detected on the fracture surface along the nanochannels linking directions, where the stress state is higher. The obtained results confirm the inherent toughening mechanisms of nanofibrous-reinforced polymers, thanks to tortuous crack paths, characterized by multiple deviation and forking through the nano-structured layer.

This multiscale study opens to the development of a new approach that allows predicting the macroscale mechanical properties of nanocomposite starting from the nanoscale. Future studies will focus on the development of multiscale models that integrate the effect of nanofibers and their extrinsic toughening mechanisms in epoxy nano-reinforced composites. Moreover, this method is particularly helpful for the improvement of vascular tissue engineering applications, like bone, cartilage, tendon and ligaments biofabrication and for the design of self-healing materials, which use a network of nano-vascular core-shell nanofibers containing low viscosity liquid healing agents to hinder the crack propagation.

2.6   Nomenclature

D_{nf}	nanofibers diameter
$V_{nf\%}$	percentage nanofibers volume
F	yield function
q	deviatoric Cauchy stress tensor
J_2	second deviatoric stress invariant
K	triaxial stress ratio
m	uniaxial stress ratio
σ_m	hydrostatic stress component
d	material cohesion parameter of the extended Drucker-Prager model
$tan\beta$	pressure sensitivity parameter
β	friction angle parameter of the extended Drucker-Prager model
φ	angle of internal friction of the Mohr-Coulomb model
c	material cohesion parameter of the Mohr-Coulomb model
a	indentation radius
R	radius of the spherical indenter
P	nanoindentation load
σ_t	tensile stress
σ_c	compressive stress

2.7   References

[1]   J. Chen, A.J. Kinloch, S. Sprenger, A.C. Taylor, The mechanical properties and toughening mechanisms of an epoxy polymer modified with polysiloxane-based core-shell particles, Polymer. 54 (2013) 4276–4289. https://doi.org/10.1016/j.polymer.2013.06.009.

[2]   U.G.K. Wegst, H. Bai, E. Saiz, A.P. Tomsia, R.O. Ritchie, Bioinspired structural materials, Nature Materials. 14 (2015) 23–36. https://doi.org/10.1038/nmat4089.

[3]   M.E. Launey, R.O. Ritchie, On the fracture toughness of advanced materials, Advanced Materials. 21 (2009) 2103–2110. https://doi.org/10.1002/adma.200803322.

[4]   M.A. Meyers, P.Y. Chen, A.Y.M. Lin, Y. Seki, Biological materials: Structure and mechanical properties, Progress in Materials Science. 53 (2008) 1–206. https://doi.org/10.1016/j.pmatsci.2007.05.002.

[5]   R. Wang, H.S. Gupta, Deformation and fracture mechanisms of bone and nacre, Annual Review of Materials Research. 41 (2011) 41–73. https://doi.org/10.1146/annurev-matsci-062910-095806.

[6]   M.E. Launey, M.J. Buehler, R.O. Ritchie, On the mechanistic origins of toughness in bone, 2010. https://doi.org/10.1146/annurev-matsci-070909-104427.

[7]   B. Ji, H. Gao, Mechanical principles of biological nanocomposites, Annual Review of Materials Research. 40 (2010) 77–100. https://doi.org/10.1146/annurev-matsci-070909-104424.

[8]   A.R. Studart, Towards high-performance bioinspired composites, Advanced Materials. 24 (2012) 5024–5044. https://doi.org/10.1002/adma.201201471.

[9]   P. Fratzl, R. Weinkamer, Nature's hierarchical materials, Progress in Materials Science. 52 (2007) 1263–1334. https://doi.org/10.1016/j.pmatsci.2007.06.001.

[10]   B. Liu, L. Huang, L. Geng, F. Yin, Multiscale Hierarchical Structure and Laminated Strengthening and Toughening Mechanisms, Lamination - Theory and Application. (2018). https://doi.org/10.5772/intechopen.69976.

[11]   C. Gotti, A. Sensini, A. Zucchelli, R. Carloni, M.L. Focarete, Hierarchical fibrous structures for muscle-inspired soft-actuators: A review, Applied Materials Today. 20 (2020) 100772. https://doi.org/10.1016/j.apmt.2020.100772.

[12]   A.J. Kinloch, S.J. Shaw, D.A. Tod, D.L. Hunston, Deformation and fracture behaviour of a rubber-toughened epoxy: 1. Microstructure and fracture studies, Polymer. 24 (1983) 1341–1354. https://doi.org/10.1016/0032-3861(83)90070-8.

[13]   R.A. Pearson, A.F. Yee, Toughening mechanisms in elastomer-modified epoxies - Part 2 Microscopy studies, Journal of Materials Science. 21 (1986) 2475–2488. https://doi.org/10.1007/BF01114294.

[14]   A.J. Kinloch, Toughening epoxy adhesives to meet today's challenges, MRS Bulletin. 28 (2003) 445–448. https://doi.org/10.1557/mrs2003.126.

[15]   B.B. Johnsen, A.J. Kinloch, R.D. Mohammed, A.C. Taylor, S. Sprenger, Toughening mechanisms of nanoparticle-modified epoxy polymers, Polymer. 48 (2007) 530–541. https://doi.org/10.1016/j.polymer.2006.11.038.

[16]   D.J. Bray, P. Dittanet, F.J. Guild, A.J. Kinloch, K. Masania, R.A. Pearson, A.C. Taylor, The modelling of the toughening of epoxy polymers via silica nanoparticles: The effects of volume fraction and particle size, Polymer. 54 (2013) 7022–7032. https://doi.org/10.1016/j.polymer.2013.10.034.

[17]   A.J. Kinloch, M.L. Yuen, S.D. Jenkins, Thermoplastic-toughened epoxy polymers, Journal of Materials Science. 29 (1994) 3781–3790. https://doi.org/10.1007/BF00357349.

[18]   M. Quaresimin, K. Schulte, M. Zappalorto, S. Chandrasekaran, Toughening mechanisms in polymer nanocomposites: From experiments to modelling, Composites Science and Technology. 123 (2016) 187–204. https://doi.org/10.1016/j.compscitech.2015.11.027.

[19]   T.H. Hsieh, A.J. Kinloch, K. Masania, A.C. Taylor, S. Sprenger, The mechanisms and mechanics of the toughening of epoxy polymers modified with silica nanoparticles, Polymer. 51 (2010) 6284–6294. https://doi.org/10.1016/j.polymer.2010.10.048.

[20]   M. Quaresimin, M. Salviato, M. Zappalorto, A multi-scale and multi-mechanism approach for the fracture toughness assessment of polymer nanocomposites, Composites Science and Technology. 91 (2014) 16–21. https://doi.org/10.1016/j.compscitech.2013.11.015.

[21]   M. Salviato, M. Zappalorto, M. Quaresimin, Plastic shear bands and fracture toughness improvements of nanoparticle filled polymers: A multiscale analytical model, Composites Part A: Applied Science and Manufacturing. 48 (2013) 144–152. https://doi.org/10.1016/j.compositesa.2013.01.006.

[22]   X. Wang, J. Jin, M. Song, An investigation of the mechanism of graphene toughening epoxy, Carbon. 65 (2013) 324–333. https://doi.org/10.1016/j.carbon.2013.08.032.

[23]   S. Chandrasekaran, N. Sato, F. Tölle, R. Mülhaupt, B. Fiedler, K. Schulte, Fracture toughness and failure mechanism of graphene based epoxy composites, Composites Science and Technology. 97 (2014) 90–99. https://doi.org/10.1016/j.compscitech.2014.03.014.

[24]   A. Allaoui, S. Bai, H.M. Cheng, J.B. Bai, Mechanical and electrical properties of a MWNT/epoxy composite, Composites Science and Technology. 62 (2002) 1993–1998. https://doi.org/10.1016/S0266-3538(02)00129-X.

[25]   F.F. Lange, The interaction of a crack front with a second-phase dispersion, Philosophical Magazine. 22 (1970) 983–992. https://doi.org/10.1080/14786437008221068.

[26]   M.T. Aljarrah, N.R. Abdelal, Improvement of the mode I interlaminar fracture toughness of carbon fiber composite reinforced with electrospun nylon nanofiber, Composites Part B: Engineering. 165 (2019) 379–385. https://doi.org/10.1016/j.compositesb.2019.01.065.

[27]   M.H.G. Wichmann, K. Schulte, H.D. Wagner, On nanocomposite toughness, Composites Science and Technology. 68 (2008) 329–331. https://doi.org/10.1016/j.compscitech.2007.06.027.

[28]   T. Liu, W.C. Tjiu, Y. Tong, C. He, S.S. Goh, T.S. Chung, Morphology and fracture behavior of intercalated epoxy/clay nanocomposites, Journal of Applied Polymer Science. 94 (2004) 1236–1244. https://doi.org/10.1002/app.21033.

[29]   H. Saghafi, T. Brugo, G. Minak, A. Zucchelli, The effect of PVDF nanofibers on mode-I fracture toughness of composite materials, Composites Part B: Engineering. 72 (2015) 213–216. https://doi.org/10.1016/j.compositesb.2014.12.015.

[30]   T. Brugo, R. Palazzetti, The effect of thickness of Nylon 6,6 nanofibrous mat on Modes I–II fracture mechanics of UD and woven composite laminates, Composite Structures. 154 (2016) 172–178. https://doi.org/10.1016/j.compstruct.2016.07.034.

[31]   R. Palazzetti, A. Zucchelli, Electrospun nanofibers as reinforcement for composite laminates materials – A review, Composite Structures. 182 (2017) 711–727. https://doi.org/10.1016/j.compstruct.2017.09.021.

[32]   R. Mohammadi, M.A. Najafabadi, H. Saghafi, D. Zarouchas, Fracture and fatigue behavior of carbon/epoxy laminates modified by nanofibers, Composites Part A: Applied Science and Manufacturing. 137 (2020). https://doi.org/10.1016/j.compositesa.2020.106015.

[33]   T.M. Brugo, J. Belcari, F. Musiari, A. Pirondi, D. Menozzi, L. Zomparelli, A. Zucchelli, Development of a electrospun nanofiber mat pre-preg for application in adhesive bonding, (2017) 6–9.

[34]   T.M. Brugo, F. Musiari, A. Pirondi, A. Zucchelli, D. Cocchi, D. Menozzi, Development and fracture toughness characterization of a nylon nanomat epoxy adhesive reinforcement, Proceedings of the Institution of Mechanical Engineers, Part L: Journal of Materials: Design and Applications. 233 (2019) 465–474. https://doi.org/10.1177/1464420718807733.

[35]   S.L. Omairey, P.D. Dunning, S. Sriramula, Development of an ABAQUS plugin tool for periodic RVE homogenisation, Engineering with Computers. 35 (2019) 567–577. https://doi.org/10.1007/s00366-018-0616-4.

[36]   L. Daelemans, W. Van Paepegem, K. De Clerck, Effect of interleaved polymer nanofibers on the properties of glass and carbon fiber composites, INC, 2020. https://doi.org/10.1016/b978-0-12-819904-6.00011-6.

[37]   M. Quaresimin, M. Salviato, M. Zappalorto, Strategies for the assessment of nanocomposite mechanical properties, Composites Part B: Engineering. 43 (2012) 2290–2297. https://doi.org/10.1016/j.compositesb.2011.12.012.

[38]   J.G. Williams, Particle toughening of polymers by plastic void growth, Composites Science and Technology. 70 (2010) 885–891. https://doi.org/10.1016/j.compscitech.2009.12.024.

[39]   B. Lauke, On the effect of particle size on fracture toughness of polymer composites, Composites Science and Technology. 68 (2008) 3365–3372. https://doi.org/10.1016/j.compscitech.2008.09.011.

[40]   A.A. Gawandi, J.M. Whitney, G.P. Tandon, R.B. Brockman, Three-dimensional analysis of the interaction between a matrix crack and nanofiber, Composites Part B: Engineering. 40 (2009) 698–704. https://doi.org/10.1016/j.compositesb.2009.04.001.

[41] E. García-Macías, C.F. Guzmán, E.I. Saavedra Flores, R. Castro-Triguero, Multiscale modeling of the elastic moduli of CNT-reinforced polymers and fitting of efficiency parameters for the use of the extended rule-of-mixtures, Composites Part B: Engineering. 159 (2019) 114–131. https://doi.org/10.1016/j.compositesb.2018.09.057.

[42] Y. Li, G.D. Seidel, Multiscale modeling of the interface effects in CNT-epoxy nanocomposites, Computational Materials Science. 153 (2018) 363–381. https://doi.org/10.1016/j.commatsci.2018.07.015.

[43] C. Gualandi, A. Zucchelli, M. Fernández Osorio, J. Belcari, M.L. Focarete, Nanovascularization of polymer matrix: Generation of nanochannels and nanotubes by sacrificial electrospun fibers, Nano Letters. 13 (2013) 5385–5390. https://doi.org/10.1021/nl402930x.

[44] A. Torre-Muruzabal, L. Daelemans, G. Van Assche, K. De Clerck, H. Rahier, Creation of a nanovascular network by electrospun sacrificial nanofibers for self-healing applications and its effect on the flexural properties of the bulk material, Polymer Testing. 54 (2016) 78–83. https://doi.org/10.1016/j.polymertesting.2016.06.026.

[45] V. Mironov, V. Kasyanov, R.R. Markwald, Nanotechnology in vascular tissue engineering: from nanoscaffolding towards rapid vessel biofabrication, Trends in Biotechnology. 26 (2008) 338–344. https://doi.org/10.1016/j.tibtech.2008.03.001.

[46] F. Cristofari, B. Piotrowski, R. Pesci, Mechanical properties of a nanoporous membrane used in implantable medical devices. Correlation between experimental characterization and 2D numerical simulation, Journal of the Mechanical Behavior of Biomedical Materials. 74 (2017) 43–53. https://doi.org/10.1016/j.jmbbm.2017.05.021.

[47] J. Venkatesan, S.K. Kim, Nano-hydroxyapatite composite biomaterials for bone tissue engineering - A review, Journal of Biomedical Nanotechnology. 10 (2014) 3124–3140. https://doi.org/10.1166/jbn.2014.1893.

[48] M. Qasim, D.S. Chae, N. Lee, Advancements and frontiers in nano-based 3d and 4d scaffolds for bone and cartilage tissue engineering, International Journal of Nanomedicine. 14 (2019) 4333–4351. https://doi.org/10.2147/IJN.S209431.

[49] A. Sensini, L. Cristofolini, A. Zucchelli, M.L. Focarete, C. Gualandi, A. de Mori, A.P. Kao, M. Roldo, G. Blunn, G. Tozzi, Hierarchical electrospun tendon-ligament bioinspired scaffolds induce changes in fibroblasts morphology under static and dynamic conditions, Journal of Microscopy. 277 (2020) 160–169. https://doi.org/10.1111/jmi.12827.

[50] Y.C. Yuan, T. Yin, M.Z. Rong, M.Q. Zhang, Self healing in polymers and polymer composites. Concepts, realization and outlook: A review, Express Polymer Letters. 2 (2008) 238–250. https://doi.org/10.3144/expresspolymlett.2008.29.

[51] D. Cocchi, F. Musiari, T.M. Brugo, A. Pirondi, A. Zucchelli, F. Campanini, E. Leoni, L. Mazzocchetti, Characterization of aluminum alloy-epoxy bonded joints with nanofibers obtained by electrospinning, Journal of Adhesion. 96 (2020) 384–401. https://doi.org/10.1080/00218464.2019.1666716.

[52] E.M. Odom, D.F. Adams, Specimen size effect during tensile testing of an unreinforced polymer, Journal of Materials Science. 27 (1992) 1767–1771. https://doi.org/10.1007/BF01107202.

[53] J.D. Littell, C.R. Ruggeri, R.K. Goldberg, G.D. Roberts, W.A. Arnold, W.K. Binienda, Measurement of epoxy resin tension, compression, and shear stress-strain curves over a wide range of strain rates using small test specimens, Journal of Aerospace Engineering. 21 (2008) 162–173. https://doi.org/10.1061/(ASCE)0893-1321(2008)21:3(162).

[54] S. Zike, B.F. Sørensen, L.P. Mikkelsen, Experimental determination of the micro-scale strength and stress-strain relation of an epoxy resin, Materials and Design. 98 (2016) 47–60. https://doi.org/10.1016/j.matdes.2016.02.102.

[55] W.D. Pilkey, Peterson's stress concentration factors, 2nd ed., Wiley-Interscience, New York, 1997. https://doi.org/10.1002/9780470211106.ch3.

[56] A.M. Díez-Pascual, M.A. Gómez-Fatou, F. Ania, A. Flores, Nanoindentation in polymer nanocomposites, Progress in Materials Science. 67 (2015) 1–94. https://doi.org/10.1016/j.pmatsci.2014.06.002.

[57] M. Sánchez, J. Rams, M. Campo, A. Jiménez-Suárez, A. Ureña, Characterization of carbon nanofiber/epoxy nanocomposites by the nanoindentation technique, Composites Part B: Engineering. 42 (2011) 638–644. https://doi.org/10.1016/j.compositesb.2011.02.017.

[58] P. Nikaeen, D. Depan, A. Khattab, Surface mechanical characterization of carbon nanofiber reinforced low-density polyethylene by nanoindentation and comparison with bulk properties, Nanomaterials. 9 (2019). https://doi.org/10.3390/nano9101357.

[59] H. Lee, S. Mall, V. Nalladega, S. Sathish, A. Roy, K. Lafdi, Characterization of carbon nanofibre reinforced epoxy composite using nanoindentation and AFM/UFM techniques, Polymers and Polymer Composites. 14 (2006) 549–562. https://doi.org/10.1177/096739110601400601.

[60] R.F. Gibson, A review of recent research on nanoindentation of polymer composites and their constituents, Composites Science and Technology. 105 (2014) 51–65. https://doi.org/10.1016/j.compscitech.2014.09.016.

[61] P. Tyagi, S.A. Catledge, A. Stanishevsky, V. Thomas, Y.K. Vohra, Nanomechanical properties of electrospun composite scaffolds based on polycaprolactone and hydroxyapatite, Journal of Nanoscience and Nanotechnology. 9 (2009) 4839–4845. https://doi.org/10.1166/jnn.2009.1588.

[62] E. Le Bourhis, Indentation mechanics and its application to thin film characterization, Vacuum. 82 (2008) 1353–1359. https://doi.org/10.1016/j.vacuum.2008.03.077.

[63] B. Bhushan, X. Li, Nanomechanical characterisation of solid surfaces and thin films, International Materials Reviews. 48 (2003) 125–164. https://doi.org/10.1179/095066003225010227.

[64] G. Marchiori, N. Lopomo, M. Boi, M. Berni, M. Bianchi, A. Gambardella, A. Visani, A. Russo, M. Marcacci, Optimizing thickness of ceramic coatings on plastic components for

orthopedic applications: A finite element analysis, Materials Science and Engineering C. 58 (2016) 381–388. https://doi.org/10.1016/j.msec.2015.08.067.

[65] E. Martínez, J. Romero, A. Lousa, J. Esteve, Nanoindentation stress-strain curves as a method for thin-film complete mechanical characterization: Application to nanometric CrN/Cr multilayer coatings, Applied Physics A: Materials Science and Processing. 77 (2003) 419–426. https://doi.org/10.1007/s00339-002-1669-0.

[66] S. Pathak, S.R. Kalidindi, Spherical nanoindentation stress-strain curves, Materials Science and Engineering R: Reports. 91 (2015) 1–36. https://doi.org/10.1016/j.mser.2015.02.001.

[67] R.C. Paietta, S.E. Campbell, V.L. Ferguson, Influences of spherical tip radius, contact depth, and contact area on nanoindentation properties of bone, Journal of Biomechanics. 44 (2011) 285–290. https://doi.org/10.1016/j.jbiomech.2010.10.008.

[68] W.C. Oliver, G.M. Pharr, Measurement of hardness and elastic modulus by instrumented indentation: Advances in understanding and refinements to methodology, Journal of Materials Research. 19 (2004) 3–20. https://doi.org/10.1557/jmr.2004.0002.

[69] S.E. Olesiak, M.L. Oyen, V.L. Ferguson, Viscous-elastic-plastic behavior of bone using Berkovich nanoindentation, Mechanics of Time-Dependent Materials. 14 (2010) 111–124. https://doi.org/10.1007/s11043-009-9098-5.

[70] S.W. Moore, M.T. Manzari, Y.L. Shen, Nanoindentation in elastoplastic materials: Insights from numerical simulations, International Journal of Smart and Nano Materials. 1 (2010) 95–114. https://doi.org/10.1080/19475411003589889.

[71] R. Iankov, M. Datcheva, S. Cherneva, D. Stoychev, Finite element simulation of nanoindentation process, in: Lecture Notes in Computer Science (Including Subseries Lecture Notes in Artificial Intelligence and Lecture Notes in Bioinformatics), 2013: pp. 319–326. https://doi.org/10.1007/978-3-642-41515-9_35.

[72] Ansys® Academic Research Mechanical, Release 19.3, Help System, Theory Reference for the Mechanical APDL and Mechanical Applications, ANSYS, Inc., (2019).

[73] S.D.J. Mesarovic, N.A. Fleck, Spherical indentation of elastic-plastic solids, Proceedings of the Royal Society A: Mathematical, Physical and Engineering Sciences. 455 (1999) 2707–2728. https://doi.org/10.1098/rspa.1999.0423.

[74] D.C. Drucker, Limit analysis of two and three dimensional soil mechanics problems, Journal of the Mechanics and Physics of Solids. 1 (1953) 217–226. https://doi.org/10.1016/0022-5096(53)90001-5.

[75] D.C. Drucker, Plasticity theory strength-differential(SD) phenomenon, and volume expansion in metals and plastics, Metallurgical Transactions. 4 (1973) 667–673. https://doi.org/10.1007/BF02643073.

[76] D. Ashouri Vajari, C. González, J. Llorca, B.N. Legarth, A numerical study of the influence of microvoids in the transverse mechanical response of unidirectional composites, Composites Science and Technology. 97 (2014) 46–54. https://doi.org/10.1016/j.compscitech.2014.04.004.

[77] S. Zike, Micro-Scale Experiments and Models for Composite Materials with Materials Research, DTU, Department of Wind Energy, PhD No. 0050(EN), 2015.

[78] X.P. Morelle, J. Chevalier, C. Bailly, T. Pardoen, F. Lani, Mechanical characterization and modeling of the deformation and failure of the highly crosslinked RTM6 epoxy resin, Mechanics of Time-Dependent Materials. 21 (2017) 419–454. https://doi.org/10.1007/s11043-016-9336-6.

[79] R. Seltzer, A.P. Cisilino, P.M. Frontini, Y.W. Mai, Determination of the DruckerPrager parameters of polymers exhibiting pressure-sensitive plastic behaviour by depth-sensing indentation, International Journal of Mechanical Sciences. 53 (2011) 471–478. https://doi.org/10.1016/j.ijmecsci.2011.04.002.

[80] W.-F. Chen, D.-J. Han, Plasticity for Structural Engineers, J. Ross Publishing, 2007.

[81] A.J. Kinloch, R.J. Young, Fracture Behaviour of Polymers, 1995. https://doi.org/10.1007/978-94-017-1594-2.

[82] Systemes Dassault, Abaqus Analysis User's Guide, ABAQUS Inc., Dassault Systèmes, France, (2017).

[83] M.Y.M. Chiang, C. Herzl, Plastic deformation analysis of cracked adhesive bonds loaded in shear, International Journal of Solids and Structures. 31 (1994) 2477–2490. https://doi.org/10.1016/0020-7683(94)90032-9.

[84] R. Quinson, J. Perez, M. Rink, A. Pavan, Yield criteria for amorphous glassy polymers, Journal of Materials Science. 32 (1997) 1371–1379. https://doi.org/10.1023/A:1018525127466.

[85] R. Hill, Elastic properties of reinforced solids: Some theoretical principles, Journal of the Mechanics and Physics of Solids. 11 (1963) 357–372. https://doi.org/10.1016/0022-5096(63)90036-X.

[86] L. Collini, F. Moroni, A. Pirondi, Modeling the influence of stress triaxiality on the failure strain of nodular cast iron microstructures, Procedia Structural Integrity. 18 (2019) 671–687. https://doi.org/10.1016/j.prostr.2019.08.215.

[87] A. Sensini, G. Pisaneschi, D. Cocchi, A. Kao, G. Tozzi, A. Zucchelli, High-resolution X-ray tomographic workflow to investigate the stress distribution in vitreous enamel steels, Journal of Microscopy. (2020) 1–12. https://doi.org/10.1111/jmi.12996.

[88] S. Buell, Multiscale modeling and analysis of nanofibers and nonwoven materials, Mit.Edu. (2010). http://dspace.mit.edu/handle/1721.1/59213%5Cnhttp://web.mit.edu/vvgroup/img/SezenPoster.pdf.

[89] L. Vinet, A. Zhedanov, A "missing" family of classical orthogonal polynomials, 2011. https://doi.org/10.1088/1751-8113/44/8/085201.

[90] E. Tuncer, R. l'Abee, Numerical modeling of non-woven fiber mats: Their effective mechanical and electrical properties, International Journal of Computational Materials Science and Engineering. 04 (2015) 1550011. https://doi.org/10.1142/s2047684115500116.

[91]   S. Yu, J.Y. Hwang, S.H. Hong, 3D microstructural characterization and mechanical properties determination of short basalt fiber-reinforced polyamide 6,6 composites, Composites Part B: Engineering. 187 (2020) 107839. https://doi.org/10.1016/j.compositesb.2020.107839.

[92]   S. Domaschke, M. Zündel, E. Mazza, A.E. Ehret, A 3D computational model of electrospun networks and its application to inform a reduced modelling approach, International Journal of Solids and Structures. 158 (2019) 76–89. https://doi.org/10.1016/j.ijsolstr.2018.08.030.

[93]   T. Kanit, S. Forest, I. Galliet, V. Mounoury, D. Jeulin, Determination of the size of the representative volume element for random composites: Statistical and numerical approach, International Journal of Solids and Structures. 40 (2003) 3647–3679. https://doi.org/10.1016/S0020-7683(03)00143-4.

[94]   A.R. Boccaccini, Fabrication, microstructural characterisation and mechanical properties of glass compacts containing controlled porosity of spheroidal shape, Journal of Porous Materials. 6 (1999) 369–379. https://doi.org/10.1023/A:1009673814848.

[95]   B. Fiedler, M. Hojo, S. Ochiai, K. Schulte, M. Ando, Failure behavior of an epoxy matrix under different kinds of static loading, Composites Science and Technology. 61 (2001) 1615–1624. https://doi.org/10.1016/S0266-3538(01)00057-4.

[96]   C.S. Han, S.H.R. Sanei, F. Alisafaei, On the origin of indentation size effects and depth dependent mechanical properties of elastic polymers, Journal of Polymer Engineering. 36 (2016) 103–111. https://doi.org/10.1515/polyeng-2015-0030.

[97]   F. Alisafaei, C.S. Han, Indentation depth dependent mechanical behavior in polymers, Advances in Condensed Matter Physics. 2015 (2015). https://doi.org/10.1155/2015/391579.

[98]   F. Alisafaei, C.S. Han, N. Lakhera, Characterization of indentation size effects in epoxy, Polymer Testing. 40 (2014) 70–78. https://doi.org/10.1016/j.polymertesting.2014.08.012.

[99]   T.H. Hsieh, A.J. Kinloch, K. Masania, J. Sohn Lee, A.C. Taylor, S. Sprenger, The toughness of epoxy polymers and fibre composites modified with rubber microparticles and silica nanoparticles, Journal of Materials Science. 45 (2010) 1193–1210. https://doi.org/10.1007/s10853-009-4064-9.

[100] E.H. Andrews, Fracture in polymers, 1st ed., Oliver and Boyd, Edinburgh, 1968.

PART II

ELECTROSPUN NANOFIBERS FOR ENGINEERING APPLICATIONS

In this second part, an analysis of some pioneering implementations of electrospun nanofibrous membranes to engineering applications is presented. Nanofibers of different materials are analysed in each Chapter, depending on the functions they are intended to perform. In Chapter 3, the use of thermoplastic nanofibers made of nylon 6,6 to increase the fracture toughness of epoxy adhesive bonding is presented. In Chapter 4, recently developed rubbery nanofibers made by NBR / PCL (nitrile butadiene rubber / poly(ϵ-caprolactone)) blend are used to enhance the damping properties of unidirectional carbon fiber composite laminates. Finally, a novel self-sensing composite laminate capable of detecting impacts on its surface is presented in Chapter 5 using piezoelectric poly(vinylidenefluoride-trifluoroethylene) (PVDF-TrFE) nanofibers.

Chapter 3

Nanofibrous reinforced epoxy adhesive joints

3.1 Introduction

Adhesive bonding is an attractive alternative to traditional joining methods, such as welding and mechanical fasteners [1]. Bonded joints guarantee high strength-to-weight ratios, uniform stress distribution, corrosion resistance, hydraulic sealing, thermal and electrical insulation, and dynamic damping [2,3]. These characteristics, together with the cost-effectiveness and the ability to join multi-material, have favoured the use of adhesives in several industrial sectors such as automotive, aerospace, electronics, and for all those fields where lightweighting is mandatory [4].

Among structural adhesives, epoxy resins are the most used, as they exhibit high modulus and strength, low creep, and good performance at high temperatures [1–4]. However, as already mentioned for applications in composite laminates, epoxies are relatively brittle if not toughened by modifying their chemical composition or adding, for instance, organic (rubber-like), inorganic (mineral, ceramic) particles, or chopped fibers [5,6].

One of the most adopted methods to mitigate the epoxy resin brittleness is the use of rubber [7]. The rubber-toughening effect is achieved either by adding already cross-linked [8,9] or core-shell rubbery particles [10], or by mixing the liquid rubber (i.e. not cross-linked) with resin precursors, thus forming rubbery particles due to the rubber precipitation during the cross-linking process [9,11]. It has been shown that to improve the fracture toughness of epoxy systems a rubber fraction between 5 %wt and 20 %wt is required. Such a high amount, however, may negatively impact other mechanical and physical properties, reducing the glass transition temperature (T_g), the elastic modulus, and the strength of the neat resin [12].

In their review work, Nemati Giv *et al.* [6] quoted nano-reinforcement as an effective way to improve the mechanical properties of adhesive joints. However, they also concluded that these properties strongly depend on the manufacturing procedures and parameters such as particle size, content, and reinforcement/matrix interface. Epoxy adhesive reinforced with alumina nanospheres and nanorods prepared by Gupta *et al.* [13] by in-situ polymerisation technique showed a significant effect on shear strength as well as Mode I fracture toughness.

The addition of Carbon Nanotubes (CNTs) as nanofillers was also studied to improve properties such as stiffness, strength, and fracture toughness, besides electrical conductivity [14–23]. However, the results of these studies showed that both an increase or a decrease in strength and fracture toughness was possible depending on the CNT content and type, surface treatment, dispersion, testing methodology, and temperature. The addition of graphene nanoplatelets, graphene oxide nanoplatelets, and fullerene C60, besides carbon nanotubes, was studied by Akpinar *et al.* [15] on three different types of epoxy adhesives, showing that all these doping nanofillers can improve the stress-strain capacity of bonded joints.

On the other hand, it has been shown that the use of polymeric, composite, or ceramic nanofibers yields a reinforcement more effective than with conventional fibers [24,25]. In this perspective, as previously widely discussed, nanofibers generated by electrospinning provide a simple and versatile method for the reinforcement of composite laminates against delamination, by simply interleaving a randomly oriented or an aligned nanofibrous membrane (nanomat) between adjacent plies. This yields a ply-to-ply bridging effect that increases Mode I and Mode II fracture toughness as well as fatigue delamination strength of the composite laminate, as shown several times during the last decade [26–33]. This toughening strategy was also confirmed by Maloney and Fleck [34], who found that the introduction of a cylindrical woven copper wire mesh with polytetrafluoroethylene strips at regular intervals along the bondline caused large-scale bridging of the crack.

The toughening effect induced by electrospun nanomats in composite materials can be potentially exploited also in adhesive joints, yielding at the same time to producing alternative prepregs to conventional glass fiber mats employed in pre-cured supporting adhesive films. This application field is still little explored, with only a few papers published [35–38]. These studies are mainly focused on the use of medium-low fracture toughness epoxy resins. Razavi *et al.* [37] realized Double Cantilever Beam (DCB) tests with 7075-T651 aluminium substrates using a 2k epoxy adhesive (UHU plus Endfest 300) and verified that the integration of polyacrylonitrile (PAN) nanofibers directly electrospun onto the epoxy resin led to a two-fold increase in fracture toughness with respect to neat adhesive, although this latter was quite low (avg. value G_{Ic} = 0.11 N/mm over 30 mm up to 60 mm crack length propagation). Ekrem and Avcı [38], on the other hand, manufactured single-lap and DCB

joints using an epoxy adhesive and placing polyvinyl alcohol (PVA) electrospun nanofibers mats between adherents before curing. The shear strength revealed an increase of 13.50 %, while Mode I fracture toughness was about twice the neat adhesive. In these works, however, no one attempted to develop a prepreg nanomat to facilitate the application of the nanofibers since nanofibrous mats are generally difficult to handle due to the small stiffness and the tendency to fold and wrinkle.

The potential of an electrospun nylon nanofibrous mat as an adhesive carrier and reinforcing web in adhesive bonding has been proven by our research group in a previous work [39]. In that work, a prepreg nanomat was developed using a low-viscosity epoxy resin for composite hand lay-up, to favour wetting of the nanofibers and to minimize air entrapment. The choice of a 2k epoxy resin for composite hand lay-up instead of a 2k epoxy adhesive was made at that time to reduce difficulties in the impregnation of the nanomat and to keep curing cycle time and temperature compatible with the application. However, it exhibited poor adhesion and a fracture toughness well below that typical of epoxy adhesive systems.

Therefore, the present work is aimed at developing a laboratory route to manufacture a joint where a nylon nanomat is placed between the adherents as a potential reinforcement for a 2k epoxy adhesive. This research work involved three steps. The first one, reported in Section 3.2, was aimed to assess the possibility of developing a nanofibrous prepreg that would also contribute to the fracture toughness of an intermediate viscosity epoxy adhesive. The integration of a nanofibrous mat into a multi-purpose unfilled structural adhesive is reported in Section 3.3 as an intermediate step towards the addition of the nanomat to a high-viscosity and high-strength, two-component epoxy adhesive system, described in Section 3.4. These three different steps are presented in detail and in chronological order in the next Sections.

3.2 Development and fracture toughness characterization of a nylon nanomat epoxy adhesive reinforcement

Tommaso Maria Brugo[1], Francesco Musiari[2], Alessandro Pirondi[2],

Andrea Zucchelli[1], Davide Cocchi[1], Daniela Menozzi[3]

[1]Dipartimento di Ingegneria Industriale, Alma Mater Studiorum - Università di Bologna
viale del Risorgimento 2, 40136 Bologna, Italy

[2]Dipartimento di Ingegneria e Architettura - Università di Parma
Parco Area delle Scienze 181/A, 43124 Parma, Italy

[3]ELANTAS Europe Srl, Collecchio, Strada Antolini 1, 43044 Collecchio (PR), Italy

3.2.1 Abstract

The potential of an electrospun nylon nanofibrous mat as adhesive carrier and reinforcing web in adhesive bonding has been proven by the Authors in a previous work. In that work, a prepreg nanomat was developed using a low-viscosity epoxy resin for composite hand lay-up, in order to favour wetting of the nanofibers and to minimize air entrapment. However, the resin for hand lay-up exhibited a poor bonding performance when compared to the one typical of epoxy adhesives. The present work is therefore aimed at developing a laboratory route to add an electrospun polymeric nanomat to a two-part epoxy adhesive joint. Three different adhesives with increasing viscosity were preliminarily evaluated regarding the entrapment of air after curing. The most promising one was used to manufacture a small-size, Al-alloy double cantilever beam joint and the performance with and without the nanomat were compared. Three different precracking procedures were also developed and evaluated, namely fatigue precracking (A), razor blade tapping (B) and nanomat exfoliation (C). The results indicate that the fracture toughness of the nanomat-reinforced adhesive joint is similar to the neat adhesive one at the beginning of the propagation, but it becomes much higher as the crack advances.

Keywords: nanomaterials/nanostructures, bonding reinforcement, fracture toughness, bonded joints, aluminium alloys

3.2.2 Introduction

The present work is aimed at developing a laboratory route to manufacture a joint where a nylon nanomat is placed between the adherent as a potential reinforcement for a 2k epoxy adhesive. This is regarded as a first step towards the development of a prepreg that is necessary to evaluate if the nanomat gives a positive contribution to the fracture toughness. Three different epoxy systems with increasing viscosity were preliminarily evaluated regarding the entrapment of air after curing. The most promising one was used to manufacture a small-size, Al-alloy DCB joint to compare the Mode I fracture toughness with and without the nanomat. Three different precracking procedures were also developed and evaluated, namely fatigue precracking (A), razor blade tapping (B) and nanomat exfoliation (C).

3.2.3 Experimental methodology

3.2.3.1 Polymeric nanofibrous mats

Pellets of nylon 6,6 Zytel E53 NC010 (DuPont de Nemours Italiana S.r.l., Cernusco Sul Naviglio (MI), Italy) were dissolved in 10:60:30 by volume trifluoroacetic acid / formic acid / chloroform solution (Sigma-Aldrich S.r.l., Milan, Italy). The concentration of nylon 6,6 in the solution was 13 % by weight. The solution was injected in a needle, kept under high voltage by a power supply and then electrospun in the form of a 400×300 mm^2 foil, using a Spinbow$^®$ electrospinning machine unit equipped with four 5 mL syringes (Figure 3.1).
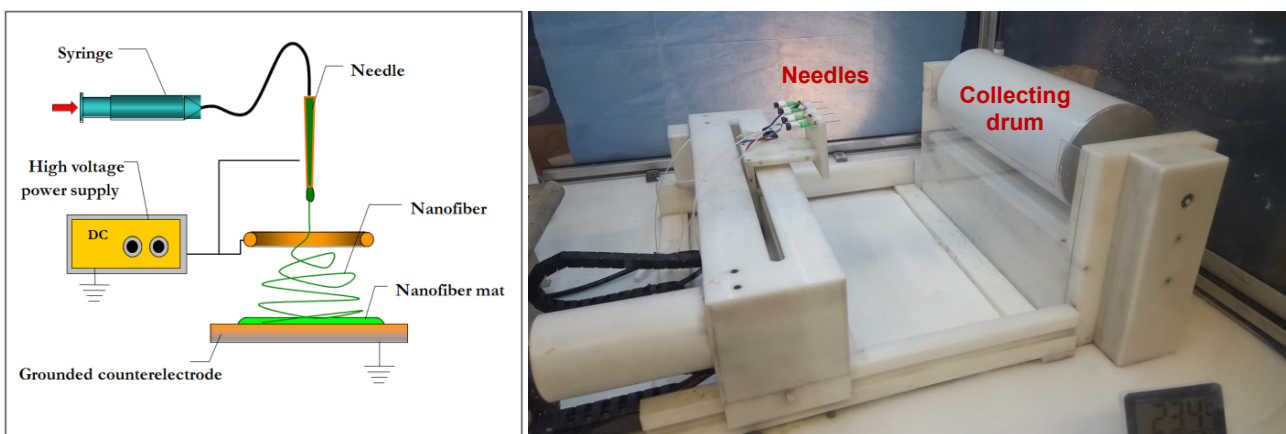

Figure 3.1 – Outline of the electrospinning process.

In electrospinning, when the electric field attains a threshold, the repulsive electric forces overcome surface tension, resulting in flash evaporation of the solvent and polymerization of the nylon in the first millimetres after the needle. The filament is accelerated towards a rotating drum

(kept at zero electric potential) that collects it; during the travel, the filament whirled around by electric forces forming a random mat. The electrospinning parameters are summarized in Table 3.1.

Table 3.1 – Electrospinning process parameters.

Nylon concentration	Flow rate (per noozle)	Electric potential	Needle inner diameter	Needle-collector distance	Tang. speed collecting drum	Temperature	Relative humidity
%wt	mL/h	kV	mm	mm	m/s	°C	%
13	0.70	25	0.51	65	0.39	24	40

The thickness of the nanomat could vary from some nanometres to hundreds of micrometres, depending on manufacturing time. In the current case, the thickness of the nanomat, measured with an optical microscope, was included in the range between 200 and 300 μm. While the nanofibers diameter, evaluated with a SEM (Phenom ProX), was assessed in 150 ± 20 nm (Figure 3.2).
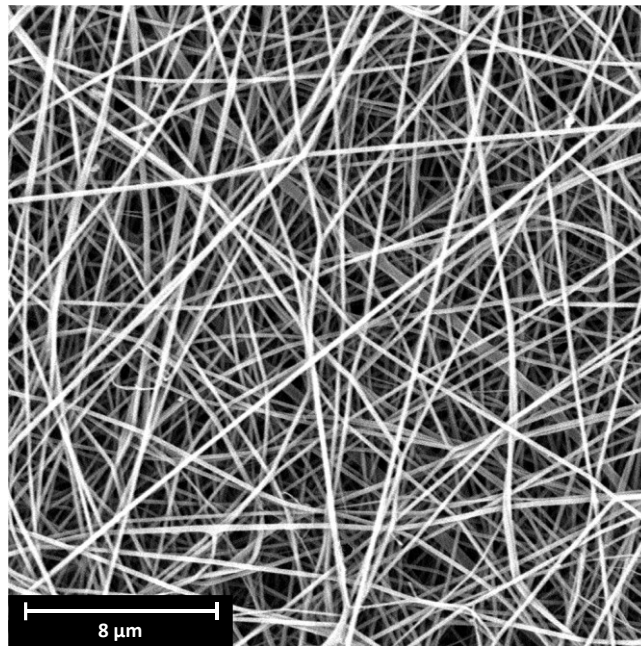
Figure 3.2 – SEM image of the nanomat at 10,000x magnification.

It is worth to underline that, though the nylon/epoxy adhesion is poor, in Palazzetti *et al.* [27] it was shown that a reinforcing mechanism existed related to fiber bridging. The choice of nylon was done also for coherence with the previous work [39].

3.2.3.2 Adherents

A 2024-T3 aluminium plate was cut and machined to obtain $120(l) \times 20(b) \times 6(h)$ mm^3 adherents. This size, smaller than that prescribed in the ASTM D3433 standard, was selected for the sake of an easier manipulation of the nanomat. The properties declared from the supplier (Aviometal, Arsago

Seprio (VA), Italy) are R_m = 615 MPa, $R_{p0,2}$ = 551 MPa. The surface to be bonded was cleaned, immersed in sodium hydroxide solution for 10 min, rinsed in distilled water, etched with P2-etching solution for 12 min at 60 °C according to ASTM D2651-01 and rinsed again with distilled water. Chemical etching was preferred over mechanical surface treatment (e.g. sandpaper or sandblasting) because of the potential in yielding higher adhesion on this aluminium alloy and also because the pronounced roughness of sandblasting might promote the formation of neat adhesive pockets close to the surface, where the crack can run in [39]. The results in terms of surface morphology are shown in Figure 3.3, where only scratches with a roughness R_a = 0.3 mm due to the finishing process with P800 sandpaper (FEPA standard – ISO6344) were present before etching (Figure 3.3A), while P2-etching treatment generated pits of hemispherical shape (Figure 3.3B). Two classes of pit size can be distinguished, which differ of one order of magnitude with each other. The smaller size pits are the most present on the surface and the related value of roughness is R_a = 0.45 mm.
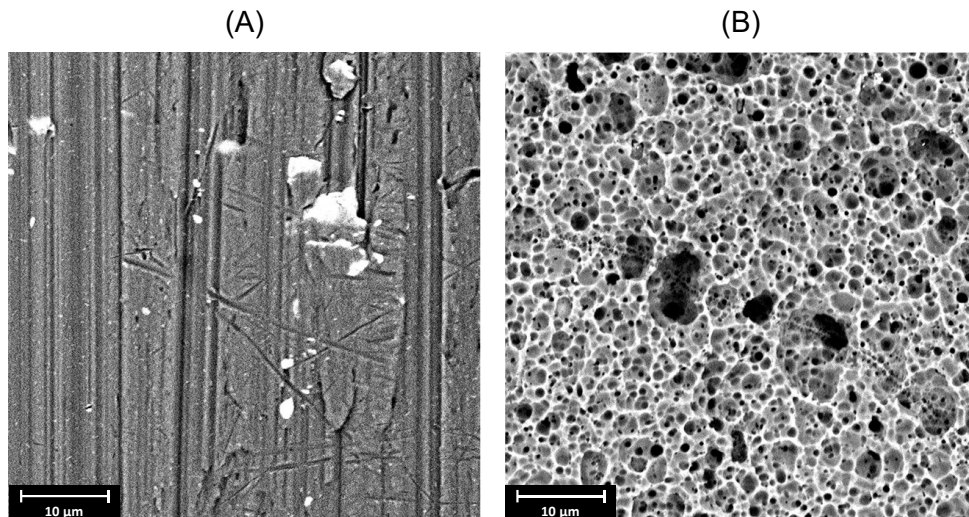

Figure 3.3 – Surface morphology of the aluminium (A) before and (B) after P2-etching.

3.2.3.3 Specimen fabrication

Since the adhesive must penetrate the dense fiber network of the nanomat, three two-part epoxy systems with different levels of room temperature viscosity were preliminarily evaluated. All of them were supplied by ELANTAS (ELANTAS Europe Srl, Collecchio (PR), Italy). Bulk properties from the datasheet of the supplier are summarized in Table 3.2. The two parts were mixed in a glass beaker in the resin:hardener weight ratio suggested by the supplier. The mixture is then poured in a large bowl where the nanomat was immersed for a few minutes to fully wet. Full wetting is evaluated as the attainment of transparency of the mat when picked up and exposed to light. In these preliminary tests aimed at evaluating qualitatively the impregnation, the wet nanomat strips were cured in a vacuum bag following the cycle in Table 3.2 without placing them between adherents.

Table 3.2 – Bulk properties at room temperature of the two-part epoxy adhesives Elan-tech® AS46/AW46, Elan-tech® AS53/AW09, and the two-part epoxy resin for hand lay-up Elan-tech® EC52TIX/AW192 (ELANTAS Italia Srl, Italy).

Property	Unit	AS46 / AW46	AS53 / AW09[a]	EC152TIX/ AW192
Viscosity	mPa s	20–32,000	12–18,000	5–7,500
Gel time	h	5–6	4–6	11.5–12.5
Suggested cure cycle	h	3	24 + 15	24 + 15
	°C	50	RT + 80	RT + 60
Glass transition temperature, T_g (ASTM D3418) after 24 h at RT	°C	48–54	90–100	88–94
Flexural strength (ASTM D790)	MPa	56–64	–	–
Maximum strain (ASTM D790)	%	4.5–6.5	–	–
Strain at break (ASTM D790)	%	> 15	–	–
Flexural modulus (ASTM D790)	MPa	1,600–2,000	–	–
Tensile strength (ASTM D638)	MPa	36–44	–	–
Elongation at break (ASTM D638)	%	4–6	–	–
Shear strength (ASTM D1002) on aluminium, cured 16 h at 40 °C	MPa	20–25	–	–
Peel strength (ASTM D1876) on aluminium, cured 3 h at 50 °C	N/cm	48–58	–	–

[a] 100:50 resin:hardener weight ratio

The cured epoxy + nanomat strips were examined optically on the outer surface to look for entrapped air bubbles ('External surface' row of images in Figure 3.4), then they were broken manually and examined at the SEM ('Rupture surface' row of images in Figure 3.4).
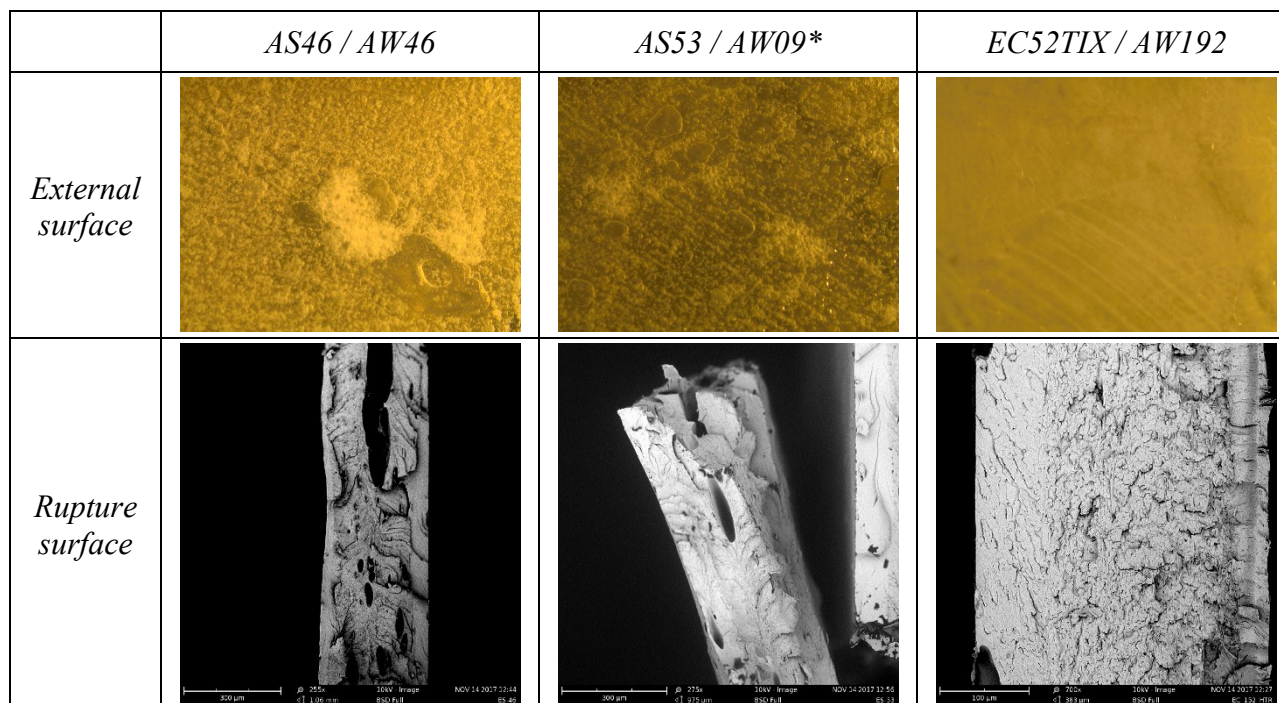

Figure 3.4 – Results of preliminary tests in terms of air entrapment after curing of the two-part epoxy systems + nanomat.

From the SEM images in Figure 3.4, the resulting final thickness was assessed in the range 300 ÷ 330 mm for the three adhesive + nanomat combinations. It is also evident that the adhesive with the lowest viscosity (Elan-tech® EC152TIX / AW192) showed the minimal presence of air bubbles. However, since the supplier datasheet suggested this adhesive for composite impregnation but not for structural bonding, the intermediate viscosity, unfilled epoxy adhesive system Elan-tech® AS53 / AW09 was preferred, though at the risk of some air entrapment. The following procedure and tests were therefore carried on using this latter adhesive. Two specimen configurations were manufactured: a so-called virgin (V) one where the adhesive was used alone and a nano-modified one (N), in which the adherents were bonded with the presence of the nanomat. The nano-modified joints were manufactured first to evaluate the bondline thickness after curing. Alike preliminary tests, nanomat strips were immersed into the adhesive in a large bowl for a few minutes. Full wetting is then evaluated as the attainment of transparency of the mat when picked up and exposed to light. The nanomat was laid onto the surface of one adherent placed in a template. A 27 mm long defect was obtained by placing a Teflon sheet between the adherents before closing the joint. The excess resin was removed, and specimens were inserted in a vacuum bag (Figure 3.5) and cured (according with the adhesive supplier) for 15 h at 80 °C + 3 h at 115 °C, in order to speed up the process with respect to the 24 h at RT + 15 h at 80 °C as reported in Table 3.2. Vacuum was held in the bag while curing to increase the evacuation of the residual air trapped within the polymer.

Figure 3.5 – DCB joints placed in the vacuum bag.

Specimens were then removed from the vacuum bag and the effective thickness of the bondline was measured close to the beginning, at middle length and close to the end on both sides of the specimen by an optical microscope. The average calculated on all the specimens was 384 µm with a standard deviation of 83 µm. Since the fracture toughness is dependent on bondline thickness [3], to avoid a bias in the comparison the neat resin ('virgin') DCBs were manufactured with spacers placed

at the extremities to get the same thickness of the nano-modified ones. Three batches were manufactured to test different precrack insertion methodologies:

A)   Fatigue precracking from Teflon foil starter (one virgin and two nano-modified joints);

B)   Tapping of a razor blade on the crack front given by the Teflon foil starter (one nano-modified);

C)   Inserting the Teflon foil starter for a few millimetres into the nanomat (one virgin and three nano-modified).

To insert the Teflon, the nanofibrous strip was cut about 5 mm longer than the nominal size of the specimen. Adhesive tape is then applied to both sides of the portion of nanomat in excess, which is then peeled apart, Figure 3.6A. The Teflon foil was inserted between the two peeled arms of the nanomat and then everything is wrapped together with adhesive tape in the portion exceeding the specimen size (Figure 3.6B). The nanomat – Teflon assembly is thereby passed to the manufacturing phase of the joint and the exceeding portion was removed only after the specimen is held in the template.

(A)   (B)
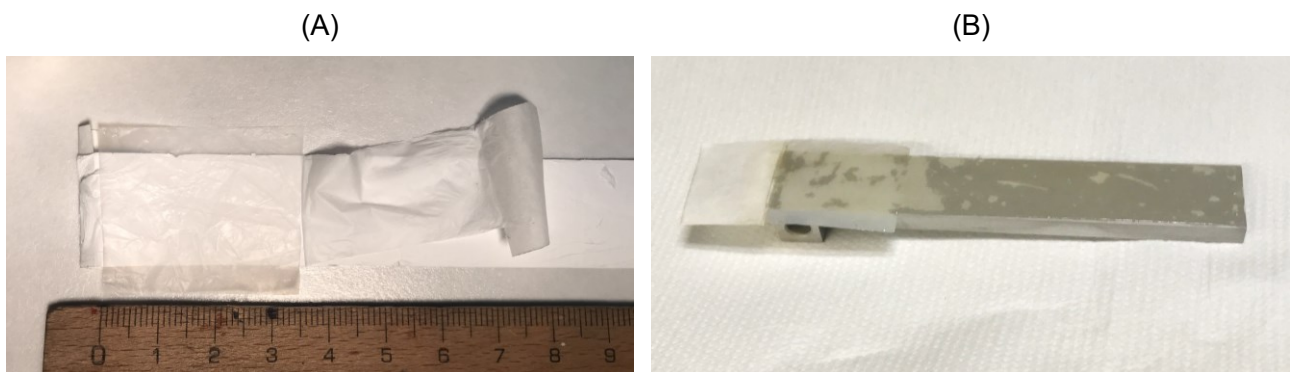
Figure 3.6 – Illustration of precrack insertion procedure C: (A) Exfoliation of the nanomat at one side and (B) Teflon foil inserted in the exfoliated zone of the nanomat.

3.2.3.4 DCB testing

A servo-hydraulic testing machine MTS 810 equipped with a 3 kN load cell was used to perform tests under displacement control at a constant crosshead speed. A clip gage was used to measure the Crack Mouth Opening Displacement (CMOD) δ', reported in Figure 3.7. Partial unloadings were performed during the fracture test to record the specimen compliance and, in turn, to evaluate the actual crack length using the Krenk's model [41], represented by Equation 3.1. The latter is based on the beam on an elastic foundation model that accounts for the out-of-plane deformation of the adhesive layer and the rotation at the crack tip. The equation was corrected considering the distance

g of the CMOD measurement point from the load axis and the effect of shear (rightmost term in Equation 3.1):
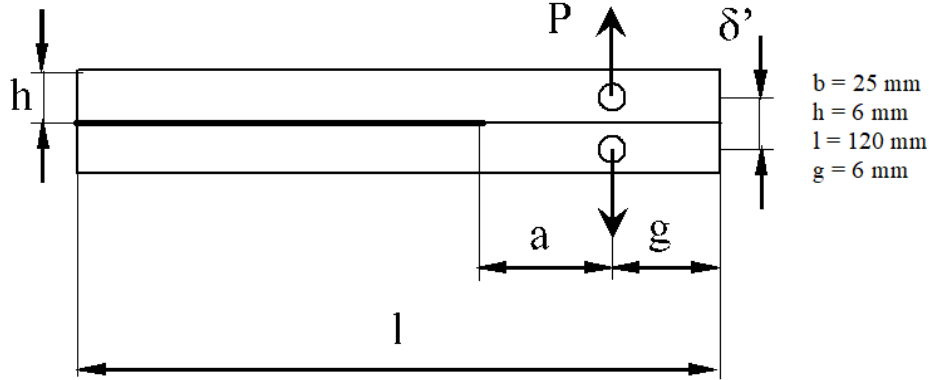

Figure 3.7 – Outline of the DCB test setup.

$$\frac{\delta'}{P} = 2\left[\frac{2\lambda_\sigma}{k}(1 + \lambda_\sigma a) + (a + g)\frac{2\lambda_\sigma^2}{k}(1 + 2\lambda_\sigma a) + \frac{a^3}{3EJ} + g\frac{a^2}{2EJ}\right] \qquad \text{Eq. 3.1}$$

where λ_σ and k, i.e. the length scale of the stress distribution in a DCB joint and the elastic foundation stiffness [41], respectively, are expressed as:

$$\lambda_\sigma = \left(\frac{6}{h^3 t}\frac{E_a}{E(1 - v_a^2)}\right)^{1/4} \qquad \text{Eq. 3.2}$$

$$k = \frac{2E_a b}{t\,(1 - v_a^2)} \qquad \text{Eq. 3.3}$$

The Mode I strain energy release rate G_I is defined as:

$$G_I = \frac{(Pa)^2}{bEJ}\left(1 + \frac{1}{\lambda_\sigma a}\right)^2 \qquad \text{Eq. 3.4}$$

A Young's modulus of $E = 70$ GPa was considered for 2024-T3 adherents, as a typical value for these alloys. Concerning the adhesive, since the Young's modulus was not given in the technical datasheet, E_a was taken equal to the flexural modulus of the companion adhesive Elan-tech® AS46 / AW46 (2,000 MPa, see Table 3.2) and the Poisson's ratio $v_a = 0.4$ as common for epoxies. Since the elastic modulus of nylon 6,6 is approximatively the same as the epoxy resin and the nanofibers volume fraction is at most 10÷15 %, also the Young's modulus of the nanomat prepreg can be considered approximately the same as the neat adhesive.

3.2.4 Results and discussion

The force versus CMOD relative to both the virgin (V) and nano-modified (N) specimens are presented in Figure 3.8A (precracking methodologies A and B) and Figure 3.9A (precracking methodology C), while the corresponding diagrams of fracture toughness as a function of crack propagation are reported in Figure 3.8B and Figure 3.9B, respectively.
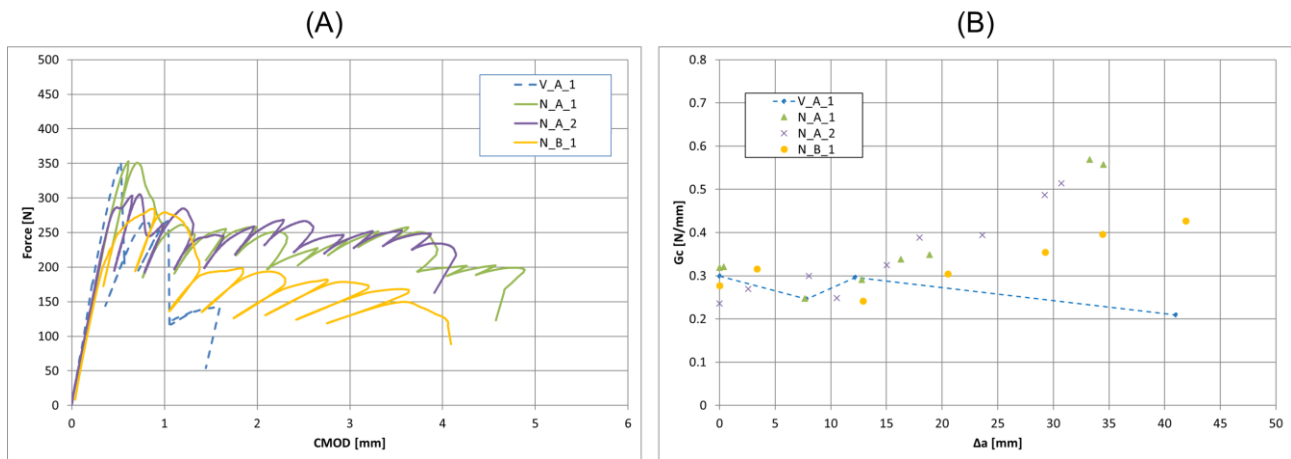

Figure 3.8 – (A) Force versus CMOD and (B) fracture toughness versus crack propagation. V: virgin, neat adhesive; N: nanomat reinforced adhesive; A, B: precrack insertion technique type A or B.
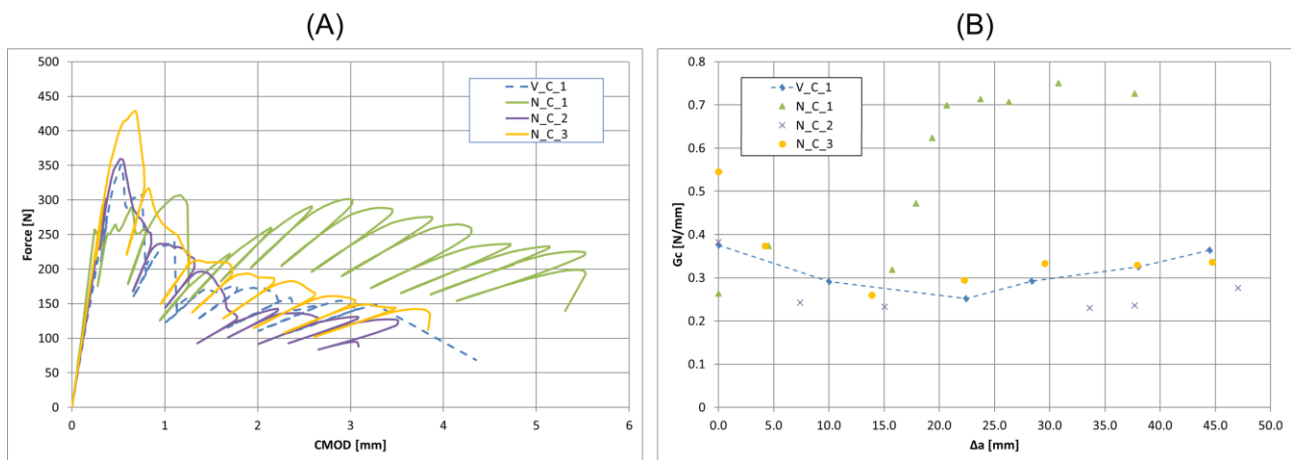
Figure 3.9 – (A) Force versus CMOD and (B) fracture toughness versus crack propagation. V: virgin, neat adhesive; N: nanomat reinforced adhesive; C: precrack insertion technique type C.

The force versus CMOD in Figure 3.8A exhibits a sawtooth shape with large drops of force at a given displacement indicating the propagation occurred by crack jumps, although no clues of this process are left on the fracture surface (Figure 3.10A). The fracture toughness of the virgin joint in Figure 3.8A is not very high (G_{Ic} = 40.3 N/mm) because the adhesive used was an unfilled untoughened epoxy. Only one test was performed on the virgin configuration, using type A and none using type B precracking. However, a predominantly cohesive failure was found with a smooth

fracture surface, which means the fracture resistance of the adhesive was exploited at the best. The force peak of the nano-modified joint is comparable or even lower with respect to that of the virgin one, but the force during the propagation phase is higher and the decrease is smoother (no sawtooth shape with large force drops). This behaviour is reflected in the fracture toughness (Figure 3.8B), that is initially constant and similar to that of the virgin joint but after 10 mm of crack propagation it starts to increase steadily becoming about twice that of the virgin specimen after 40 mm of crack advance. An examination of the fracture surface of the nano-modified specimens (Figure 3.10B) revealed that the separation takes part initially at or close to the interface even though the specimen surface treatment was the same of the virgin joint. For this reason, an apparent *R*-curve seems not to be the explanation of the behaviour. Rather, in the first millimetres the crack probably ran close to the interface in a thin layer of adhesive not expelled during the vacuum bag consolidation and that constitutes the weaker part of the joint. This mechanism explains also why the fracture toughness of the nano-modified and of the virgin is similar in the first part of the test. As the crack progresses, areas of cohesive failure appear. This is probably the reason for the increase in fracture toughness. The development of a partly cohesive failure may be related to the local development of an intimate contact between adherent and nanomat either due to a complete expulsion of the adhesive in excess or a higher thickness of the nanomat.
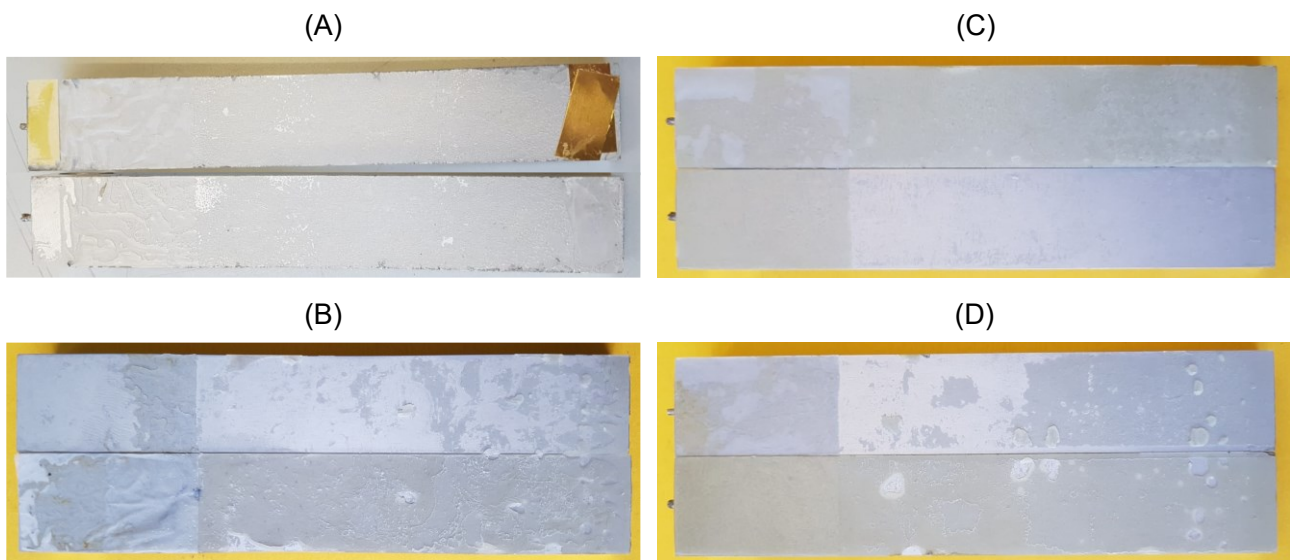

Figure 3.10 – Fracture surface of (A) V_A_1, (B) N_A_1, (C) N_C_2, and (D) N_C_1 specimens.

A result very similar to that of techniques A and B was found in the case of type C precrack insertion technique concerning the virgin joint, that showed a cohesive failure. Also force versus opening (Figure 3.9A) and fracture toughness (Figure 3.9B) showed trends and values very similar to those of techniques A and B, meaning that the different precrack insertion technique does not alter

the results. Two of the nano-modified specimens (N_C_2 and N_C_3) showed a force peak comparable or higher than that of the virgin one, but the values became closer during the crack propagation phase. This is reflected in the fracture toughness values that get close to each other as the crack progresses. Looking at the fracture surface of N_C_2 specimen (Figure 3.10C), it is clear that the crack did not progress into the nanomat but, in this case, an examination at the SEM revealed the naked aluminium surface (the pickled aspect due to P2-etching is evident) except ripples of adhesive + nanomat that were left randomly on the crack surface (Figure 3.11A). Therefore, it seems that the presence of these anchor points was sufficient to guarantee a fracture toughness comparable to that of the virgin joint.

(A)   (B)
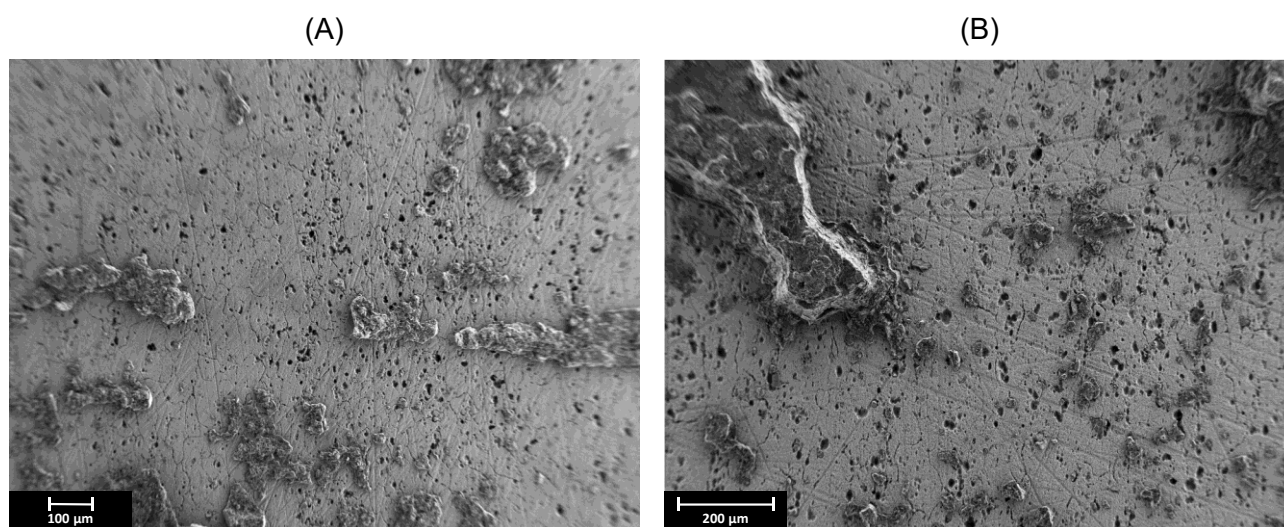
Figure 3.11 – SEM image of the fracture surface of (A) N_C_2 and (B) N_C_1 specimens.

The real potential of the nano-reinforcement is visible in the specimen N_C_1, where the crack started in a way similar to the other two specimens but, after about 20 mm of crack propagation the mechanism switched from close to the interface to cohesive in the nanomat (Figure 3.10D), yielding a sharp increase of fracture toughness from 0.3 to 0.7 N/mm (see Figure 3.9B). The SEM image in Figure 3.11B investigates the crack surface region before the change in the propagation modality. A close resemblance with Figure 3.11A is evident, with perhaps a higher number and finer ripples of adhesive left on the surface. In both Figure 3.11A and Figure 3.10B the adhesive + nanomat leftover seems to be locked into the pits caused by etching. Whether the number of anchor points is related to the transition from mostly interfacial to cohesive fracture is difficult to ascertain at the moment; however, a more careful control on the wetting of the surface is probably the key to exploit completely the potential of the nano-reinforcement, that so far can be estimated to give at least a factor of two increase in fracture toughness with respect to the neat adhesive.

3.2.5 Conclusions

In the present work a manufacturing route to obtain a two-part epoxy adhesive bonded joint reinforced with an electrospun polymeric nanomat was developed. The potential of the nanomat to act as reinforcing web in adhesive bonding was analysed by DCB fracture testing. Three different precracking procedures were developed and evaluated, namely fatigue precracking (A), razor blade tapping (B) and nanomat exfoliation (C). The effectiveness of this technique in improving the fracture toughness of the neat resin was proven even though in some cases it was detected that the crack did not progress into the nanomat, rather it ran at the interface leaving a series of adhesive + nanomat ripples locked into the etching pits on the surface. A more careful control of this phenomenon, i.e. on the wetting of the surface, is probably the key to completely exploit the potential of the nano-reinforcement that, where the fracture was cohesive in the nanomat, yielded at least a two-fold increase in fracture toughness with respect to the neat adhesive.

3.3 Characterization of aluminium alloy-epoxy bonded joints with nanofibers obtained by electrospinning

Davide Cocchi[1], Francesco Musiari[2], Tommaso Maria Brugo[1], Alessandro Pirondi[2], Andrea Zucchelli[1], Fabio Campanini[3], Enrico Leoni[4], Laura Mazzocchetti[4]

[1]Dipartimento di Ingegneria Industriale, Alma Mater Studiorum - Università di Bologna viale del Risorgimento 2, 40136 Bologna, Italy

[2]Dipartimento di Ingegneria e Architettura - Università di Parma Parco Area delle Scienze 181/A, 43124 Parma, Italy

[3]ELANTAS Europe Srl, Collecchio, Strada Antolini 1, 43044 Collecchio (PR), Italy

[4]Dipartimento di Chimica Industriale "Toso Montanari", Alma Mater Studiorum - Università di Bologna viale del Risorgimento 4, 40136 Bologna, Italy

3.3.1 Abstract

In previous works, the Authors showed that nylon nanofibers in the form of a random nanomat obtained by electrospinning can be used in bonded joints, where they may also work as an adhesive carrier. In those works, the setup of the bonding procedure started from a low-viscosity epoxy resin for hand lay-up to facilitate wetting of the nanomat, then a medium viscosity, two-component, unfilled epoxy adhesive was employed as an intermediate development step towards the addition of the nanomat to a high-viscosity, high strength, two-component epoxy adhesive system. The present work was therefore aimed at analysing the performance of an epoxy adhesive for structural bonding, modified with the addition of a nylon nanomat generated by electrospinning. The adhesive was mixed and air bubbles were evacuated, then the nanomat was immersed in the adhesive, gently squeezed through two adjacent drums, counter-rotating at a given distance, to eliminate excess adhesive and to calibrate the wet nanomat thickness. The wet nanomat strip was finally placed between AA6082-T4 adherents and let to consolidate to obtain DCB bonded specimens. Fracture tests were performed and the Mode I fracture toughness with and without the nanomat was compared.

Keywords: nanomaterials, bonding reinforcement, fracture, aluminium and alloys

3.3.2 Introduction

The potential of electrospun nylon nanofibrous mats to carry the adhesive and reinforce the joint was evaluated by the Authors in previous works [39,40]. The setup of the bonding procedure started from a low-viscosity epoxy resin for hand lay-up [39] in order to facilitate wetting of the nanomat, then a medium-viscosity, two-component, multi-purpose unfilled epoxy adhesive was employed as an intermediate development step in [40] towards the addition of the nanomat to a high-viscosity, high strength, two-component epoxy adhesive system. However, in those works the joint exhibited limited adhesion and a fracture toughness lower that typical of epoxy adhesive systems. Therefore, the present work was aimed at manufacturing a structural epoxy adhesive joint with a nylon nanomat generated by electrospinning as a reinforcing web. The adhesive was mixed and air bubbles were evacuated, then the nanomat was immersed in the adhesive, gently squeezed through two adjacent drums, counter-rotating at a given distance, to eliminate excess adhesive and to calibrate the wet nanomat thickness. The wet nanomat strip was finally placed between AA6082-T4 adherents and let to consolidate to obtain DCB bonded specimens. Fracture tests were performed and the Mode I fracture toughness with and without the nanomat was compared.

3.3.3 Experimental methodology

3.3.3.1 *Polymeric nanofibrous mats*

For coherence with previous works [39,40], also in this study nylon 6,6 was used to produce the nanofibrous membrane. The nanomat manufacturing procedure was the same reported in Section 3.2.3.1, as well as the electrospinning parameters (Table 3.1). The thickness of the nanomat was included in the range between 50 and 82 μm, that was the average value detected along the nanomat strip by a digital indicator (ALPA, Pontoglio (BS), Italy) with a 0.65 N preload, resolution of 1 μm, max error of 4 μm, and repeatability of 2 μm. While the nanofibers were assumed to have a diameter of 150 ± 20 nm alike previous works, since the electrospinning process parameters are the same. A thickness of the nanomat lower than that of those works was instead chosen to facilitate the wetting of the nanomat by the adhesive, that has a viscosity higher than the resins used in [39,40]. One hour before adhesive application, the nanomat was placed for 15 min under vacuum and then heated in an oven at 40 °C for at least 30 min to eliminate humidity and solvent residues.

3.3.3.2 Adherents

A AA6082-T4 aluminium plate was cut and machined to obtain $100(l) \times 10(b) \times 5(h)$ mm^3 adherents. This non-standard small size was selected for the sake of an easier manipulation of the nanomat, especially after the wetting in the adhesive. The surfaces to be bonded undergone the following preparation sequence, developed after a careful literature survey:

1)   polishing;

2)   cleaning and degreasing;

3)   pickling with an alkaline solution (100 g/L NaOH) at 60 °C for 1 min;

4)   rinsing and sonication in water;

5)   wiping with blotting paper and cleaning;

6)   P2-etching at 65 °C for 12 min according to ASTM D2651-01;

7)   repeating of steps 4 and 5;

8)   5 hours self-passivation in air;

9)   15 min under vacuum 1 h before bonding;

10)   oven heating at 40 °C for 30 min.

Chemical etching was performed instead of sandpapering/sandblasting because of the potential in yielding higher adhesion and to avoid the formation of adhesive pockets close to the surface as detected in [39]. The results in terms of surface morphology are shown in Figure 3.12.
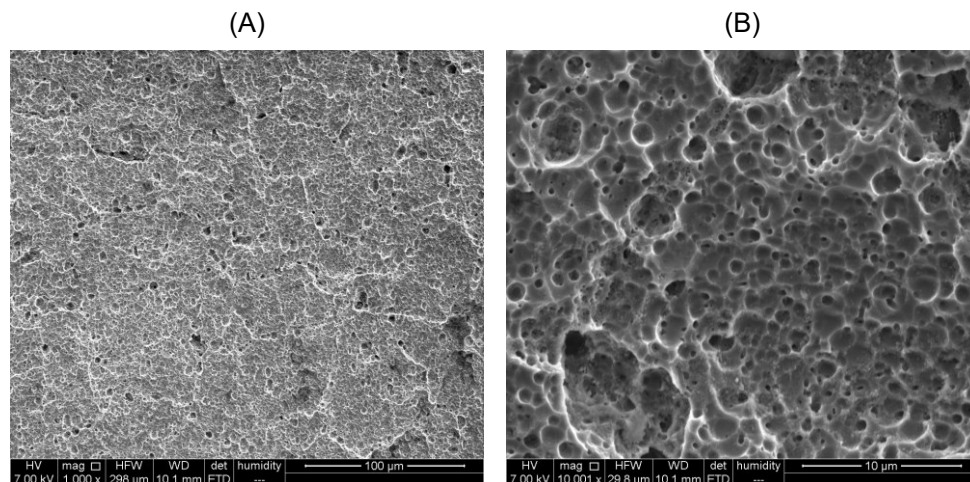

Figure 3.12 – Aluminium adherent surface after preparation at (A) 1,000x and (B) 10,000x magnification.

It can be observed the distribution of pit sizes, ranging about 1÷10 μm, and that smaller pits developed also inside larger ones because of the etching process. The value of roughness, measured with a Taylor-Hobson CCI non-contact profilometer (resolution 340 nm longitudinal, 1 nm vertical; Taylor-Hobson Ltd, Leicester, UK) was $R_a = 0.91$ μm instead of $R_a = 0.45$ μm obtained in [40].

3.3.3.3 Specimen fabrication

The 2k epoxy adhesive adopted for this study is the Elan-tech® AS46 / AW46 supplied by ELANTAS (ELANTAS Europe Srl, Collecchio (PR), Italy). This adhesive is the most viscous of those used in the previous study [40], as an intermediate development step towards the addition of the nanomat to a high-viscosity, high strength, two-component epoxy adhesive system. Bulk properties from the supplier datasheet are summarized in Table 3.2. In the previous work, preliminary tests aimed at evaluating qualitatively the impregnation of the nanomat were performed (Section 3.2.3.3). The rupture surfaces of the impregnated and cured mats were examined at the SEM, evidencing the presence of large air bubbles for the Elan-tech® AS46 / AW46 system (Figure 3.4). Therefore, in this work a new procedure was developed, consisting of the following steps:

1)   pour the two parts of the adhesive in a beaker;

2)   gently mix under vacuum;

3)   drip the mixed adhesive on the nanomat strip and distribute using a spatula;

4)   wait for the absorption of the adhesive into the nanomat until it becomes transparent;

5)   calibrate the wet nanomat through two motorized counter-rotating drums (Figure 3.13).
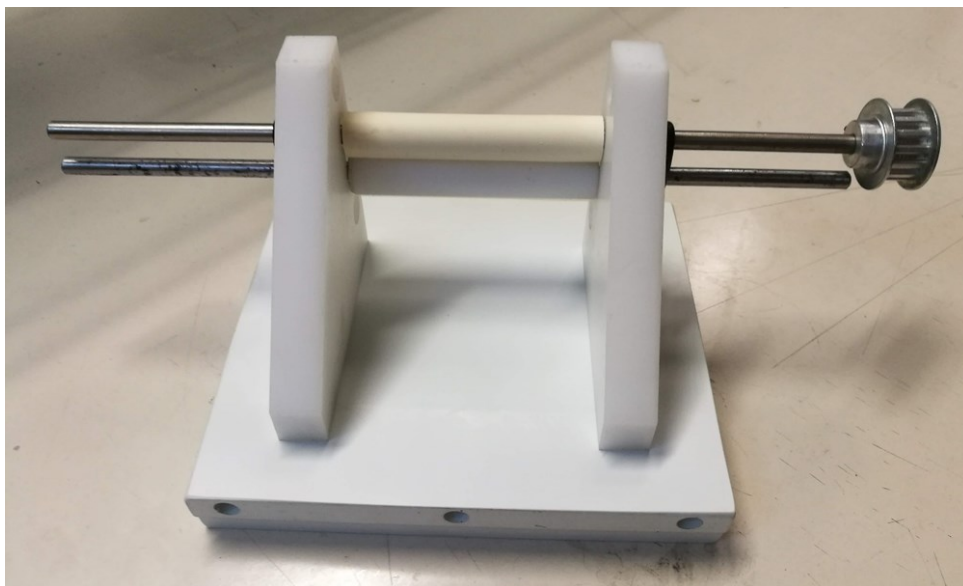
Figure 3.13 – Calibration device based on counter-rotating drums.

A so-called 'virgin' (V) and a nano-modified (N) joints were manufactured, wherein the latter the adherents were bonded with the addition of the nanomat. The N joints were manufactured before the V ones to evaluate the bondline thickness after curing. The nanomat was wet according to the procedure described previously, placed on one adherent, then the second adherent closed the joint. The bonding was done in a template where the specimens were left until consolidation (Figure 3.14).

A 35 mm-long defect was obtained by inserting a PTFE foil into the nanomat before wetting, according to the procedure described in [40] (Section 3.2.3.3) and illustrated in Figure 3.15.
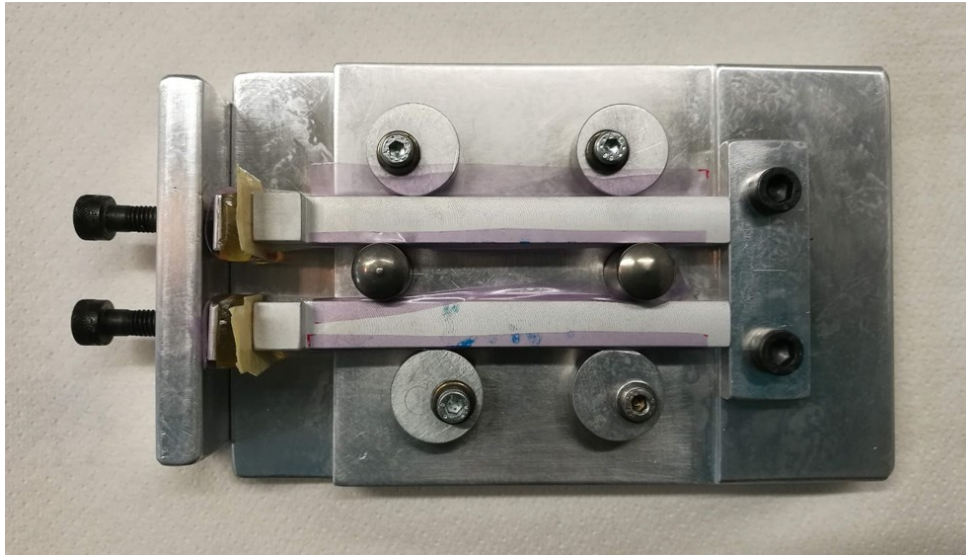

Figure 3.14 – DCB joints placed in the template. One can notice the pink polyethylene foils wrapping the specimens to avoid adhesion to the template.
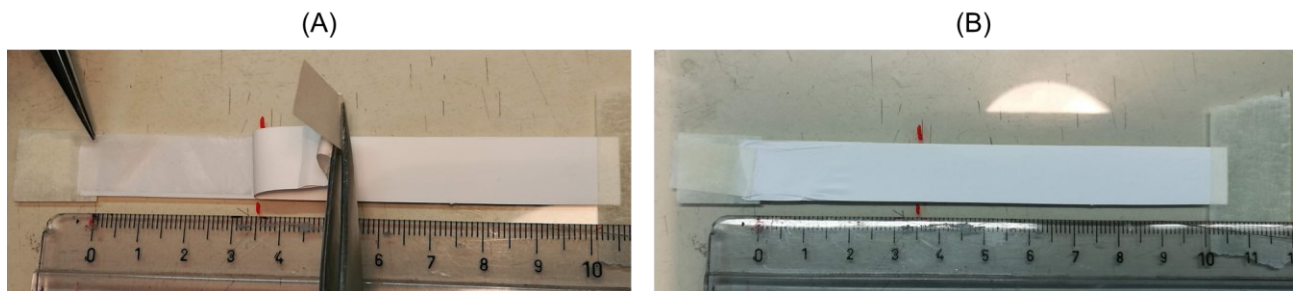

Figure 3.15 – Illustration of precrack insertion procedure: (A) exfoliation of the nanomat at one side and insertion of the Teflon foil; (B) precracked nanomat ready for being wet with the adhesive.

The specimens were subjected to a dead load (average pressure generated equal to 50 kPa) to evacuate the adhesive in excess and then cured in air according to the supplier prescriptions. The choice of curing in air was related to the observation that the application of vacuum in the case of V specimen promoted the suction of the not yet cured adhesive.

After curing, the N-type specimens were removed from the template and the effective thickness of the bondline was measured by an optical microscope at three equally spaced points on both sides. The thickness varies from 58 to 95 μm, that was with a slight increase with respect to the dry nanomat due to the presence of the adhesive. To avoid the dependency of fracture toughness on bondline thickness [3], the V specimens were manufactured with spacers at the extremities that result a thickness in the same range of the N ones.

3.3.3.4 DCB testing

The DCB tests were performed in the same way as the previous study [40]. Please refer to Section 3.2.3.4 for further details. The only difference concerns the geometry of the DCB specimen, which was reduced as compared to the previous study. In Figure 3.16 is reported the reduced one here adopted. In this study, as well, Krenk's model was used to evaluate the crack length [41].
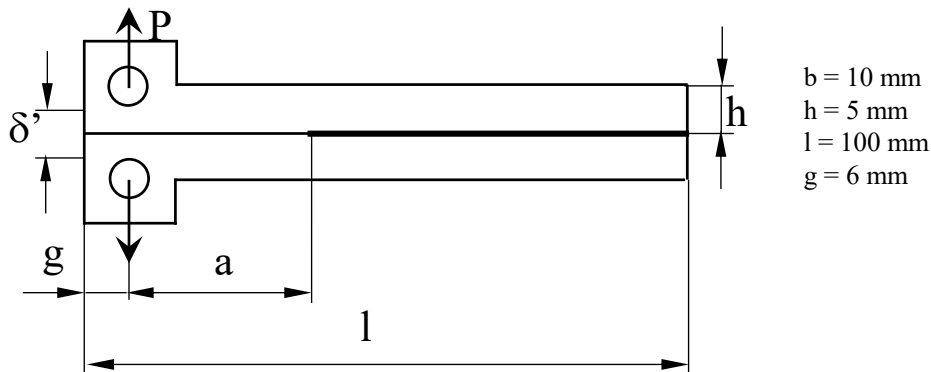

Figure 3.16 – Outline of the DCB test setup.

The Young's modulus of AA6082-T4 was considered to be E = 70 GPa, a typical value for aluminium alloys. Concerning the adhesive, the Young's modulus E_a was taken equal to the average value of the flexural modulus indicated in the supplier datasheet (1,800 MPa, see Table 3.2) and the Poisson's ratio v_a = 0.4 as common for epoxies. As previously explained, the Young's modulus of the nanomat prepreg can be considered approximately the same of the neat adhesive.

3.3.4 Results and discussion

The force versus CMOD relative to both the virgin (V) and nano-modified (N) specimens are presented in Figure 3.17A and Figure 3.17B, respectively, in order to have a more clear overview of the trends. Loading-unloading steps for the evaluation of the compliance are also reported. For both the V and the N joints the behaviour is smooth, indicating a progressive growth of the crack, i.e. without jumps and following arrests. The peak forces of the V joints are lower than those of the N ones, from which a higher fracture toughness of nano-modified joints can be foreseen. For values of CMOD greater than 2 mm the overall trends of the N and V joints get closer, hence the force shows a sharper decrease in the case of N joints. Therefore, to establish if a difference in terms of fracture toughness persists, the whole R-curve presented in Figure 3.18 was examined. Differently from what the examination of the overall force-CMOD data indicated, the N joints that start from values of G_{Ic} comparable or lower than the V ones (average value of 0.23 N/mm against 0.26 N/mm) that may imply a similar crack initiation mechanism.
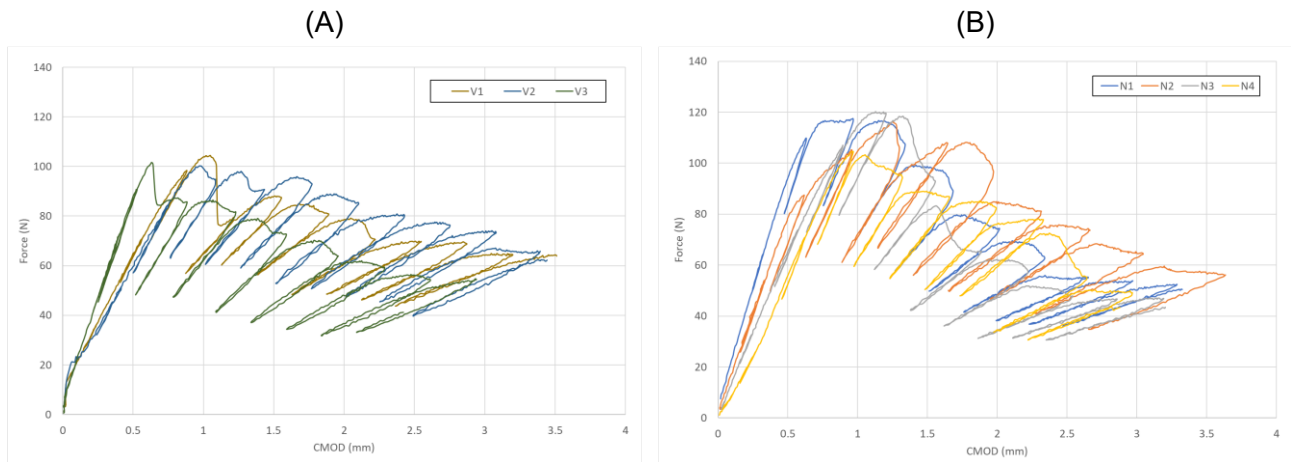
Figure 3.17 – Force vs. CMOD for (A) virgin and (B) nano-modified DCB joints.

From the visual inspection of the fracture surfaces in two selected cases, one N (Figure 3.19A) and one V (Figure 3.19B), it was indeed not possible to distinguish a different failure mechanism, that was characterized by a failure at or close to the interface despite the etching treatment of the aluminium adherents and the low thickness of the bondline. This mechanism may justify also the relatively moderate value of fracture toughness for a structural adhesive. On the other hand, with increasing crack propagation the fracture toughness of N joints increased more rapidly than that of V joints, meaning that some kind of toughening mechanism related to the nanofibers developed. This is corroborated, for crack propagations in the range 4÷8 mm, by the fact that the scatter bands of N and V joints, represented in Figure 3.18 by the average value ± one-half standard deviation, are not overlapped.
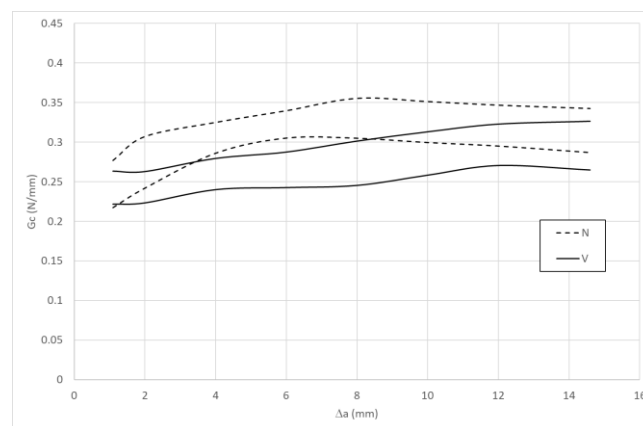

Figure 3.18 – Fracture toughness vs. crack propagation. The lines represent the scatter band of experiments (average value ± one-half standard deviation).

The fracture surfaces in Figure 3.19A and Figure 3.19B are characterized in both cases by frequent crack path deviations from close to one adherent to the other one, with a balance of the adhesive left on the two surfaces. Only in the case of N joints, some adhesive seems to be left also on

the brighter side, that may justify the higher fracture toughness with respect to the V ones. In the case of specimen N3 Figure 3.20A, the crack path deviations were less frequent. Therefore, the value of G_{Ic}, initially higher than V joints, decreased with crack propagation approaching the one of the V3 joint, where a similar crack path was detected, Figure 3.20B. Hence, the joints that performed better were those with more frequent crack path deviations because it implies more energy dissipation.
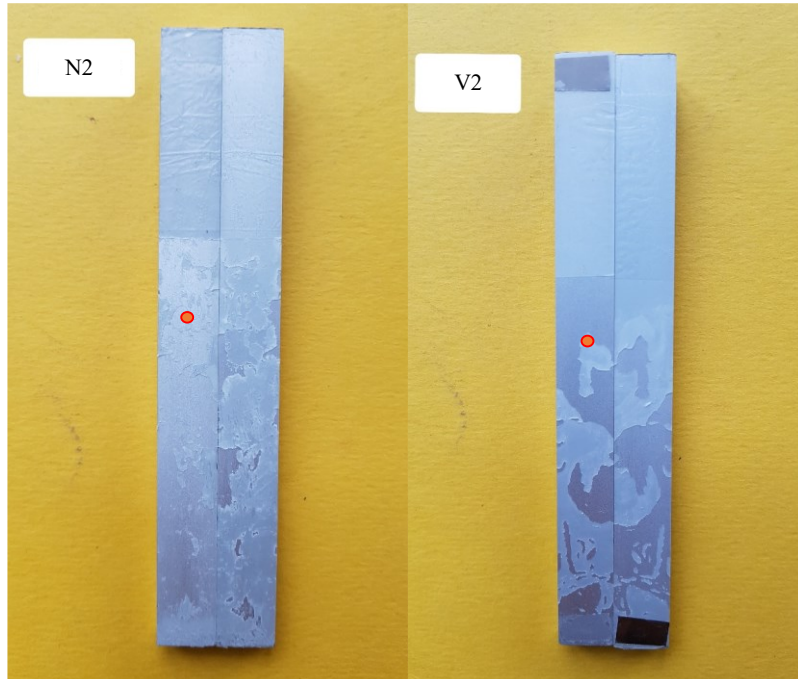
Figure 3.19 – Fracture surfaces of N2 (a) and V2 (b) joints. The red dots represent the position where the ESEM images reported in Figure 3.21 and Figure 3.22 were taken.
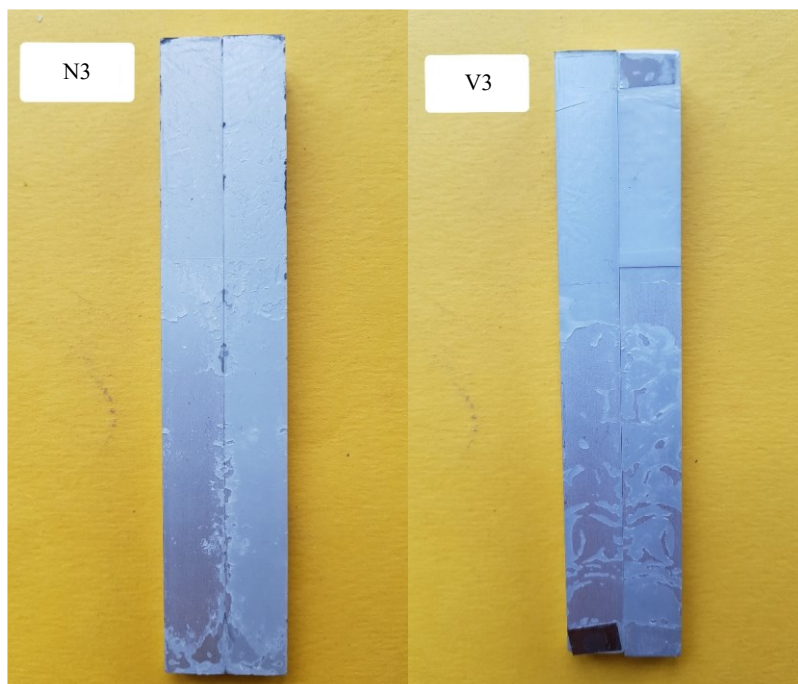
Figure 3.20 – Fracture surfaces of N3 (a) and V3 (b) joints.

To better understand if N joints had some residue of adhesive on the brighter adherent and why they perform a little bit better than V joints, the fracture surfaces were examined with a Quanta 250 FEG scanning electron microscope (FEI Company, Hillsboro, Oregon, USA) with environmental mode (ESEM). In Figure 3.21A (see Figure 3.19 for the position where pictures were taken) a mechanism was revealed, that is very similar to the one identified in [40] in the case of a nanomat-reinforced, general-purpose, non-structural epoxy adhesive: the crack did not progress into the nanomat (see the pickled aspect of the naked aluminium surface due to P2 etching) but ripples of adhesive + nanomat were left in correspondence of deeper grooves on the surface that acted as anchor points. A higher magnification picture of the same region is reported in Figure 3.21B, that highlights the presence of nanofibers in the adhesive but without signs of fiber pull-out due to crack bridging.
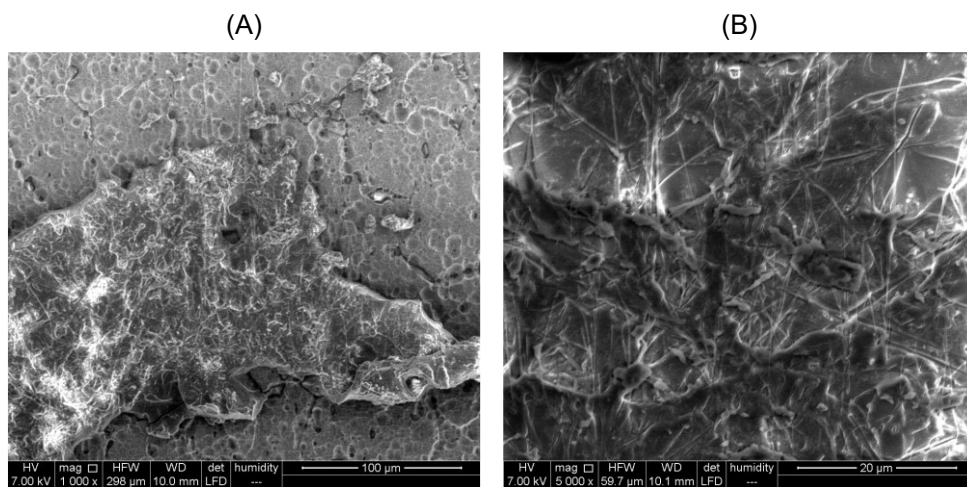
(A)   (B)

Figure 3.21 – ESEM images of the fracture surface of a N specimen at (A) 1,000x and (B) 5,000 x magnification.

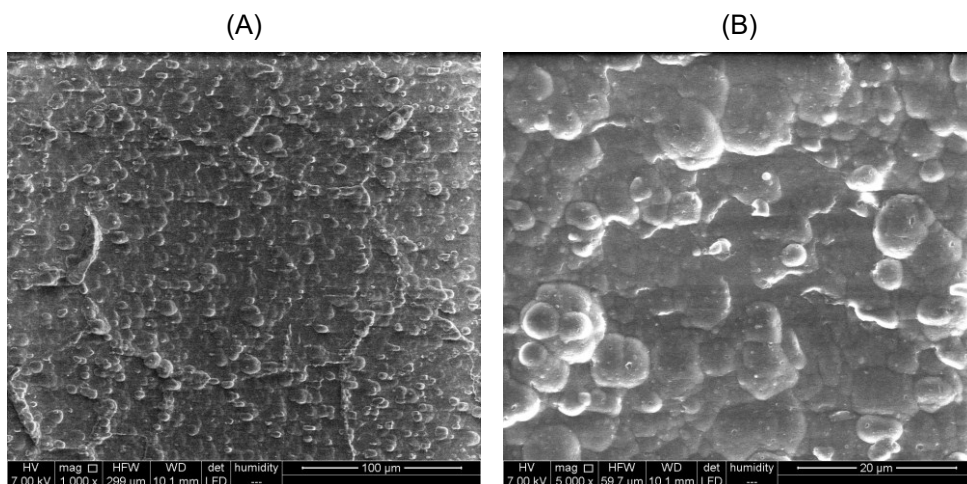(A)   (B)

Figure 3.22 – ESEM images of the fracture surface of a V specimen (adhesive side) at (A) 1,000x and (B) 5,000x magnification.

Therefore, it seems that the presence of the number of anchor points was enough to guarantee a fracture toughness comparable or tendentially higher than that of the virgin joint. A picture of the

fracture surface of the neat adhesive (V joint) is reported in Figure 3.22 for the sake of comparison with Figure 3.21: one can see the smoother surface that essentially replicates the adherent surface, justifying a lower resistance to crack propagation. Why anchor points are very limited in this case (see example on Figure 3.23) is not fully understood, but it might be related to the manufacturing conditions, that include the use of spacers to guarantee the same thickness of the N joints. In this way, the weights applied while curing may not yield the same pressure as in the case of N joints where spacers are not present. Since keeping the same adhesive layer thickness is deemed to be essential for a proper comparison between N and V joints, an even more effective surface preparation has to be developed to ensure enough adhesion in all cases.
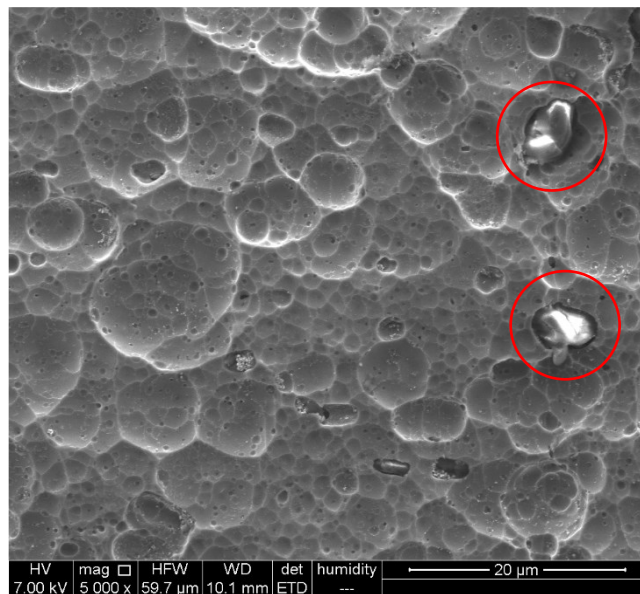

Figure 3.23 – ESEM image of the fracture surface of a V specimen (adherent side) at 5,000x magnification, showing a few adhesive leftovers entrapped in surface pits (circled in red).

3.3.5 Conclusions

The Mode I fracture toughness of a structural epoxy adhesive modified with the addition of a nylon nanomat generated by electrospinning (N joints) was evaluated by DCB testing, in comparison with that of the neat adhesive (V joints). The nanofibers do not have shown detrimental effects on the fracture toughness of the adhesive joint, rather a trend of improvement was found, with a mechanism characterized in both N and V joints by frequent crack path deviations from one adherent to the other one, where the nanofibers seems to give a contribution to keep at least some ripples of adhesive on both sides. As failure was essentially interfacial also in V joints, it means that nanofibers did not affect the failure mechanism and, despite the etching treatment, adhesion was still not optimal. Therefore, further efforts have to be directed in future to the improvement of adhesion to understand

the full potential of nanofiber as a reinforcement. At the moment, it has been demonstrated that the technique developed in this work can be used to generate prepreg nanomats out of a structural epoxy adhesive as an alternative to more conventional carriers (e.g. glass fiber mats).

3.4 Integration of nylon electrospun nanofibers into structural epoxy adhesive joints

Stefania Minosi[1], Davide Cocchi[2], Alessandro Pirondi[1], Andrea Zucchelli[2], Fabio Campanini[3]

[1]Dipartimento di Ingegneria e Architettura - Università di Parma

Parco Area delle Scienze 181/A, 43124 Parma, Italy

[2]Dipartimento di Ingegneria Industriale, Alma Mater Studiorum - Università di Bologna

viale del Risorgimento 2, 40136 Bologna, Italy

[3]ELANTAS Europe Srl, Collecchio, Strada Antolini 1, 43044 Collecchio (PR), Italy

The candidate is one of the Authors of this study. He contributes to the conception and design of the study, data acquisition and analysis, and manuscript drafting. The work was presented at the AIAS2020 Virtual Conference (2-4 September 2020) and it is currently being published on the Open Access Proceedings Journal of Physics – IOP Conference Series: Materials Science and Engineering. Here it is partially reproduced with respect to the version to be published.

3.4.1 Abstract

The fracture toughness is a key parameter in the development of bonded joints for several structural applications. Adhesives are commonly toughened with fillers or modifying the resin chemical composition. Many studies also suggest that resin toughening could be achieved through electrospun polymer nanomat. In previous works, the Authors proved that nylon nanomats can be used as an adhesive carrier and reinforcing web for the adhesive layer. This allowed developing a laboratory route to produce high-quality prepregs of electrospun nylon carrier using medium viscosity, two-component, unfilled epoxy adhesive. By applying the same methodology, in the present work, electrospun nylon prepregs were produced using a high strength and high toughness 2k structural epoxy adhesive to toughen the joint. The wet nano-reinforced strips were placed between S235 steel sandblasted adherents and oven-cured to obtain DCB joints. DCB tests were performed to compare the Mode I fracture toughness with and without the nanofibrous mat. Unlike previous works with medium-low toughness epoxies, this time the fracture toughness was reduced after the integration of an electrospun nano-reinforcement. From the SEM images it seems that the nanomat hinders the ductile failure mechanism which instead develops in the neat resin.

Keywords: nanomaterials, bonding reinforcement, fracture toughness, steel

3.4.2 Introduction

In previous works [39,40,42], the Authors studied the effect of the integration of nylon 6,6 electrospun nanofibers into 2k unfilled epoxy resin. In those works, a laboratory route was developed to produce high-quality prepregs and was proved that the nanomat acts as a support for the adhesive layer and tends to improve the mechanical performance of the joints.

In the present work, electrospun nylon 6,6 nanomat prepregs were produced applying the same methodology developed in the previous studies. A structural 2k epoxy resin, characterized by higher strength and fracture toughness compared to the ones employed in previous works, was used. Thixotropic agents were not added to the epoxy adhesive formulation to reduce viscosity and to improve the wetting of nanofibers without affecting the mechanical properties of the adhesive itself. The wet nanofibrous strips were placed between S235 steel adherents to obtain DCB bonded joints. DCB tests have been performed on both nano-reinforced and neat joints to compare the mode-I fracture toughness. SEM analysis were performed to investigate the failure mechanisms on the fracture surfaces. The aim was to evaluate the effect of the nylon nanomat in high-strength and high-toughness epoxy system and to compare the results with those obtained in previous studies, in which medium-low toughness epoxies were used.

3.4.3 Experimental methodology

3.4.3.1 Nanofibrous mat production

The electrospun nylon 6,6 nanomat was produced following the same procedure developed in the previous works [39,40,42]. The manufacturing process was the same reported in Section 3.2.3.1, as well as the electrospinning parameters (Table 3.1). The nanomat thickness was measured along the nanomat strip by a digital indicator, as reported in Section 3.3.3.1. Its value lay between 120 to 160 μm. As obtained for the previous works, the nanofibers diameter was assumed to be 150 ± 20 nm.

3.4.3.2 Steel S235 adherents

From a cold drawn bar of S235 steel, 14 adherents were machined to produce 3 DCB specimens defined as virgin (V, without nylon nanomat) and 4 DCB nano-reinforced specimens (N) with the nylon nanomat. The elastic modulus of the steel was assumed to be 210 GPa, while its yield strength 235 MPa. Perforated steel blocks were bonded to the adherents (one for each adherent), to fix the cured joints on the testing machine. The dimensions of the adherents and blocks are shown in Figure 3.24.
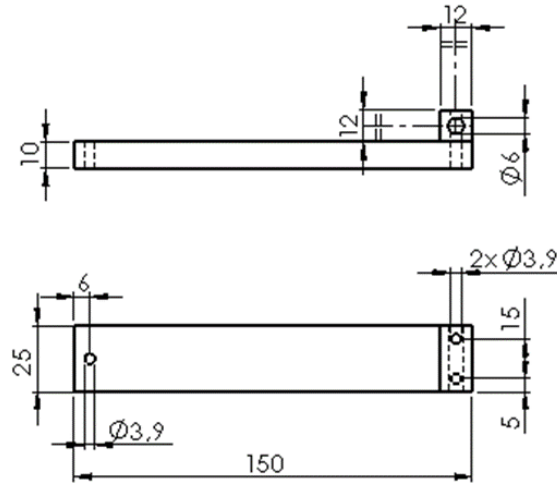
Figure 3.24 – Steel adherent and block dimensions.

The DCB dimensions are smaller compared to ASTM D3433 standards, to ensure the easy handling of the nanomat, especially after impregnation. Before bonding, the adherents were cleaned with acetone, sandblasted at 6 bar with quartz powders resulting in a roughness R_a = 3.9 μm, and sonicated with acetone. This surface treatment was necessary to obtain clean surfaces and to ensure good adhesion between adherents and epoxy resin.

3.4.3.3 Resin system

Nylon nanomat prepreg was produced following the procedure developed in previous works for unfilled 2k epoxy adhesives characterized by medium-low viscosity [39,40,42]. The adhesive selected for this work is the 2k epoxy system Elan-tech® AS90 / AW91, developed specifically for structural applications, supplied by ELANTAS (ELANTAS Europe S.r.l., Collecchio (PR), Italy). The supplier removed the thixotropic agents from the resin to make it suitable for the nanomat impregnation. In this way, epoxy viscosity was reduced without affecting the resin mechanical properties. The properties of the resin are summarized in Table 3.3.

The resin was supplied in cartridges to avoid manual mixing and, therefore, air entrapment. An impregnation test was performed to verify the ability of the epoxy system to impregnate the nanomat properly. To this end, a nylon nanomat strip was placed on an epoxy resin layer. When the nanomat completely soaked up the resin, it was rolled between two calibrated and counter-rotating drums to remove excess adhesive. The obtained prepreg was embedded within two S235 steel supports and cured at 70 °C for 5 h. After nylon nanofibers dissolution in formic acid and surface polishing, the cross-section of the bonded joint was observed under SEM, as shown in Figure 3.25. The fibers distribution into the adhesive layer appears uniform through the entire bondline, and no air bubbles

were found. This preliminary test demonstrated that the resin is suitable for nanomat impregnation, allowing high-quality prepregs production.

Table 3.3 – Mechanical and physical properties of the Elan-tech® AS90 / AW91 epoxy structural adhesive supplied by ELANTAS (ELANTAS Italia Srl, Italy).

| Property	Unit	AS90 / AW91
Viscosity	mPa s	5,000
Gel time	h	5–6
Suggested cure cycle	h	5
	°C	70
Glass transition temperature, T_g (ASTM D3418) after 24 h at RT	°C	40–47
Flexural strength (ASTM D790)	MPa	70–80
Strain at break (ASTM D790)	%	4.5–7.5
Flexural modulus (ASTM D790)	MPa	2,000–2,500
Tensile strength (ASTM D638)	MPa	45–55
Elongation at break (ASTM D638)	%	4.5–6.5
Shear strength (ASTM D1002) on AISI316, cured 5 h at 70 °C	MPa	25.5–31
Peel strength (ASTM D1876) on aluminium, cured 5 h at 70 °C	N/cm	35–43

(A)　　　　　　　　　　(B)　　　　　　　　　　(C)
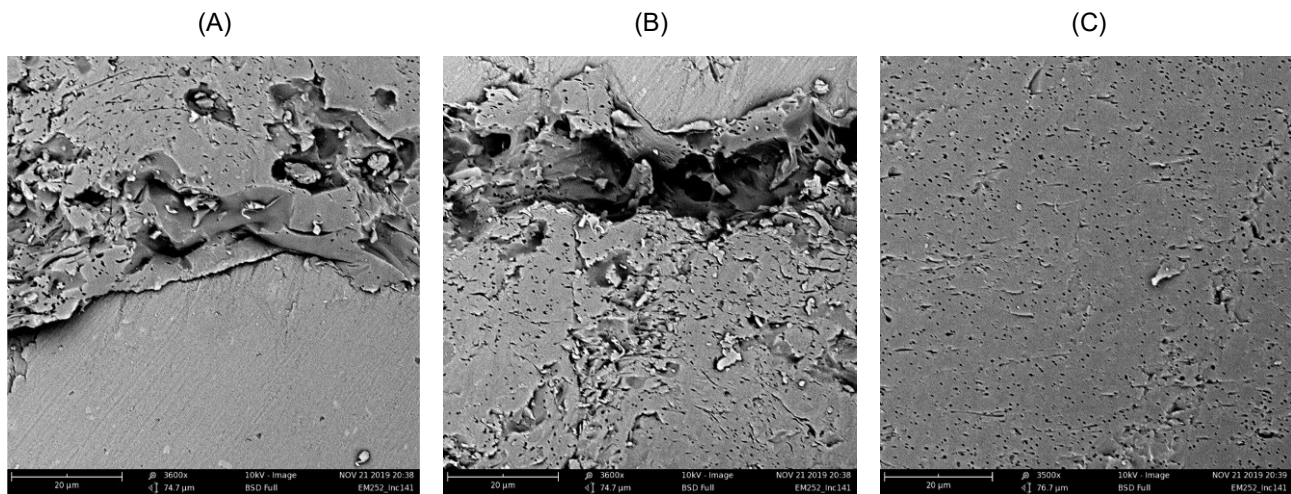
Figure 3.25 – SEM images of cross-section of nano-reinforced adhesive layer.

3.4.3.4 DCB fabrication

Two series of DCB joints were produced to evaluate the effect of the nylon nanomat integration on the performance of the structural epoxy resin. The first series comprises 3 DCB virgin specimens, bonded with the neat adhesive, while the second one 4 nano-reinforced DCB specimens. The steel surfaces were prepared as previously described.

Regarding virgin specimens, two metal spacers, 150 μm thick, were placed both at the beginning and at the end of the DCB adherent, then a Teflon foil was cut and placed on the same steel substrate to obtain a 30 mm long defect. The adhesive was then spread on the surfaces to be bonded. The adherents were consequently overlapped and bolted at the joint extremities, ensuring their correct positioning. The DCB joint was cured in an oven at 70 °C for 5 h. At the end of the curing cycle, the bolts were removed.

To manufacture the nano-reinforced DCB, it was first necessary to precrack the nylon nanomat, exfoliating it for a length of 30 mm in order to insert the Teflon sheet initial defect. The precracked nanomat was then impregnated with the epoxy resin and gently squeezed throughout two calibrated and counter-rotating drum to remove the adhesive excess. The adherents surfaces were prepared as specified in Section 3.4.3.2. The nanofibrous prepreg was then placed on the bonding surface of one steel supports. The second adherent was overlapped and bolted together with the first one. In this case, the bondline thickness is defined by the nanomat thickness. Again, after the same curing cycle of virgin specimens, bolts were removed.

3.4.3.5 DCB testing

The tests were performed under displacement control with constant crosshead speed, using the same equipment and experimental conditions reported in Section 3.2.3.4. In this study, as well, the crack propagation was calculated by means of compliance measurements during the partial unloading of the test and the fracture toughness was evaluated using the Krenk's model [41]. Before the tests, precracking was carried out at 5 Hz under load control to obtain the initial crack propagation of 5 mm.

The Poisson's ratio v_a was considered equal to 0.4 as common for epoxies. Since the elastic modulus of nylon 6,6 is approximatively the same of the epoxy resin, also the Young's modulus of the nanomat prepreg can be considered approximately the same of the neat adhesive. The obtained bondline thickness after curing was in the range 150÷200 μm for both virgin and nano-reinforced joints.

3.4.4 Results

The DCB test results are summarized in Figure 3.26A, where the load against CMOD is reported for both a virgin (V) and a nano-reinforced (N) specimens taken as representative. Figure 3.26B shows the *R*-curves for each tested specimen. Dashed curves represent the results of the nano-reinforced joints, while solid curves refer to the virgin ones. The black markers of Figure 3.26B refer to the G_{Ic} values considered to calculate the fracture toughness mean value during the steady-state crack propagation phase for each DCB series. The grey markers, instead, represent the values

excluded from the calculation. Virgin joints have an average G_{Ic} value of 1.05 ± 0.28 N/mm, while for the nano-reinforced joints this value is equal to 0.38 ± 0.07 N/mm.
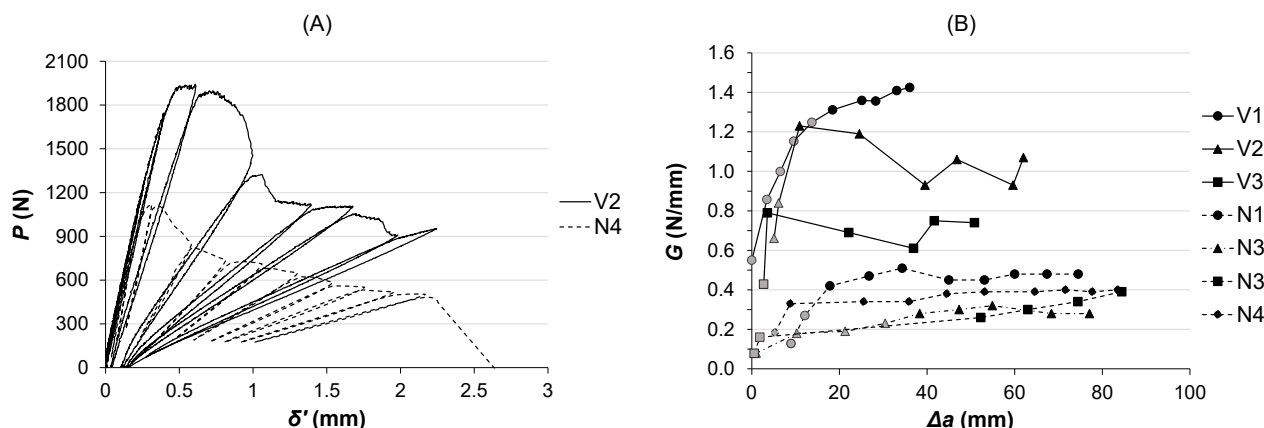

Figure 3.26 – (A) Load against CMOD (δ') for both a virgin (V) and a nano-reinforced (N) specimens taken as representative. (B) R-curves for all the tested specimens. Solid lines refer to virgin specimens, while dashed lines refer to nano-reinforced ones. The black markers of the R-curves graph indicate the G_{IC} values considered for the steady-state fracture toughness average value calculation, whilst the grey ones the excluded values.

From the present experiments, the nanofibrous reinforcement seems to yield a detrimental effect on the fracture toughness of high strength and high toughness structural adhesive. Nano-reinforced DCB *R*-curves show low initial G_{Ic} values, which increases before stabilizing during crack propagation. The *R*-curves becomes flat for almost all the N specimens after the *Δa* range 10÷20 mm. Virgin DCB specimens reveal higher G_{Ic} values, despite their *R*-curve behaviour is more scattered respect to the nano-reinforced ones. For the N specimens, the G_{Ic} value increases approximately three times when it becomes stationary. While, the fracture toughness of the neat adhesive increases only two times compared to the initial G_{Ic} values, although with higher absolute values. In particular, the nano-reinforced specimens showed a 64 % fracture toughness reduction compared to the virgin ones.

To better understand the phenomena that act in the nano-reinforced adhesive, SEM analyses were carried out on the fracture surfaces of both V and N tested DCB specimens. The fracture surfaces of virgin DCB were mainly cohesive, while they look mixed for the nano-reinforced ones. In Figure 3.27 are reported the fracture surfaces of V2 and N4 samples, whose *P–δ'* curves are reported in Figure 3.26. As shown in Figure 3.28A, fracture surfaces of the V2 sample reveal the presence of micro-dimples into the adhesive layer, which proves that ductile fracture mechanisms occurred in the neat resin.

This morphology was not observed in nano-reinforced specimens. The SEM image of Figure 3.28B of N1 sample shows a brittle fracture surface, with no presence of microcavities and no areas with fiber bridging. Compared to N1 sample, the N4 one was also analysed (Figure 3.28C) and no significant differences were found, showing comparable G_{Ic} values in the investigated area, i.e. for

Δa values between 40÷50 mm. From the SEM images of N samples, it appears that nanomat exfoliation occurs without fiber pull-out, representing a preferential fracture zone inside the adhesive layer. The absence of micro-dimples underlines that the adhesive did not deform and fail in a ductile way, resulting in a fracture energy reduction compared to virgin samples.
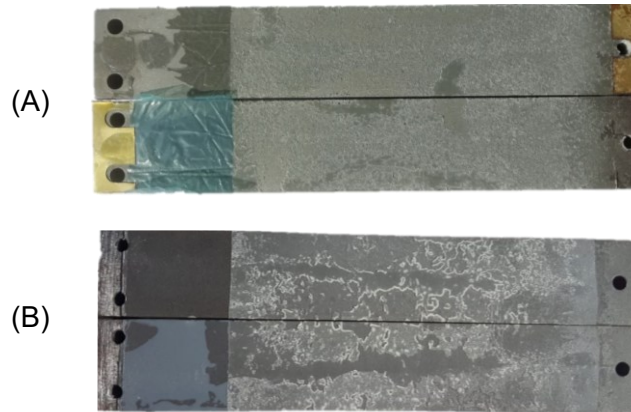

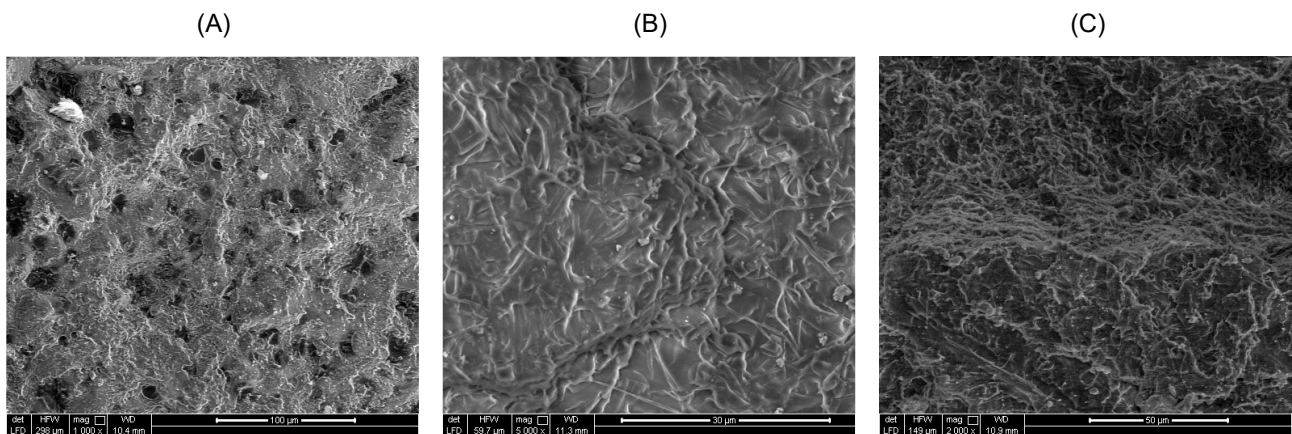*Figure 3.27 – Fracture surfaces of (A) virgin V2 and (B) nano-reinforced N4 DCB specimens.*

Figure 3.28 – SEM images of fracture surfaces of (a) V2, (b) N1, and (c) N4 specimens.

3.4.5 Conclusions

In the present work electrospun nylon 6,6 prepregs were produced using a high strength and high toughness 2k structural epoxy resin to toughen adhesive joints. DCB virgin and nano-reinforced specimens were produced to compare the fracture toughness values. Unlike medium-low toughness epoxies, DCB tests showed that the electrospun nanomat seems to yield a detrimental effect on the fracture toughness of a high-performance structural adhesive. The integration of the nylon nanofibrous prepreg caused a G_{Ic} reduction of the 64 % respect to the neat adhesive.

To better understand the phenomena that act in the nano-reinforced adhesive, SEM analyses were carried out on the fracture surfaces of both virgin and nano-reinforced tested DCB specimens. The fracture surfaces of virgin DCB were mainly cohesive, while they look mixed for the nano-reinforced

ones. Virgin specimens are characterized by the presence of micro-dimples, caused by ductile fracture mechanisms. Contrarily, the nano-reinforced specimens show brittle fracture surfaces, with no microcavities. Their SEM analyses did not reveal areas characterized by fiber bridging. Instead, it appears that nanomat exfoliation occurred, representing a preferential fracture zone inside the adhesive layer. The nanomat seems therefore to hinder the ductile deformation mechanisms of the adhesive without adding other toughening mechanisms or even giving a preferential way to the crack because of its tendency to exfoliate, causing an absorbed energy reduction compared to virgin samples. This is also confirmed by the absence of micro-dimples.

This peculiar behaviour, not detected with medium-low toughness epoxies where the nanomat improved someway the fracture toughness, could also depend on the nanomat thickness. A lower thickness could reduce the exfoliation risk, ensuring also tighter control over the adhesive bondline. The adhesion at the interface between the epoxy resin and the nanofibers can play a role as well in determining whether the final result is good or not, especially if a high toughness epoxy is used.

Therefore, before coming to a definitive conclusion about the effect of nylon 6,6 nanofibers, further tests are foreseen with a lower nanomat thickness and by optimizing the solvent system for the electrospinning polymeric solution. Moreover, plasma treatment is planned to improve the adhesion at the interface between the epoxy resin and the nanofibers, without compromising their wettability.

3.5 Future works

In these works, a laboratory route was developed and optimized through different steps to produce high-quality nanofibrous prepregs. The obtained results proved the capability of nylon 6,6 electrospun nanomat to act as an adhesive carrier. The nano-reinforcement tends to improve the fracture toughness of the joint for medium-low toughness epoxy adhesives, but it seems to have a detrimental effect on high-performance structural adhesives, themselves characterized by a high basic-toughness.

Future studies will focus on the optimization of the manufacturing parameters, like the nanomat thickness, the solvent system, and the surfaces preparation to improve the adhesion between the adherents and the adhesive and between the nanofibers and the epoxy resin.

Moreover, further studies will take into consideration nanofibers of different materials and with specific functions, like rubbery and poly(vinylidenefluoride-trifluoroethylene) (PVDF-TrFE) ones. About rubbery nanofibers, introduced in Chapter 4 for damping applications on composite laminates, are currently ongoing DCB tests to evaluate the effect on the fracture toughness of adhesive joints. While PVDF-TrFE piezoelectric nanofibers, presented in Chapter 5 to produce self-sensing composite laminates capable of detecting impacts on their surface, will also be implemented in adhesive joints to detect the crack propagation so producing smart joints.

3.6   Nomenclature

a   crack length

A   cross-section of the adherent

b   width of the specimen

g   distance from load axis of CMOD measurement point

E   Young's modulus of the adherent

E_a Young's modulus of the adhesive

G_I Mode I strain energy release rate

G_{Ic} fracture toughness

h   thickness of the adherent

J   area moment of inertia of the adherent

k   elastic foundation stiffness [41]

P   force

R_m tensile strength of the aluminium alloy

$R_{p0,2}$ yield strength of the aluminium alloy

t   thickness of the bonding interface

δ'   Crack Mouth Opening Displacement (CMOD)

$λ_σ$ length scale of the stress distribution in a DCB joint [41]

v_a Poisson's ratio of the adhesive

3.7 References

[1]   L.F.M. da Silva, A. Öchsner, R.D. Adams, Handbook of Adhesion Technology: Second Edition, 2018. https://doi.org/10.1007/978-3-319-55411-2.

[2]   A.J. Kinloch, Adhesives in engineering, Proc. Inst. Mech. Eng. Part G J. Aerosp. Eng. 211 (1997) 307–335. https://doi.org/10.1243/0954410971532703.

[3]   A. Kinloch, Adhesion and adhesives: Science and technology, 1st ed., Chapman & Hall, London, UK, 1987. https://doi.org/10.1007/978-94-015-7764-9.

[4]   M.D. Banea, M. Rosioara, R.J.C. Carbas, L.F.M. da Silva, Multi-material adhesive joints for automotive industry, Compos. Part B Eng. 151 (2018) 71–77. https://doi.org/10.1016/j.compositesb.2018.06.009.

[5]   A.J. Kinloch, Toughening epoxy adhesives to meet today's challenges, MRS Bull. 28 (2003) 445–448. https://doi.org/10.1557/mrs2003.126.

[6]   A. Nemati Giv, M.R. Ayatollahi, S.H. Ghaffari, L.F.M. da Silva, Effect of reinforcements at different scales on mechanical properties of epoxy adhesives and adhesive joints: a review, J. Adhes. 94 (2018) 1082–1121. https://doi.org/10.1080/00218464.2018.1452736.

[7]   E.B. Caldona, A.C.C. De Leon, B.B. Pajarito, R.C. Advincula, A Review on Rubber-Enhanced Polymeric Materials, Polym. Rev. 57 (2017) 311–338. https://doi.org/10.1080/15583724.2016.1247102.

[8]   C. Keith Kiew, A.R. Siebert, R.W. Smith, M. Fernando, A.J. Kinloch, Toughened epoxy resins: Preformed particles as tougheners for adhesives and matrices, Adv. Chem. Ser. 252 (1996) 33–44. https://doi.org/10.1021/ba-1996-0252.ch003.

[9]   R.J.J. Williams, B.A. Rozenberg, J.P. Pascault, Reaction-Induced Phase Separation in Modified Thermosetting Polymers, Adv. Polym. Sci. 128 (1997) 95–156. https://doi.org/10.1007/3-540-61218-1_7.

[10]   W.L. Tsang, A.C. Taylor, Fracture and toughening mechanisms of silica- and core–shell rubber-toughened epoxy at ambient and low temperature, J. Mater. Sci. 54 (2019) 13938–13958. https://doi.org/10.1007/s10853-019-03893-y.

[11]   C.W. Wise, W.D. Cook, A.A. Goodwin, CTBN rubber phase precipitation in model epoxy resins, Polymer (Guildf). 41 (2000) 4625–4633. https://doi.org/10.1016/S0032-3861(99)00686-2.

[12]   R. Bagheri, B.T. Marouf, R.A. Pearson, Rubber-toughened epoxies: A critical review, Polym. Rev. 49 (2009) 201–225. https://doi.org/10.1080/15583720903048227.

[13]   S.K. Gupta, D.K. Shukla, D. Kaustubh Ravindra, Effect of nanoalumina in epoxy adhesive on lap shear strength and fracture toughness of aluminium joints, J. Adhes. (2019). https://doi.org/10.1080/00218464.2019.1641088.

[14]   T. Takeda, F. Narita, Fracture behavior and crack sensing capability of bonded carbon fiber composite joints with carbon nanotube-based polymer adhesive layer under Mode I loading,

Compos. Sci. Technol. 146 (2017) 26–33.
https://doi.org/10.1016/j.compscitech.2017.04.014.

[15]   I.A. Akpinar, A. Gürses, S. Akpinar, K. Gültekin, H. Akbulut, A. Ozel, Investigation of mechanical and thermal properties of nanostructure-doped bulk nanocomposite adhesives, J. Adhes. 94 (2018) 847–866. https://doi.org/10.1080/00218464.2017.1415809.

[16]   G.L. Burkholder, Y.W. Kwon, R.D. Pollak, Effect of carbon nanotube reinforcement on fracture strength of composite adhesive joints, J. Mater. Sci. 46 (2011) 3370–3377. https://doi.org/10.1007/s10853-010-5225-6.

[17]   J. Cha, J. Kim, S. Ryu, S.H. Hong, Comparison to mechanical properties of epoxy nanocomposites reinforced by functionalized carbon nanotubes and graphene nanoplatelets, Compos. Part B Eng. 162 (2019) 283–288. https://doi.org/10.1016/j.compositesb.2018.11.011.

[18]   M.R. Gude, S.G. Prolongo, A. Ureña, Toughening effect of carbon nanotubes and carbon nanofibres in epoxy adhesives for joining carbon fibre laminates, Int. J. Adhes. Adhes. 62 (2015) 139–145. https://doi.org/10.1016/j.ijadhadh.2015.07.011.

[19]   M.B. Jakubinek, B. Ashrafi, Y. Zhang, Y. Martinez-Rubi, C.T. Kingston, A. Johnston, B. Simard, Single-walled carbon nanotube-epoxy composites for structural and conductive aerospace adhesives, Compos. Part B Eng. 69 (2015) 87–93. https://doi.org/10.1016/j.compositesb.2014.09.022.

[20]   P. Jojibabu, Y.X. Zhang, A.N. Rider, J. Wang, B. Gangadhara Prusty, Synergetic effects of carbon nanotubes and triblock copolymer on the lap shear strength of epoxy adhesive joints, Compos. Part B Eng. 178 (2019). https://doi.org/10.1016/j.compositesb.2019.107457.

[21]   H. Khoramishad, M. Khakzad, Toughening epoxy adhesives with multi-walled carbon nanotubes, J. Adhes. 94 (2018) 15–29. https://doi.org/10.1080/00218464.2016.1224184.

[22]   A.H. Korayem, S.J. Chen, Q.H. Zhang, C.Y. Li, X.L. Zhao, W.H. Duan, Failure of CFRP-to-steel double strap joint bonded using carbon nanotubes modified epoxy adhesive at moderately elevated temperatures, Compos. Part B Eng. 94 (2016) 95–101. https://doi.org/10.1016/j.compositesb.2016.03.042.

[23]   W. Zielecki, A. Kubit, T. Trzepieciński, U. Narkiewicz, Z. Czech, Impact of multiwall carbon nanotubes on the fatigue strength of adhesive joints, Int. J. Adhes. Adhes. 73 (2017) 16–21. https://doi.org/10.1016/j.ijadhadh.2016.11.005.

[24]   Z.M. Huang, Y.Z. Zhang, M. Kotaki, S. Ramakrishna, A review on polymer nanofibers by electrospinning and their applications in nanocomposites, Compos. Sci. Technol. 63 (2003) 2223–2253. https://doi.org/10.1016/S0266-3538(03)00178-7.

[25]   R. Palazzetti, A. Zucchelli, Electrospun nanofibers as reinforcement for composite laminates materials – A review, Compos. Struct. 182 (2017) 711–727. https://doi.org/10.1016/j.compstruct.2017.09.021.

[26] A. Zucchelli, M.L. Focarete, C. Gualandi, S. Ramakrishna, Electrospun nanofibers for enhancing structural performance of composite materials, Polym. Adv. Technol. 22 (2011) 339–349. https://doi.org/10.1002/pat.1837.

[27] R. Palazzetti, A. Zucchelli, I. Trendafilova, The self-reinforcing effect of Nylon 6,6 nano-fibres on CFRP laminates subjected to low velocity impact, Compos. Struct. 106 (2013) 661–671. https://doi.org/10.1016/j.compstruct.2013.07.021.

[28] F. Moroni, R. Palazzetti, A. Zucchelli, A. Pirondi, A numerical investigation on the interlaminar strength of nanomodified composite interfaces, Compos. Part B Eng. 55 (2013) 635–641. https://doi.org/10.1016/j.compositesb.2013.07.004.

[29] G. Giuliese, R. Palazzetti, F. Moroni, A. Zucchelli, A. Pirondi, Cohesive zone modelling of delamination response of a composite laminate with interleaved nylon 6,6 nanofibres, Compos. Part B Eng. 78 (2015) 384–392. https://doi.org/10.1016/j.compositesb.2015.03.087.

[30] G.W. Beckermann, K.L. Pickering, Mode i and Mode II interlaminar fracture toughness of composite laminates interleaved with electrospun nanofibre veils, Compos. Part A Appl. Sci. Manuf. 72 (2015) 11–21. https://doi.org/10.1016/j.compositesa.2015.01.028.

[31] T.M. Brugo, G. Minak, A. Zucchelli, H. Saghafi, M. Fotouhi, An Investigation on the Fatigue based Delamination of Woven Carbon-epoxy Composite Laminates Reinforced with Polyamide Nanofibers, in: Procedia Eng., 2015: pp. 65–72. https://doi.org/10.1016/j.proeng.2015.06.208.

[32] L. Daelemans, S. van der Heijden, I. De Baere, H. Rahier, W. Van Paepegem, K. De Clerck, Using aligned nanofibres for identifying the toughening micromechanisms in nanofibre interleaved laminates, Compos. Sci. Technol. 124 (2016) 17–26. https://doi.org/10.1016/j.compscitech.2015.11.021.

[33] L. Daelemans, S. van der Heijden, I. De Baere, H. Rahier, W. Van Paepegem, K. De Clerck, Improved fatigue delamination behaviour of composite laminates with electrospun thermoplastic nanofibrous interleaves using the Central Cut-Ply method, Compos. Part A Appl. Sci. Manuf. 94 (2017) 10–20. https://doi.org/10.1016/j.compositesa.2016.12.004.

[34] K. Maloney, N. Fleck, Toughening strategies in adhesive joints, Int. J. Solids Struct. 158 (2019) 66–75. https://doi.org/10.1016/j.ijsolstr.2018.08.028.

[35] H.J. Oh, H.Y. Kim, S.S. Kim, Effect of the core/shell-structured meta-aramid/epoxy nanofiber on the mechanical and thermal properties in epoxy adhesive composites by electrospinning, J. Adhes. 90 (2014) 787–801. https://doi.org/10.1080/00218464.2013.843458.

[36] S.Y. On, M.S. Kim, S.S. Kim, Effects of post-treatment of meta-aramid nanofiber mats on the adhesion strength of epoxy adhesive joints, Compos. Struct. 159 (2017) 636–645. https://doi.org/10.1016/j.compstruct.2016.10.016.

[37] S.M.J. Razavi, R.E. Neisiany, M.R. Ayatollahi, S. Ramakrishna, S.N. Khorasani, F. Berto, Fracture assessment of polyacrylonitrile nanofiber-reinforced epoxy adhesive, Theor. Appl. Fract. Mech. 97 (2018) 448–453. https://doi.org/10.1016/j.tafmec.2017.07.023.

[38]   M. Ekrem, A. Avcı, Effects of polyvinyl alcohol nanofiber mats on the adhesion strength and fracture toughness of epoxy adhesive joints, Compos. Part B Eng. 138 (2018) 256–264. https://doi.org/10.1016/j.compositesb.2017.11.049.

[39]   F. Musiari, A. Pirondi, A. Zucchelli, D. Menozzi, J. Belcari, T.M. Brugo, L. Zomparelli, Experimental investigation on the enhancement of Mode I fracture toughness of adhesive bonded joints by electrospun nanofibers, J. Adhes. 94 (2018) 974–990. https://doi.org/10.1080/00218464.2017.1402301.

[40]   T.M. Brugo, F. Musiari, A. Pirondi, A. Zucchelli, D. Cocchi, D. Menozzi, Development and fracture toughness characterization of a nylon nanomat epoxy adhesive reinforcement, Proc. Inst. Mech. Eng. Part L J. Mater. Des. Appl. 233 (2019) 465–474. https://doi.org/10.1177/1464420718807733.

[41]   S. Krenk, Energy release rate of symmetric adhesive joints, Eng. Fract. Mech. 43 (1992) 549–559. https://doi.org/10.1016/0013-7944(92)90198-N.

[42]   D. Cocchi, F. Musiari, T.M. Brugo, A. Pirondi, A. Zucchelli, F. Campanini, E. Leoni, L. Mazzocchetti, Characterization of aluminum alloy-epoxy bonded joints with nanofibers obtained by electrospinning, J. Adhes. 96 (2020) 384–401. https://doi.org/10.1080/00218464.2019.1666716.

Damping and mechanical behaviour of composite laminates interleaved with rubbery nanofibers

Marco Povolo[1], Emanuele Maccaferri[2], Davide Cocchi[1], Tommaso Maria Brugo[1], Laura Mazzocchetti[2], Loris Giorgini[2], Andrea Zucchelli[1]

[1]Dipartimento di Ingegneria Industriale, Alma Mater Studiorum - Università di Bologna
viale del Risorgimento 2, 40136 Bologna, Italy

[2]Dipartimento di Chimica Industriale "Toso Montanari", Alma Mater Studiorum - Università di Bologna
viale del Risorgimento 4, 40136 Bologna, Italy

The candidate is one of the Authors of this experimental study. He contributes to the conception and design of the study, data acquisition and analysis, manuscript drafting, revision and approval. The article has been recently submitted to Composite Structures journal and it is under revision.

4.1   Abstract

The development of composite components with superior damping capacity is welcome in fields like automotive and aerospace for improving comfort and reducing composite damages. Here, a structural composite with improved damping and unaffected overall mechanical properties is presented. Vibration hampering is achieved by interleaving electrospun Nitrile Butadiene Rubber / poly(ϵ-caprolactone) (NBR/PCL) blend nanofibrous mats into epoxy unidirectional Carbon Fiber Reinforced Polymer (CFRP) prepregs. Three laminate configurations were produced using rubbery nonwoven layers with different thicknesses (5, 10 and 20 μm) for evaluating the effect of grammage layer on CFRP damping and mechanical properties. A preliminary thermomechanical behaviour of modified CFRPs was evaluated via Dynamic Mechanical Analysis (DMA), while the influence of both interleaved mat grammage and testing temperature was more deeply investigated via destructive three-point bending (3PB) analyses. Flexural elastic modulus and strength of rubbery-modified

CFPSs are comparable to unmodified laminate. Some lowering occurs only at relatively high temperature when present the highest mat grammage.

Damping behaviour was evaluated by single cantilever beam vibration tests using the advanced Modified Coulomb Damping (MCD) model. The interleaved NBR/PCL mats improved the composite damping up to +77 %, without significantly affecting the laminate mechanical properties, weight, and thickness.

Keywords: damping, nanofibers, composite laminates, rubber, electrospinning, CFRP

4.2   Introduction

Fiber Reinforced Polymers (FRPs) have many advantages over traditional materials mainly because of their favourable specific stiffness, specific strength, and the capacity of dissipating energy. These characteristics make composite laminates suitable for high-performance applications like aerospace, automotive, industrial, sport, etc. Traditional materials, like metals, have low damping capabilities resulting in high amplitude vibrations that can cause damages to structures [1]. FRP laminates, on the other hand, show higher damping properties than traditional ones. At the micromechanical level, the energy dissipation is induced by different phenomena such as the viscoelasticity of the matrix, the damping of fibers and matrix, their interfaces, or by damages [2]. At the laminate level, instead, damping depends on the layer orientations, stacking sequence, and interlaminar effects [3–5].

The fiber type also influences the damping value of the composite. Kevlar fiber composites show a greater damping power compared to glass and carbon fiber ones [3,6]. Instead, the addition of flax fibers to carbon fiber provides good damping behaviour, but the mechanical properties of the hybrid composite quickly decay as the flax fiber content increases [4].

The matrix nature also impacts on the final composite performance. Thermoplastic matrix confers to FRPs higher damping respect to thermosets, like epoxy resin, but the overall composite mechanical properties are poor, making thermoplastics not suitable for structural applications [7].

A common solution to increase the damping capacities of composite materials is the integration of bulk viscoelastic layers between FRP plies [1,8,9]. The damping enhancement using viscoelastic layers appears to be an effective, constructively simple, and low-cost solution. However, their integration compromises the overall stiffness and strength of the laminate besides causing an increase in its weight and size [10].

A novel method to increase the dynamic performance of composite laminates is to integrate nano-reinforcements into the matrix, like nanoparticles [11,12] carbon nanotubes (CNTs) [13–15], and nanofibers [16]. CNTs offer a greater surface to volume ratio interfaces than classic fibers, enhancing the damping behaviour of the hosting composite laminate [13,15,17]. Thermoplastic nanofibers are also used for hindering delamination by increasing the interlaminar fracture toughness [16], but may not significantly improve damping properties [18,19]. On the contrary, elastomers may positively contribute to the damping enhancement, thanks to their intrinsic viscoelastic nature [20]. Few attempts to obtain rubbery nanofibers are reported in the literature due to difficulties in their production, arising from the rubber cold flow which leads to the formation of a compact bulk film. Usually, papers report just the proof of concepts of the possibility to electrospin rubber polymeric solutions [21–24], or they attain microfibers rather than nanofibers [25,26]. Often, rubbery nanofibers need to be crosslinked for avoiding nanofiber coalescence [27]. The rubber cold flow phenomenon may be so important that the crosslinking step has to be applied during electrospinning [28] or immediately after the process [25,29], thus strongly limiting the obtainable final membrane thickness. Recently, the production of rubbery nanofibers by single-needle electrospinning of polymeric blends made of Nitrile Butadiene Rubber and poly(ϵ - caprolactone) (NBR/PCL) was reported by Maccaferri *et al*. [30]. This method allows producing rubbery nanofibers with a high amount of NBR fraction without the need for a crosslinking step: the nanofibrous morphology is stable at room temperature, and there are no restrictions to the obtainable mat thickness. The same rubbery nanofibrous mats were successfully interleaved in Carbon Fiber Reinforced Polymer (CFRP) epoxy laminates, resulting in the first reported work on CFRP laminates modified with rubbery nanofibers [18]. The Authors found up to +480 % of Mode I energy release rate, in addition to an impact on the overall composite thermomechanical properties which has to be further investigated.

In this work, an advanced structural composite with improved damping is presented, by interleaving NBR/PCL blend nanofibrous mats into unidirectional epoxy-based CFRPs. A preliminary thermomechanical behaviour of modified CFRPs was evaluated via Dynamic Mechanical Analysis (DMA), while the influence of both interleaved mat grammage and testing temperature was more deeply investigated via destructive three-point bending (3PB) analyses. Damping behaviour was assessed via single cantilever beam vibration tests. To perform an accurate measurement of damping and separating the damping contribution of the air and the joint from the contribution of the material, the advanced Modified Coulomb Damping (MCD) model was adopted [31,32]. Moreover, mechanical properties were evaluated as a function of temperature performing three-point bending (3PB) tests.

4.3   Materials and methods

4.3.1 Electrospinning

Carboxylated nitrile butadiene rubber (NBR) NIPOL 1072CGX was purchased from Zeon Chemicals (68 %mol butadiene, 28 %mol acrylonitrile, 4 %mol methacrylic acid). Poly(ε-caprolactone) (PCL), M_w 70,000-90,000, was purchased from Sigma-Aldrich. Polymers were both used without any preliminary treatment. N,N-dimethylacetamide (DMAc), N,N-dimethylformamide (DMF) and chloroform (CHCl$_3$) were purchased from Sigma-Aldrich and used without further purifications.

Rubbery NBR/PCL nanofibrous mats were prepared following the method proposed by Maccaferri *et al.* [30]. NBR solution (S-NBR, 10 %wt) was prepared in DMAc (e.g., 1.0 g of polymer in 9.6 mL of solvent) under magnetic stirring at room temperature until the formation of a homogeneous solution. PCL solution (S-PCL, 10 %wt) was prepared in CHCl$_3$ / DMF 1:1 wt (e.g., 1.0 g of polymer in 3.0 mL of CHCl$_3$ and 4.8 mL of DMF) under magnetic stirring at room temperature until complete polymer solubilization. NBR/PCL blend was prepared by mixing 60 %wt of S-NBR and 40 %wt of S-PCL solutions. The polymer blend was stirred for a minimum of 2 h to ensure proper homogenization. Nanofibrous mats (named *n*-60/40) were produced using a Spinbow® electrospinning machine equipped with four 5 mL syringes. Needles (length 55 mm, internal diameter 0.84 mm) were joined to syringes via Teflon tubing. Nanofibers were collected on a drum covered with poly(ethylene)-coated paper rotating at 50 rpm (tangential speed 0.39 m/s). Mats had final dimensions of approximately 30 × 40 cm. To achieve different nanofiber thicknesses/grammages, only the electrospinning time was changed. The electrospinning process parameters and environmental conditions are reported in Table 4.1.

Table 4.1 – Electrospinning process parameters and nanofibers diameter.

Nanofibrous mat	Flow rate	Electric potential	Distance	Electric field[a]	Temperature	Relative humidity	Nanofibers diameter[b]
	mL/h	kV	cm	kV/cm	°C	%	nm
n-60/40	0.55	18.3	13	1.4	22-24	20-22	268 ± 43

[a] calculated as electric potential to distance ratio

[b] as spun nanofiber

To assess the thickness of the nanofibrous layers, a digital comparator (Alpa MegaRod) was used. To calculate the mat grammage (i.e., the mat weight per square meter), the nanofibrous layers were weighted by a scale with a resolution of 0.01 mg (Radwag AS 60/220.R2). Nanofiber morphology (Figure 4.1) was observed through a Scanning Electron Microscope (SEM, Phenom ProX).
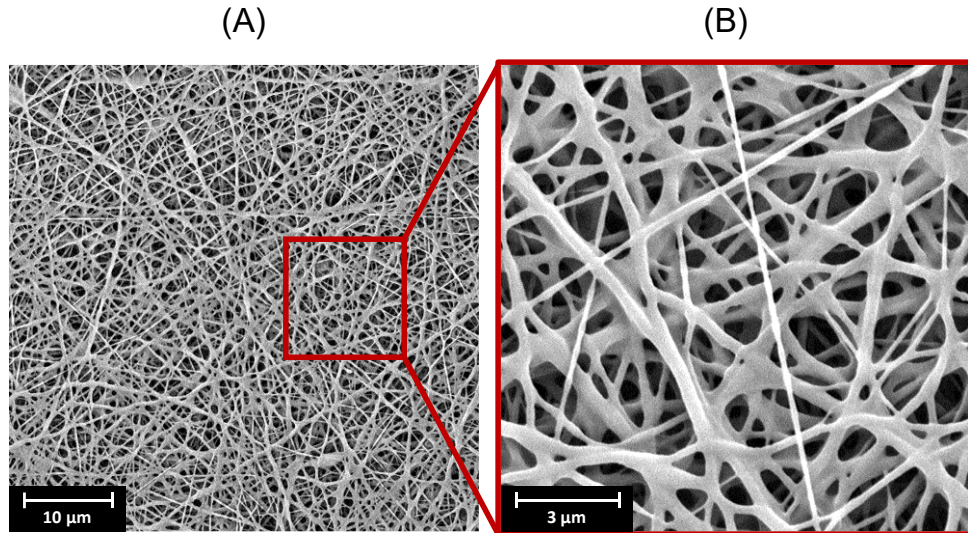
(A)   (B)

Figure 4.1 – SEM micrographs of NBR/PCL rubbery nanofibrous mat (n-60/40) at (A) 5,000x magnification and (B) 20,000x magnification.

4.3.2 Laminates and specimens preparation

The carbon fiber epoxy unidirectional prepreg was T700S-24K/DT210 epoxy-based resin provided by Deltapreg (Toray group, Italy), with V_f = 53 % and 350 g/m^2 of carbon fibers.

Four laminate configurations, reported in Table 4.2, were fabricated by staking 7 layers of unidirectional prepreg all oriented at 0°. A reference configuration composed of only prepreg plies without interleaved layers (named ref.) and three nano-structured ones with 5 µm, 10 µm, and 20 µm thick nanofibrous layers interleaved at each prepreg interface (named int. 5, int. 10, and int. 20, respectively) were produced.

Table 4.2 – Configurations of produced sample laminates.

Configuration	Mat thickness	Mat grammage
	µm	g/m^2
ref.	-	-
int. 5	5	2.5
int. 10	10	5.1
int. 20	20	9.6

Laminates were cured with vacuum bag technology in autoclave at 130 °C for 2 hours and 6 bar pressure. The resulting laminates thickness was 2.6 mm without significant difference among laminates configurations. For each configuration, the specimens for thermomechanical (DMA),

mechanical (3PB) and dynamic (damping) tests were extracted from the same laminate. Their dimensions, defined according to ASTM D7264, ISO 6721-1 and ASTM E756-05, are reported in Table 4.3.

Table 4.3 – Specimens geometry.

Test	Length mm	Width mm	Thickness mm
3PB	110	15	2.6
Damping	280	25	2.6
DMA	50	7.5	2.6

4.3.3 Thermomechanical, mechanical, and damping tests

Overall thermomechanical properties of CFRPs were evaluated via DMA, using a Netzsch DMA 242 E Artemis instrument in a three-point bending configuration with a fixed span of 40 mm. DMA analyses were carried out with a heating ramp from 0 to 170 °C, 3 °C/min heating rate, 1 Hz oscillating frequency, 20 µm amplitude and a static / dynamic force ratio of 1.5. For each laminate configuration 3 specimens were tested.

Flexural tests were carried out to assess the effect of the nanofibrous rubbery membranes on the mechanical properties of the different laminate configurations. Two different types of flexural tests under different conditions were performed: i) the destructive one, carried out until failure, to evaluate the elastic modulus and the flexural strength at three different temperatures (20, 50, and 80 °C) and ii) a dynamic test performed in the elastic regime at a frequency of 1 Hz to evaluate the elastic modulus degradation as a function of the temperature. Regarding type i) 3PB test, the aforementioned temperatures were chosen because 20 °C is the reference RT, 50 °C because it is slightly lower than the melting of the PCL crystalline fraction of the rubbery blend, and 80 °C because it is enough above the PCL melting temperature. Type ii) 3PB test, despite similar to the DMA one, allowed a more precise assessment of the flexural modulus as a function of the temperature. In fact, since UD CFRP laminates exhibit a very high flexural stiffness, the evaluation of storage modulus (E') by the DMA may be not accurate. 3PB tests were performed on Instron Model 8033 equipped with a climatic chamber using a 2 kN load cell. The destructive tests were conducted at a crosshead speed of 2 mm/min. The dynamic ones were sinusoidally loaded between 0.15 % and 0.30 % maximum flexural strain amplitude. A total of 12 3PB specimens were tested for each laminate configuration.

The dynamic tests for damping evaluation were performed according to ASTM E756-05 in a cantilever beam configuration with a laser sensor (optoNCDT 1402 - Micro-Epsilon) pointed at the specimen tip, as shown in Figure 4.2. The specimen was excited by preloading its tip and then instantaneously releasing it. For each laminate configuration, 3 specimens were tested and for each one 5 repetitions were performed. The setup parameters, depicted in Figure 4.2, were $L = 255$ mm, $d = 105$ mm, $C = 25$ Nm, $a = 5$ mm.
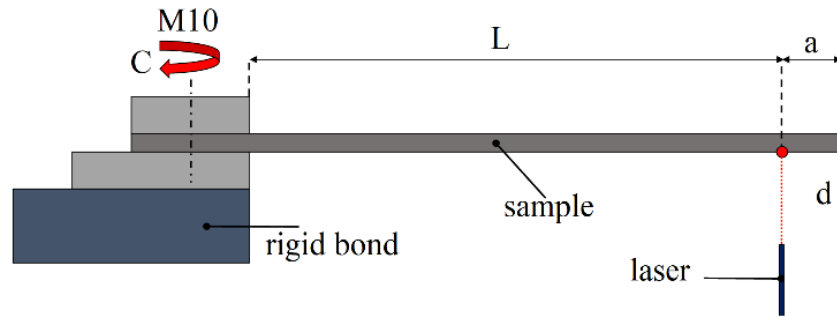

Figure 4.2 – Damping test setup scheme.

The tip displacement measured by the laser was acquired at 2 kHz by ADC converter (NI-9215 National Instruments) and processed by a MATLAB custom software based on MCD model. First, the signal was cut with a 10 s time window (Figure 4.3A). Subsequently, the Short Time Fourier Transform (STFT) was performed to obtain the spectrogram of the signal. In Figure 4.3B each curve represents the amplitude vs frequency for a specific time segment of the signal.
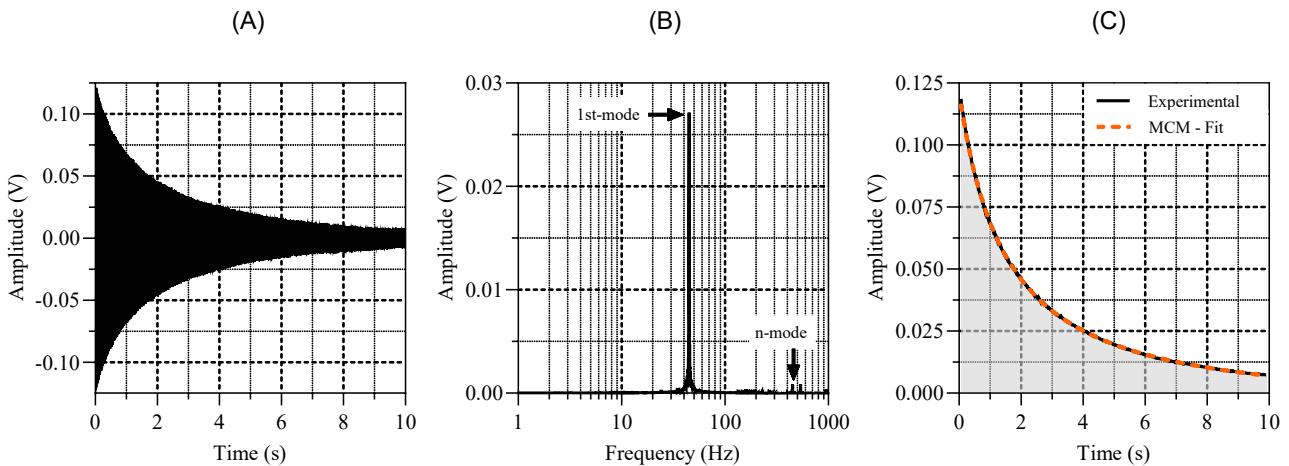
Figure 4.3 – (A) Original signal acquired by laser sensor; (B) Short Time Fourier Transform (STFT) of the signal; (C) Experimental amplitude decay as a function of time and fitting with the Modified Coulomb Damping (MCD) model.

The STFT was performed in MATLAB by using the *spectrogram* function. The signal was cut into time segments 0.1 s long, by using the Hamming window function. Then, each signal segment was extended on 1 s time span by using the zero-padding technique, in order to increase the frequency

resolution of the Fast Fourier Transform (FFT). A high signal segment overlap of 15/16 was chosen to have a high time resolution. The aforementioned parameters have been experimentally optimized for the specific type of signal analysed in this work. Then, for each amplitude vs frequency curve of the STFT of Figure 4.3B, the maximum amplitude of the first resonance frequency was extracted and expressed as function of time (Figure 4.3C). In this way, it was possible to find the amplitude decay curve in the time domain.

According to the Modified Coulomb Damping (MCD) model [32] the time varying amplitude can be defined as:

$$\dot{y}(t) = -c - by(t) - ay(t)^2 \qquad \text{Eq. 4.1}$$

where t is the time and a, b and c are coefficients accounting for viscous (air), material (structural or hysteretic) and Coulomb (friction) damping contributions, respectively. Solving the first-order Equation 4.1, under the assumption that the Coulomb damping is not dominant (i.e. $4ac < b^2$), the amplitude can be expressed as:

$$y(t) = \frac{b(p-1) + r(p+1)}{2a(1-p)} \qquad \text{Eq. 4.2}$$

where $r = (b^2 - 4ac)$, $\alpha = 2ay_0 + b - r$, $\beta = 2ay_0 + b + r$, $p = {^\alpha/_\beta}\, e^{-rt}$ and y_0 the initial amplitude. Equation 4.2 was fitted on the experimental amplitude decay curve using the robust regression with least absolute residuals weight function. In this way it was possible to separate the material damping contribution (coefficient b) from the air and friction ones.

An equivalence with the well-known classic damping ratio ζ can be done assuming that the material damping contribution is dominant. Hence, the MCD time varying amplitude (Equation 4.1) can be simplified as $\dot{y}(t) = -by(t)$. The solution of this first-order equation is:

$$y(t) = y_0 e^{-bt} \qquad \text{Eq. 4.3}$$

In the same manner, it is possible to express the response of the well-known single-degree of freedom mass-spring-damper model (given by $m\ddot{x}(t) + c\dot{x}(t) + kx(t) = 0$) as $x(t) = x_0 e^{-\zeta\omega_n t} \cos(\omega_n\sqrt{1 - \zeta^2})$ or in terms of amplitude as:

$$y(t) = y_0 e^{-\zeta\omega_n t} \qquad \text{Eq. 4.4}$$

where ω_n is the resonance frequency. Finally, matching the amplitude of the MCD model (Equation 4.3) with the one of the classical single-degree of freedom mass-spring-damper model (Equation 4.4), it is possible to express the equivalent damping ratio as:

$$\xi = \frac{b}{\omega_n}$$

Eq. 4.5

4.4 Results

4.4.1 Thermomechanical characterization

An overview of the overall thermomechanical properties of the different laminate configurations was evaluated via DMA. In Figure 4.4 the storage modulus (*E′*) and loss factor (*tanδ*) versus temperature are plotted. The laminates int. 5 and int. 10 show an *E′* trend similar to the reference one. The storage modulus is comparable to the one displayed by the unmodified CFRP, while the *E′* onset slightly lowers (107 °C vs 113 °C for the ref.). By contrast, int. 20 shows a first *E′* onset at 55 °C, and a main *E′* drop characterized by an onset at 99 °C. The first onset can be attributed to the melting of the PCL crystalline fraction, while the second drop is due to the glass transition of the toughened epoxy resin. The behaviour of the last sample is similar to what evidenced by a previous study [30].
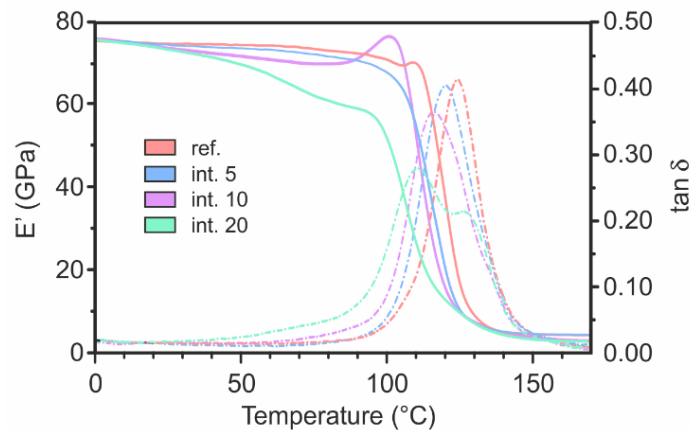
Figure 4.4 – DMA analyses for the different laminate configurations.

Regarding the *tanδ*, the peaks do not show relevant shifts for increasing grammage of interleaved mats, except for int. 20 configuration (main peak at 111 °C vs 124 °C for the ref. one). Besides, the shape of the curve is different, displaying two peaks. The first peak accounts for the toughened epoxy resin thanks to mixing with NBR/PCL blend, while the second one, at 128 °C, is due to the unmodified resin fraction. It is worth mentioning that in almost all the modified laminates, the presence of the

NBR/PCL blend widens the window dissipation energy of the composite to lower temperatures, indicating a potentially damping enhancement also at room temperature.

4.4.2 Mechanical tests and fracture analysis

The influence of both interleaved mat grammage and temperature was more deeply investigated via destructive 3PB analyses. Flexural elastic modulus and strength of the different sample configurations do not evidence significant differences at RT (Figure 4.5), which stay near 100 GPa and 1100 MPa, respectively. However, with increasing temperature, the effect of the nanomat becomes more noticeable, especially for higher mat grammages. Indeed, at 80 °C the int. 20 configuration shows a reduction of 13 % in elastic modulus and 20 % in flexural strength compared to the ref. configuration. These results agree with the overall performance of E' identified by the DMA tests.
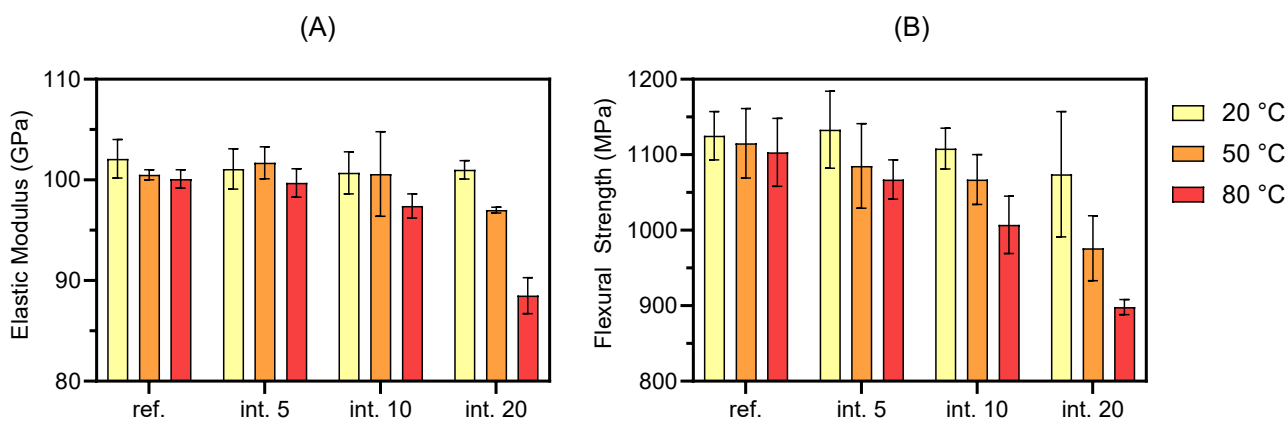
Figure 4.5 – (A) Flexural elastic modulus and (B) flexural strength for different sample configurations and temperatures.

The variation of laminate elastic modulus upon temperature was deeply elucidated carrying out 3PB cyclic loading-unloading tests. Figure 4.6 shows the flexural modulus as a function of temperature. As can be noticed, the elastic modulus shows a significant reduction only when high temperatures (> 80 °C) and high grammages (> 5 g/m^2, int. 10) are combined. However, during the life-cycle of common composite components, these high temperatures are rarely reached, except for special applications.

Although the qualitative trends of E' and flexural modulus are similar, the numerical values shown in Figure 4.6 are much more reliable than those obtained from the DMA, where E' is strongly influenced by the specific specimen loading region (e.g., local fiber/matrix ratio under solicitation). On the contrary, since the imposed deformation in 3PB test is macroscopic, the local effects become negligible because the stressed volume is increased.
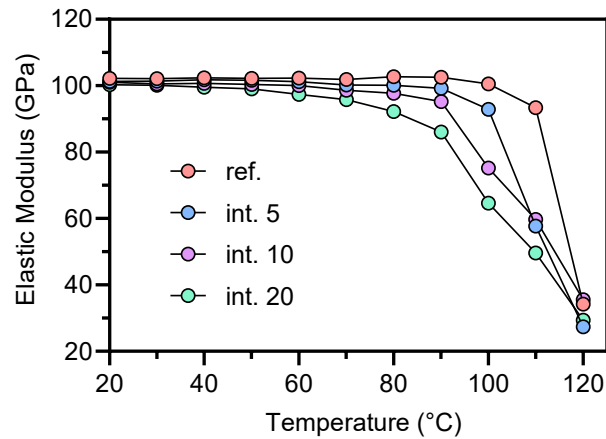
Figure 4.6 – Temperature dependence of flexural modulus for the different sample configurations.

In Figure 4.7 are displayed the perpendicular and parallel views of the fracture surfaces of 3PB specimens tested up to failure at RT for each laminate configuration. In this way, it was possible to observe both pulled out fibers (in blue in the sketch of Figure 4.7) and fibers broken in correspondence of the fracture surface of the specimen (in red). Moreover, int. 20 was analysed also at 50 and 80 °C.

The fracture surfaces of the ref. laminate appear sharp and brittle, with a marked fiber/matrix debonding (perpendicular view) and naked pulled out carbon fibers (parallel view). This behaviour is typical of low-toughened thermosetting polymers.

For nano-interleaved laminates, it can be noticed that the nanofibrous morphology is completely lost. Indeed, as previously observed in Figure 4.7, during the curing cycle the NBR/PCL blend mixed with the epoxy resin, leading to toughened matrix. As a matter of fact, by increasing the grammage of interleaved mat, the fracture surfaces become more irregular with more pronounced indented markings, meaning a greater ductile deformation. Moreover, a higher adhesion between carbon fibers and toughened epoxy matrix (perpendicular view) is found, and the matrix remains attached to the pulled out fibers (parallel view). This effect is maximized in int. 20, particularly when the testing temperature is increased from RT to 50 and 80 °C.

4.4.3 Damping analysis

Regarding damping tests, the fitting of the experimental signal with MCD model has always guaranteed a $R^2 \geq 0.99$. It was therefore possible to calculate the normalized material damping value for each configuration by excluding the contribution of both air and joint friction. This method was adopted because the damping effect of the air is predominant compared to the material one.
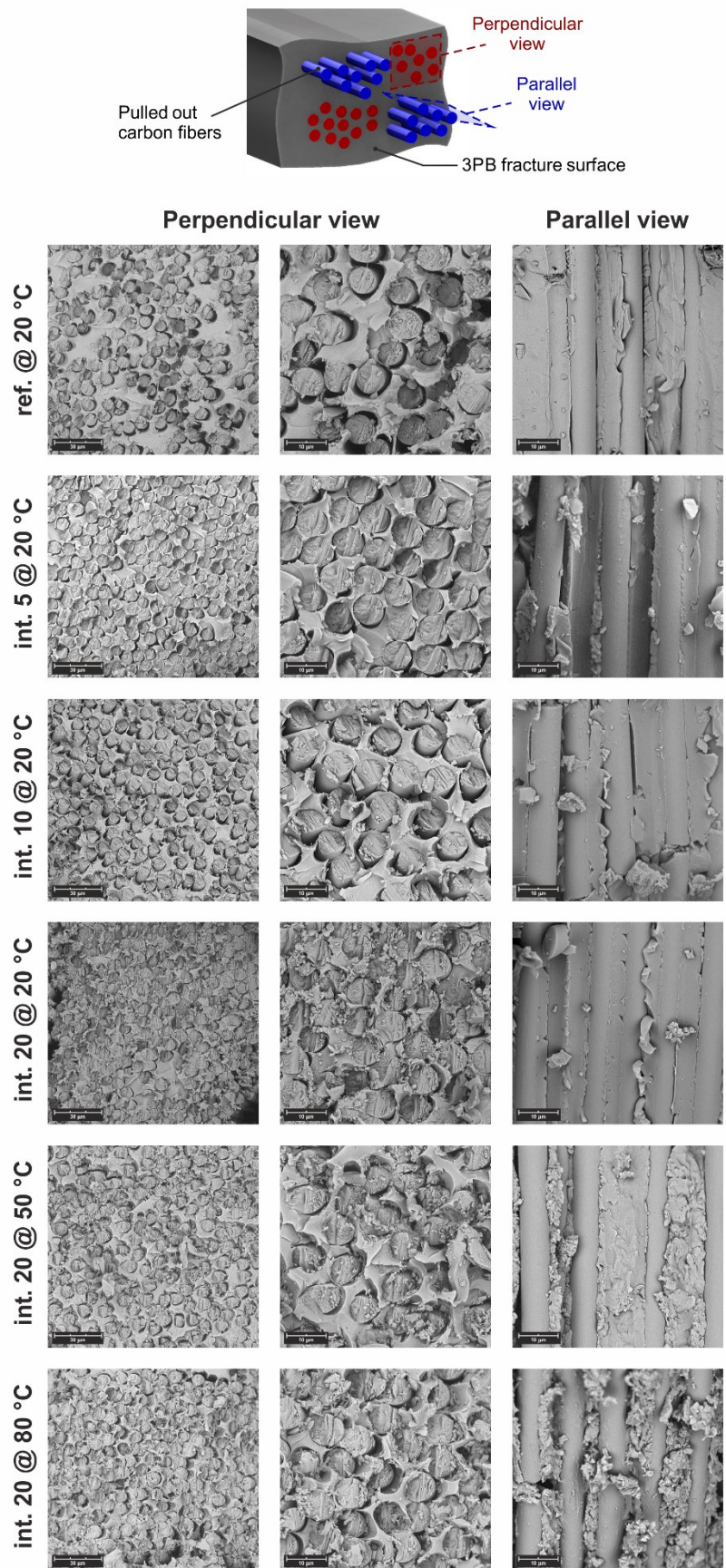
Figure 4.7 – SEM micrographs of 3PB specimens after destructive tests (magnification: first column 2,000x; second and third columns 5,000x).

The material damping factor ranges from $1.75 \cdot 10^{-3}$ to $3.10 \cdot 10^{-3}$ for the ref. and int. 20 configurations, respectively (Figure 4.8A). Figure 4.8B shows the material damping enhancement versus the laminate weight variation for the different configurations. It is interesting to note that as the grammage of the nanofibrous membranes increases an exponential trend is observed in material damping. The major damping enhancement was obtained with the int. 20 configuration, achieving an improvement of 77 % for a laminate weight increment of 1.5 % only.
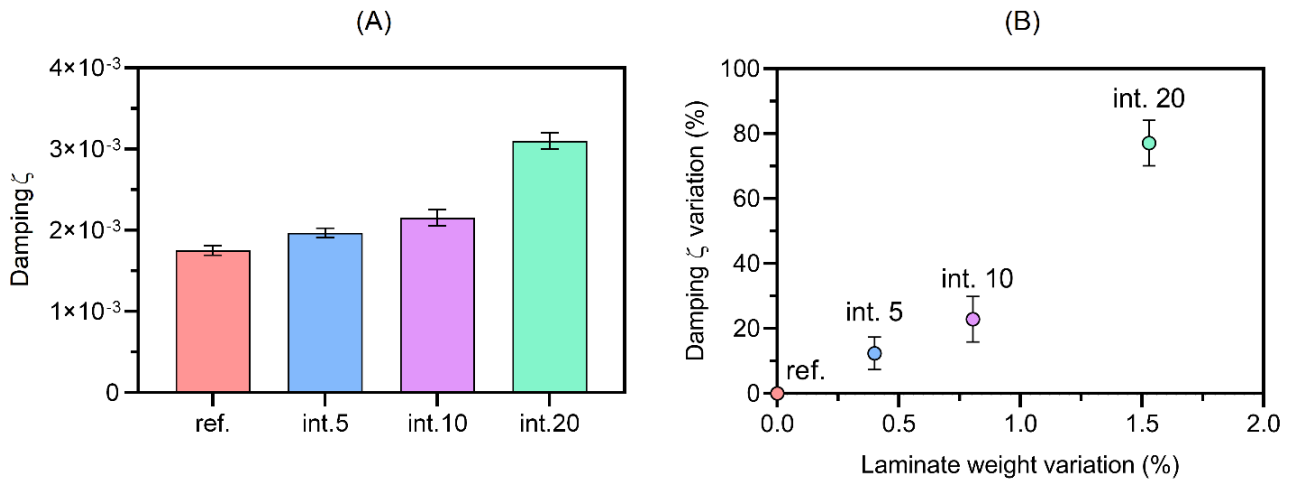
Figure 4.8 – (A) Material damping of the different sample configurations and (B) material damping percentage variation as a function of the laminate percentage weight variation.

4.5 Conclusions

In this work a structural composite was prepared by interleaving rubbery NBR/PCL nanofibrous layers between unidirectional CFRP prepreg laminates. Thermomechanical properties were experimentally evaluated using 3PB tests and DMA. Flexural tests show no significant differences at room temperature in elastic modulus and flexural strength between reference and nano-modified configurations. Only for the highest grammage and for temperatures over 50 °C, the effect of the nanomat becomes noticeable. In particular, when 80 °C are reached, the int. 20 configuration shows a reduction of 13 % in elastic modulus and 20 % in flexural strength compared to the ref. one. These results are in good accordance with DMA ones, which shows an E' onset drop from 113 °C to 55 °C. The morphology of the fracture surfaces as well appears to be affected by the amount of interleaved rubbery nanofibers, becoming more irregular and ductile.

Damping behaviour was evaluated by single cantilever beam vibration tests. Thanks to the advanced Modified-Coulomb-Damping (MCD) model, an accurate measurement of the material damping was obtained excluding the air and joint contributions.

The interleaved NBR/PCL nanofibrous mats greatly improved the composite damping capacity with a maximum increase of 77 % in the composite loss factor, with a negligible influence on flexural strength and modulus below *E'* onset temperature. Moreover, no significant impact on laminate weight and thickness, respect to reference samples without nano-reinforcement, were found.

Hence, this type of nano-modified composite material is suitable for all those applications that require high energy dissipation ensuring at the same time high mechanical performance even at intermediate in-service temperature. The integration of nanofibrous rubbery membranes interspersed between the composite laminae overcomes the limits related to the use of bulk viscoelastic layers, which could negatively affect the laminate weight and integrity, even increasing its fracture toughness. This technique may allow engineers to design advanced composite components with high damping capacity by ultra-low grammage rubbery nanofibrous layers addition.

4.6   Nomenclature

M_w molecular weight

V_f prepreg carbon fiber volume percentage

E' DMA conservative modulus

$tan\delta$ DMA damping factor

L fixed support – laser distance for the damping test setup

d laser–specimen distance for the damping setup

a laser – specimen free edge distance

C fastening bolt torquing moment

a,b,c coefficients for viscous, material and Coulomb contributions

m,k,c coefficients for mass-spring-damper model

t time

ω_n resonance frequency

ζ material damping ratio

4.7 References

[1] J.M. Berthelot, M. Assarar, Y. Sefrani, A. El Mahi, Damping analysis of composite materials and structures, Composite Structures. (2008). https://doi.org/10.1016/j.compstruct.2007.10.024.

[2] A.D. Nashif, D. Jones, J. Henderson, Vibration damping, 1985.

[3] J.M. Berthelot, Y. Sefrani, Damping analysis of unidirectional glass and Kevlar fibre composites, Composites Science and Technology. 64 (2004) 1261–1278. https://doi.org/10.1016/j.compscitech.2003.10.003.

[4] M.J. Le Guen, R.H. Newman, A. Fernyhough, G.W. Emms, M.P. Staiger, The damping-modulus relationship in flax-carbon fibre hybrid composites, Composites Part B: Engineering. 89 (2016) 27–33. https://doi.org/10.1016/j.compositesb.2015.10.046.

[5] A. Treviso, B. Van Genechten, D. Mundo, M. Tournour, Damping in composite materials: Properties and models, Composites Part B: Engineering. 78 (2015) 144–152. https://doi.org/10.1016/j.compositesb.2015.03.081.

[6] R.M. Crane, J.W. Gillespie, Characterization of the vibration damping loss factor of glass and graphite fiber composites, Composites Science and Technology. 40 (1991) 355–375. https://doi.org/10.1016/0266-3538(91)90030-S.

[7] D.D.L. Chung, Structural composite materials tailored for damping, in: Journal of Alloys and Compounds, 2003: pp. 216–223. https://doi.org/10.1016/S0925-8388(03)00233-0.

[8] J. Li, Y. Narita, Analysis and optimal design for the damping property of laminated viscoelastic plates under general edge conditions, Composites Part B: Engineering. (2013). https://doi.org/10.1016/j.compositesb.2012.09.014.

[9] M.R. Maheri, The effect of layup and boundary conditions on the modal damping of FRP composite panels, Journal of Composite Materials. (2011). https://doi.org/10.1177/0021998310382314.

[10] H. Kishi, M. Kuwata, S. Matsuda, T. Asami, A. Murakami, Damping properties of thermoplastic-elastomer interleaved carbon fiber-reinforced epoxy composites, Composites Science and Technology. (2004). https://doi.org/10.1016/j.compscitech.2004.05.006.

[11] B.B. Johnsen, A.J. Kinloch, R.D. Mohammed, A.C. Taylor, S. Sprenger, Toughening mechanisms of nanoparticle-modified epoxy polymers, Polymer. 48 (2007) 530–541. https://doi.org/10.1016/j.polymer.2006.11.038.

[12] T.H. Hsieh, A.J. Kinloch, K. Masania, A.C. Taylor, S. Sprenger, The mechanisms and mechanics of the toughening of epoxy polymers modified with silica nanoparticles, Polymer. 51 (2010) 6284–6294. https://doi.org/10.1016/j.polymer.2010.10.048.

[13] S. Tahan Latibari, M. Mehrali, L. Mottahedin, A. Fereidoon, H.S.C. Metselaar, Investigation of interfacial damping nanotube-based composite, Composites Part B: Engineering. (2013). https://doi.org/10.1016/j.compositesb.2013.02.022.

[14]   N.A. Koratkar, J. Suhr, A. Joshi, R.S. Kane, L.S. Schadler, P.M. Ajayan, S. Bartolucci, Characterizing energy dissipation in single-walled carbon nanotube polycarbonate composites, Applied Physics Letters. 87 (2005). https://doi.org/10.1063/1.2007867.

[15]   A. Montazeri, N. Montazeri, Viscoelastic and mechanical properties of multi walled carbon nanotube/epoxy composites with different nanotube content, Materials and Design. 32 (2011) 2301–2307. https://doi.org/10.1016/j.matdes.2010.11.003.

[16]   R. Palazzetti, A. Zucchelli, Electrospun nanofibers as reinforcement for composite laminates materials – A review, Composite Structures. 182 (2017) 711–727. https://doi.org/10.1016/j.compstruct.2017.09.021.

[17]   Y. Li, S. Cai, X. Huang, Multi-scaled enhancement of damping property for carbon fiber reinforced composites, Composites Science and Technology. (2017). https://doi.org/10.1016/j.compscitech.2017.03.008.

[18]   E. Maccaferri, L. Mazzocchetti, T. Benelli, T.M. Brugo, A. Zucchelli, L. Giorgini, Rubbery nanofibrous interleaves enhance fracture toughness and damping of CFRP laminates, Materials & Design. (2020). https://doi.org/10.1016/j.molliq.2020.112490.

[19]   C. Garcia, J. Wilson, I. Trendafilova, L. Yang, Vibratory behaviour of glass fibre reinforced polymer (GFRP) interleaved with nylon nanofibers, Composite Structures. 176 (2017) 923–932. https://doi.org/10.1016/j.compstruct.2017.06.018.

[20]   Z.D. Xu, Y.X. Liao, T. Ge, C. Xu, Experimental and theoretical study of viscoelastic dampers with different matrix rubbers, Journal of Engineering Mechanics. 142 (2016) 1–12. https://doi.org/10.1061/(ASCE)EM.1943-7889.0001101.

[21]   X. Zhang, G.G. Chase, Electrospun elastic acrylonitrile butadiene copolymer fibers, Polymer. 97 (2016) 440–448. https://doi.org/10.1016/j.polymer.2016.05.063.

[22]   H. Wu, Q. Hu, L. Zhang, H. Fong, M. Tian, Electrospun composite nanofibers of polybutadiene rubber containing uniformly distributed Ag nanoparticles, Materials Letters. 84 (2012) 5–8. https://doi.org/10.1016/j.matlet.2012.06.039.

[23]   X. Zhang, X. Yang, G.G. Chase, Filtration performance of electrospun acrylonitrile-butadiene elastic fiber mats in solid aerosol filtration, Separation and Purification Technology. 186 (2017) 96–105. https://doi.org/10.1016/j.seppur.2017.06.002.

[24]   K. Phatcharasit, W. Taweepreda, K. Boonkerd, J.K. Kim, Electrospun epoxidized natural rubber with poly(vinyl chloride) (ENR-PVC) nanofibrous for PEMFC applications, in: Advanced Materials Research, 2014: pp. 507–510. https://doi.org/10.4028/www.scientific.net/AMR.844.507.

[25]   M.W. Thielke, E.P. Bruckner, D.L. Wong, P. Theato, Thiol-ene modification of electrospun polybutadiene fibers crosslinked by UV irradiation, Polymer. 55 (2014) 5596–5599. https://doi.org/10.1016/j.polymer.2014.09.002.

[26]   T.E. Kerr-Phillips, V. Woehling, R. Agniel, G.T.M. Nguyen, F. Vidal, P. Kilmartin, C. Plesse, J. Travas-Sejdic, Electrospun rubber fibre mats with electrochemically controllable

pore sizes, Journal of Materials Chemistry B. 3 (2015) 4249–4258. https://doi.org/10.1039/c5tb00239g.

[27] M. Tian, Q. Hu, H. Wu, L. Zhang, H. Fong, L. Zhang, Formation and morphological stability of polybutadiene rubber fibers prepared through combination of electrospinning and in-situ photo-crosslinking, Materials Letters. (2011). https://doi.org/10.1016/j.matlet.2011.06.089.

[28] S.S. Choi, J.P. Hong, Y.S. Seo, S.M. Chung, C. Nah, Fabrication and characterization of electrospun polybutadiene fibers crosslinked by UV irradiation, Journal of Applied Polymer Science. 101 (2006) 2333–2337. https://doi.org/10.1002/app.23764.

[29] H. Liu, B. Lin, C. Jiang, A new method for determining coal seam permeability redistribution induced by roadway excavation and its applications, Process Safety and Environmental Protection. 131 (2019) 1–8. https://doi.org/10.1016/j.psep.2019.08.019.

[30] E. Maccaferri, L. Mazzocchetti, T. Benelli, T.M. Brugo, A. Zucchelli, L. Giorgini, Rubbery nanofibers by co-electrospinning of almost immiscible NBR and PCL blends, Materials and Design. (2020). https://doi.org/10.1016/j.matdes.2019.108210.

[31] C.W. De Silva, Vibration monitoring, testing, and instrumentation, 2007. https://doi.org/10.1201/9781420053203.

[32] C.W. De Silva, Vibration and Shock Handbook, 1st ed., Boca Raton, 2005. https://doi.org/https://doi.org/10.1201/9781420039894.

Chapter 5

Self-sensing hybrid composite laminate by piezoelectric nanofibers interleaving

Tommaso Maria Brugo[1], Emanuele Maccaferri[2], Davide Cocchi[1]
Laura Mazzocchetti[2], Loris Giorgini[2], Davide Fabiani[3], Andrea Zucchelli[1]

[1]*Dipartimento di Ingegneria Industriale, Alma Mater Studiorum - Università di Bologna*
viale del Risorgimento 2, 40136 Bologna, Italy

[2]*Dipartimento di Chimica Industriale "Toso Montanari", Alma Mater Studiorum - Università di Bologna*
viale del Risorgimento 4, 40136 Bologna, Italy

[3]*Dipartimento di Ingegneria Elettrica, Alma Mater Studiorum - Università di Bologna*
viale del Risorgimento 4, 40136 Bologna, Italy

The candidate is one of the Authors of this pioneering study. He contributes to the investigation, data analysis and manuscript drafting, revision and approval. The work was published on Composite Part B: Engineering journal (2021). Reproduced with kind permission from Elsevier.

5.1   Abstract

One of the most critical aspects of composite materials is their vulnerability to impact loadings. In recent years, Structural Health Monitoring (SHM) systems have been developed to continuously watch over on the event of an impact and so monitor the health status of the structure. However, this technique needs the integration of sensors in the composite laminate, like Fiber Bragg Grating or piezoelectric ceramic transducers, which often can dramatically reduce the inherent strength of the hosting material. The aim of this work is the integration of the composite laminate with a nano-structured piezoelectric sensor, based on PVDF-TrFE nanofibers and aluminium sheets as electrodes. Structurally, the resulting composite is a hybrid laminate known as Glass Laminate Aluminium Reinforced Epoxy (GLARE), consisting of aluminium sheets alternatively bonded to glass-epoxy prepreg layers, functionalized with PVDF-TrFE interleaved nanofibrous mats. Hence, this nano-structured hybrid laminate becomes itself a piezoelectric sensor, capable to detect impacts on its

whole surface. Non-destructive impact tests were performed using an instrumented drop-weight tower to investigate the real-time electrical response of the self-sensing laminate. A lumped electric model was applied to study and optimize the circuit electrical parameters. Then, the self-sensing laminate performance were evaluated in terms of linearity and spatial uniformity.

Keywords: nano-structures, smart materials, impact behaviour, non-destructive testing, Structural Health Monitoring (SHM)

5.2   Introduction

The use of Fiber Reinforced Plastics (FRP) composite laminates is rapidly growing in different fields, such as aerospace and wind energy, thanks to their higher specific stiffness and strength compared to conventional materials. However, due to their laminar structure, they are prone to delamination and are susceptible to out-of-plane impact loads. Often, the flaw initiates and propagates inside the laminate without any visible damage on the outer surfaces, until it reaches a critical dimension that causes the sudden and catastrophic failure of the component. The safety is therefore guaranteed by over-dimensioning them and by time-consuming periodic non-destructive testing (NDT) inspections, that negatively impact on the overall weight and life-cycle cost of the structure [1,2].

To overcome these limitations, Structural Health Monitoring (SHM) systems are being developed to continuously watch over the health status of the structure during operation and immediately detect the damage. The monitoring sensors can be either externally mounted or integrated into the laminate. External sensors usually do not affect mechanical performance of the laminate, however, they are bulky and exposed to external environmental conditions, electronic interferences and impacts [1]. For this reason, efforts have been made to embed commercial sensors into the composite between the laminate plies. The most widely used are Fiber Bragg Grating (FBG) [3] and piezoelectric ceramic-based sensors, like lead zirconate titanate (PZT) wafers [4] or microfibers [5]. FBG sensors, thanks to their multiplexing capacity, allow the strain measurement on different spots along with a single optical fiber [6,7]. However, inserting a sub-millimetric optical fiber between composite plies perpendicularly to the reinforcing fiber produce an eye-shaped resin pocket defect which can cause matrix cracking and subsequent delamination [8]. Piezoelectric sensors are widely employed to measure frequency vibrations, like Lamb waves or acoustic emission, due to their reduced weight, size and cost [6]. Thanks to their high piezoelectric constant, PZT wafers show an excellent sensitivity with respect to other conventional sensors like strain gauges, fiber optics and more flexible

piezoelectric polymers [9,10]. However, their ceramic inherent nature makes them extremely brittle. In fact, PZT fracture causes an interface crack nucleation, which brings to unstable delamination [11]. This aspect affects the composite fatigue strength and limits the bearing strength capacity of the laminate [12]. By changing the morphology of the PZT from wafer disks to microfibers (micro-sized lead zirconate titanate fibers) the intrusiveness of the sensor on the hosting laminate can be reduced. For instance, the laminate shear strength is reduced by 7 % by embedding PZT microfibers in unidirectional GFRP prepreg plies compared to 15 % by embedding PZT disks [5]. An alternative to brittle piezoceramic sensors is polyvinylidene difluoride (PVDF) polymeric films. These have the advantages of high flexibility, low mass and cost and high internal damping [13,14]. However the interface strength between the sensor and the hosting matrix can be an issue [15,16]. Another possibility is to make the matrix system self-sensing through additives, e.g. by adding carbon nanotubes (CNTs) [17]. Compared to the previously described extrinsic sensors, that constitute a foreign body hosted in the laminate, the matrix itself when reinforced with CNTs becomes intrinsically a sensor. This concept overcomes the issues related to mechanical performance reduction [17–19]. The use of a small amount of CNTs makes the polymer matrix electrically conductive and piezo-resistive, ensuring a strict relationship between the mechanical deformations and the measured electrical resistance [20]. However, the sensing performances are susceptible to the unavoidable inhomogeneous dispersion of the filler (entanglements) within the resin, which impacts on the electrical response of the obtained nanocomposites [17,20].

In this work, the integration of a nanostructured piezoelectric sensor made by poly(vinylidenefluoride-trifluoroethylene) (PVDF-TrFE) nanofibers into a composite laminate with aluminium sheets as electrodes is proposed. Structurally, the resulting composite is a hybrid laminate consisting of aluminium sheets alternatively bonded to glass-fiber reinforced plastics (GFRP) prepreg layers and interleaved with PVDF-TrFE nanofibrous mats. Such lay-up belongs to a special class of hybrid laminates known as Glass Laminate Aluminium Reinforced Epoxy (GLARE), well known for its superior impact strength [21]. Moreover, nanofibrous mat interleaving is a consolidated technique used to increase the delamination toughness and impact strength of composite laminates without affecting the overall stiffness [22–24]. Hence, the resulting nanostructured hybrid laminate constitutes itself a piezoelectric sensor capable of detecting an impact load on its whole surface, with potentially superior impact resistance compared to pristine ones.

5.3   Materials and methods

5.3.1 Fabrication process of the self-sensing laminate

5.3.1.1 Piezoelectric polymer and electrospinning

The piezoelectric nanofibrous non-woven mat was fabricated by electrospinning method (Figure 5.1a) and nanofibers were made of PVDF-TrFE 70:30 %mol copolymer (Solvene®300 EAP, courtesy of Solvay S.p.A. Milan). The copolymer shows a Curie temperature (T_c) of 103 °C and a melting temperature (T_m) of 145 °C, measured by Differential Scanning Calorimetry (DSC) analysis. As will be clarified afterward, these specific thermal features are crucial both for the fabrication and poling of the piezoelectric composite laminate.

The copolymer was dissolved at 20 %wt in a mixture of 55:45 %wt of acetone (AC) and dimethylformamide (DMF). The non-woven nanofibrous mat was fabricated with a four needle - drum collector electrospinning machine (Lab Unit, Spinbow®). Electrospinning process was carried out under the following optimized conditions: 0.8 ml/h flow rate per nozzle, 18 kV electric potential, 18 cm needle to collector distance, 0.2 m/s tangential speed, 20÷24 °C temperature at 40÷50 % of relativity humidity (RH). Process was carried out for 8 hours to obtain an A3 size randomly oriented nanofibrous mat.
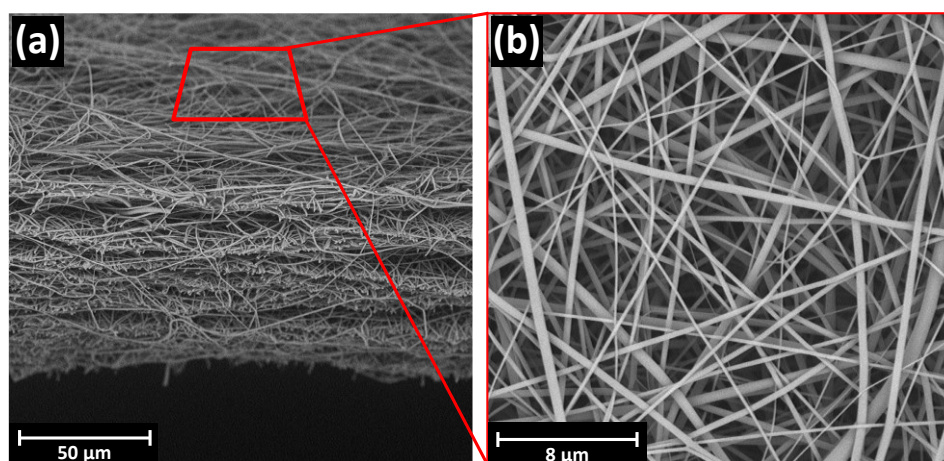
Figure 5.1 – SEM micrographs of the piezoelectric nanofibrous mat: (a) cross-section and (b) morphology.

In Figure 5.1a and Figure 5.1b Scanning Electron Microscope (SEM) micrographs of the cross-section and morphology of the nanofibrous mat so obtained are shown, respectively. The measured mat thickness was 50 μm (evaluated with a digital indicator having a measuring pressure of 100 g/cm^2), while the areal weight was 16 g/m^2. The average fiber diameter, evaluated on 100 different

fibers, was 340 ± 120 nm. The electrospinning process was stable and it has the potential to be scaled up at industrial level (e.g. by needleless technology), reducing the fabrication time by one or two orders of magnitude [25].

5.3.1.2 Stacking sequence and curing

The self-sensing laminate is composed of thin layers of aluminium (Al 2024-T3, 60 x 70 x 0.5 mm), interspersed with layers of woven Glass Fiber Reinforced Polymer (GFRP) prepreg (E-glass 8H Satin 300 g/m^2 - epoxy matrix, VV300S - DT121H-34 Deltapreg, 80 x 90 x ~0.22 mm) and the piezoelectric nanofibrous mat interleaved at the laminate midplane (80 x 90 x ~0.05 mm). The resulting stacking sequence is $[Al_1/(GFRP\text{-}0°)_4/\ Al_1/(GFRP\text{-}0°)_2/Nano_1]_S$, as depicted in Figure 5.2. The aluminium sheets, in addition to the structural function of increasing the impact resistance as occurs in standard GLARE laminates, have the electrical function of collecting the piezoelectric signal and shielding the sensor. For the sake of comparison, a laminate with the same stacking sequence of the self-sensing one (hereafter named Piezo) but lacking the nanofibrous mat (hereafter named Reference) was also fabricated.

Before stacking, the aluminium sheets were subjected to surface treatment by chemical etching in sulfuric acid/ferric sulphate solution (P-2 Etching according to ASTM D2651), to improve the adhesion with the epoxy matrix of the GFRP plies. Moreover, signal cables (430-FST, Micro-Measurements), coated with a Teflon jacket, to withstand the high temperatures of the composite curing cycle, were soldered on the aluminium sheets with a Sn/Cu 97/3 soldering paste specific for aluminium (Flux SN35). If difficulties in placing the signal cable should arise, due to the needs of trimming and/or constraining the edges of the composite structure, the cables can be let to come out from the laminate surface by making a small incision on the prepreg and aluminium sheets at the laminate edge, as proposed in [26].

After stacking, both Piezo and Reference laminates were cured in autoclave with a vacuum bag pressure of -850 mbar and external pressure of 6 bar, using a custom 3 steps cure cycle (see graph of Figure 5.3) made up of: (i) a 30 min isotherm @ 50 °C, (ii) a 120 min isotherm @ 100 °C, and (iii) a 60 min isotherm @ 150 °C, with 2 °C/min heating and cooling ramps. Step (i) was introduced to promote the impregnation of the nanofibrous mat, by decreasing the viscosity of the epoxy resin without significantly triggering the cross-linking. The second step (ii) allows the gradual cross-linking of the epoxy matrix in mild conditions, trying to avoid exotherm-triggered temperature overshot that might outgrow the melting temperature of the polymeric nanofibers, thus helping preserving their morphology. The third step (iii) completes the cross-linking of the epoxy resin and brings the glass

transition temperature (T_g) over the Curie one (T_c). Despite the step (iii) temperature is above the melting temperature of PVDF-TrFE the nanofiber morphology is preserved because the surrounding epoxy matrix has already a sufficient crosslinking degree to act as a mould. Note that in Figure 5.3 the T_g reached by the resin at each step are also reported. The resulting final thickness of the cured laminate was 4.6 ± 0.05 mm.
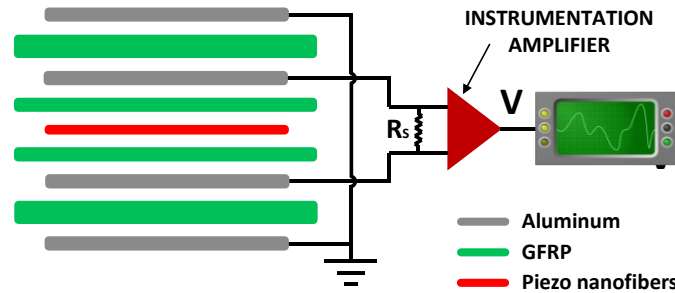

Figure 5.2 – Stacking sequence of the self-sensing GLARE laminate and electric connections.
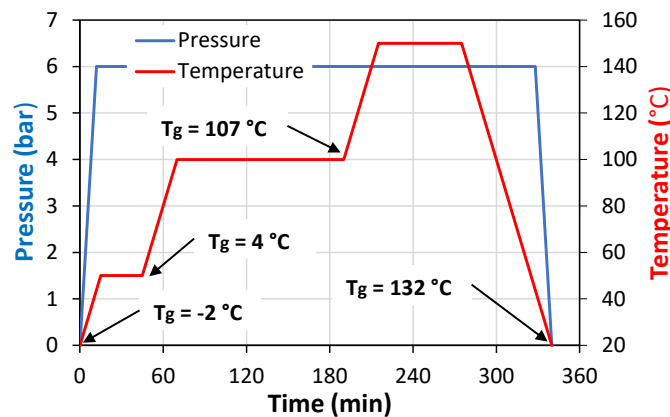
Figure 5.3 – Cure cycle of the self-sensing GLARE laminate.

5.3.1.3 Poling

Despite the ferroelectric nanofibrous mat could be self-polarized by the strong electric field employed in the electrospinning process [27] the preferential dipole orientation is lost during the subsequent curing of the composite laminate, which is carried out above the Curie temperature. Therefore, after curing, the self-sensing laminate with the embedded PVDF-TrFE nanofibrous mat was poled by applying an electric field of 6 kV/mm between the two inner electrodes (aluminium plies) at a temperature of 110 °C for 30 minutes and then cooling it down to room temperature at 2 °C/min, keeping the electric field on to stabilize the polar alignment. Finally, to remove any residual electrostatic charge induced by the electrospinning and poling processes, the laminate was left at 60 °C for 72 hours with short-circuited electrodes.

The polarization temperature of 110 °C was selected because is higher than the PVDF-TrFE Curie temperature (T_c = 103 °C), but at the same time lower than the glass transition temperature of the laminate epoxy matrix (T_g = 132 °C). Indeed, the mobility of the electric dipoles above Curie temperature increases and as consequence they can be aligned by applying a significantly lower poling electric field than the one necessary at room temperature (150 kV/mm as suggested by the supplier), reducing the risk of electrical breakdown. At the same time, the poling temperature was kept lower than the T_g temperature, above which the electric permittivity of the epoxy matrix would rapidly decrease [28], with consequent increases of the conductivity and, in turn, risk of electrical breakdowns. Another critical aspect in the poling process is the presence of voids which can trigger electrical discharges. Indeed, in preliminary samples cured out of autoclave, poling was not possible due to electrical discharges caused by a high void content.

The poling step represents the most critical aspect in the fabrication of the self-sensing laminate, because of the risk of electric breakdowns. However, if the poling temperature is kept between the Curie and T_g temperatures and composite voids are minimized (as in this case by using prepreg and autoclave technology), the piezoelectric nanofibers can be successfully polarized.

5.3.1.4 Signal conditioning

As shown in the diagram of Figure 5.2, the electrical charges generated by the nanofibrous piezoelectric mat are collected by the two internal electrodes (aluminium sheets) of the laminate. While the two external aluminium plies of the laminates are connected to ground, to shield the sensor from triboelectric noise and external electromagnetic interferences.

The piezoelectric sensor, composed by the nanofiber embedded in the GFRP and the two aluminium electrodes, acts as a capacitor in parallel with a very high internal leakage resistance (thanks to the high permittivity of the GFRP). Therefore, the high impedance signal output of the piezoelectric sensor has to be converted by a pre-amplifier to a low impedance signal, suitable for the direct transmission to the acquisition system. The voltage amplifier is composed of an instrumentation amplifier (INA 118, Texas Instruments) with an impedance input of 10 GΩ and an interchangeable shunt resistor (varied from 1 kΩ to 1 GΩ) connected in parallel to the circuit, to tune the sensor electric response.

5.3.2 Low velocity impact test

Non-destructive low-velocity impact tests were performed to investigate and optimize the electrical response of the self-sensing laminate to impact. For this purpose, a drop-weight tower was

employed, built according to the ASTM D7136 standard, as showed in Figure 5.4. The impactor had a total mass of 1.3 kg and a 12.7 mm diameter hemispherical steel tip, instrumented with a piezoelectric commercial load cell (208C05, PCB Piezotronics). The laminate was placed on a plane with a 60 x 50 mm pit (smaller than the standard one) and clamped with two harmonic steel strips, to avoid rebounds. The signal generated by the self-sensing laminate and the contact force measured by the impactor load cell were synchronously acquired at 100 kHz by means of an ADC converter (NI cDAQ 9171 combined with NI 9215, National Instrument). The electrical response of the laminate was investigated for different shunt resistances and with or without shielding. For this purpose, laminates were impacted multiple times keeping the maximum impact force lower than 0.5 kN to avoid damaging the laminate.
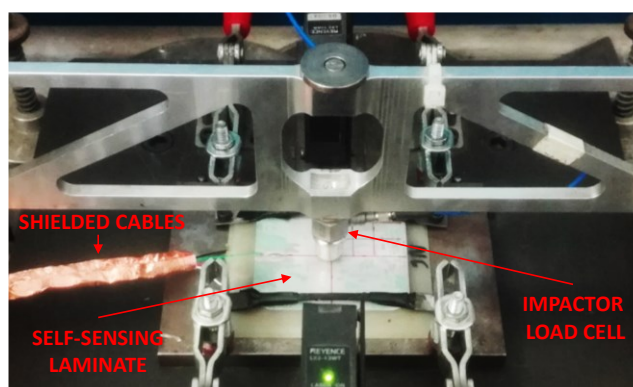
Figure 5.4 – Low velocity impact test setup.

5.4   Results and discussion

5.4.1 Characterization of the embedded piezoelectric nanofibers

5.4.1.1 Morphology

The integration of the GLARE laminate with the piezoelectric nanofibrous mat was investigated by optical micrograph (Figure 5.5a) and SEM (Figure 5.5b and Figure 5.5c) analyses of the cross-section. In Figure 5.5a the resulting stacking sequence of the self-sensing laminate can be observed, with the aluminium sheets, appearing as the white layers, interspersed with GFRP woven plies.

Focusing on the laminate mid-plane (see Figure 5.5b and Figure 5.5c), the piezoelectric nanofibrous mat embedded in the epoxy matrix can be observed. It is worth noting that PVDF-TrFE was removed by flushing the laminate in acetone, to help pointing out the empty traces left by the nanofibers, that clearly stand out from the matrix in the SEM micrographs. Figure 5.5b clearly shows that the nanofibrous mat completely fills the matrix-rich interlayer between the upper and lower glass plies, by varying its thickness from 12 to 44 µm, to adapt to the weave of the fiberglass fabric. In the

composite matrix, few voids can be observed, with a maximum diameter of 10 µm. However, their dimension did not compromise the poling process. Moreover, Figure 5.5c shows that the nanofibrous mat is completely impregnated and integrated with the epoxy matrix. Generally, it can be noted that the contribution in volume and thickness of the piezoelectric nanofibrous mat on the GLARE laminate is negligible.
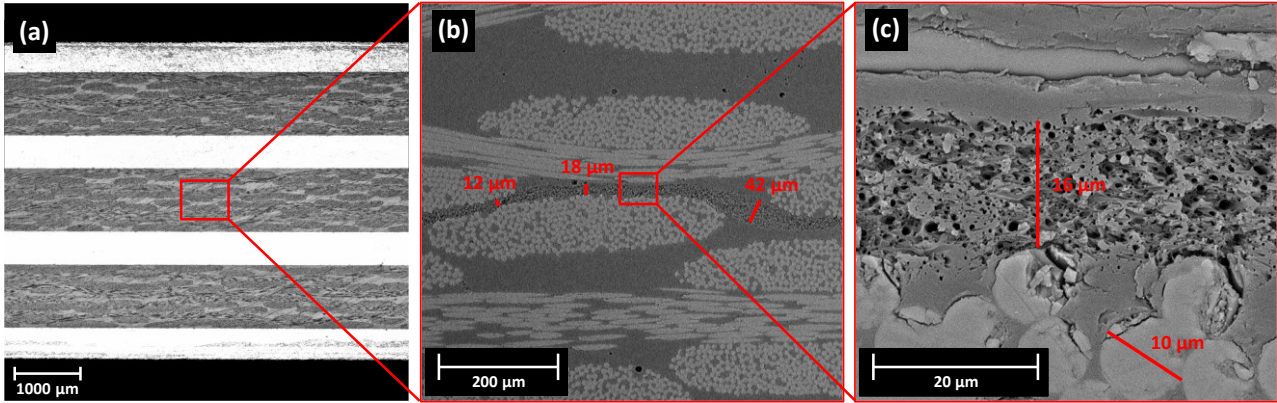

Figure 5.5 – Cross-section micrograph analysis of the piezoelectric nanofibrous mat integrated with GLARE laminate at different magnifications: (a) full laminate cross-section, (b) piezoelectric nanofibrous mat interlayer and (c) nanofibers.

5.4.1.2 Crystallinity

While PVDF homopolymer has several polymorphs including four known chain conformations, with the most common crystalline phase that shows no significant piezoelectric behaviour, in PVDF-TrFE copolymer, on the contrary, the presence of the TrFE co-monomer helps the natural formation of the ferroelectric β crystalline phase, independently of the processing method [29,30]. The β-phase is, indeed, the one exhibiting the highest dipole moment and hence the most active piezoelectric phase. While the developed crystal phase (β-phase) is process-insensitive, the crystallinity degree χ_c and the average size of the crystallites, instead, may depend on the processing conditions, i.e. the cooling rate [31].

The Wide-angle X-ray scattering (WAXS) analysis was carried out in order to assess the actual crystal phase type and content in the obtained nanofibers: the diffraction pattern recorded for the "as spun" PVDF-TrFE (blue curve, Figure 5.6) shows a reflection positioned at $2\Theta = 19.75°$, typical of sole electroactive β-phase crystal lattice [32]. Moreover, the as-spun nanofibers present a shoulder associated to a relevant amorphous phase fraction. Indeed, the high evaporation rate occurring during electrospinning process can act similarly to a high cooling rate for the polymeric melt (a similar shoulder is found in quenched PVDF-TrFE [32]). The annealing at 150 °C for 1 h (red curve)

significantly modifies the diffraction pattern of the nanofibrous membrane, with the crystal lattice 19.75° reflection that increases in intensity and definition and a contemporary reduction of the broad amorphous shoulder, denoting an improvement of the *β*-phase. The crystallinity degree, as calculated from the diffractograms deconvolution, also account for such an increase in *β*-phase content, with χ_c, that increases from 33 % for as-spun nanofibers up to 52 % for the annealed ones.
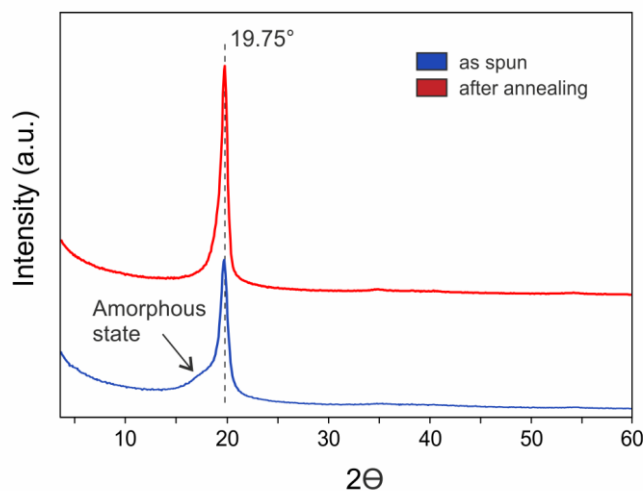

Figure 5.6 – WAXS diffractograms of PVDF-TrFE nanofibers: as-spun (blue) and after annealing at 150 °C for 1 h (red) and cooling at 2 °C/min.

Note that the annealing conditions applied to the fibers are chosen to replicate the thermal condition at which the nanofibrous mat embedded in the composite are subjected during the curing cycle (see Figure 5.3). Therefore, it can be assumed that the nanofibers embedded in the self-sensing laminate present an enhanced *β*-phase compared to as spun ones.

5.4.2 Piezoelectric response to impact

5.4.2.1 Shielding vs triboelectricity

During an impact, when the two colliding objects come into contact, a current flow may occur in between them. The current flow can be caused by the different electric potential between the two objects or the triboelectric charging generated by their friction [33]. This electric discharge, even if low, can interfere with the low voltage and high impedance piezoelectric signal. Moreover, the internal electrodes, due to the large area of the laminate, can behave as an antenna and collect the external electromagnetic interferences, thus disturbing the piezoelectric signal.
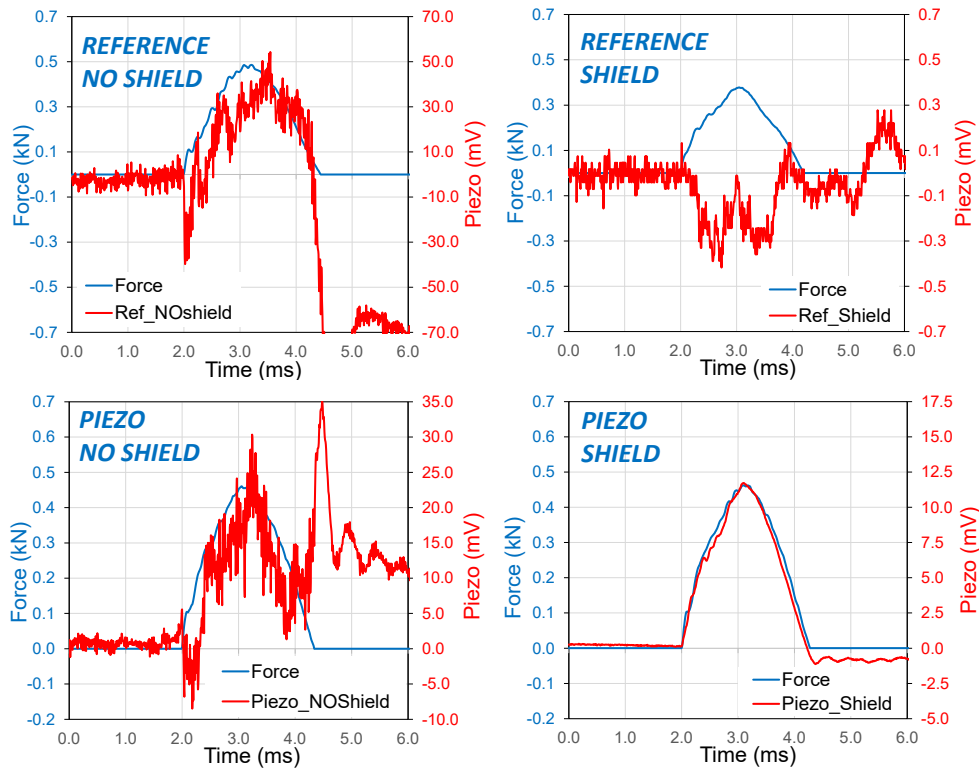
In the graphs of Figure 5.7 the laminate electric response (red curve) was compared to the contact force measured by the impactor load cell (blue curve). In the top row is shown the Reference laminate behaviour while in the bottom row the Piezo one, with the external electrodes floating (left column) and

grounded (right column). Theoretically, the reference laminate (GLARE without nanofibers) should be electrically inert, however, in the floating configuration a signal is recorded when the two colliding objects come into contact, which could be erroneously attributed to the contact force. Nevertheless, the signal does not fit the contact force curve and its shape, magnitude and sign were noticed to be random for multiple impacts with similar conditions. When the two external electrodes are grounded, instead, the signal is reduced by 3 orders of magnitude. This proves that the signal is generated by electrical disturbs and the external electrodes can shield them. Regarding the self-sensing laminate (Piezo), when the external electrodes are floating the piezoelectric signal is remarkably disturbed by the similar magnitude external electric noise. Instead, when the external electrodes are grounded the interference is shielded and the piezoelectric signal faithfully reproduces the contact force.

Figure 5.7 – Electric response (red curve) compared to the contact force measured by the impactor load cell (blue curve), for the Reference laminate (top row) and Piezo one (bottom row), with the external electrodes floating (left column) and grounded (right column) and a shunt resistance of 100 MΩ.

5.4.2.2 Signal proportionality vs shunt resistance

When the self-sensing laminate is subjected to impact, an electric charge proportional to the force magnitude is developed in the piezoelectric element (composed by the nanofibers embedded in the GFRP and the two aluminium electrodes) [34]. By virtue of the element capacitance this charge is stored in the element and is prevented from leaking away, by the high leakage resistance of the

piezoelectric element. However, the impedance of the piezo element and the instrument amplifier input is not really infinite. Moreover, a shunt resistance is necessary to discharge the time accumulated electric charges, coming from ambient noise. Hence over time charges leak away and the piezoelectric signal loses its proportionality with the force magnitude.

In Figure 5.8 the piezoelectric response of the self-sensing laminate (continuous red curve) generated during impact is reported and compared to the contact force measured by the impactor commercial load cell (blue curve), for different shunt resistance values. With 1 kΩ resistor the piezoelectric signal is too low to be distinguished from the electric noise. By raising the resistance to 100 kΩ and then to 1 MΩ, the piezoelectric signal magnitude increases and becomes detectable. However, the piezoelectric signal does not follow the contact force trend, while it seems to be more proportional to its slope (time derivate). By further increasing the shunt resistance value from 1 MΩ to 1000 MΩ, the piezoelectric signal trend changes from semi-derivative to fully proportional, fitting better and better to the contact force curve. However, with a 1000 MΩ resistor the signal starts to drift (visible as a signal offset). Indeed, when the shunt resistance is too high, the electric charges coming from ambient noise cannot be dissipated. Therefore, a shunt resistance of 100 MΩ was chosen as the best compromise between signal proportionality and drifting.
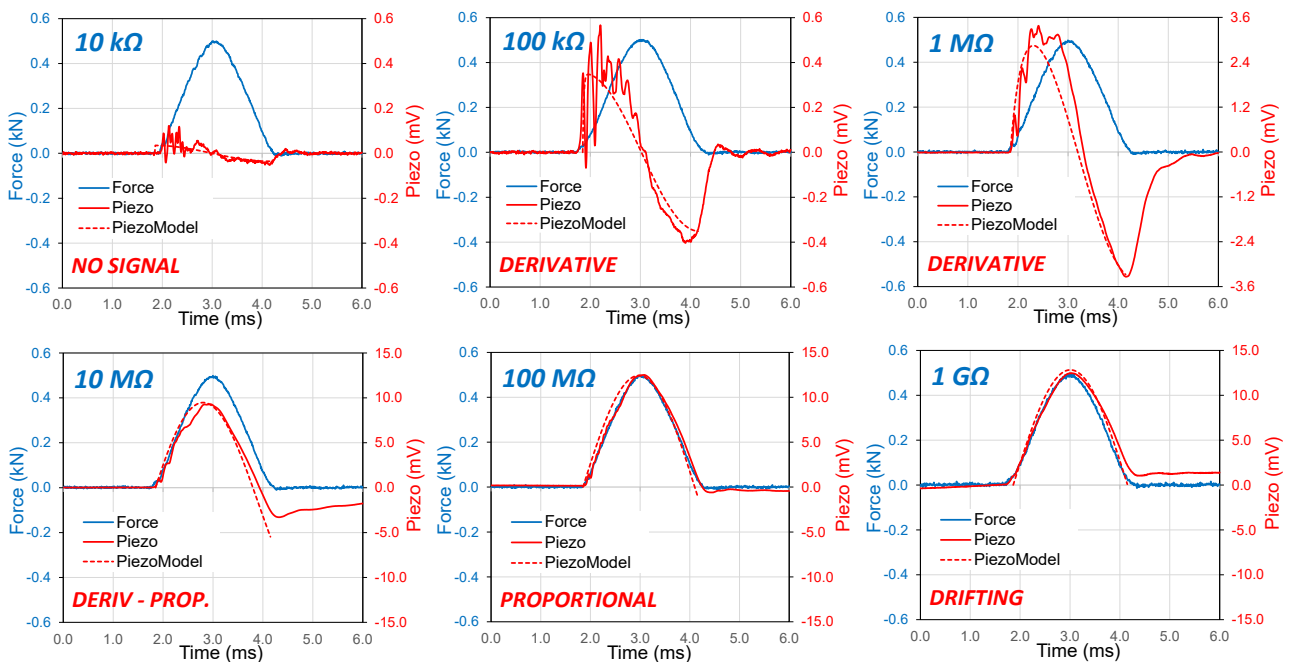
Figure 5.8 – Piezoelectric response of the self-sensing laminate (continuous red curve) compared to the contact force measured by the impactor load cell (blue curve) and the piezoelectric model estimated response (dotted red curve), for different shunt resistance values.

5.4.3 Electric model for the impact response of the self-sensing laminate

In Figure 5.9 is shown the equivalent electric circuit of the self-sensing laminate connected to the voltage amplifier. In the circuit, the piezoelectric element can be modelled as a charge source Q_p, in parallel with a capacitor C_p and a very high internal leakage resistance which can be neglected [35]. The cable capacitance C_c is in parallel with the sensor one, while the low cable resistance can be neglected. The shunt resistor R_s is connected in parallel to the circuit. The impedance of the amplifier is, instead, high enough to be neglected. Therefore, according to Kirchhoff's law, the equivalent capacitance C is the sum of the piezo and cable capacitances in parallel ($C = Cp + Cc$), while the equivalent resistance R can be reduced to the shunt resistance R_s. A capacitance of 182 pF and 19 pF was measured for the piezo element and the signal cable, respectively.
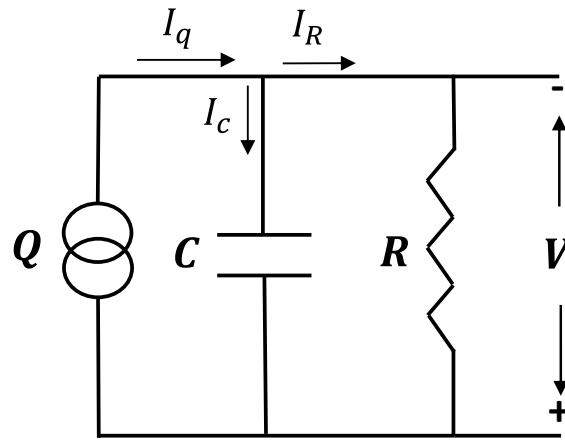
Figure 5.9 – Equivalent electric circuit of the self-sensing laminate connected to the voltage amplifier.

By applying Kirchhoff's law and expressing the relationships of the electric components in complex form ($I_Q = dQ/dt = d_{33}\, dF/dt$; $I_C = V\, J\omega C$; $I_R = V/R$), the circuit equation can be simply written as:

$$V(t) = \frac{R}{j\omega RC + 1} d_{33} \frac{dF(t)}{dt} \qquad \text{Eq. 5.1}$$

being the electric charges Q generated by the piezoelectric element proportional to the applied stress [34] and hence, in this case, to the impact force: $Q = d_{33}F$, with d_{33} the piezoelectric coefficient.

Under the assumption that non-linearities (indentation, membrane stiffness, damage) and mass of the laminate would be negligible, the impact can be modelled as a simple single degree of freedom spring-mass system [36], in which the impact force response is a half-sine wave: $F(t) = F \sin(\omega t)$, with $\omega = 2\pi/T$ and T equal to two times the impact duration. Therefore, by solving Equation 5.1 in

Laplace domain for a sine wave load and then anti transforming it back to the time domain, the piezoelectric voltage output for an impact load can be expressed as:

$$V(t) = \frac{F d_{33} \omega R}{\omega^2 R^2 C^2 + 1} \left(-e^{-\frac{t}{RC}} + \cos(\omega t) + \omega RC \sin(\omega t) \right) \qquad \text{Eq. 5.2}$$

Equation 5.2 is composed of a transient component (exponential term) and a steady-state one (harmonic terms). It can be observed that for high time constant values ($\tau = RC$) compared to the impact time duration ($\omega = 2\pi/T$), the transient term and the first steady-state one can be neglected and the expression can be reduced to:

$$V(t) = \frac{F d_{33}}{C} \sin(\omega t) \qquad \text{Eq. 5.3}$$

Equation 5.3 shows that for high time constant values compared to the impact time duration, the piezoelectric voltage output becomes proportional to the contact force, confirming what was qualitatively observed in the graphs of Figure 5.8. Moreover, the sensibility (signal voltage – impact force ratio) of the self-sensing laminate results to be proportional to the piezoelectric coefficient d_{33}, independent by the resistance and inversely proportional to the capacitance C. The unknown d_{33} coefficient was derived from the impact test results depicted in Figure 5.8 for 100 MΩ resistance (high time constant value), by expressing Equation 5.3 as function of it. An equivalent piezoelectric coefficient of $5.12 \cdot 10^{-3}$ pC/N was so obtained for the self-sensing laminate, which is 3 orders of magnitude lower than the one reported by the supplier for the pure PVDF-TrFE (22 pC/N). The remarkably lower value may be attributed to the piezoelectric nanofibers integration into the composite (see Figure 5.5). In fact, being the laminate remarkably stiffer than the PVDF-TrFE polymer, the impact load directly transferred to the nanofibers is reduced and thus the generated electric charges.

In the graphs of Figure 5.8 the piezoelectric voltage output estimated by the model (dotted red lines) for an impact duration of 2.35 ms, is compared to the experimental results (continuous red lines), for different shunt resistance values. As can be observed, the model curves have a similar trend to the experimental ones up to the impactor rebound because after that moment the impact force drop to zero, while the model hypothesized that the force after the initial transient continues as a steady state sine wave. In Figure 5.10 the blue triangles represent the ratio between maximum voltage generated by the self-sensing laminate and the maximum force recorded during impact, for different shunt resistance values (experimental tests of Figure 5.8), while the red curve is the ratio estimated by the piezoelectric model. As can be observed, the model fits the experimental results with good

approximation. Moreover, the experimental results confirm what observed for Equation 5.3, that for high time constant values the sensibility becomes independent of the resistance value.

As previously mentioned, according to Equation 5.3, the sensibility is inversely proportional to the capacitance and, being the capacitance proportional to the laminate area, the latter is limited by the signal-to-noise ratio. Considering a noise level of 0.1 mV of the measuring chain and a resolution target of 0.1 kN, the maximum allowable area of the self-sensing laminate is 0.25×0.25 m^2. Over this value the electrodes, i.e. the internal aluminium sheets, have to be separated and the signals acquired independently. The multiple signals can be then conveyed to a common spot by cutting the internal aluminium sheets, mimicking the tracks of a PCB board. Moreover, the electrodes subdivision may be exploited for impact localization.
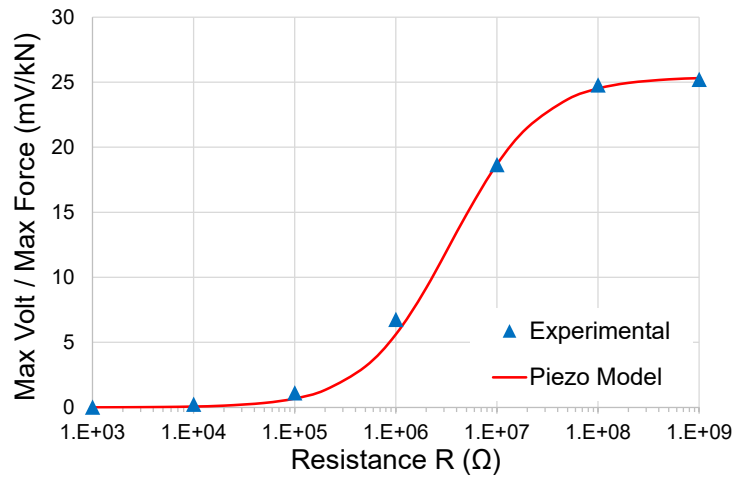
Figure 5.10 – Maximum output voltage - force ratio estimated by the electric model as function of the shunt resistance (red curve), compared to the ones obtained in the experimental tests of Section 5.4.2.2 (blue triangles).

5.4.4 Sensor performances: linearity and spatial uniformity

Electrical performances of the self-sensing laminate were evaluated in terms of linearity (piezoelectric signal versus impact force) and spatial uniformity (sensor sensibility versus impact position). The sensor linearity has been evaluated by recording the piezoelectric voltage peak and contact force peak for impacts performed at different magnitude levels. Results are reported in the scatter plot of Figure 5.11 and interpolated with a linear regression model with 95 % of probability confidence bands computed using the likelihood method as reported in ASTM E739. The sensitivity of the self-sensing laminate turns out to be 25.2 ± 1.7 mV/kN with a coefficient of determination R^2 equal to 0.999. It must be mentioned that the observed remarkable linearity (R^2) is quite common in piezoelectric sensors and also in a wide force range. The detected lower limit of the sensor sensitivity was of 0.05 kN and was attributed mostly to the inherent noise in the measurement chain (electrodes,

cables and amplification circuit). The measured sensitivity results to be adequate to detect an impact that can damage the composite, being generally in the kN scale. However, for the localization of the impact spot by triangulation, the sensitivity should be optimized (e.g., by varying the piezoelectric nanofibrous mat and GFRP thicknesses) in order to be able to detect elastic wave propagations into the laminate.
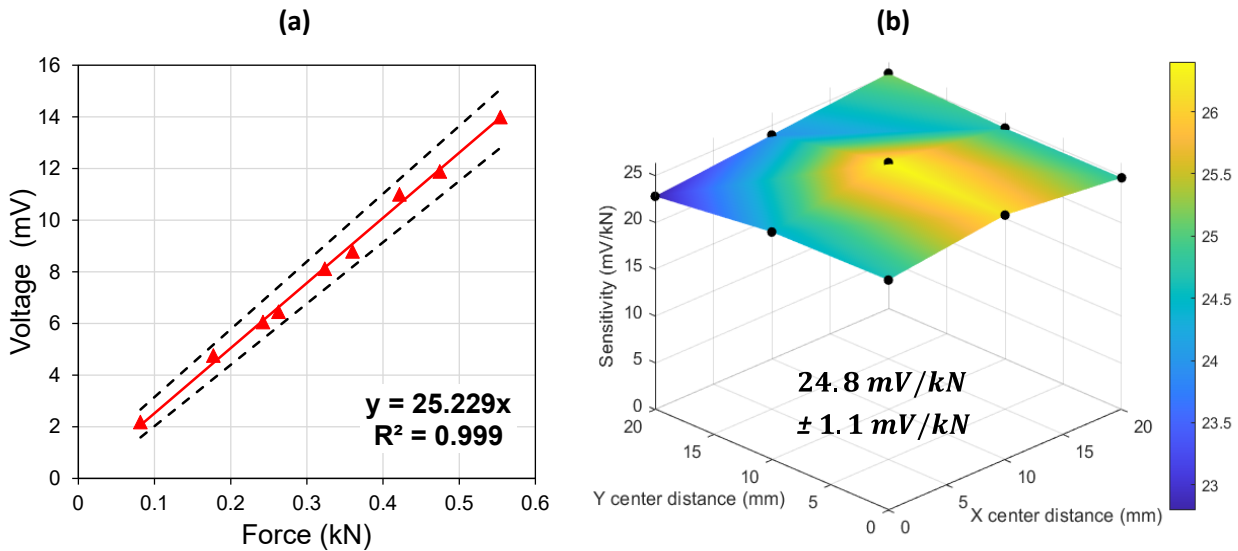

Figure 5.11 – (a) Sensor linearity: piezoelectric voltage peak versus contact force peak for impacts performed at different magnitude levels. (b) Spatial uniformity: sensitivity of the self-sensing laminate impacted at different points on its surface.

The self-sensing laminate should have the capability to detect an impact event on its whole surface for structural health monitoring purposes. Moreover, to provide a reliable response on the impact magnitude, and hence the consequent damage, the sensitivity should be as much homogeneous as possible on its surface. For this reason, the laminate was impacted with a magnitude of 0.5 kN at different points on its surface with a grid pattern of 3×3, 10 mm step between each point and origin in the laminate centre. The measured sensitivity for each impact point is reported in the three-dimensional scatter plot of Figure 5.11b. The calculated sensitivity has a confidence interval of ± 1.1 mV/kN with 95 % confidence level, which corresponds to a relative error of ± 4.6 % and should be acceptable for structural health monitoring purposes. The measured relative error can be considered representative for larger laminates because the grid tested area is bigger than the unit dimensions of the glass fiber fabric texture and nanofibrous one.

By performing low-velocity impact tests, damage evolution can be experimentally correlated to the maximum impact force and therefore to the linear piezoelectric response of the self-sensing laminate. Hence, the SHM system can be alerted when the piezoelectric signal overcomes a certain threshold value [37,38].

5.5 Conclusions

In this work, the integration of a nano-structured piezoelectric sensor, made of PVDF-TrFE nanofibers, into a composite laminate with aluminium sheets as electrodes has been achieved. Structurally, the resulting composite is a hybrid laminate known as Glass Laminate Aluminium Reinforced Epoxy (GLARE), consisting of aluminium sheets alternatively bonded to GFRP prepreg layers, functionalized with PVDF-TrFE interleaved nanofibrous mats. Such a nano-structured hybrid laminate becomes itself a piezoelectric sensor, capable to detect on its whole surface an impact load. This concept overcomes the issues related to the mechanical performance reduction due to the embedding of an extrinsic commercial sensor, which act as damage triggering. The self-sensing laminate stacking sequence was designed to reduce the triboelectric and ambient noise. Moreover, a simple and compact electronic circuit, based on an instrumentation amplifier and a shunt resistance, was realized for the conditioning of the piezoelectric signal.

Non-destructive impact tests were performed using an instrumented drop-weight tower to investigate the real-time electrical response of the self-sensing laminate. A lumped electric model was applied to study and optimize the circuit electrical parameters. The piezoelectric signal response was studied for different shunt resistance values, and an optimized resistance value was found as the best compromise between signal proportionality and drifting. The sensor linearity, defined as sensor signal versus impact force, is of 0.99. While the spatial uniformity response, i.e. the sensor sensitivity versus different impact positions, showed a relative error of 4.6 %. Future studies will focus on the evaluation of the impact strength of the self-sensing hybrid laminate functionalized by piezoelectric nanofibrous mat interleaving.

5.6 Future works

The work presented is the first part of a more extensive investigation, which, besides the self-sensing sensor characterization, includes the mechanical characterization of the composite laminates subjected to impact loads. To this end, destructive impact tests are in progress to evaluate the mechanical impact strength of the self-sensing laminate.

This new type of smart nanofibers allows implementation in different fields, such as to monitor the crack initiation and propagation even in bonded joints.

5.7 Nomenclature

T_c PVDF-TrFE Curie temperature

T_m PVDF-TrFE melting temperature

T_g epoxy resin glass transition temperature

2Θ Wide-angle X-ray scattering (WAXS) diffraction angle

χ_c PVDF-TrFE crystallinity degree

Q circuit electric charge

Q_p piezo charge source

C_p piezo capacitance

C_c cable capacitance

C equivalent capacitance

R circuit equivalent resistance

R_s shunt resistance

I circuit current

d_{33} piezoelectric coefficient

F impact force

ω angular frequency

T period

τ time constant

5.8 References

[1] P. Hofmann, A. Walch, A. Dinkelmann, S.K. Selvarayan, G.T. Gresser, Woven piezoelectric sensors as part of the textile reinforcement of fiber reinforced plastics, Composites Part A: Applied Science and Manufacturing. 116 (2019) 79–86. https://doi.org/10.1016/j.compositesa.2018.10.019.

[2] J. Cai, L. Qiu, S. Yuan, L. Shi, P. Liu, D. Liang, Structural Health Monitoring for Composite Materials, in: Composites and Their Applications, 2012. https://doi.org/10.5772/48215.

[3] N. Takeda, Y. Okabe, J. Kuwahara, S. Kojima, T. Ogisu, Development of smart composite structures with small-diameter fiber Bragg grating sensors for damage detection: Quantitative evaluation of delamination length in CFRP laminates using Lamb wave sensing, Composites Science and Technology. 65 (2005) 2575–2587. https://doi.org/10.1016/j.compscitech.2005.07.014.

[4] S. Masmoudi, A. El Mahi, S. Turki, Use of piezoelectric as acoustic emission sensor for in situ monitoring of composite structures, Composites Part B: Engineering. 80 (2015) 307–320. https://doi.org/10.1016/j.compositesb.2015.06.003.

[5] H.P. Konka, M.A. Wahab, K. Lian, The effects of embedded piezoelectric fiber composite sensors on the structural integrity of glass-fiber-epoxy composite laminate, Smart Materials and Structures. 21 (2012). https://doi.org/10.1088/0964-1726/21/1/015016.

[6] A. Loayssa, New Developments in Sensing Technology for Structural Health Monitoring, 2011. https://doi.org/10.1007/978-3-642-21099-0.

[7] H.N. Li, D.S. Li, G.B. Song, Recent applications of fiber optic sensors to health monitoring in civil engineering, Engineering Structures. 26 (2004) 1647–1657. https://doi.org/10.1016/j.engstruct.2004.05.018.

[8] K. Shivakumar, A. Bhargava, Failure mechanics of a composite laminate embedded with a fiber optic sensor, Journal of Composite Materials. 39 (2005) 777–798. https://doi.org/10.1177/0021998305048156.

[9] B. Lin, V. Giurgiutiu, Modeling and testing of PZT and PVDF piezoelectric wafer active sensors, Smart Materials and Structures. 15 (2006) 1085–1093. https://doi.org/10.1088/0964-1726/15/4/022.

[10] L. Lampani, F. Sarasini, J. Tirillò, P. Gaudenzi, Analysis of damage in composite laminates with embedded piezoelectric patches subjected to bending action, Composite Structures. 202 (2018) 935–942. https://doi.org/10.1016/j.compstruct.2018.04.073.

[11] J. Cheng, C. Qian, M. Zhao, S.W.R. Lee, P. Tong, T.Y. Zhang, Effects of electric fields on the bending behavior of PZT-5H piezoelectric laminates, Smart Materials and Structures. 9 (2000) 824–831. https://doi.org/10.1088/0964-1726/9/6/312.

[12] S. Butler, M. Gurvich, A. Ghoshal, G. Welsh, P. Attridge, H. Winston, M. Urban, N. Bordick, Effect of embedded sensors on interlaminar damage in composite structures,

Journal of Intelligent Material Systems and Structures. 22 (2011) 1857–1868. https://doi.org/10.1177/1045389X11414225.

[13]   I.M. De Rosa, F. Sarasini, Use of PVDF as acoustic emission sensor for in situ monitoring of mechanical behaviour of glass/epoxy laminates, Polymer Testing. 29 (2010) 749–758. https://doi.org/10.1016/j.polymertesting.2010.04.006.

[14]   J.H. Bae, S.H. Chang, Characterization of an electroactive polymer (PVDF-TrFE) film-type sensor for health monitoring of composite structures, Composite Structures. 131 (2015) 1090–1098. https://doi.org/10.1016/j.compstruct.2015.06.075.

[15]   B. Tang, J. Mommaerts, R.K. Duncan, J.C. Duke, D.A. Dillard, Nondestructive evaluation of model adhesive joints by PVDF piezoelectric film sensors, Experimental Mechanics. 33 (1993) 102–109. https://doi.org/10.1007/BF02322485.

[16]   N.A. Chrysochoidis, E. Gutiérrez, Evaluation of the sensitivity and fatigue performance of embedded piezopolymer sensor systems in sandwich composite laminates, Smart Materials and Structures. 24 (2015). https://doi.org/10.1088/0964-1726/24/2/025032.

[17]   H. Zhang, E. Bilotti, T. Peijs, The use of carbon nanotubes for damage sensing and structural health monitoring in laminated composites: a review, Nanocomposites. 1 (2015) 167–184. https://doi.org/10.1080/20550324.2015.1113639.

[18]   I. Kang, Y.Y. Heung, J.H. Kim, J.W. Lee, R. Gollapudi, S. Subramaniam, S. Narasimhadevara, D. Hurd, G.R. Kirikera, V. Shanov, M.J. Schulz, D. Shi, J. Boerio, S. Mall, M. Ruggles-Wren, Introduction to carbon nanotube and nanofiber smart materials, Composites Part B: Engineering. 37 (2006) 382–394. https://doi.org/10.1016/j.compositesb.2006.02.011.

[19]   I. Kang, M.J. Schulz, J.H. Kim, V. Shanov, D. Shi, A carbon nanotube strain sensor for structural health monitoring, Smart Materials and Structures. 15 (2006) 737–748. https://doi.org/10.1088/0964-1726/15/3/009.

[20]   G. Spinelli, P. Lamberti, V. Tucci, L. Vertuccio, L. Guadagno, Experimental and theoretical study on piezoresistive properties of a structural resin reinforced with carbon nanotubes for strain sensing and damage monitoring, Composites Part B: Engineering. 145 (2018) 90–99. https://doi.org/10.1016/j.compositesb.2018.03.025.

[21]   A. Vlot, W. Gunnink, Fibre Metal Laminates, 2001. https://doi.org/10.1007/978-94-010-0995-9.

[22]   T. Brugo, R. Palazzetti, The effect of thickness of Nylon 6,6 nanofibrous mat on Modes I–II fracture mechanics of UD and woven composite laminates, Composite Structures. 154 (2016) 172–178. https://doi.org/10.1016/j.compstruct.2016.07.034.

[23]   H. Zarei, T. Brugo, J. Belcari, H. Bisadi, G. Minak, A. Zucchelli, Low velocity impact damage assessment of GLARE fiber-metal laminates interleaved by Nylon 6,6 nanofiber mats, Composite Structures. (2017). https://doi.org/10.1016/j.compstruct.2017.01.079.

[24]   L. Daelemans, W. Van Paepegem, K. De Clerck, Effect of interleaved polymer nanofibers on the properties of glass and carbon fiber composites, INC, 2020. https://doi.org/10.1016/b978-0-12-819904-6.00011-6.

[25]   H. Niu, T. Lin, Fiber generators in needleless electrospinning, Journal of Nanomaterials. 2012 (2012). https://doi.org/10.1155/2012/725950.

[26]   T. Feng, D. Bekas, M.H. Ferri Aliabadi, Active health monitoring of thick composite structures by embedded and surface-mounted piezo diagnostic layer, Sensors (Switzerland). 20 (2020) 1–19. https://doi.org/10.3390/s20123410.

[27]   D. Mandal, S. Yoon, K.J. Kim, Origin of piezoelectricity in an electrospun poly(vinylidene fluoride-trifluoroethylene) nanofiber web-based nanogenerator and nano-pressure sensor, Macromolecular Rapid Communications. 32 (2011) 831–837. https://doi.org/10.1002/marc.201100040.

[28]   W. Jilani, N. Mzabi, O. Gallot-Lavallée, N. Fourati, C. Zerrouki, R. Zerrouki, H. Guermazi, Dielectric relaxations investigation of a synthesized epoxy resin polymer, European Physical Journal Plus. 130 (2015) 1–10. https://doi.org/10.1140/epjp/i2015-15076-6.

[29]   P. Martins, A.C. Lopes, S. Lanceros-Mendez, Electroactive phases of poly(vinylidene fluoride): Determination, processing and applications, Progress in Polymer Science. 39 (2014) 683–706. https://doi.org/10.1016/j.progpolymsci.2013.07.006.

[30]   R.G. Kepler, R.A. Anderson, Ferroelectric polymers, Advances in Physics. 41 (1992) 1–57. https://doi.org/10.1080/00018739200101463.

[31]   E. Maccaferri, L. Mazzocchetti, T. Benelli, T.M. Brugo, A. Zucchelli, L. Giorgini, Rubbery nanofibers by co-electrospinning of almost immiscible NBR and PCL blends, Materials and Design. (2020). https://doi.org/10.1016/j.matdes.2019.108210.

[32]   W. Xia, Z. Xu, Q. Zhang, Z. Zhang, Y. Chen, Dependence of dielectric, ferroelectric, and piezoelectric properties on crystalline properties of p(VDF-co-TrFE) copolymers, Journal of Polymer Science, Part B: Polymer Physics. 50 (2012) 1271–1276. https://doi.org/10.1002/polb.23125.

[33]   Z.L. Wang, A.C. Wang, On the origin of contact-electrification, Materials Today. 30 (2019) 34–51. https://doi.org/10.1016/j.mattod.2019.05.016.

[34]   Piezoelectric sensorics: force, strain, pressure, acceleration and acoustic emission sensors, materials and amplifiers, Choice Reviews Online. 40 (2002) 40-0924-40–0924. https://doi.org/10.5860/choice.40-0924.

[35]   M. Serridge, T.R. Licht, Accelerometers Piezoelectric and Vibration Preamplifiers. Theory and Application Handbook, Bruel & Kjaer, 1987. http://www.bksv.com/Products/transducers/vibration/accelerometers/handbook.aspx.

[36]   S. Abrate, Impact on Composite Structures, 1998. https://doi.org/10.1017/cbo9780511574504.

[37]   H. Fu, Z. Sharif Khodaei, M.H.F. Aliabadi, An Event-Triggered Energy-Efficient Wireless Structural Health Monitoring System for Impact Detection in Composite Airframes, IEEE

Internet of Things Journal. 6 (2019) 1183–1192.
https://doi.org/10.1109/JIOT.2018.2867722.

[38]   H. Fu, Z. Sharif Khodaei, M.H. Aliabadi, An energy efficient wireless module for on-board aircraft impact detection, in: 2019: p. 46. https://doi.org/10.1117/12.2513534.

ACKNOWLEDGEMENTS